Multi-Strange Baryon Production in p–Pb Collisions with ALICE at the LHC

EMILY JADE WILLSHER LLOYD

A Thesis submitted to the University of Birmingham for the degree of Doctor of Philosophy

Nuclear Physics Group

School of Physics and Astronomy

College of Engineering and Physical Sciences

University of Birmingham

Jul, 2020

Abstract

A strongly-interacting state of matter known as the Quark-Gluon Plasma (QGP) is formed at high temperatures and energy densities. These conditions are achieved in heavy-ion collisions, such as the lead-lead (Pb–Pb) collisions carried out at the Large Hadron Collider (LHC), and key results have confirmed a QGP formation. Smaller systems formed in proton–proton (pp) and proton–lead (p–Pb) collisions are not expected to achieve the conditions required to form a QGP. The results from the most recent high energy collisions achieved at the LHC, suggest this is no longer certain. One of the key signals used to explore the properties of the matter formed in collisions, is the production of strange hadrons. The excellent tracking and particle identification capabilities of the ALICE detector can be utilised to study the production of multi-strange baryons ($\Xi^{\pm}$, $\Omega^{\pm}$). This thesis presents the results of the production of multi-strange baryons in p–Pb collisions at a centre of mass energy of 8.16 TeV. The transverse momentum (p_T) distributions and mean transverse momentum, $\langle p_{\mathrm{T}} \rangle$, are studied as a function of particle multiplicity. An increase with multiplicity in $\langle p_{\mathrm{T}} \rangle$ is observed that is greater for the $\Omega^{\pm}$ than the $\Xi^{\pm}$, indicating the presence of radial flow. The yields of the baryons are also measured and normalised to pion yields in order to study the strangeness enhancement effect, originally predicted to indicate the presence of a QGP. A comparison to other collision energies and systems, pp, Pb–Pb and Xe–Xe, indicates that the hyperon-to-pion ratios follow a continuously increasing trend from low multiplicity pp to high-multiplicity Pb–Pb, independent of the initial collision energy and system size.

Author's Contribution

Over the course of completing my PhD, I have been a member of the ALICE collaboration. Therefore, I cannot claim to be the sole contributor to all of the work presented in this thesis. I am entirely indebted to the whole team of scientists and engineers who work on the ALICE experiment and the LHC. I have spent my time in ALICE as part of the Light Flavour Physics Working Group (PWG-LF) and in particular the Strangeness Physics Analysis Group (PAG), whose members have provided advice and guidance throughout my time in ALICE.

Due to the nature of the large data sets produced at the LHC, in order to make the analysis data files more manageable, an initial analysis is carried out on the raw Event Summary Data (ESD) files to produce data containing only information needed for the analysis in this thesis in so-called TTrees using the ROOT analysis framework [1]. These contain data for potential cascade candidates and have a much reduced file size. The code to produce these TTrees was originally written by David Chinellato[1] for Pb–Pb data. Once I began the analysis presented in this thesis on Run 2 p–Pb data, I made modifications to this code to make it work for a p–Pb analysis. Over the course of the analysis, I have also developed and updated post-processing macros, originally inher-

[1] University of Campinas, Brazil

ited from Livio Bianchi[2], to include new features. These macros are used to analyse the TTrees produced to obtain baryon yields, optimise the selection procedures and calculate the systematic errors. The plots presented in this thesis have been produced by me unless otherwise stated.

The preliminary results from this work were approved by the collaboration to present at Strangeness in Quark Matter (SQM) in May 2019 in Bari, Italy and the International Nuclear Physics Conference (INPC) in July 2019 in Glasgow, UK. I gave talks on my results at both conferences and also wrote a proceedings for SQM that has been published in Springer Proceedings in Physics [2] and is shown in appendix D.

During my Long-Term Attachment (LTA) at CERN, I was also involved in work on the upgrade of the Central Trigger Processor (CTP) of ALICE for Run 3. I tested the functioning of the first batch of CTP LTU boards produced. I also completed an aging test on a selection of the boards to check for any design flaws, by placing them in a temperature test chamber and cycling the temperature for a number of weeks, before removing and retesting their functionality. This work was supervised by Anton Jusko, Marian Krivda and Roman Lietava.

[2]University of Turin, Italy

To Matthew

Acknowledgements

Firstly, I must thank the Science and Technology Facilities Council (STFC) and the School of Physics and Astronomy for funding this research. Over the course of my PhD, I have received support from numerous people that I would also like to take the chance to thank now. First and foremost, my supervisors David Evans and Roman Lietava, who have always made time to discuss my work with me and patiently explain many of the concepts mentioned in this work. Many thanks also to my masters supervisor Peter Jones who initially introduced me to the ALICE collaboration and the QGP. I would also like to thank the other members of the group for their support of my work both at CERN and in Birmingham: Orlando Villalobos-Baillie, Anton Jusko and Marian Krivda.

The work in this thesis would not be possible without every member of the ALICE collaboration and their work on the experiment, therefore I would like to thank them all. In particular, I would like to thank my colleagues in the Strangeness PAG as well as those in the Light Flavour Working Group who have provided feedback and advice over the course of my PhD during numerous exchanges and interesting discussions. I would particularly like to thank Livio Bianchi whose help and advice as I began this analysis was invaluable.

I would like to also thank the people I have shared an office with over the years of my PhD in Physics West, Physics East and at CERN who provided many hours of entertainment: Andy, Maria, Lorenza, Kae, Nima, Luis, Harry, Jack, Tony, Pedro, Stuart, Beckie, Ollie, Jakub, Håkan, Yiming, Ross, Angus, Simone, Mark, David and Sammy. Thanks to Josie, Jamie, Chris, Beccie and Morgan who visited me while I was living in France and provided much-needed company and a welcome break from physics. To my flatmates Isabel and Hannah for the many evenings spent together laughing. To all of my family for their continued support, but in particular my parents who have always provided never-ending encouragement and advice. Finally, I thank my husband Matthew for sharing all the stress over the last few years and for providing constant dedication and support, without which I would not have been able to complete this PhD.

Contents

List of Figures

List of Tables

Chapter 1

The Physics Behind the Quark-Gluon-Plasma

For millennia, scientists have been trying to establish what the fundamental building blocks of matter are, as well as their properties and how they interact with each other. The original idea that all matter is made from atoms was first postulated by the Greek philosopher Democritus in ∼450 B.C. The word atom derives from the Greek *atomos*, meaning indivisible, as it was originally believed that the atom was the smallest unit of matter to exist. Aristotle's theory, that all matter is made up of the four fundamental elements of earth, fire, water, and air, was much more popular and prevailed for many years. The idea of atoms was later revived in 1800 when the British chemist John Dalton conducted experiments on compounds. He showed that a compound contains elements in the same ratio and that different compounds can be formed with a different ratio of the elements [3]. In order to explain his observations, he used the concept of atoms by suggesting the elements consist of tiny particles that can be combined in different ways. However, Dalton's theory suggested atoms were particles made of solid matter.

JJ Thompson updated this model after his discovery of the first fundamental particle,

the electron, in 1897 [4]. Atoms were known to be neutral but Thompson had measured electrons to be negatively charged, therefore he suggested the plum pudding model in which atoms consist of a sphere of positive matter embedded with negatively charged electrons. Ernest Rutherford developed the model further with the results of his famous gold foil experiment in 1911 [5], which indicated most of the atom is in fact empty space and the positive charge is concentrated in an area at the centre of the atom, which he named the nucleus. He also later discovered that the nucleus was made up of positively-charged particles called protons and also predicted the existence of a neutral particle called the neutron, which his student James Chadwick discovered in 1932 [6]. In Rutherford's planetary model, the atom consists of a positive nucleus with electrons orbiting around it in random orbits. The work of Niels Bohr later showed that the electrons actually occupy fixed energy levels, which they can move between when an atom emits or absorbs energy [7].

The two types of particle in the nucleus, the positively charged protons and the neutral neutrons, are known as nucleons. They were originally thought to be fundamental, like the electron; however later studies showed they are actually made up of the fundamental particles known as quarks. The quarks are bound together into hadrons via the strong force, which is mediated by massless particles known as gluons. The strong force is one of the four fundamental forces and is responsible for holding the quarks within the nucleons, as well as the nucleons within the nucleus. This force in particular is the focus of the research in this thesis. The remainder of this chapter will introduce the model describing the fundamental particles and their interactions, which is known as the Standard Model. The discovery of the quarks and the gluons (collectively called partons) will be outlined and the key properties of the strong force, which allow a phase transition into a new state of matter, called a quark-gluon plasma (QGP), will be explained. The theory behind the strong force, Quantum Chromodynamics (QCD), will be introduced and the formation of a QGP in heavy-ion collisions will be described.

1.1 | The Standard Model

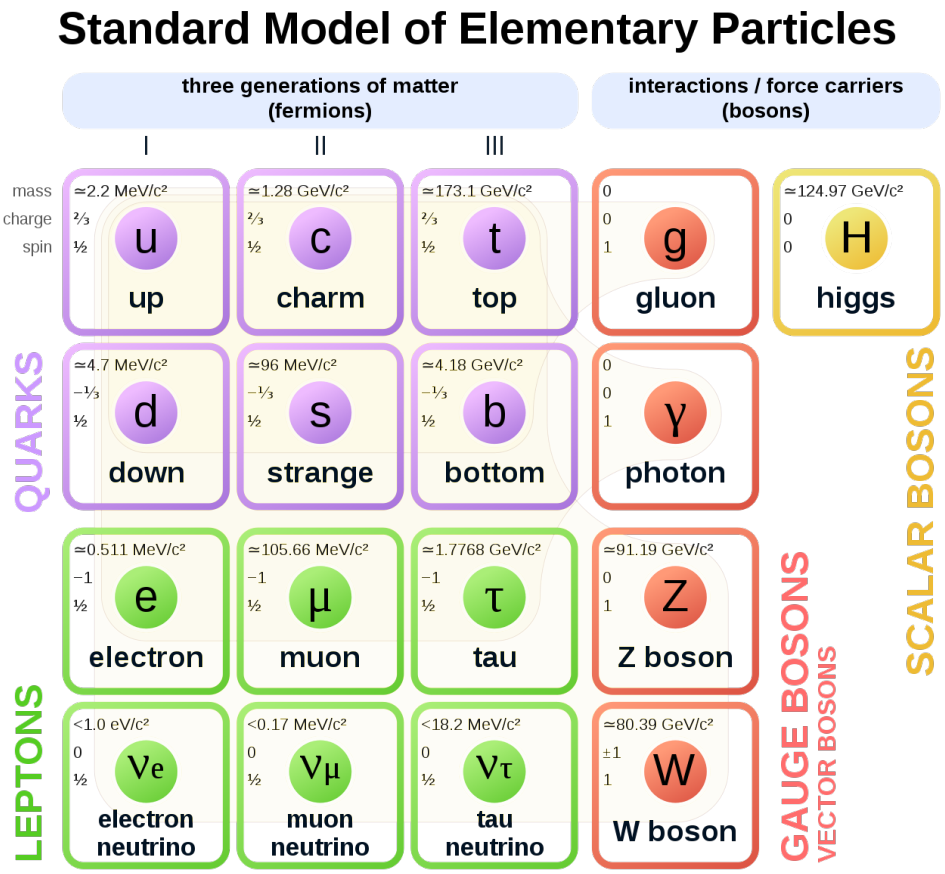

Figure 1.1: The particles that make up the standard model of particle physics [8].

The Standard Model of particle physics is a theory that describes the fundamental particles and forces of particle physics, including the weak force, the strong force and the electromagnetic force. Figure 1.1 shows that the Standard Model particles are divided into fermions, that make up matter, and bosons, which carry force. The fermions consist of quarks and leptons, where the quarks carry fractional electric charge and colour charge, the charge associated with the strong force. There are six quarks of different flavour called: up, down, strange, charm, top and bottom. The leptons consist of the negatively charged electron, as well as the heavier copies called a muon and a tau, and the corresponding neutrinos which are chargeless particles, originally thought to be massless when the Standard Model was first conceived. However, the observation of neutrino

flavour oscillations at Super-Kamiokande [9] verified that neutrinos have a small but finite mass and provided the first evidence of beyond-the-standard model physics.

The electromagnetic force is carried by virtual photons and its behaviour is described by the theory of Quantum Electrodynamics, developed by Shini'chiro Tomonaga, Julian Schwinger and Richard Feynman in the 1940's [10–14], which earned them the Nobel prize in 1965. The weak force is mediated by the $W^{\pm}$ and Z^0 bosons and described by Electroweak theory which unifies the weak force and the electromagnetic force. This theory was developed by Sheldon Lee Glashow, Steven Weinberg and Abdus Salam in the 1960's [15–17] and was awarded the Nobel prize in 1979. The later experimental observation of the W/Z bosons at the Proton Antiproton Collider in 1983 at CERN [18–21] led to a Nobel prize being awarded to Carlo Rubbia and Simon van der Meer in 1984. The strong force is carried by the gluons and is described by the theory of Quantum Chromodynamics, which will be discussed further later in this chapter.

The standard model also includes the existence of antiparticles. For every particle, there exists an antiparticle with the same mass but opposite charge. The first antiparticle, the positron, was observed experimentally in 1932 by Carl Anderson [22] using a cloud chamber, which earned him the Nobel prize in 1936. A cloud chamber is a container filled with supersaturated vapour that is ionised by a charged particle passing through. The vapour condenses on the ions formed, creating visible tracks that show the path of the charged particles. If a magnetic field is applied across the chamber, the tracks are curved and the charge-to-mass ratio of the particle can be extracted by measuring the curvature of the track. The tracks measured by Anderson had the same charge-to-mass ratio as the electron, but were positively charged and were therefore determined to be positrons. When matter and antimatter collide they annihilate, creating energy equivalent to the masses of the colliding particles. In collisions of particles, such as those carried out at the Large Hadron Collider, matter and antimatter is created in equal amounts.

1.2 | QCD

In the late 1940's physicists believed the particles of the atom, electrons, protons and neutrons, to be elementary particles. They were aware that there must be some form of strong interaction to overcome the electromagnetic repulsion inside of nuclei and particles that experience this force, such as protons and neutrons, were named hadrons. In the 1950's, due to developments in particle accelerators and detectors, particle physicists began to discover new hadrons at an ever-increasing rate leading to a 'particle zoo' of hundreds of so-called elementary particles. The physicists Murray Gell-Mann and Yuval Ne'eman began trying to find a pattern in the newly discovered particles just as Mendeleev had done with the elements [23]. They organised the particles into groups of similar properties using a symmetry based on flavour known as the 'eightfold way' [24, 25], which won Gell-Mann the Nobel prize in 1969.

In 1964 Gell-Mann and George Zweig independently suggested that the structure of the groups of hadrons could be explained by the existence of more fundamental particles with non-integer values of electric charge, which Gell-Mann named quarks and Zweig named aces. These particles could be combined in groups to form hadrons with the observed properties [26, 27]. Gell-Mann's name, quarks, is the one that stuck and is still used today. The quarks and their anti-quarks can be combined together to form mesons ($q\bar{q}$) and baryons (qqq).

1.2.1 | Colour

States that are a combination of the same flavour of quark, such as the Ω^- (sss), the Δ^{++} (uuu) and the Δ^- (ddd), seem to violate the Pauli exclusion principle for fermions [28], which states two identical fermions cannot occupy the same quantum state (have identical quantum numbers for properties such as angular momentum, baryon number and electric charge). Therefore, it was proposed by Oscar W. Greenberg, Moo-Young

Han and Yoichiro Nambu that the quarks have an additional quantum number, later named colour [29, 30]. The three states of this new quantum number are represented as red (r), blue (b) and green (g) colour charge. All hadrons are colour neutral with baryons made up of rgb or $\bar{r}\bar{g}\bar{b}$ and mesons formed of either $r\bar{r}$, $g\bar{g}$ or $b\bar{b}$ colour-anticolour pairs. This colour charge is analogous to the electromagnetic charge; however, the force carriers for the strong force, gluons, also carry colour charge, unlike the photons which carry no electric charge. This gives the strong interaction its unique properties known as confinement and asymptotic freedom.

1.2.2 | Confinement

In Quantum Electrodynamics (QED) the potential is inversely proportional to the separation of the charges, r,

$$V_{QED}(r) \propto \frac{-\alpha_{em}}{r}, \tag{1.1}$$

where α_{em} is the electromagnetic coupling constant. However, the behaviour is different for a strong potential in Quantum Chromodynamics (QCD). As two colour charges are pulled apart, the gluons self-interact and the energy in the field creates more gluons which pull the field lines together as shown schematically in figure 1.2a. This behaviour adds an additional 'string-like' term proportional to the 'string' constant, k, to the potential. This gives the Cornell potential for QCD

$$V_{QCD}(r) \propto -\frac{4}{3}\frac{\alpha_s}{r} + kr, \tag{1.2}$$

where α_s is the strong coupling constant [31]. As the colour charges are separated further, the second term dominates and the equation indicates the force will increase infinitely. However, as the energy increases it actually becomes energetically favourable to break the string and create a new quark-antiquark pair from the gluon field, rather than separate the quarks further as shown schematically in figure 1.2b. This leads to the confinement of quarks in hadrons, preventing single quarks from being observed experimentally.

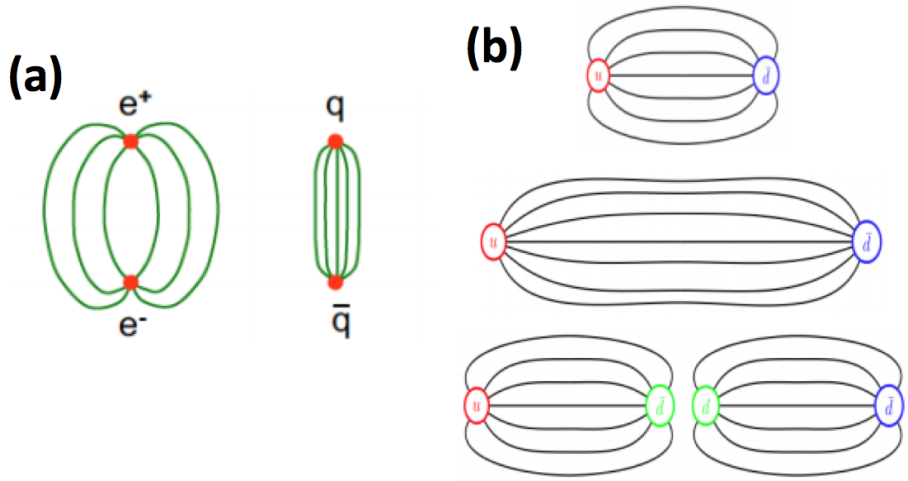

Figure 1.2: (a) A diagram demonstrating the different behaviour of field lines in a QED (left) and QCD (right) potential. In QED the field lines spread out over space, whereas in QCD, the self-interaction of the gluons squeezes the field lines into a flux tube. (b) Diagram demonstrating the breaking of colour strings when a quark pair is separated. Adapted from [32].

1.2.3 | Asymptotic freedom

In both QED and QCD the coupling 'constants' actually vary depending on the separation of bare charges, due to vacuum fluctuations allowed by Heisenberg Uncertainty Principle. In QED, an electron is surrounded by electron-positron pairs which screen the charge of the electron. As another charge is brought closer to the electron, the screening is reduced and the magnitude of the charge of the electron appears to be greater. This effect is represented by the coupling constant, α_{em} increasing. Therefore, the strength of the electromagnetic force is dependent on the distance scale of the interaction. Reduced distances indicate high momentum transfers in the interaction, so the strength of the coupling constant is usually described in terms of the four momentum, Q. For the QED coupling constant, this is described by

$$\alpha_{em}(Q) = \frac{\alpha}{1 - \frac{2\alpha}{3\pi}\ln(Q/m_e)} \tag{1.3}$$

where $\alpha = \frac{e^2}{4\pi}$ and m_e is the mass of the electron [33].

In QCD, a similar effect is seen, however, a colour charge will be surrounded by virtual

gluon loops as well as quark-antiquark pairs. These gluon loops have an anti-screening effect that counteracts the screening of the quark-antiquark pairs. The strength of the coupling constant is described by

$$\alpha_s(Q^2) = \frac{\alpha_s(Q_0^2)}{1 + \frac{11N_c - 2n_f}{12\pi}\alpha_s(Q_0^2)\ln(Q^2/Q_0^2)} \tag{1.4}$$

which gives the value of α_s at Q^2 relative to a value measured at Q_0^2 [34]. The factors N_c and n_f are given by the number of colour charges (three) and the number of quark flavours (six) respectively. With these values, the anti-screening effect of the gluons dominates. As the colour charges are brought closer together, or Q^2 increases, the anti-screening is reduced and the strength of the colour charge decreases. This can be seen in figure 1.3, which shows the results of calculating α_s using experimental data from different measurements such as the hadronic branching fractions of τ lepton decays, jet production rates in deep inelastic scattering (DIS) processes, e^+e^- annihilation and the masses, mass splittings and decay rates of heavy quarkonia. This figure demonstrates the running of the QCD coupling constant known as asymptotic freedom which was discovered by David Politzer, David Gross and Frank Wilczek [35–37], and won them the Nobel prize in 2004.

The asymptotically free behaviour of quarks at small separation scales, led John Collins and Malcolm Perry to hypothesise the existence of a new superdense state of matter made of deconfined quarks rather than hadrons that could exist in the centre of neutron stars and in the very early stages of the Universe after the Big Bang [38]. This state of matter is known as a quark-gluon plasma (QGP).

1.2.4 | Debye Screening

In a hot and dense medium, a common phenomenon known as Debye screening can occur. It is common in electromagnetic plasmas, but can also be used to model the deconfinement of quarks at lower energy scales than asymptotic freedom. When the

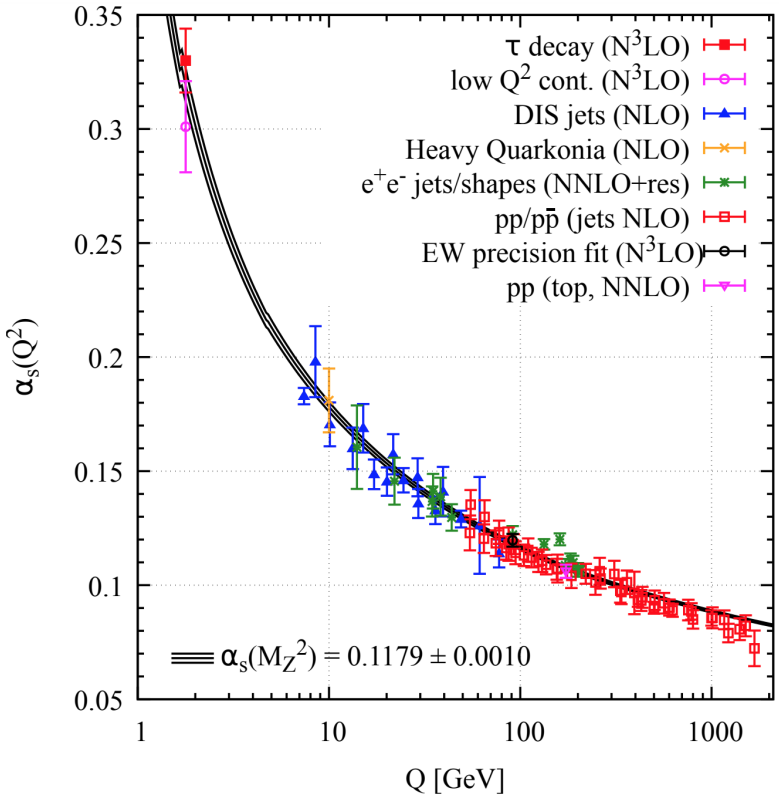

Figure 1.3: Measurements of the coupling constant, α_s, as a function of the energy scale, Q. The curves show the QCD predictions [39].

distances separating colour charges is reduced significantly, long range interactions are screened so only short-range interactions need to be considered. This modifies the QCD potential to

$$V_{QCD}(r) = -\frac{4}{3}\frac{\alpha_s}{r}e^{-r/R_D}, \tag{1.5}$$

where R_D represents the Debye screening length [40]. As the density of the matter increases through heating or compression, the Debye screening length reduces. When R_D becomes comparable to hadronic radii at ≈ 1 fm, the forces between the quarks become smeared by nearby colour charges and the hadrons melt into a quark medium in which quarks and gluons continue to interact strongly but can not be bound into hadrons.

1.2.5 | Phase Diagram

A phase diagram is used to show the different states of a substance under different conditions. The phase diagram for hadronic matter is shown in figure 1.4. It shows

the relationship between the temperature, T and the chemical potential, μ_B, where μ_B is related to the net baryon number density of the system and is zero in a vacuum and approximately 1 GeV for normal nuclear matter. Phase transitions occur when matter changes from one state to another, indicated by the curved lines on the diagram. At the critical point, different phases can coexist in the same conditions. As shown on the diagram, the QGP of the early universe is found at high temperatures, where μ_B is almost zero. This is the region of the phase diagram being explored by ALICE [41] at the LHC [42].

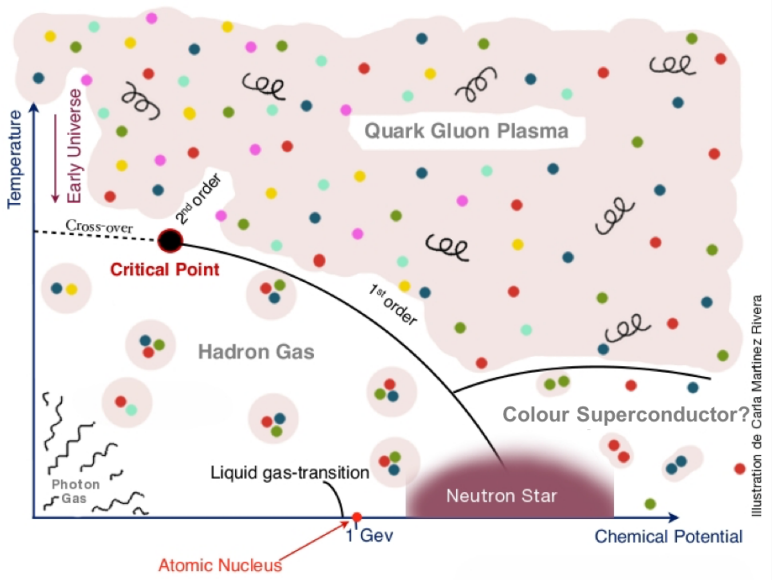

Figure 1.4: Phase diagram of hadronic matter. Adapted from [43].

1.2.6 | MIT Bag Model

In order to extract useful, measurable parameters, such as the temperature of the phase transition, the dissolving of the quarks into a quark-gluon plasma can be modelled using a model such as the MIT bag model [44]. This model treats the quarks as massless particles in a finite region of space referred to as the bag. Confinement is provided by an external bag pressure, B, which balances the internal pressure from the quarks. In the high temperature, T, limit, the coupling constant approaches zero due to asymp-

totic freedom. This means the quarks and gluons themselves are non-interacting and they can be modelled as an ideal gas. The equation of state for an external gas of pions and an internal free gas of quarks and gluons can be compared and an approximation of the transition temperature and density can be found, where the pressure of both is equal.

From this model, with a value of $B^{1/4} \approx 220$ MeV, the values obtained for critical temperature and density at which matter transitions to a QGP are $T_c \approx 160$ MeV and $\epsilon_c \approx 1.2$ GeV fm^{-3} [31]. For a more rigorous approach that takes into account the interactions of the particles near the critical temperature, Lattice QCD calculations have to be used.

1.2.7 | Lattice QCD

Lattice QCD is a technique for studying QCD and the QGP that uses a discretisation of the QCD Lagrangian, which describes the dynamics of the quarks and gluons, onto a 4D grid of three spatial dimensions and a time dimension [45]. Figure 1.5 shows calculations of the energy density, ϵ, over T^4 plotted as a function of T/T_c, where T_c is the critical temperature, for three different numbers of quark flavours; two or three light quark masses are used in calculations or the 2+1 label corresponds to the case where two light quark masses and a strange quark mass four times heavier is used. There is a clear, sharp increase in energy density indicating a phase transition from hadronic matter to a deconfined QGP at a temperature of $T_c(N_f = 3) = 154 \pm 8$ MeV and $T_c(N_f = 2) = 173 \pm 8$ MeV [46]. The value of energy density in the ideal gas model, ϵ_{SB}, is indicated in the diagram. At higher temperatures, the deconfined matter is predicted to approach this limit, however this does not seem to be approached for temperatures close to T_c for any of the number of flavours studied, indicating that interactions between quarks and gluons remain in a QGP.

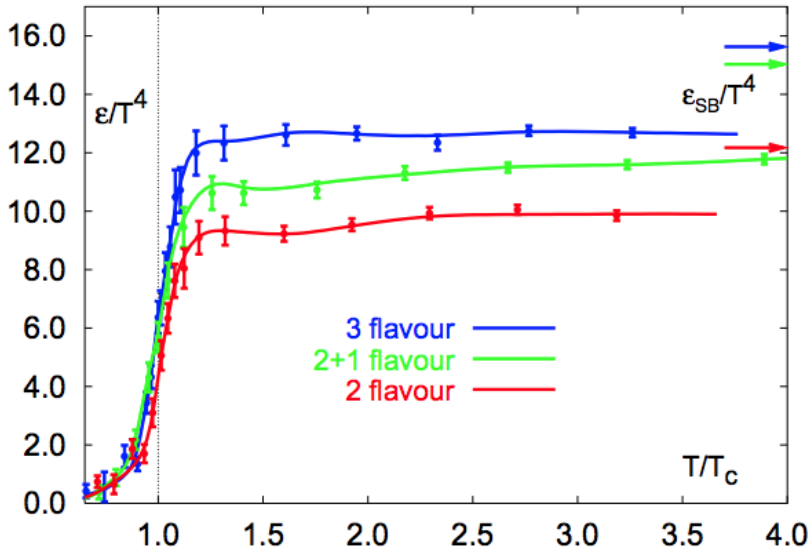

Figure 1.5: Energy density as a function of T/T_c for different numbers of quark flavours in QCD. The curve labeled 2+1 flavour corresponds to a calculation using two light quark masses and a four times heavier strange quark mass [46].

1.3 | QGP formation in a Collider

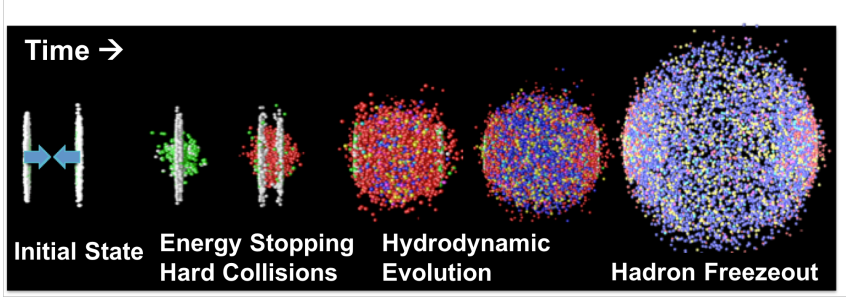

Figure 1.6: Time evolution of a heavy-ion collision. Adapted from [47].

In order to create the extreme conditions required for nuclear matter to undergo a phase transition to a QGP, two heavy nuclei can be collided at sufficiently high energies. In heavy-ion collisions, the colliding ions are travelling at almost the speed of light so are Lorentz-contracted and can be considered as two thin disks as indicated in figure 1.6. The collision of these disks leads to a large amount of energy being deposited in a small region of space, therefore creating the critical conditions for QGP formation. Once the QGP reaches thermal equilibrium it is governed by the laws of thermodynamics as it expands and cools until it reaches hadron (also known as chemical) freeze-out at which

point the deconfinement ceases and the particles hadronise.

When the nuclei collide, the nucleons can be considered as either participants or spectators of the collision, where a participant is defined by a nucleus undergoing at least one inelastic collision. The number of participants, N_{part}, and spectators, N_{spec}, are connected to the centrality of the collision. This is defined by the value of the impact parameter, b, of the collision which is the distance between the centres of the colliding nuclei in the plane perpendicular to the collision axes *ie.* the overlap of the colliding nuclei. The centrality is defined to be very central at low values of b and peripheral at high values of b. The centrality of a collision cannot be measured directly so a measurable quantity is mapped onto Monte Carlo simulations, as explained in more detail in sections 2.2.1 and 3.2.5. Different classes of events can be defined by dividing the total integrated cross-section into percentile classes based on the centrality of the collision. A 0-10% centrality class would include the most central events and a 80-100% class would include the most peripheral events. When looking at small collision systems such as pp, multiplicity can be used as an indicator of event activity instead. The multiplicity of the event is defined by measuring the number of charged particles produced in the collision and dividing the data up into multiplicity percentile classes. A 0-10% multiplicity class would contain events with the highest multiplicity and a 80-100% class would contain the lowest multiplicity events. An example of this is given in section 3.2.5.

The space-time evolution of the QGP after a collision at $t = 0$ fm/c has occurred, is illustrated in the right-hand side of figure 1.7. In the pre-equilibrium phase ($t < 1$ fm/c), the quarks and gluons scatter and high-momentum particles and photons are produced in abundance. At this stage, particle production involves large Q^2 transfer so particle production can be calculated using perturbative QCD (pQCD). The inelastic collisions modify the flavour of the colliding particles. Due to the collisions, the system eventually thermalises. The rapid collective expansion of the system between $t = 1 - 10$ fm/c

can be modelled using relativistic hydrodynamics. Between $t = 10 - 15$ fm/c the QGP cools and the energy density decreases until the system is no longer deconfined and hadronisation starts. The point at which momentum exchanges become insufficient for inelastic interactions, chemical freeze-out occurs, after which the flavour composition of the system is fixed and the system evolves into a hadron gas. The matter continues to expand until kinetic freeze-out at $t > 15$ fm/c, at which point, the mean distance between the hadrons is greater than the range of the strong interaction and therefore elastic interactions also cease and the hadrons leave the interaction region.

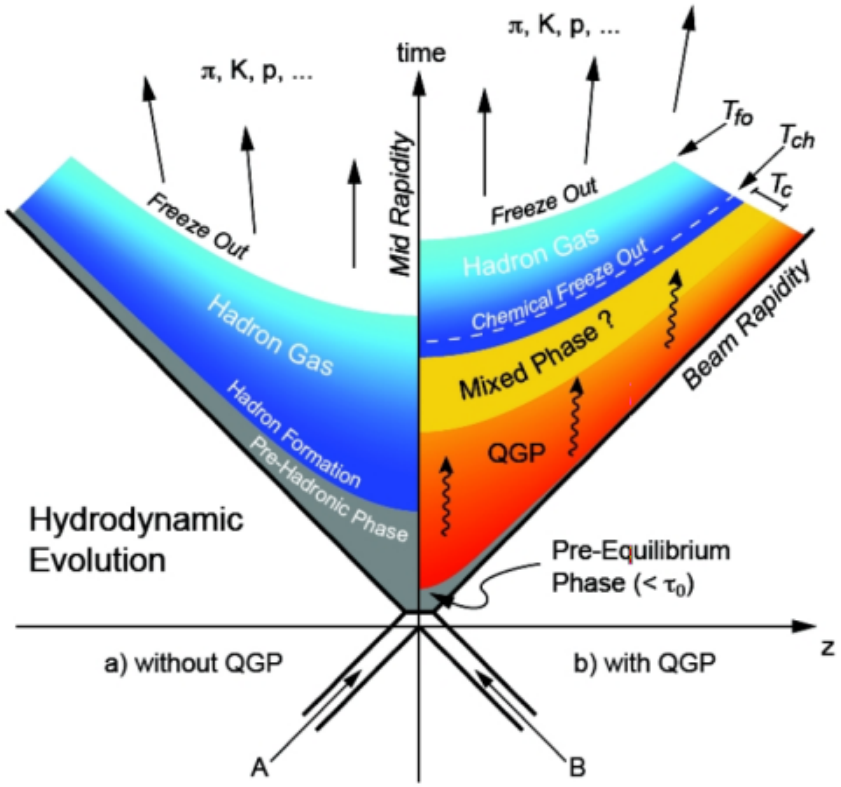

Figure 1.7: Space-time evolution of a heavy-ion collision for two scenarios. The left shows the evolution without any QGP production and the right shows the result including initial QGP production, with the kinetic freeze-out temperature T_{fo} and the chemical freeze-out temperature, T_{ch} indicated [48].

Chapter 2

Heavy-Ion Collisions

The following chapter will outline the experiments that have been carried out to search for the QGP and the analysis methods that have been used to confirm its existence and study its properties in more detail.

2.1 | Heavy-Ion Collider Experiments

After its theoretical prediction, two particle accelerators began the search for a deconfined state of matter simultaneously in 1986 through fixed target experiments at the Alternating Gradient Synchrotron (AGS) [49] at Brookhaven National Lab (BNL) [50] and the Super Proton Synchrotron (SPS) [51] at CERN. The experiments initially began colliding light nuclei such as oxygen-16, silicon-28 and sulphur-32, but in the early 1990's began collisions with heavy nuclei such as gold-197 and lead-208. The AGS achieved centre-of-mass energies per colliding nucleon pair of $\sqrt{s_{NN}} = 4.6$ GeV [52], however, the SPS reached $\sqrt{s_{NN}} = 17.2$ GeV in Pb–Pb collisions and $\sqrt{s_{NN}} = 19$ GeV in S–S collisions [53]. The results from the SPS programme provided enough evidence for CERN to announce the creation of a new state of matter in 2000 [54, 55]. The evidence for QGP formation was based on results from seven complimentary experiments at the SPS:

NA44 [56, 57], NA45 [58, 59], NA49 [60, 61], NA50 [62, 63], NA52 [64, 65], WA97/NA57 [66, 67] and WA98 [68, 69].

At the same time, a new high-energy collider at BNL called the Relativistic Heavy-Ion Collider (RHIC) went into operation. Here, gold ions were collided at top energies of $\sqrt{s_{NN}} = 200$ GeV. At this energy, larger, hotter fireballs (the hot and dense matter formed in the collision) with a longer lifetime were created, allowing the creation of a QGP to be confirmed in a series of white papers published in 2005, summarising the results from the four different experiments, STAR, PHENIX, PHOBOS and BRAHMS [70–73], which were all in good agreement with each other. The temperatures and densities created in the collisions at RHIC far exceeded the predicted critical values for QGP formation of $T_c = 154 \pm 8$ MeV and $\epsilon_c \approx 0.5$ - 1 GeV/fm^3 [46]. The onset of the LHC, capable of colliding Pb–Pb ions at energies of $\sqrt{s_{NN}} = 2.76$ TeV in Run 1 and $\sqrt{s_{NN}} = 5.02$ TeV in Run 2 [1], has created even more extreme conditions of temperature and energy density and has allowed a more detailed characterisation of the QGP and its properties. For example, an effective temperature of $T_{eff} = 297 \pm 12^{stat} \pm 41^{syst}$ MeV [74] has been measured in central Pb–Pb collisions at $\sqrt{s_{NN}} = 2.76$ TeV at ALICE using direct photons (see section 2.2.3 for details). This is 34% higher than the $T_{eff} = 221 \pm 19^{stat} \pm 19^{syst}$ MeV [75] measured in central Au–Au collisions at $\sqrt{s_{NN}} = 200$ GeV at RHIC.

2.1.1 | Charged-Particle Multiplicity

The charged-particle multiplicity of a collision relates to the number of particles produced in the final state. This is expected to be of the order of thousands for Pb–Pb collisions and ~ 10 on average for p–p collisions, with p–Pb providing intermediate values. The energy density, ϵ, of matter created in a collision can be related to the charged-

[1] LHC data-taking periods are divided into runs as described in more detail in section 3.1

particle multiplicity by the Bjorken formula,

$$\epsilon = \frac{1}{A\tau}\frac{\mathrm{d}E_T}{\mathrm{d}y} \approx \frac{1}{A\tau}\frac{\mathrm{d}N}{\mathrm{d}y}\langle p_T \rangle, \tag{2.1}$$

where $\frac{\mathrm{d}E_T}{\mathrm{d}y}$ is the transverse energy per unit rapidity [2] produced, τ is the time taken for the QGP to form and A is the overlapping area of the colliding nuclei [76]. The transverse energy can be approximated by the transverse momentum, p_T, and charged-particle multiplicity, N, of the event. This led Bjorken to originally suggest that even proton–proton collisions could create energy densities high enough for QGP formation, if multiplicities are high enough [77]. However, experiments have not yet shown conclusive evidence of this.

2.2 | Experimental Observables

The QGP cannot be observed directly, so in order to study it, observables have to be identified that can be measured from the particles produced in the collision. They can provide information about the QGP and its properties. Five such observables are summarised here.

2.2.1 | Jet Quenching

One of the key signatures of QGP formation involves studying the production of jets, where jets are defined as cones of hadrons formed by the hadronisation of a parton produced in a hard scattering process. Within a QGP, the scattered partons lose energy due to interactions with the hot and dense medium through collisional or radiative energy loss. This means the hadrons produced in the jet have a lower momentum than expected, leading to the QGP signature known as jet quenching. This is illustrated in figure 2.1, which demonstrates the interaction of the parton with the medium before hadron-

[2] Transverse energy is the energy component transverse to the beam and the rapidity is a variable related to the angle of the particles produced relative to the beam axis. See section 3.2.1 on the ALICE coordinate system for more details.

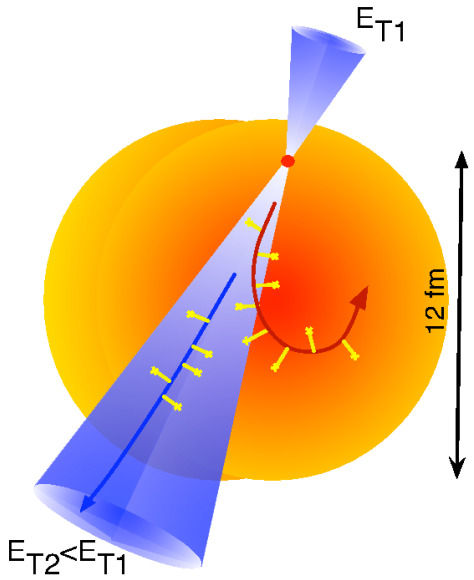

Figure 2.1: Diagram showing a back-to back jet produced near the edge of a QGP fireball. One jet leaves the medium with energy E_{T1}. The other travels a significantly larger distance through the medium and interacts through multiple random scatterings and gluon radiation before hadronisation, therefore it is detected with energy $E_{T2} < E_{T1}$. [78].

isation occurs.

The level of suppression can be measured using a quantity called the nuclear modification factor,

$$R_{AA} = \frac{dN_{AA}/dp_T}{\langle N_{coll}\rangle dN_{pp}/dp_T}, \tag{2.2}$$

which gives the ratio of the charged particle yield, N, as a function of p_T in heavy-ion (AA) collisions compared to pp collisions, scaled by the average number of binary nucleon-nucleon collisions, N_{coll}. The value of N_{coll} is a theoretical parameter related to the centrality of the collision (the overlap of the colliding nuclei) that can be calculated using a Glauber model [79]. This simulates millions of Pb–Pb collisions with varying impact parameter, b, and calculates the number of individual nucleon-nucleon collisions that occur in each event, N_{coll}. The distribution of N_{coll} maps onto the measured track multiplicity in the data that is used to form centrality percentile classes. Therefore, the

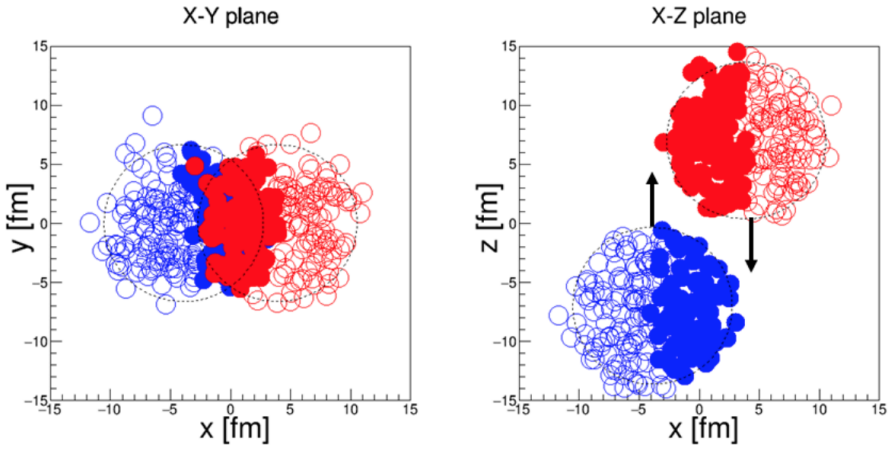

Figure 2.2: Diagram showing a Glauber modelled Pb–Pb event with impact parameter, $b = 7.8$, in the transverse (left) and longitudinal (right) plane. The shaded particles indicate those participating in a collision, whereas the unshaded indicate spectators of the collision [80].

same classes in the data can be used in the N_{coll} distribution to find the average $\langle N_{coll} \rangle$ for each class. An example of a Pb-Pb Glauber event is shown in figure 2.2 with an impact parameter of $b = 7.8$.

A value of $R_{AA} < 1$ indicates jet quenching. Figure 2.3 shows results from ALICE at the LHC at $\sqrt{s_{NN}}$ = 2.76 TeV that indicate there is a strong amount of jet quenching in central heavy-ion collisions compared to peripheral collisions, reaching a minimum of $R_{AA} \approx 0.2$ at $p_T \approx 7$ GeV/c [81], providing evidence for the presence of a QGP in these events.

Measurements of R_{AA} have also been made in p-Pb collisions at $\sqrt{s_{NN}}$ = 5.02 TeV [82]. The results are shown in blue in figure 2.4, alongside results for central (red) and peripheral (green) Pb–Pb collisions. The measurements at ALICE show a value of R_{AA} consistent with one within systematic uncertainties across all p_T, indicating that there is no suppression and therefore no presence of a QGP in these collisions. Results for R_{AA} in run 2 p–Pb data would confirm if this is still the case at higher collision energies. However, it is also worth noting that measurements of R_{AA} make the major assumption

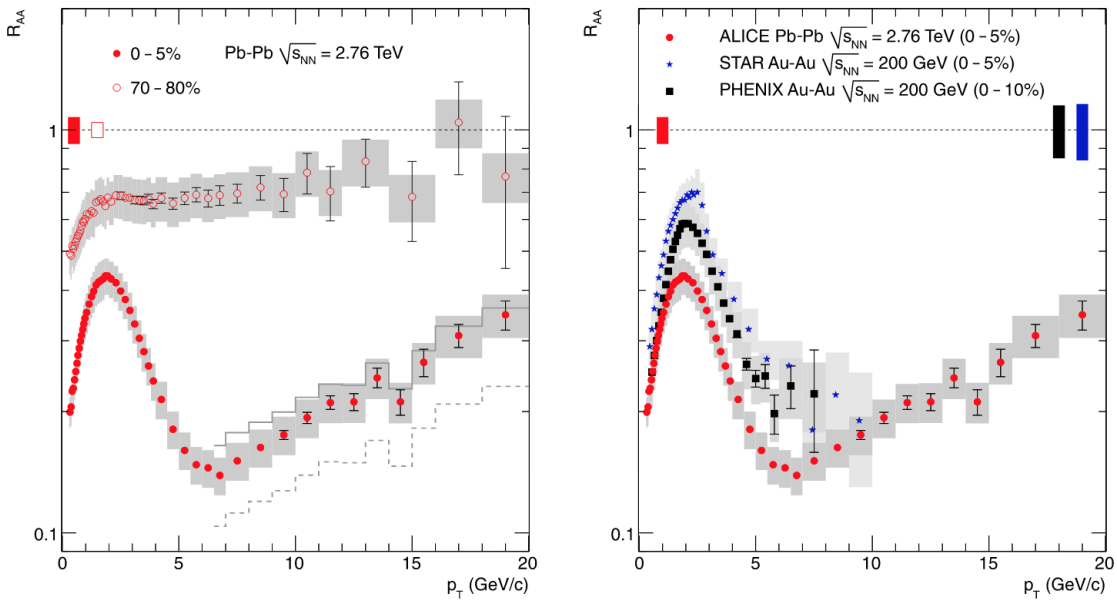

Figure 2.3: Plot showing the nuclear modification factor, R_{AA}, in central (0-5%) and peripheral (70-80%) heavy-ion collisions at ALICE (left). Central results are compared to measurements from STAR and PHENIX (right) [81].

that no QGP is produced in the reference pp collision system, which may not be valid at high collision energies where high multiplicities are produced, and therefore could bias the results.

High p_T suppression, indicating jet quenching, can also be measured using two-particle angular correlations. This involves identifying trigger (*trig*) particles within an event that have a p_T above a chosen threshold, that are assumed to originate from a jet. Associate (*assoc*) particles are then identified which have a p_T lower than the trigger particle but above a lower threshold p_T. The angular difference in the transverse plane, $\Delta\varphi$, between the trigger and associated particles can then be plotted, where φ is indicated in figure 3.4. The results give two peaks at $\Delta\varphi = 0$ and $\Delta\varphi = \pi$ as the jets are produced back-to-back. Results for ALICE are shown in figure 2.5. A suppression in the away-side jets can be seen at $\Delta\varphi = \pi$ when central (0-5%) Pb–Pb results are compared to peripheral (60-90%) Pb–Pb results and proton-proton results, indicating the jets produced in the central Pb–Pb collisions have been suppressed traversing the QGP.

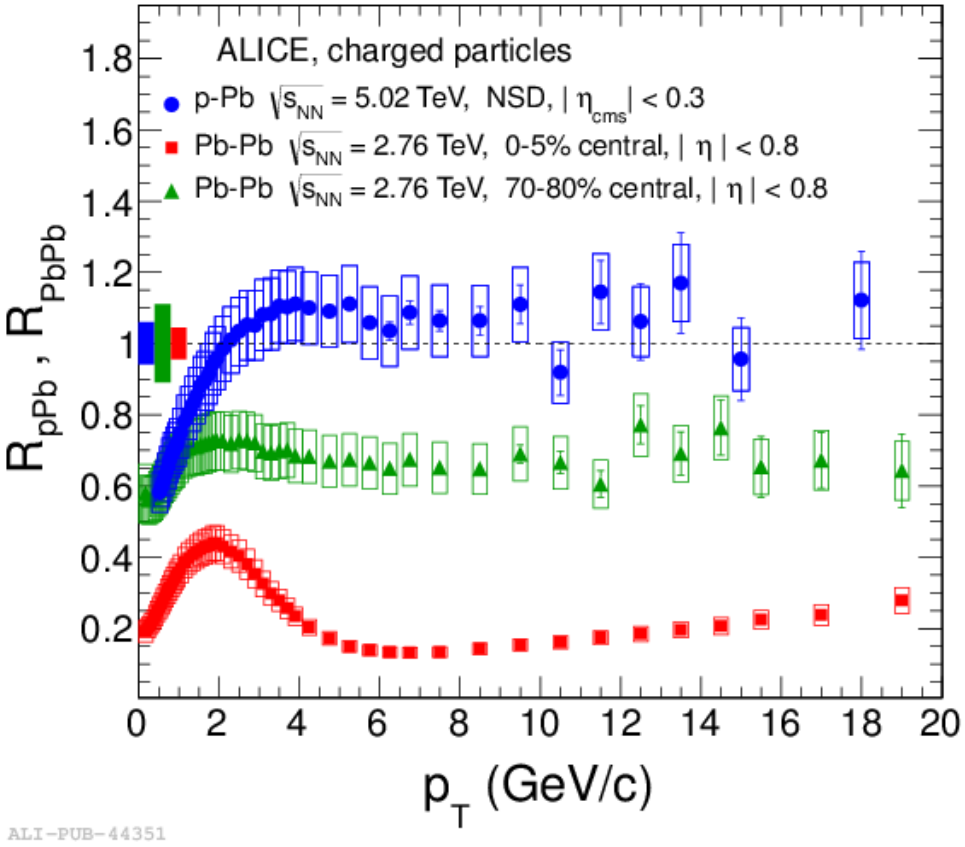

Figure 2.4: R_{AA} measured in p–Pb collisions at $\sqrt{s_{NN}} = 5.02$ TeV (blue) shown alongside measurements in central (red) and peripheral (green) Pb–Pb collisions at $\sqrt{s_{NN}} = 2.76$ TeV [82].

Measurements of two-particle correlations have also been made by CMS and ATLAS. Results from high-multiplicity collisions in small systems, including pp collisions at $\sqrt{s} = 7$ TeV [83] and $\sqrt{s} = 13$ TeV [84] and p–Pb collisions at $\sqrt{s_{NN}} = 5.02$ TeV [85, 86], have shown long-range correlations in the near-side particles (φ=0) across η (angular variable related to the polar angle, θ, defined fully in section 3.2.1), which are not predicted by MC simulations. Figure 2.6 shows results for 2D particle correlations in low-multiplicity (a) and high-multiplicity (b) pp collisions, where correlations across η at φ=0 are visible only in (b). This effect is interpreted in Pb–Pb collisions as a result of the hydrodynamic expansion of the QGP medium formed in the collision. The observation of this effect in small systems provides some evidence for QGP formation in high-multiplicity pp/p–Pb collisions, however, more results from other observables are needed to confirm this conclusion.

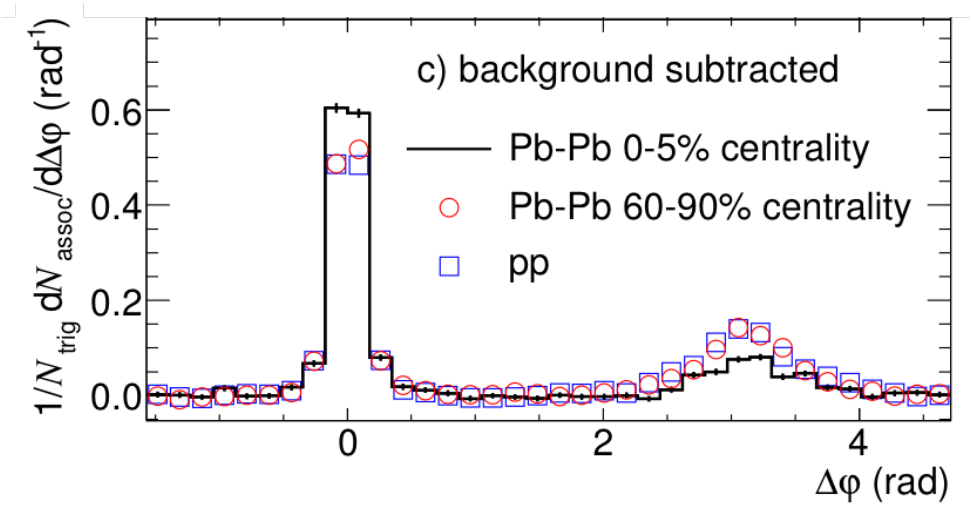

Figure 2.5: Two-particle angular correlation yields for $4 < p_T, assoc < 6$ GeV/c and $8 < p_T, trig < 15$ GeV/c in central (0-5%) Pb-Pb events (histogram), peripheral (60-90%) Pb-Pb events (red circles) and pp events (blue squares). The fully corrected results with the background subtracted are shown. Adapted from [87].

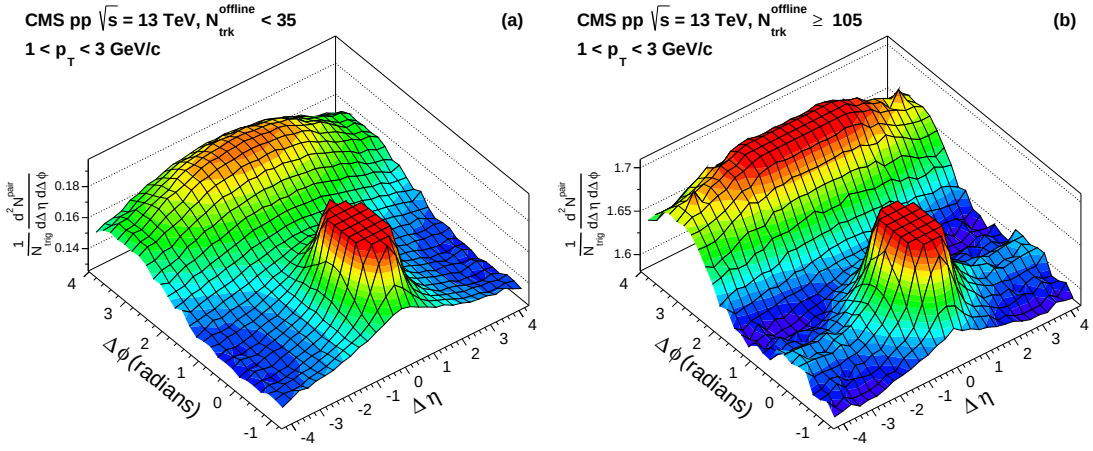

Figure 2.6: The 2D two-particle correlation functions in pp collisions at $\sqrt{s} = 13$ TeV for pairs of charged particles in the range $1 < p_T < 3$ GeV/c. Results are shown for (a) low-multiplicity and (b) high-multiplicity events. The sharp peaks from jet correlations around $(\Delta\varphi, \Delta\eta) = (0, 0)$ are truncated in order to illustrate the long-range correlations better [84]. φ is shown as ϕ on this figure.

2.2.2 | Charmonium Suppression

Charmonia, such as J/ψ, are defined to be bound states of the charm quark and its anti-quark. J/ψ suppression was predicted in 1986 [88] to be a signature of the formation of a deconfined quark-gluon plasma. The mass of the charm quark, 1.3 GeV, makes thermal production unlikely at the temperatures reached in the high-energy collisions carried out at particle colliders, therefore the charm quarks present in the final state have been produced by initial hard scattering of partons and experience the whole evolution of the system.

As discussed in section 1.2.4, the onset of a QGP causes Debye screening of the quarks. When the screening radius, r_D, is less than the radius of the hadron, r_H, the strong force can no longer hold the quarks together and the hadron becomes deconfined. The radius of a charmonium meson is more than the Debye radius in a QGP. Therefore, in the

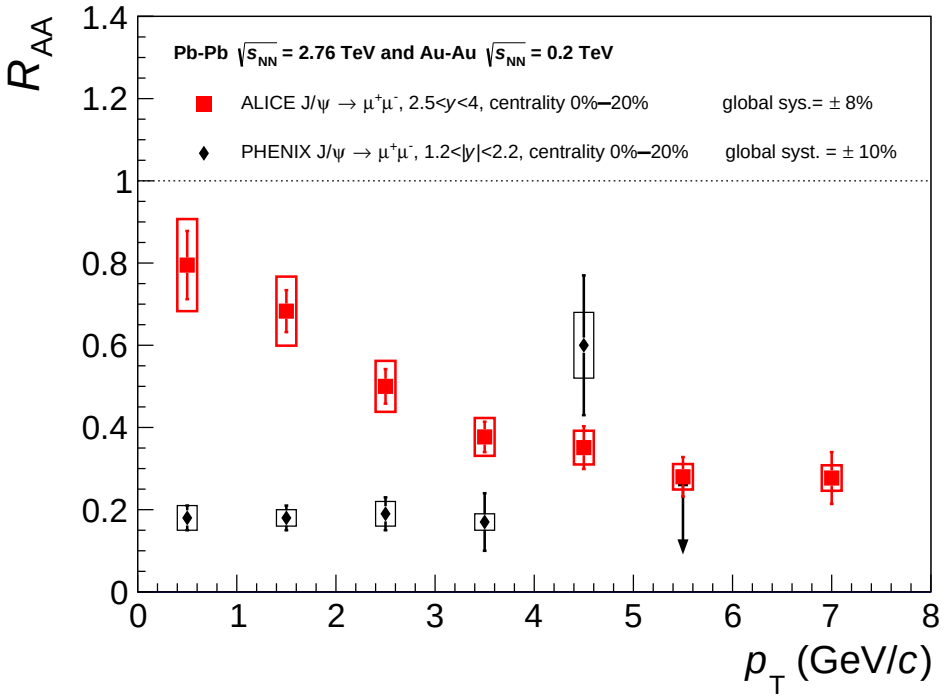

Figure 2.7: Plot showing the transverse momentum dependence of the J/ψ R_{AA} as measured by ALICE [89] in the 0%–20% most central Pb-Pb collisions at $\sqrt{s_{NN}}$ = 2.76 TeV compared to PHENIX [90] results in the 0%–20% most central Au-Au collisions at $\sqrt{s_{NN}}$ = 0.2 TeV.

QGP, the binding of $c\bar{c}$ quarks into a J/ψ meson is restricted, leading to a suppression in the measured production of J/ψ in Pb–Pb collisions compared to pp collisions. This is measured using R_{AA}, as was done for jets, where the yields of J/ψ are used rather than charged particle yields in equation 2.2. Any charmonia produced in the initial collision, 'melt' in the QGP and the c quarks then hadronise at the phase boundary with other quarks.

Extensive studies of J/ψ production at SPS and RHIC [91–95] showed suppression across a wide energy range in central heavy-ion collisions. At the higher energies achieved at the LHC the thermal production of charmonia at low momenta becomes significant. After deconfinement, low momentum $c\bar{c}$ pairs close in phase space can recombine to form charmonia in the final state, producing low momenta J/ψ. This regeneration counteracts the suppression of J/ψ and leads to a less suppressed signal for J/ψ at the LHC compared to RHIC, as shown in figure 2.7. The red points in figure 2.7 indicate the suppression of J/ψ is smallest at low p_T due to recombination contributing to the measured yield at these momenta.

2.2.3 | Direct Photons

The inclusive production of photons in a hadron collision is a combination of decay photons, produced by decaying hadrons, and direct photons. Direct photon production can therefore be measured by subtracting decay photon yields from inclusive photon yields. The direct photons are produced at all stages of the collision and escape unaffected and so carry important information about the conditions of the medium at production.

At high p_T, where the production is dominated by hard scattering of initial partons, the prompt direct photon yields can be predicted using pQCD calculations so their measurement can be a useful test of the theory. At low p_T, the thermalisation of the QGP and

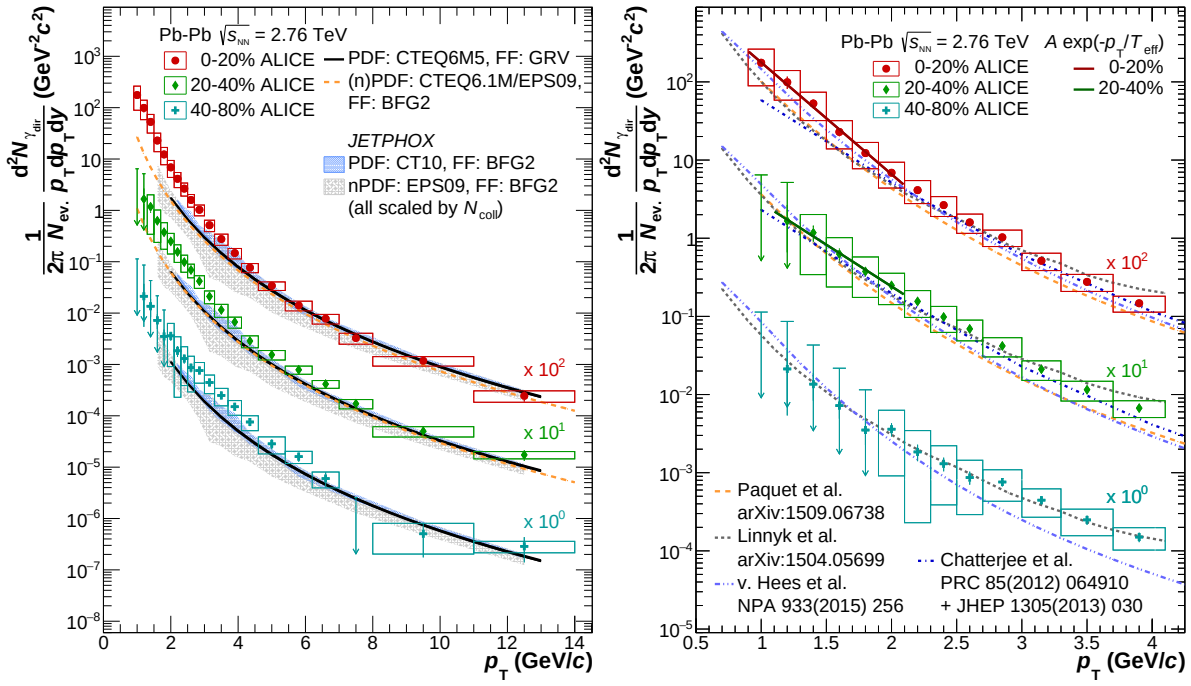

(a) (b)

Figure 2.8: Plots showing direct photon spectra in Pb–Pb collisions at $\sqrt{s_{NN}} = 2.76$ TeV measured at ALICE for the centrality classes 0-20% (scaled by 100), 20-40% (scaled by 10) and 40-80%. In (a), they are compared to NLO pQCD predictions in pp collisions at the same energy scaled by number of binary nucleon-nucleon collisions and in (b), they are compared to model calculations of direct photon spectra [74].

hadronic matter produces thermal direct photons with a spectrum strongly dependent on the properties of the QGP, so can give information on the collective flow and temperature of the medium.

The inverse slope parameter of the low p_T region can be extracted from an exponential fit $\propto exp(-p_T/T_{eff})$ of the direct photon spectrum after the prompt pQCD contribution, shown by the dashed orange line in figure 2.8a, is removed. This can be used to calculate the average temperature of the medium. A temperature of $T_{eff} = 297 \pm 12^{stat} \pm 41^{syst}$ MeV [74] has been obtained for central Pb–Pb collisions at $\sqrt{s_{NN}}$ = 2.76 TeV. A comparison of direct photon calculations using models that contain QGP formation agree with measured spectra within uncertainties as shown by figure 2.8b.

2.2.4 | Collective flow

Anisotropic collective flow refers to anisotropies seen in the final momentum distributions of particles produced in nuclear collisions that indicate the existence of collective behaviour in the matter produced in the collisions. In-plane elliptic flow was first suggested as a signature of collective behaviour in a QGP in the 1990's [96]. This signal was experimentally observed as azimuthal correlations between particle momenta and the plane of the reaction, first at AGS [97] and later at SPS [98].

It was initially predicted that a QGP would have similar properties to a weakly interacting gas, meaning the mean free path of the partons would be large, giving the medium a large viscosity which would prevent any strong collective expansion. A very strong elliptic flow measurement at RHIC [99] contributed to the understanding that a QGP is actually much more similar to a strongly interacting liquid. The measurement of flow is important in studying the early evolution of the QGP as the final anisotropies in the momentum distributions originate from the initial geometry of the overlap region of the colliding nuclei, which create pressure gradients in the hot and dense matter formed.

The anisotropies can be quantified using Fourier coefficients of the particle spectra,

$$v_n = \langle \cos[\, n(\varphi - \Psi_r)] \,\rangle, \tag{2.3}$$

where n is the flow harmonic order, φ is the azimuthal angle of the particles and Ψ_r is the azimuthal angle of the reaction plane, estimated by the event plane which can be calculated by measuring the azimuthal distribution of particles produced in the event [100–102]. The first harmonic is known as directed flow, the second harmonic as elliptic flow and the third harmonic as triangular flow.

Measurements of flow allow constraints to be put on the equation of state, as well as measurements of the kinematic viscosity, η/s (ie. shear viscosity over entropy density

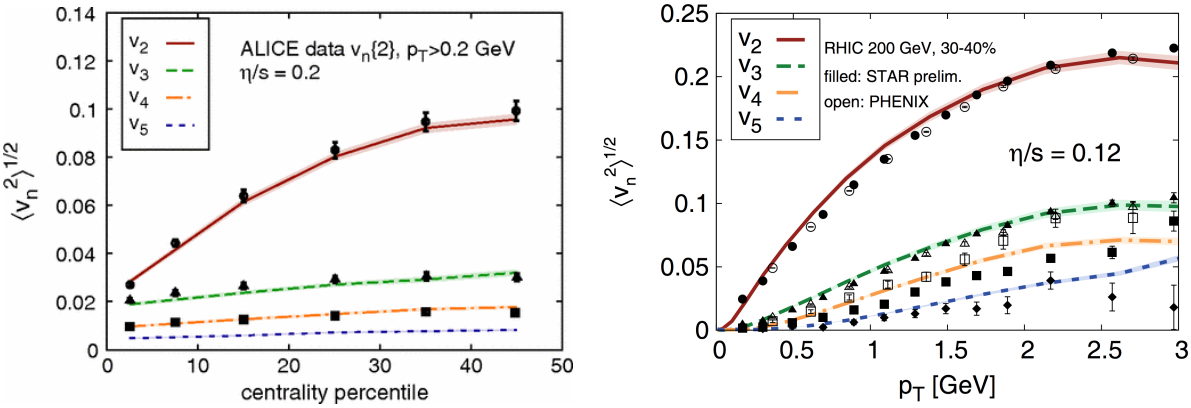

Figure 2.9: Plot showing the root-mean-square anisotropic flow coefficients computed as a function of centrality, compared to experimental data of $\left\langle v_n^2 \right\rangle^{1/2}$, $n \in 2,3,4$ from the ALICE collaboration (left) and data of $\left\langle v_n^2 \right\rangle^{1/2}$, $n \in 2,3,4,5$ from the STAR (filled points) and PHENIX (open points) collaborations (right). The bands indicate statistical errors. Adapted from [104].

ratio) to be made. The predicted quantum lower limit of η/s for all fluids is $1/4\pi$ (in natural units) [103], so a fluid with this viscosity is called a perfect fluid.

Experimental data from RHIC were found to be consistent with η/s=0.12 [104], whereas later measurements from ALICE are consistent with a value of η/s=0.2 [104] as shown in figure 2.9. These low values of η/s indicate the QGP is a near-perfect fluid and the change from RHIC to ALICE results allows constraints on the temperature dependence of η/s to be made. The flow increases moving from central to peripheral collisions at the LHC in the left of figure 2.9 due to the spatial anisotropy becoming larger as the overlap region becomes less circular and more almond-shaped.

The high energies at the LHC allow the elliptic flow to be studied in detail by measuring the variable with different identified particles to study the mass ordering effect, as well as the higher flow harmonics which can reveal more detailed information about the initial anisotropy in the matter formed.

2.2.5 | Strangeness Enhancement

The enhanced production of strange particles was one of the first proposed signatures of QGP formation in 1982 [105]. In a deconfined quark-gluon plasma, $s\bar{s}$ quark pairs can be produced abundantly through the annihilation of light quark-antiquark pairs, $q\bar{q} \rightarrow s\bar{s}$, or predominantly, the collision of two gluons, $gg \rightarrow s\bar{s}$. In fact, for a plasma large enough, the lifetime is long enough for the strange quarks to reach saturation, where the rate of $s\bar{s}$ annihilation balances the rate of formation. The hadronic, rather than partonic, degrees of freedom in a hadron gas mean far less strangeness is produced, as the energy threshold for strange hadron production is much higher than strange quark production. A measurement demonstrating enhanced strangeness production was therefore suggested as a test for QGP formation. This increased production can be measured by looking at the yields of strange hadrons compared to pion yields in heavy-ion collisions and comparing to the results in smaller systems such as proton-proton and proton-ion collisions, where QGP formation is not expected.

Evidence for the enhancement of strange hadrons was first seen in experiments at AGS, BNL, where an enhancement in strange Kaon production was seen [106], and SPS, CERN [107, 108], which also measured enhancements with Λ [109], Ξ [110] and Ω [111]. This enhancement was predicted to follow a hierarchy dependent on the strangeness content of the particle with the most enhancement expected for Ω which was confirmed experimentally [107]. The same pattern of enhancement, $\Lambda < \Xi < \Omega$, was seen at different collision energies [112–114] and with different colliding heavy ions [115]. After the LHC came online, the enhancement was measured there as well [116]. Results for the hyperon-to-pion ratios are shown in figure 2.10 as a function of $\langle N_{part} \rangle$, the average number of participating nucleons in the collision, which is a measure of the centrality of the collision. The results for Pb–Pb at all centralities are enhanced compared to pp results by $\sim$1.6 and 3.3 for Ξ and Ω respectively. The STAR results are also shown on the plot for comparison. The level of enhancement is reduced at the LHC compared to

STAR results from RHIC as the reference pp measurement is taken at a higher energy, so the relative production of strangeness is increased.

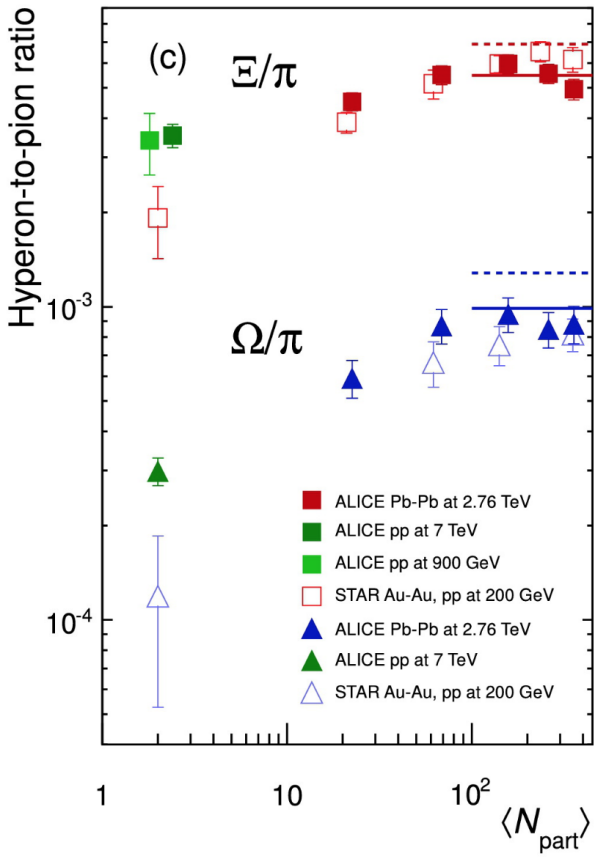

Figure 2.10: Plot showing the hyperon-to-pion ratio in Pb–Pb and pp collisions measured as a function of <N_{part}> by ALICE [116].

In order to look at the results in small systems such as pp in more detail, the strange yields were measured as a function of <$dN_{ch}/d\eta$>, instead of <N_{part}>, which is the average charged particle density in the collision and is an estimate of the multiplicity of the collision. This variable can be measured across collision systems so allows a more detailed look at pp and p–Pb collisions in order to compare to results in heavy-ion collisions. Initial measurements from p–Pb collisions led to a surprising result that demonstrated the hyperon-to-pion yields increase smoothly as a function of <$dN_{ch}/d\eta$>, almost reaching saturation levels seen in Pb–Pb collisions and predicted by thermodynamic models of the QGP [117].

When pp data were also analysed in multiplicity bins, the same trend was seen with the yield ratios rising as a function of multiplicity, seemingly independent of the collision system as figure 2.11 shows. The effect seen is not well reproduced by Monte Carlo generators commonly used at the LHC that model microscopic particle production, PYTHIA8 [118], EPOS-LHC [119] and DIPSY [120].

PYTHIA8 simulates events using colour reconnection [120], which builds on the Lund model for string hadronisation [121], in which partons are connected by strings that can stretch and break to form hadrons through string fragmentation. These strings can connect to other strings nearby to form string junctions which increase the colour field. This leads to increased baryon formation and suppressed meson production, however the model predicts a flat hyperon-to-pion ratio with multiplicity which does not reproduce the data. EPOS is a core-corona model (described further in the next section), with a central region containing a high number of strings and a surrounding region of lower string density. Locally thermalised clusters form in the core which hadronise according to statistical physics. This model predicts an increase in the hyperon-to-pion ratio with multiplicity, however, the best description of the trend seen in the data is from DIPSY. In this model, the interactions between gluon strings fuse together to form gluon 'ropes' with a higher string tension, which have an increased energy release during fragmentation and are more likely to hadronise into strange quarks and diquarks. This generates an enhanced amount of strange hadrons in the final state with increasing multiplicity. However, this model still does not match data quantitatively, especially for multi-strange baryons.

In order to check the results seen are not due to the differences in the particle masses, the baryon-to-meson ratios can be evaluated for both strange and non-strange particles. The observed ratios for Λ/K^0_s and p/π shown in figure 2.12 are approximately flat with

no multiplicity dependence, indicating that the enhancement is not related to the differences in hadron mass.

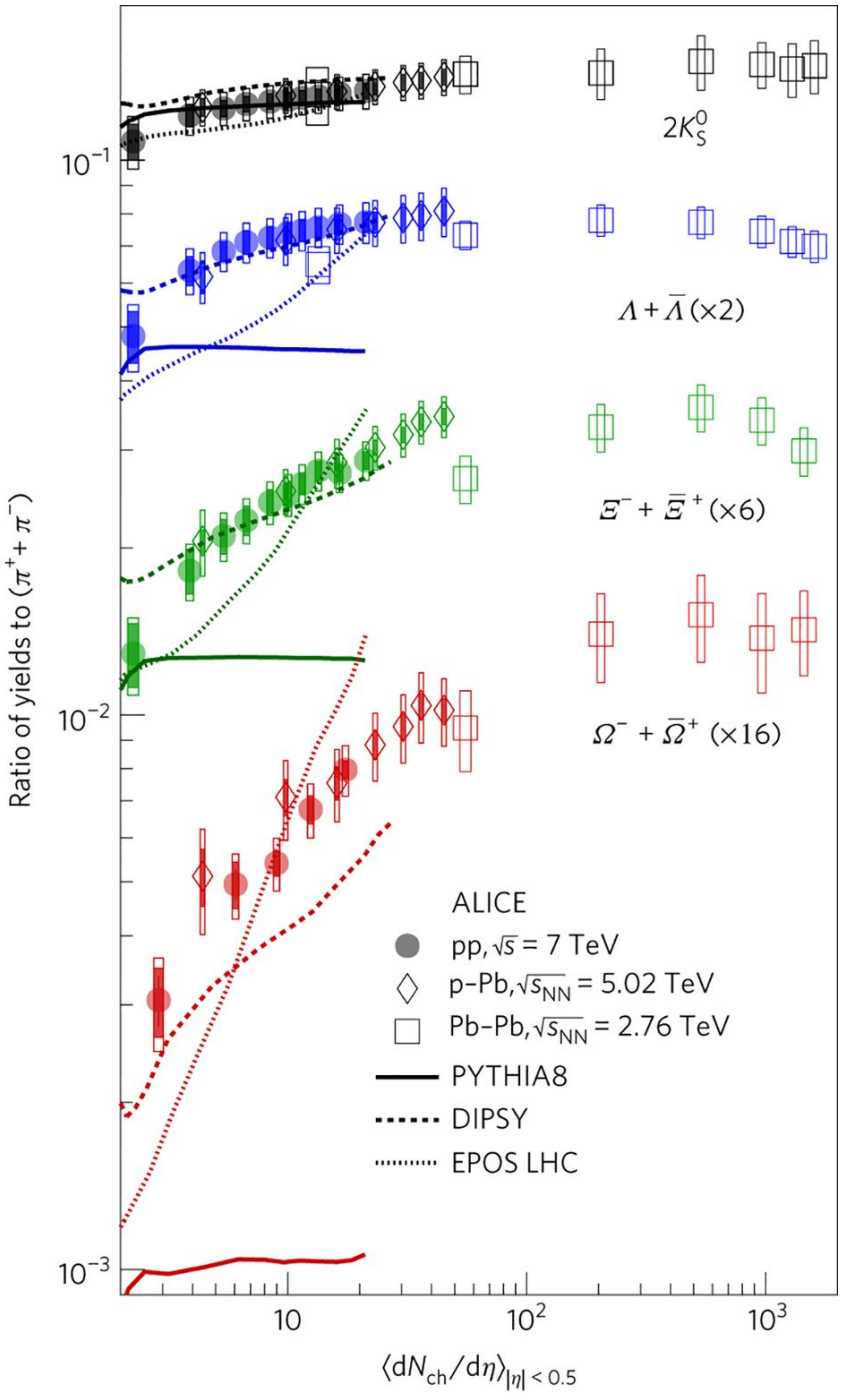

Figure 2.11: Plot showing the strange-hadron-to-pion ratio in Pb–Pb, p–Pb and pp collisions measured as a function of $<dN_{ch}/d\eta>$ by ALICE [122]. The pp data are compared to values from MC model calculations using PYTHIA8 [118], EPOS-LHC [119] and DIPSY [120].

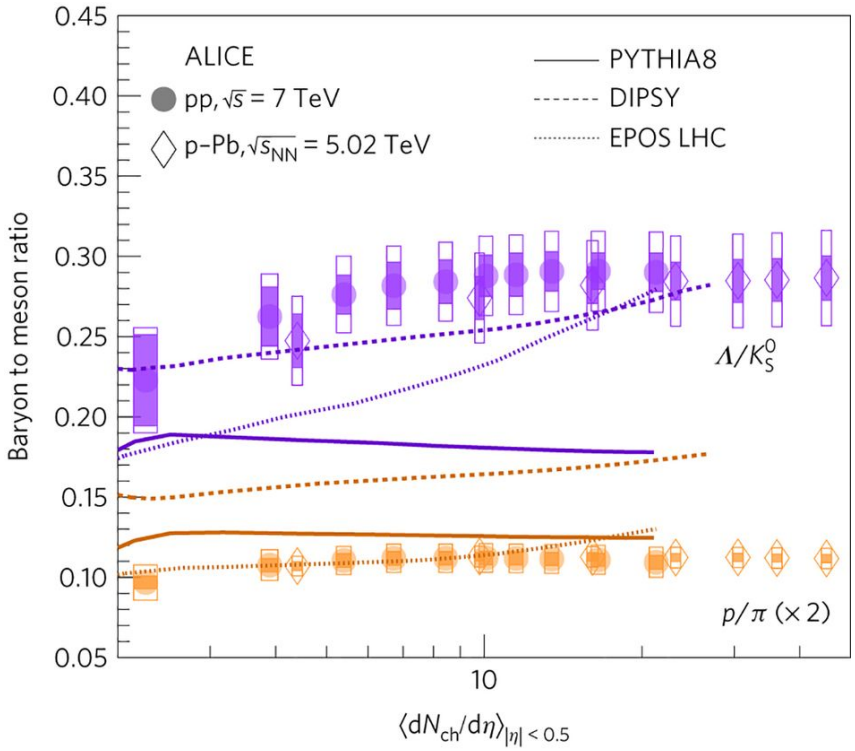

Figure 2.12: Plot showing the baryon-to-meson ratio in p–Pb and pp collisions measured as a function of $<dN_{ch}/d\eta>$ by ALICE [122]. The pp data are compared to values from MC model calculations using PYTHIA8 [118], EPOS-LHC [119] and DIPSY [120].

2.2.5.1 | Theoretical Models of Strangeness Enhancement

A statistical hadronisation model (SHM) [123] can be used to model the rates of particle production in a high-energy collision. This assumes there is a thermally equilibrated source producing the hadrons at the point of hadronisation, which is presumed to be the QGP. This means the partonic conditions before the hadronisation stage are not considered. The relative yields of particles can be predicted using a statistical model that takes into account the temperature at chemical freeze-out, the volume of the system and the chemical potential of the system. SHM were first introduced by Fermi [124] and developed further by Hagedorn [125], where the thermally equilibrated source was called a fireball. The fireball produced in the collision radiates particles, following the laws of statistical physics. Models of this type have successfully reproduced particle yields in heavy-ion collisions as shown in figure 2.13. However, results from elementary collisions, such as proton–proton collisions, have also been well reproduced as shown in

figure 2.14. This is unexpected as a locally equilibrated QGP is not expected to form.

A Grand Canonical approach can be used to describe the system produced in a heavy-ion collision, in which quantum numbers for strangeness (S), baryons (B) and electric charge (Q) are conserved on average across the whole system. Small fluctuations are considered negligible compared to the large number of particles in the system. If the volume of the system is small, such as in the smaller systems produced in proton–proton and proton–lead collisions, a canonical approach has to be used in which exact quantum numbers are conserved. This conservation reduces the phase space available for particle production. Therefore, although the observable of increased strange particle yields in A–A collisions was initially labelled strangeness enhancement, with a SHM the results can be interpreted as an absence of canonical suppression, leading to the higher strange particle yields in Pb–Pb collisions compared to p–p and p–A collisions.

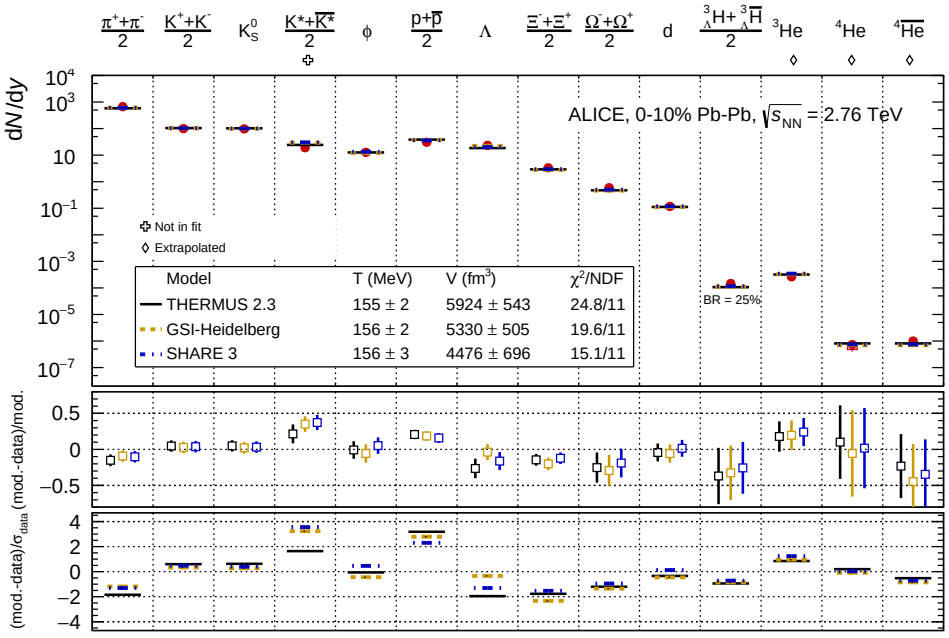

Figure 2.13: Thermal model fits [126–128] to light flavour hadron yields in central (0-10%) Pb-Pb collisions at $\sqrt{s_{NN}}$ = 2.76 TeV at ALICE. The top panel shows the fit results and the data with the lower panels showing the difference between the models and data normalised to the model value (middle panel) and to the experimental uncertainties (bottom panel) [129].

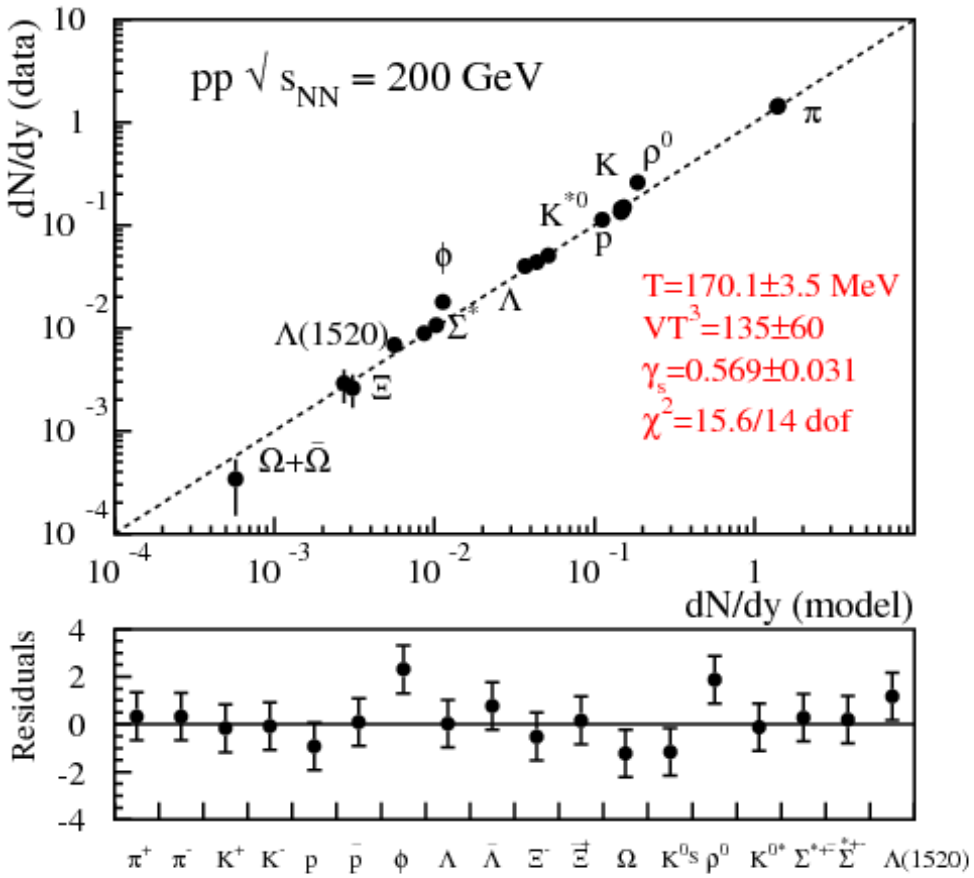

Figure 2.14: Thermal model fit of light flavour hadron yields in pp collisions at $\sqrt{s} = 200$ GeV at RHIC. The top panel shows the the measured midrapidity densities vs the model values and the bottom panel shows the residuals [130].

Results from ALICE for ratios of particle yields to pions for several particle species are shown in figure 2.15 compared with the THERMUS model [127] predictions modelling strangeness canonical suppression, which are shown by the continuous curves. There is reasonable agreement between data and model for most particles, however the largest deviations can be seen for ϕ. As ϕ consists of $s\bar{s}$, it is technically a strangeness-neutral particle, so the canonical suppression model predicts no suppression of this particle, which should lead to a flat dependence on multiplicity. However, a rising and falling trend is seen in the data, indicating the model is not capturing the particle production mechanisms in this case.

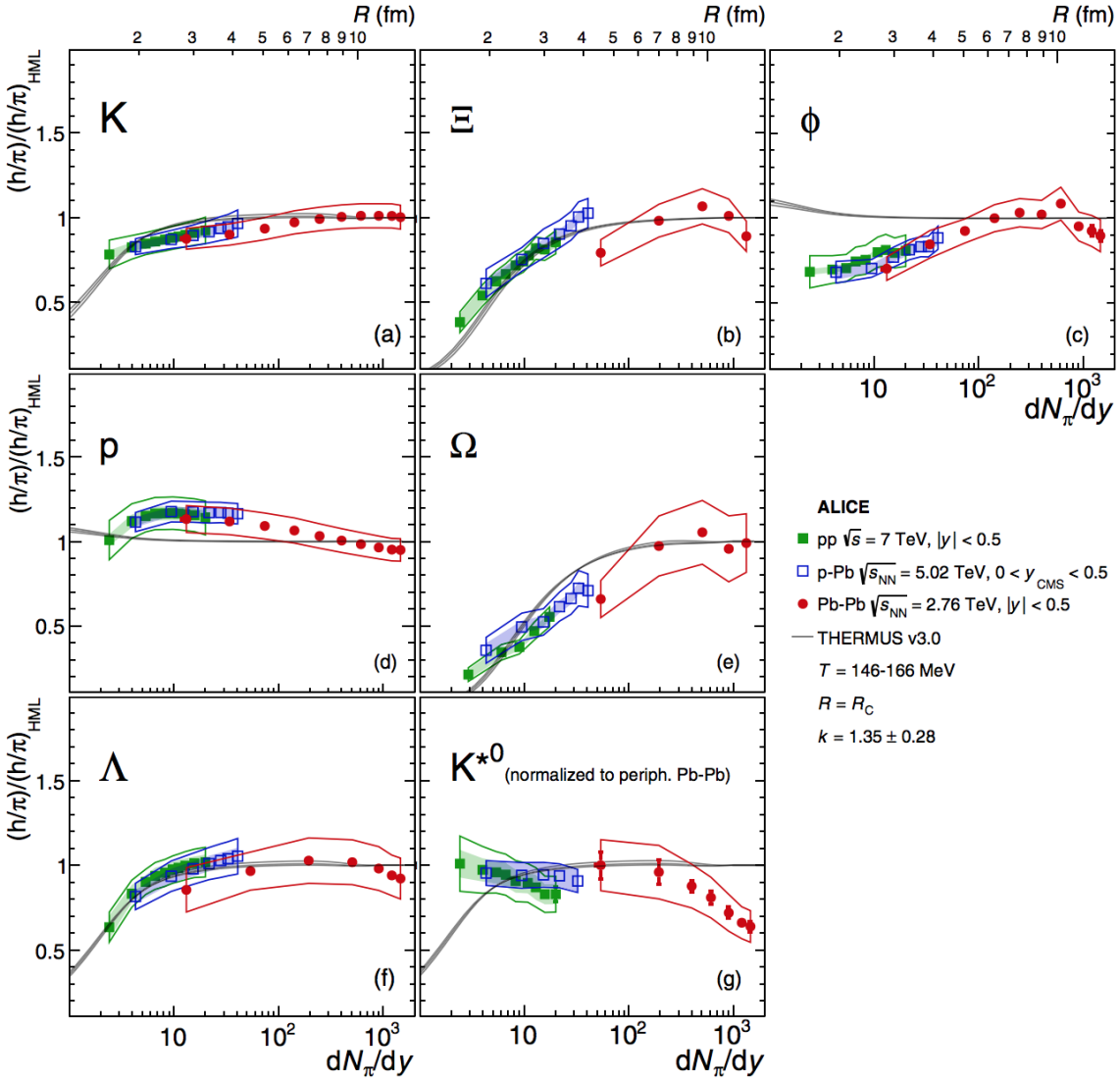

Figure 2.15: Ratio of particle to pion yields for different particle species as a function of midrapidity pion yields in p–p, p–Pb and Pb–Pb collisions compared to THERMUS model predictions shown by the continuous curves [131]. The variations in the THERMUS curves are due to variations in the chemical freeze-out temperature used in the model at 146, 156 and 166 MeV.

Another possible way of interpreting the increasing strange-to-pion yield ratios in pp collisions is by using the core-corona method. This models the matter produced in a collision as two separate components consisting of a central region, "the core", with high energy density that has reached thermal equilibrium and an outer region, "the corona", surrounding it with a much smaller energy density, where individual N-N interactions take place. The yield from the core and corona are calculated separately and summed

together to get the total yield of particles. The core can be modelled by a grand canonical ensemble, whereas the corona is represented by a canonical system. This means the total strange yields are affected by the enhancement in the core and the canonical suppression in the corona. As figure 2.16 shows, recent results using this model have demonstrated hyperon-to-pion data from ALICE can be reasonably reproduced with no system size or initial collision energy dependence observed and a ratio that purely scales with multiplicity. The deviations seen in $(p + \bar{p})$ yields are explained due to proton and anti-proton annihilation in the rescattering stage not being included in the model. These

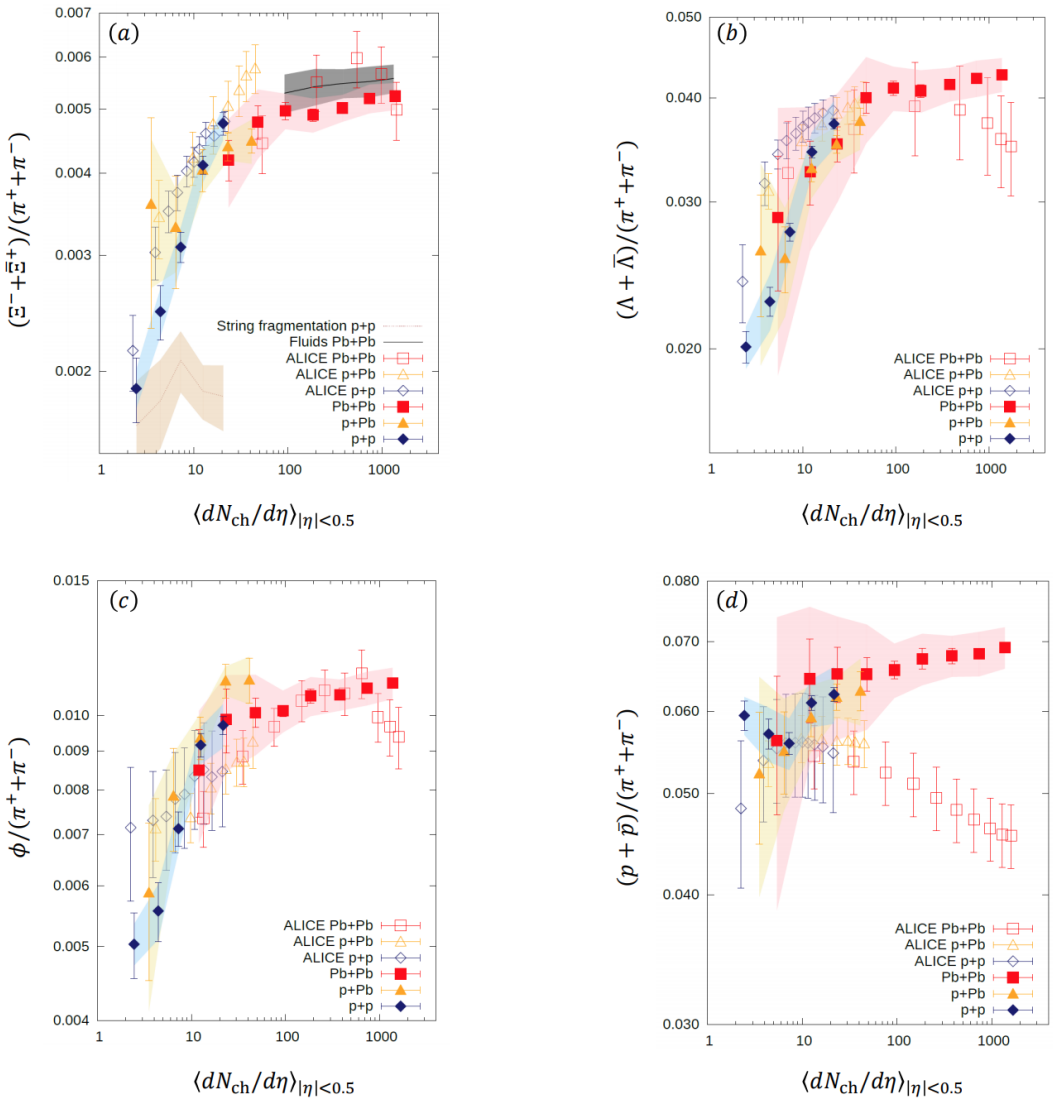

Figure 2.16: Particle yield ratios to pion yields as a function of multiplicity in p–p, p–Pb and Pb–Pb collisions for a) $\Xi^{\pm}$ b) $\Lambda + \bar{\Lambda}$ c) ϕ and d) $p + \bar{p}$. Closed points show core-corona model results and open points show ALICE data [132].

results suggest there is partial formation of a QGP in high multiplicity small collision systems.

2.2.5.2 | Transverse momentum distribution models

Statistical models can be used to describe the transverse momentum distributions of hadrons produced in the collisions. In particular, a Lévy-Tsallis fit [133] is used to fit the data in the analysis described in this thesis, so that p_T integrated yields and $\langle p_T \rangle$ can be calculated. This model describes the distribution of transverse momentum for hadrons that come from a thermally equilibrated source. Both the soft, thermal physics and the hard processes at large momenta are described by the model with exponential behaviour at low momenta and a power law at higher momenta. The p_T distribution follows the equation:

$$\frac{\mathrm{d}^2N}{\mathrm{d}p_T\mathrm{d}y} = \frac{\mathrm{d}N}{\mathrm{d}y}\, p_T\, \frac{(n-1)(n-2)}{nT_k[nT_k + m(n-2)]} \left(1 + \frac{m_T - m}{nT_k}\right)^{-n}, \tag{2.4}$$

where T_k is the kinetic freeze-out temperature, m_T is the transverse mass defined by $m_T = \sqrt{p_T^2 + m^2}$ and n is an exponent.

Additional functions for the transverse momentum given here were used for comparison to the Lévy-Tsallis results in order to estimate the systematic uncertainties, as shown in appendix C. In the following functions C corresponds to a normalisation constant:

1. A standard Boltzmann distribution,

$$\frac{\mathrm{d}^2N}{\mathrm{d}p_T\mathrm{d}y} = C\, m_T\, p_T \exp\left(-\frac{m_T}{T}\right). \tag{2.5}$$

2. The Boltzmann-Gibbs Blast-Wave model [134], which assumes an emission source undergoing radial expansion in local thermal equilibrium. The shape of the particle p_T spectra are given by the function

$$\frac{1}{p_T}\frac{\mathrm{d}N}{\mathrm{d}p_T} \propto \int_0^R r\mathrm{d}r\, m_T\, I_0\left(\frac{p_T \sinh\rho}{T_{kin}}\right) K_1\left(\frac{m_T \cosh\rho}{T_{kin}}\right) \tag{2.6}$$

with

$$\rho = \tanh^{-1}(\beta_T), \tag{2.7}$$

where I_0 and K_1 are modified Bessel functions. The parameters of the model are the transverse flow velocity β_T and the kinetic freeze-out temperature T_{kin}.

3. A m_T exponential, where the p_T spectra are assumed to decrease exponentially with m_T:

$$\frac{\mathrm{d}^2N}{\mathrm{d}p_T\mathrm{d}y} = C\ p_T \exp\left(-\frac{m_T}{T}\right). \tag{2.8}$$

4. A Bose-Einstein distribution,

$$\frac{\mathrm{d}^2N}{\mathrm{d}p_T\mathrm{d}y} = C\ p_T \frac{1}{\exp(m_T/T) - 1}. \tag{2.9}$$

5. A Fermi-Dirac distribution,

$$\frac{\mathrm{d}^2N}{\mathrm{d}p_T\mathrm{d}y} = C\ p_T \frac{1}{\exp(m_T/T) + 1}. \tag{2.10}$$

2.3 | Summary

These first two chapters have attempted to outline the physics motivation behind the research presented in this thesis. The understanding of particle production processes and how they propagate through the medium are of great interest to the QCD theory community and more data is essential to the development of new models. As section 2.2.5 showed, the current results are not being accurately reproduced by theoretical models and so more work is needed in this area for a better understanding of strangeness production. The next chapter will describe the experimental setup used to collect new data on this phenomenon.

Chapter 3

The ALICE Experiment

The following chapter will describe the Large Hadron Collider and the ALICE experimental setup itself with particular focus on the sub-detectors which are used for the analysis outlined in this thesis. This summary is based on the detailed descriptions given in [42], [135] and [41], which can be referred to for further information.

3.1 | The LHC

The Large Hadron Collider (LHC) is a particle accelerator and collider based at the European Organisation for Nuclear Research (CERN) near Geneva, Switzerland [42]. It is 27 km in circumference and located approximately 100 m underneath the French-Swiss border. During development earlier accelerators were incorporated into the design, with the tunnel built for the Large Electron-Positron Collider (LEP) [136] being utilised, as well as the Super Proton Synchrotron (SPS) [137] being reused as an injector system.

The CERN accelerator complex is illustrated in figure 3.1. A sample of protons is produced for the LHC by breaking molecular hydrogen into atomic hydrogen and stripping the hydrogen atoms of their electrons. These protons are passed into the Linear Accel-

erator 2 (LINAC2). The LINAC2 accelerates the protons up to 50 MeV, before injection into the proton synchrotron booster (labelled booster in figure 3.1), which accelerates them further to 1.4 GeV. The protons are then fed into the Proton Synchrotron (PS) for further acceleration up to 25 GeV before injection into the Super Proton Synchrotron (SPS), where the protons are accelerated up to 450 GeV. The protons are then injected directly into the LHC in bunches of 1.15 $\times 10^{11}$ protons. Each bunch crossing (BC) is separated by 25 ns (which corresponds to $\approx$ 7.5 m) and there are up to 2556 bunches per beam. They are accelerated in the LHC further up to 6.5 TeV, leading to proton–proton collisions at a centre-of mass energy of 13 TeV. Each SPS fill requires three to four cycles of the PS and the LHC requires 12 cycles of the SPS for filling. The cycling time of the PS is 3.6 s and for the SPS it is 21.6 s, therefore filling takes approximately 4 minutes per beam [135].

For lead ions the process is similar, however, the ions are produced from a source of isotopically pure lead-208. The solid metal is heated to form a vapour and then ionized. The ions are extracted and accelerated in LINAC3 and then fed into the Low Energy Ion Ring (LEIR) which splits the beam into bunches of 2.2 $\times$ 10^8 ions. Bunches are accelerated from 4.2 to 72 GeV in pairs, which takes about 2.5s. With 592 ion bunches per beam, a complete fill takes about 10 minutes [138]. From the LEIR the bunches are fed into the PS and follow the same path as the protons to the LHC.

The LHC is made up of eight sectors as shown in figure 3.2. The eight sectors consist of a straight section and two transition regions at the ends. Each insertion point is used either for collisions, injection, beam dumping or beam cleaning. Two separate beam pipes circulate the entire accelerator with two beams of particles travelling in opposite directions. They are guided around the accelerator by a magnetic field provided by superconducting magnets. These have to be kept at a temperature of 1.9 K for operation, which is achieved by using superfluid helium. Dipole magnets keep the particles

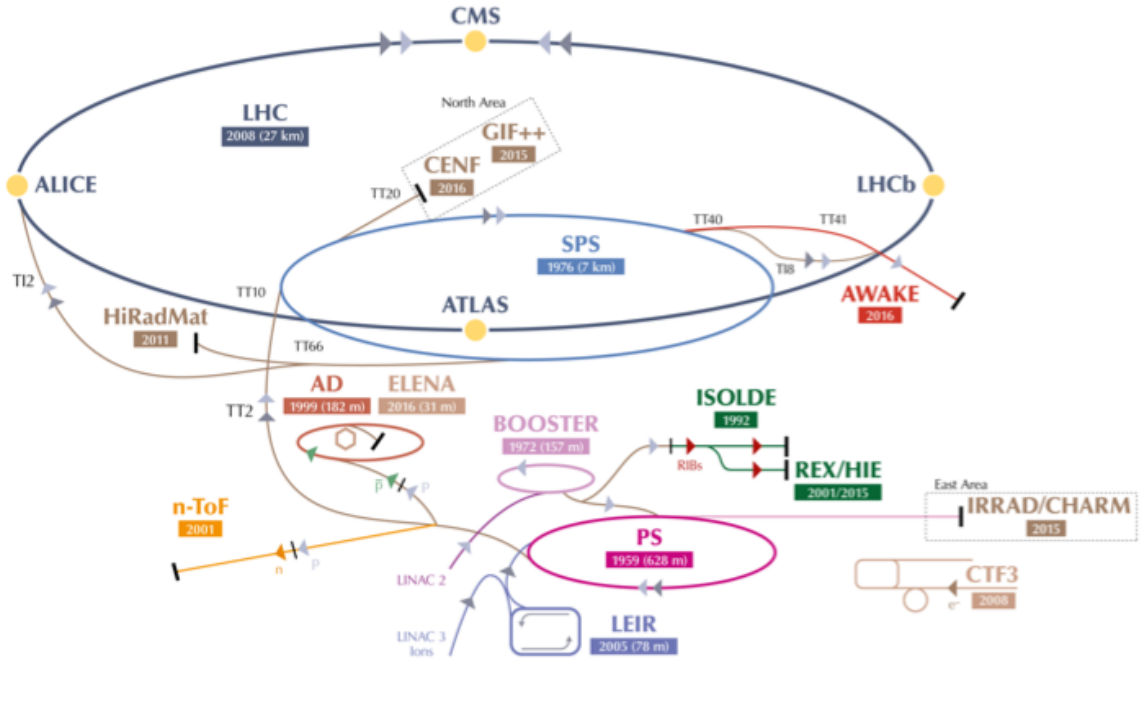

Figure 3.1: Schematic diagram detailing the layout of the CERN acccelerator complex, where the LHC is shown by the largest ring in the dark blue. The chain of smaller accelerators used to accelerate the particles before injection into the LHC, including the LINACs (Linear Accelerators), the Proton Synchotron (PS), the Super Proton Synchrotron (SPS) and the LEIR (Low Energy Ion Ring), are also shown [139].

in their circular orbit and quadrupole magnets are used to focus the beams at four interaction points around the ring. At these points, the main LHC experiments are located: ALICE, ATLAS [140], CMS [141] and LHCb [142].

LHCb is designed to study CP violation in pp collisions through b meson decays. ATLAS and CMS are general purpose detectors which are primarily used to take measurements of high-luminosity pp collisions, in order to study the Higgs Boson (discovered in 2012 [143, 144]), as well as to search for physics beyond the Standard Model. ALICE is optimised for the study of heavy-ion collisions.

The LHC first successfully collided proton beams in September 2008, however an electrical failure nine days later led to a year-long shutdown to repair the accelerator. In

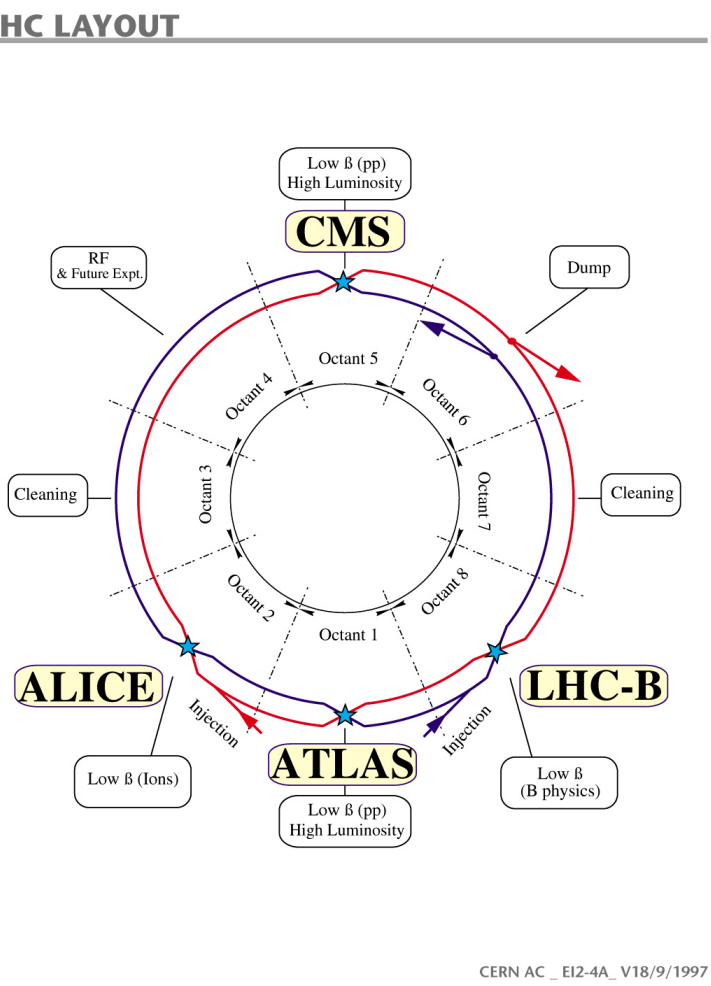

Figure 3.2: Schematic diagram showing the layout of the LHC [145].

November 2009, pp collisions restarted, beginning Run 1 of the LHC which lasted until February 2013. During this time, pp collisions at $\sqrt{s}$ = 0.9, 2.76, 7 and 8 TeV were run, as well as three heavy-ion runs with Pb–Pb collisions at $\sqrt{s_{NN}}$ = 2.76 TeV in 2010 and 2011 and with p–Pb collisions at $\sqrt{s_{NN}}$ = 5.02 TeV in 2013. A long shutdown (LS1) then commenced where many of the detectors, and the LHC itself, were upgraded. The LHC then restarted in April 2015 for Run 2 which continued until October 2018. Higher energy collisions of $\sqrt{s}$ = 13 TeV for pp collisions, $\sqrt{s_{NN}}$ = 5.02 TeV for Pb–Pb collisions and $\sqrt{s_{NN}}$ = 8.16 TeV for p–Pb collisions, were carried out during this run, as well as a brief run of Xe–Xe collisions at $\sqrt{s_{NN}}$ = 5.44 TeV.

3.2 | The ALICE Detector

The ALICE detector is optimised to study the high multiplicities produced in heavy-ion collisions, with excellent particle identification (PID) capabilities over a wide momentum range (∼0.1 - 100 GeV/c). It is designed to study nuclear matter at extreme conditions of temperature and energy density in which a QGP is produced. It is a 10,000 tonne detector with dimensions of 16 m by 16 m by 26 m. It is made up of eighteen different detector sub-systems which are designed to provide a broad range of measurements that can be used to analyse the heavy-ion collisions at the LHC. It consists of a central barrel encased in a solenoidal magnet with a field of 0.5 T and a forward muon spectrometer. The layout of the detectors within ALICE is shown in figure 3.3.

3.2.1 | ALICE coordinates

The ALICE detector follows a right-handed Orthogonal Cartesian coordinate system with the origin ($x, y, z = 0$) at the very centre of the detector. The x axes is defined to be pointing to the centre of the LHC, the y axes points up and the z axes is parallel to the beam pipe pointing away from the muon spectrometer, as indicated in figure 3.4. The variables studied can be divided into transverse and longitudinal, where the longitudinal components refer to the z-components and the transverse components combine the x and y components. For example, the transverse momentum is defined by $p_T = \sqrt{p_x^2 + p_y^2}$. As the p_T of the colliding nucleons is approximately 0, transverse momentum in the final state is of interest as it is created in the collision. The azimuthal angle, φ, increases counter-clockwise from the x axis ($\varphi = 0$) to the y axis ($\varphi = \pi/2$) with an observer at positive z. The polar angle, θ, increases from $+z$ ($\theta = 0$) to the $x - y$ plane ($\theta = \pi/2$) to $-z$ ($\theta = \pi$).

The longitudinal variable pseudorapidity is given by

$$\eta = \frac{1}{2}\ln\left(\frac{|\overrightarrow{p}| + p_z}{|\overrightarrow{p}| - p_z}\right) = -\ln\left[\tan\left(\frac{\theta}{2}\right)\right], \tag{3.1}$$

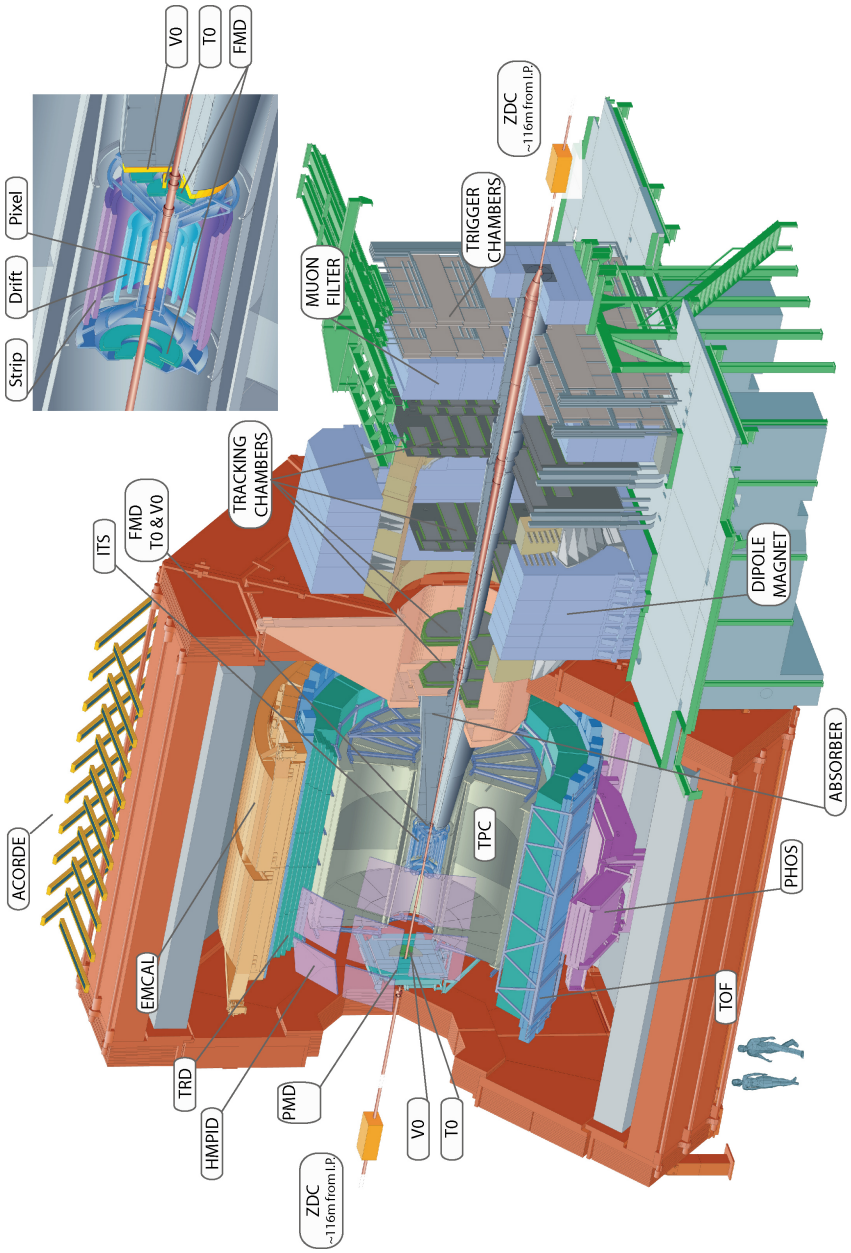

Figure 3.3: Schematic diagram of ALICE showing all the sub-detectors [41]. The red solenoidal magnet is also shown.

where $\overrightarrow{p}$ is the momentum vector for a particle, p_z is the momentum along the z axis and θ is the angle between the particle's momentum and the z axis. $\eta = 0$ when $\theta = 90^\circ$ ie. along the y axis. At very high relativistic energies, η is a good approximation of the variable rapidity defined as

$$y = \frac{1}{2}\left(\frac{E + p_z}{E - p_Z}\right). \tag{3.2}$$

These variables can be used to define different rapidity regions. Particles produced close to the beam line with small θ have $\eta \gtrapprox 3$ which is known as the forward region. Particles associated with the transverse region have $|\eta| < 0.5$, which is known as the mid-rapidity region.

The side of ALICE with the positive z-axis and y, η>0 is referred to as the A-side and the opposite region with y, η<0 is referred to as the C-side. In this thesis the analysis takes place on p–Pb collisions in which the protons travel from A to C and the lead ions travel from C to A.

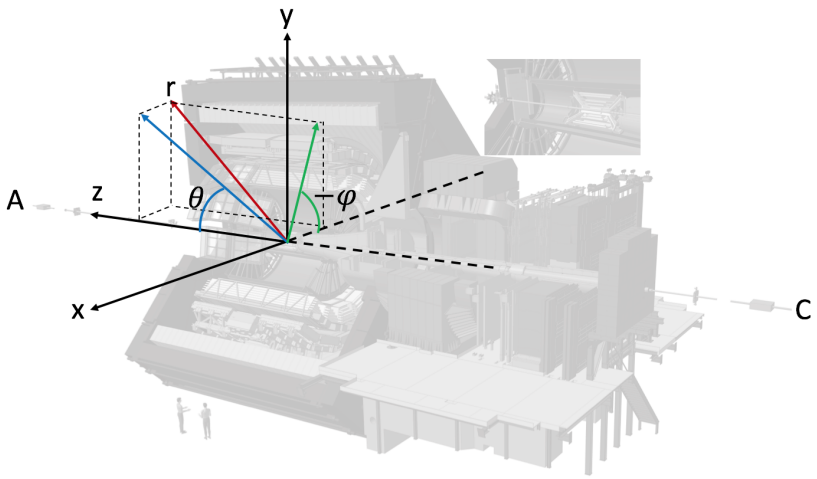

Figure 3.4: Diagram showing the ALICE coordinate system. Adapted from [146].

In symmetric systems like Pb–Pb and p–p, the centre of mass rapidity y_{CM} and lab rapidity y_{lab} are the same. However, for p–Pb collisions in the lab frame, the centre of mass

frame is moving with a shift in rapidity given by

$$\Delta y \approx \frac{1}{2}\ln\left[\frac{Z_1 A_2}{Z_2 A_1}\right] \approx \frac{1}{2}\ln\left[\frac{82\times 1}{1\times 208}\right] \approx 0.465 \tag{3.3}$$

where Z and A are the atomic and mass numbers of the colliding particles [147]. For this system, the shift is towards negative rapidities so at y_{CM} = 0 (midrapidity), y_{lab} = -0.465.

3.2.2 | ALICE subdetectors

The ALICE detector consists of 18 different subdetectors divided into three groups: central barrel detectors, forward detectors and the muon arm. The central barrel covers the pseudo-rapidity interval $-0.9 < \eta < 0.9$ and contains detectors used for vertex reconstruction, tracking, PID and momentum measurements. It consists of the inner tracking system (ITS), the time projection chamber (TPC), the transition radiation detector (TRD) and the Time of Flight detector (TOF). In the mid-rapidity region there is also the High Momentum Particle Identification Detector (HMPID), the Photon Spectrometer (PHOS) and the Electromagnetic Calorimeter (EMCAL).

The forward detectors are in the high pseudo-rapidity region and therefore at a small angle with respect to the beam pipe. They are used for triggering and measuring global event charecteristics. They consist of the Time Zero (T0), VZERO (V0), Forward Multiplicity Detector (FMD), Photon Multiplicity Detector (PMD) and Zero Degree Calorimeter (ZDC). The T0 measures the event time with a precision on the order of 10^{-11}s. The FMD and PMD can provide multiplicity information and the ZDC is used to differentiate peripheral and central collisions by measuring the energy of the spectator nucleons that do not participate in the collisions.

In the forward pseudo-rapidity region ($-4 < \eta < -2.5$) also lies the muon spectrometer, which has a front absorber, a dipole magnet as well as tracking and trigger chambers, and is used to study heavy quarkonia, open charm, W and Z bosons via their muon

decays. Finally, the ACORDE detector is an array of scintillators on top of the ALICE solenoidal magnet that is used for studies of cosmic rays. In the following sections more detailed descriptions of the detectors used in the analysis in this thesis are given.

3.2.3 | ITS

The Inner Tracking System (ITS) is a high-resolution tracking detector made up of six layers of silicon detectors illustrated in figure 3.5. The ITS can locate the primary and secondary vertices with a high resolution, which is important for strangeness analyses that measure the decays of hyperons with decay lengths on the order of centimetres. The four outermost layers also provide $\mathrm{d}E/\mathrm{d}x$ measurements for low-momentum particles that can be used for particle identification (PID). The ITS surrounds the beam pipe between $4 < r < 43$ cm, covering the rapidity range $|\eta| < 0.9$.

3.2.3.1 | Silicon Pixel Detector

In order to handle the high particle density close to the beam pipe (up to 50 particles per cm^2), the innermost two layers are Silicon Pixel Detectors (SPD) which have a spatial resolution of 12 μm in the $r\phi$ direction and 100 μm in the z direction. The SPD is made of a matrix of 2D reverse-biased silicon detector diodes connected by a conductive solder

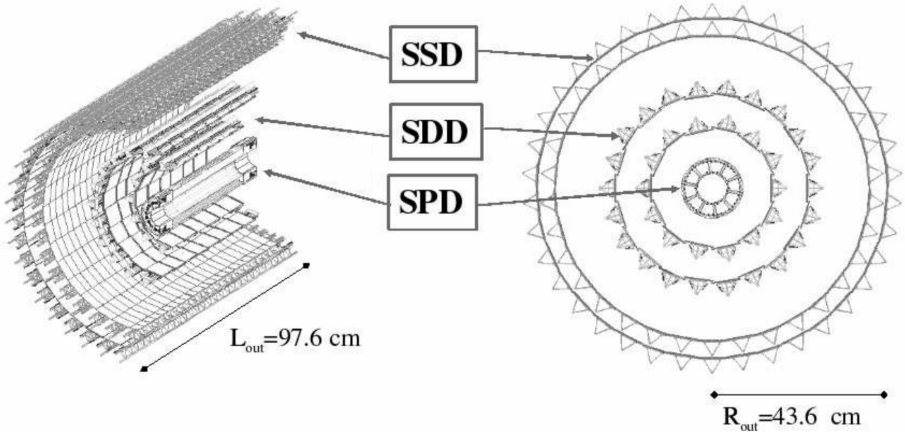

Figure 3.5: Diagram showing the layout of the 6 ITS layers at ALICE [41].

bump onto readout chips. The readout is binary, meaning the output generates a pulse when the signal in a cell increases above a set threshold. The detector modules are made of half-staves that contain two ladders of silicon sensor matrices made of 256 X 160 cells. The whole sensor matrix has an active area of 12.8 mm (rϕ) by 70.7 mm (z). The ladders are attached and bonded to a pixel bus which carries data/control lines and power/ground planes. A multi-chip module (MCM) is bonded to the pixel bus at the end of the half-stave and controls the front-end electronics and is connected to the readout system via optical fibre links. Two half-staves are connected to a carbon-fibre support sector with an MCM at each end to form a stave. The SPD contains 60 staves in total with 240 ladders of 1200 chips and 9.8 x 10^6 cells. The SPD is surrounded by an aluminium coated carbon-fibre shield that prevents heat radiating to the Silicon Drift Detector layers. The concentration of pixels in the SPD allows the primary vertex to be identified with a resolution better than 100μm, as well as measuring secondary vertices with very good accuracy.

3.2.3.2 | Silicon Drift Detector

The middle two layers are Silicon Drift Detectors (SDD) which have a spatial resolution of 35 μm and 25 μm in the $r\phi$ and z directions respectively. They provide good multi-particle tracking and two of the four dE/dx samples used for ITS PID. They are made from 300 μm thick silicon with a sensitive area of 70.17 (rϕ) x 75.26 (z) mm^2. The sensitive area is split into two drift regions by a central cathode strip with a high bias voltage of -2.4 kV applied, which generates a drift field. At the bias voltage of -2.4 kV a drift velocity of 8.1 μm/ns is provided. There are 8.91x10^4 cells per layer of 294x202 μm^2 each, which are readout by 512 electronic channels. Electrons produced by ionisation of charged particles passing through the detector, drift towards the 256 anodes at the ends of the detector. Measurement of the drift velocity allows the position of the original particle with respect to the anode to be identified. Energy loss of the particles as they interact with the detector is also measured, providing PID information.

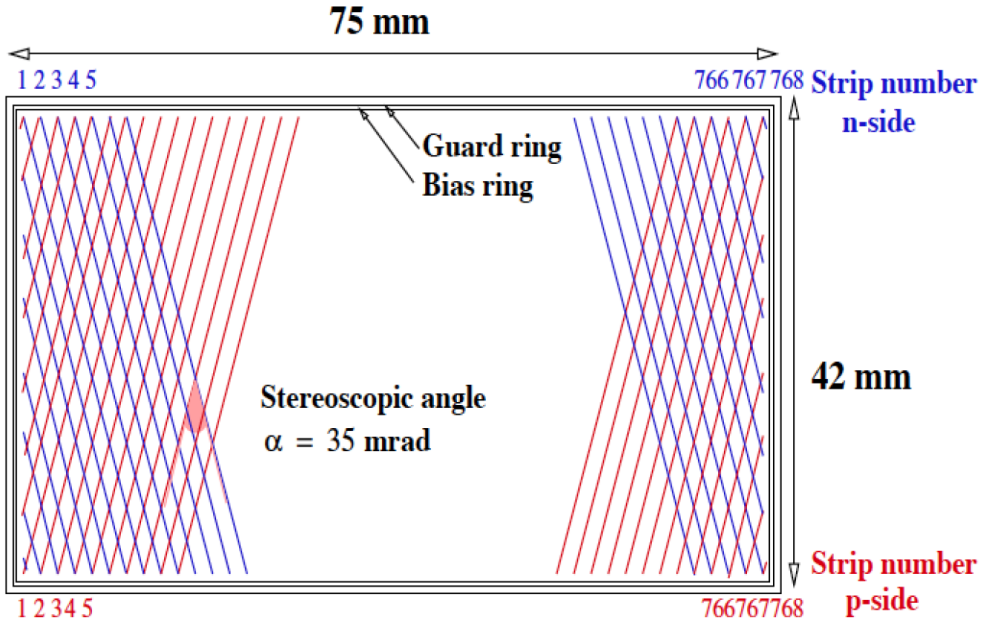

Figure 3.6: Diagram showing a silicon strip sensor [148].

3.2.3.3 | Silicon micro-Strip Detector

The track density is reduced significantly at the outermost layers (<1 particle per cm^2) so they are made with double-sided Silicon micro-Strip Detectors (SSD). They provide the necessary information to match tracks between the ITS and the TPC, as well as providing additional dE/dx information for low-momentum PID. The SSD has a resolution of 20(830) μm in the $r\phi$(z) direction. It is made of 1770 individual 300 μm thick sensors with 768 sensitive strips on each side. The strips are tilted by 17.5 mrad with respect to the sensor in two different directions as shown in figure 3.6. When two strips on opposite sides detect a signal, the position of the charged particle passing through the sensor can be located to the position of the two strips crossing.

3.2.4 | TPC

The Time Projection Chamber (TPC) is a tracking detector that surrounds the ITS, shown with the key components labelled in the schematic diagram in figure 3.7. It allows the complete reconstruction of tracks over a wide range of p_T from about 0.1 GeV/c up to

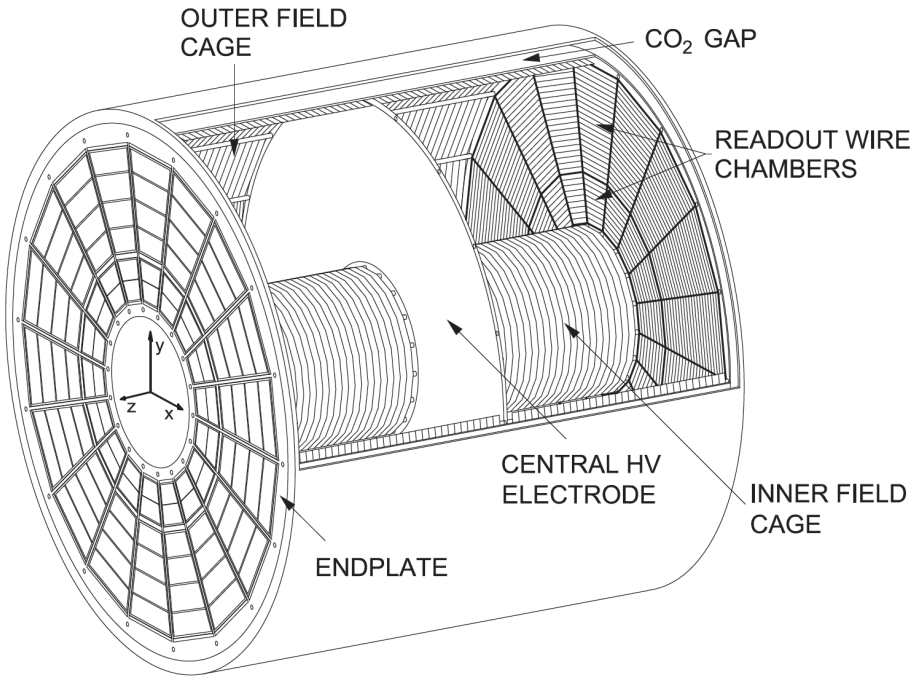

Figure 3.7: Diagram indicating the key components of the TPC [149].

100 GeV/c for $|\eta| < 0.9$. It consists of a field cage filled with 90 m^3 of gas made up of neon, carbon dioxide and nitrogen with the ratio (90:10:5). This gas mixture is optimised for drift speed, reducing multiple scattering and stability over time. The drift velocity in the gas is highly dependent on temperature, meaning a thermal stability of $\delta T \leq 0.1$ K is required, which is provided by heat screens and cooling circuits. A uniform electric drift field of 400 V/cm is applied along the z axis by a central high-voltage electrode at 100 kV. When particles traverse the gas they ionise it, causing electrons to drift along the chamber. When the electrons reach the Multi-Wire Proportional Chambers (MWPC) at the end plates, they cause an electron avalanche which reaches the cathode pads on the readout planes. The coordinates of the pad give the $r\phi$ coordinates of the track. The time taken to cross the chamber gives the z coordinate, where a constant drift velocity is assumed. This allows a position resolution of 1100(800) μm in the $r\phi$ direction and 1250(1100) μm in the z direction to be achieved for tracks at the inner (outer) radii. The p_T of a particle can also be extracted from the curvature of its track in the 0.5 T magnetic field. A momentum resolution of 0.7% can be achieved at 1 GeV/c and up to 6.5% at

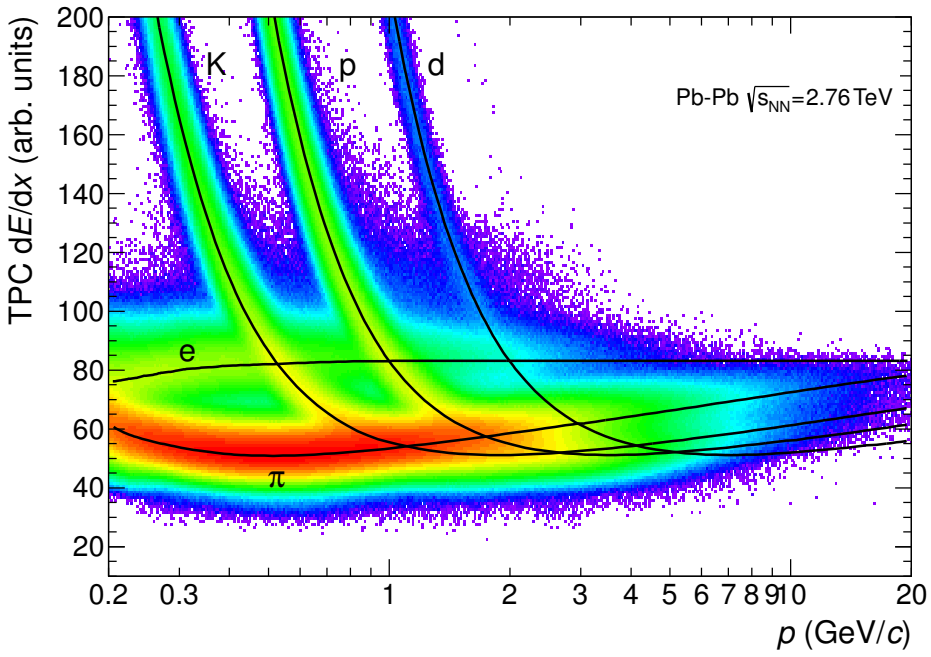

Figure 3.8: $\mathrm{d}E/\mathrm{d}x$ of charged particles vs momentum as measured by the TPC in Pb–Pb collisions. The lines show parameterisations of the detector response based on the Bethe-Bloch formula [153].

around 10 GeV/c.

PID is also performed by the TPC by measuring the energy loss per unit length or specific energy loss, $\mathrm{d}E/\mathrm{d}x$. This is described by the Bethe-Bloch [150, 151] formula which can be written as

$$-\frac{dE}{dx} \propto \frac{Z^2}{\beta^2} ln(1-\beta^2)^{-1/2}, \tag{3.4}$$

where Z is the atomic number of the atoms in the material being traversed and β is equal to $\frac{v}{c}$, using the form given in [152]. Therefore, the energy loss is dependent on the velocity of the particle. For a given momentum, particles of different masses will have a different velocity, and therefore a different $\mathrm{d}E/\mathrm{d}x$. By plotting the measured $\mathrm{d}E/\mathrm{d}x$ against the measured momenta of the particles detected, particles of different masses can easily be separated for p below $\sim$1 GeV, as shown in figure 3.8.

3.2.5 | V0

The V0 detectors are plastic scintillators located either side of the interaction point, named V0A and V0C. They are used for triggering and measuring the charged-particle multiplicity of an event, as was introduced in section 2.1.1. The detectors are placed at $z = 340$ cm (V0A) and $z = -90$ cm (V0C) and cover the pseudorapidity ranges of $2.8 < \eta < 5.1$ (V0A) and $-3.7 < \eta < 1.7$ (V0C). They consist of a disk of 32 counters in four rings, each divided into eight sectors. Particles that reach the detectors and traverse them cause the atoms of the scintillator to excite and release energy through photons. These photons are shifted down in frequency via wavelength-shifting fibres and transferred to photomultiplier tubes (PMTs) with optical fibres, where the total energy of the photons is recorded. This causes a signal which is proportional to the number of particles that have hit the detector and therefore the number of particles produced in the collision. The distribution of the amplitude of the V0 signal can be used to calculate the multiplicity of the collision using a NBD-Glauber fit to the data [79]. For pp and Pb–Pb collisions the sum of the amplitudes in the V0A and V0C detectors is used. For p–Pb collisions the data from the Pb-going side are used, which for this analysis is the V0A detector. The data are divided up into percentile classes as shown in figure 3.9, for which the average charged-particle multiplicity per unit rapidity ($< dN_{ch}/d\eta >$) can be calculated.

Measurements in the V0 detectors are also used to define the Minimum Bias (MB) trigger used in this analysis, *V0AND*, which corresponds to an event with at least one hit in the scintillators of both the V0A and the V0C detectors. The V0 detectors are also important for rejection of events caused by beam-gas interactions i.e. interactions of the beam with residual gas found in the beam-pipe. This is done by measuring the time of flight of particles by each of the V0 detector arrays. A beam-gas interaction can clearly be distinguished from beam-beam events by looking at the correlation between the timing signals in the two detectors as shown in figure 3.10.

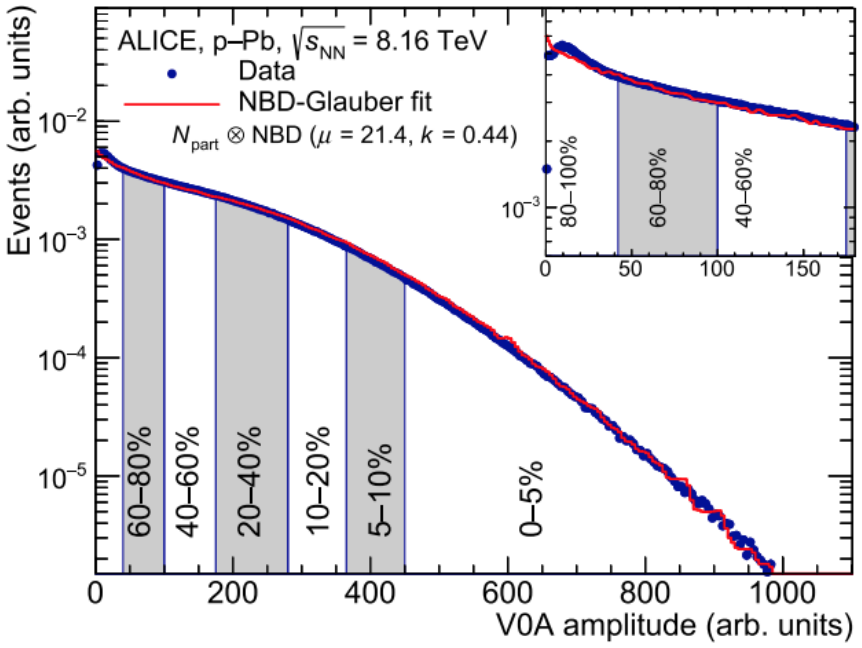

Figure 3.9: Distribution of measured V0A amplitude with NBD-Glauber model fit shown in red. The multiplicity classes are indicated by the vertical lines [154].

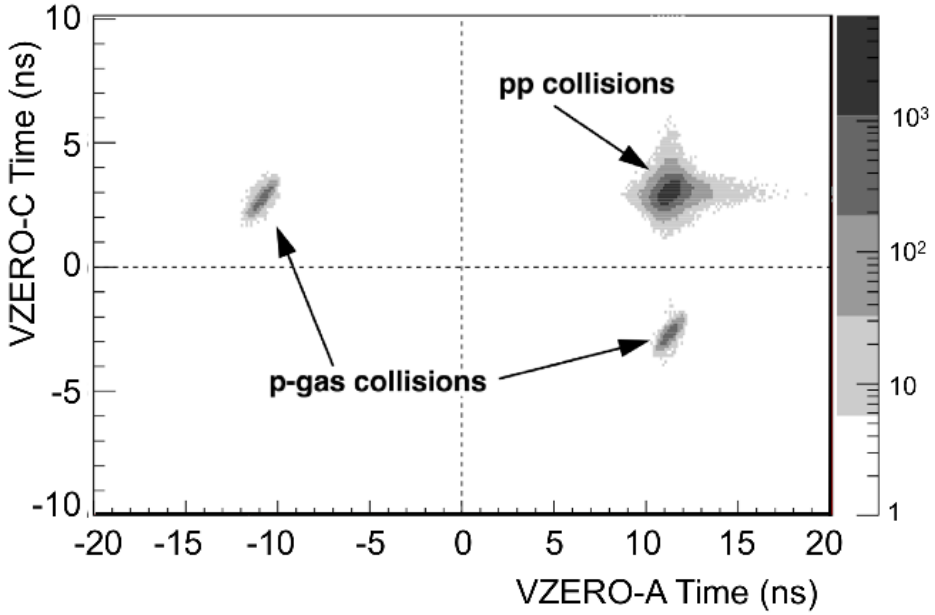

Figure 3.10: Correlation of weighted average time of flight of particles that are detected in the V0A and V0C detectors [155].

3.2.6 | TOF

The Time of Flight (TOF) detector is used to measure the time taken for particles to travel across the detector. This information can be used for PID of particles with intermediate momentum and, along with ITS and TPC information, can identify pions, kaons and protons. The TOF is made from Multi-gap Resistive-Plate Chambers (MRPC). These are a stack of ten glass plates separated with nylon wire, where a high and uniform electric field is applied. The gaps between the plates are filled with ionizing gas. A charged particle crossing the gas causes an avalanche which leads to signals on the electrodes. There is no drift time due to the small gaps between the plates and the strength of the electric field. An average time of flight can be calculated from the signals from all the gaps leading to a precision in timing of about 50 ps. Using the TOF timing measurement and momentum from the TPC, particles may be identified by mass, allowing particles with similar momenta to be distinguished from each other.

For this analysis the TOF was used as a tool to remove out-of-bunch (OOB) pileup, which is explained further in section 4.1.1.1. This was carried out by removing a cascade candidate if at least one of the daughter tracks has no corresponding TOF information in the event. The resolution of the TOF is poor at low p_T so the ITS is used in this region to compensate for this. The OOB pileup is removed in this case by checking at least one of the daughter tracks of the cascade was reconstructed using TPC and ITS information instead of just TPC information.

3.2.7 | Trigger Operation

ALICE has a two-layer Central Trigger System (CTS) including a hardware trigger controlled by the Central Trigger Processor (CTP) [156] and the high-level trigger (HLT) [157] implemented as a software trigger. The ALICE CTP is used to communicate with detectors and decide when they should read data out. Firstly, the CTP receives signals

from triggering detectors that indicate a collision has occurred. The CTP then sends signals out to detectors to read out data using the CERN Timing, Trigger and Control (TTC) system. Due to the different read out times of the detectors, the trigger system has three different levels. The L0 signal is received within 1.2 μs by detectors that require an early indication of a collision, including the T0, PHOS, ZDC, EMCAL, ACORDE and TOF. A L1 trigger and message is received by 6.5 μs, if additional messages are received from L1 trigger detectors (PHOS, TOF, TRD, ZDC and EMCAL) consistent with a collision. Finally, a L2 signal is received after the drift time of the TPC which is $\sim 100\mu$s. Detectors are read out after a positive L2 signal has been received.

All signals are transmitted via Local Trigger Unit boards (LTUs) which communicate between the CTP and the sub-detectors. Different trigger inputs are defined by the different type of events to be selected such as the *V0AND* trigger which selects MB events as mentioned in section 3.2.5. A select group of sub-detectors, called a trigger cluster, are activated to read out data for the event reconstruction. Not all sub-detectors may be included in the trigger cluster as particular physics analyses may not require all detector information. This means slower detectors, such as the SDD, may not be included in read out, allowing a faster rate of read out. Multiple inputs and a detector cluster, together defined as a trigger class, can be applied in parallel allowing data to be collected by different groups of detectors simultaneously. In Run 2, the system allowed up to 100 possible classes to be defined.

The ALICE HLT receives the data read out from the detectors and performs online analysis of the events recorded. With more information available, more sophisticated triggers can be applied by the HLT. The HLT is also important in reducing the size of the events to reduce storage requirements by selecting regions of interest for particular analyses and compressing the data. A factor of ten compression is achieved without significant impact on the offline tracking efficiency [157].

3.2.7.1 | Trigger Upgrade

During the LHC Long Shutdown 2 (2019 - 2021), many of the components of the ALICE detector are being upgraded. This includes the ALICE CTS, which will be completely upgraded for LHC Run 3 (2021-2024), in which interaction rates at ALICE will increase from 8 to 50 kHz for Pb–Pb collisions and 100 to 200 kHz for pp/p–Pb collisions. The new CTP will be able to operate in a triggerless, continuous readout mode with online data reduction, as well as the normal triggered mode. More details of the upgrade can be found in [158].

In the first production phase, 23 CTP prototype boards were produced as outlined in [159], a proceedings I contributed to the editing of. During the summer of 2018, as part of my ALICE service task, a series of tests were conducted on these boards to check their functionality. I carried out checks on all of the components connected to the Field Programmable Gate Array (FPGA) on each board to test their functionality and recorded the results in a series of log files. No faults were found in any of the boards.

Two of the boards were then used to carry out accelerated ageing tests by placing them in a climate chamber and cycling the temperature as is described in [160, 161]. This simulates the thermo-mechanical stresses the boards will undergo during a lifetime of usage at an accelerated rate. Firstly the *Clima Temperatur Systeme T-40/500* climate chamber, was tested to see how long a cycle would take. The settings used for the cycling were a minimum temperature of -40°C and a maximum temperature of 85°C, both with a tolerance of 1°C. Figure 3.11 shows the temperature recorded every minute for the duration of one cycle. From this, the length of one cycle was approximated to be $\sim$340 minutes and therefore, the 100 cycles required for the ageing test would be $\sim$ 24 days.

Two CTP boards were placed in the climate chamber for 100 cycles. They were then removed and all the previous component functionality tests were repeated to check for

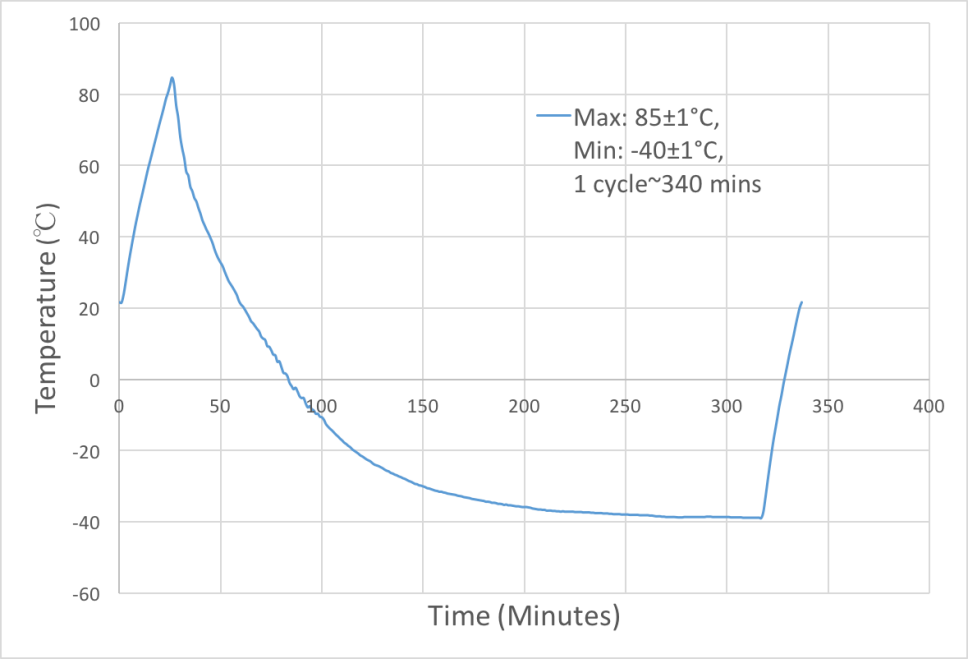

Figure 3.11: Plot showing the change in temperature over time in the climate chamber for one cycle from -40±1°C to 85±1°C, from which the duration of one cycle can be calculated.

faults. The boards were then placed back in the climate chamber for another 100 cycles and the functionality tests were carried out again. At both stages no faults were found confirming the durability and longevity of the boards under high thermal stress.

3.2.8 | Event Reconstruction

Using the raw data from the detectors, which includes information on the activated detector elements and timing information, the track trajectories of particles need to be reconstructed for analysis. This allows useful variables to be extracted such as the trajectory coordinates, particle momentum, particle energy loss and distance of closest approach to the primary vertex (PV). When particles traverse the detectors they leave behind signals in adjacent detector cells. These signal clusters give the position information of the tracks. Using cluster finding reduces the effect of random noise in position and timing measurements.

The Kalman filter technique is used on these clusters to reconstruct the tracks [162]. First a 'seed' cluster is found in the outer TPC and then tracked back through the inner TPC and the ITS, where the location of the PV can be estimated. Information from other detectors, if available, is then added to produce global tracks. Secondary vertices are located by combining tracks sufficiently far from the PV and utilising the topology of the decays of unstable particles [163]. After reconstruction, the useful information can be stored in compact Event Summary Data (ESD) files, which the analysis in this thesis is performed on.

Chapter 4

Identification of Multi-Strange Baryons

The following chapter will describe the analysis of the multi-strange baryon yields in p–Pb data taken in Run 2 at $\sqrt{s_{NN}} = 8.16$ TeV. The multi-strange particles of interest are those baryons which contain more than one strange quark. They are the $\Xi^0(uss)$, the $\Xi^-(dss)$ and the $\Omega^-(sss)$, as well as their corresponding antiparticles $\overline{\Xi}^0$, $\overline{\Xi}^+$ and $\overline{\Omega}^+$. Only charged particle tracks can be identified by the inner tracking detectors in ALICE, so the Ξ^0, which predominantly decays via $\Xi^0 \rightarrow \Lambda + \pi^0$ $(99.524 \pm 0.012)\%$ [164], cannot be identified. The analysis is therefore carried out on Ξ^-, $\overline{\Xi}^+$, Ω^- and $\overline{\Omega}^+$, which are collectively known as cascades due to the double weak decay they undergo. The analysis is completed by initial event, track and cascade candidate selection (section 4.1-4.1.1), removal of pileup (section 4.1.1.1), extraction of signal, where the selection procedures are refined, (section 4.2) and calculating efficiency corrections (section 4.3). The systematic uncertainties also have to be evaluated, which are shown in section 4.5.

4.1 | Reconstruction

The particles measured in this analysis have their properties outlined in table 4.1. The topology of the cascade decays is shown in figure 4.1. Once a $\Xi^{\pm}$ has been formed, it

will travel a short distance on average, L, before decaying, which is defined by,

$$L = \frac{p\tau}{m}, \tag{4.1}$$

where τ is the proper lifetime, m is the PDG mass of the particle and p is the total momentum of the particle. For a $\Xi^{\pm}$ this is of the order of a few centimetres. After travelling

Table 4.1: Table showing data for cascades [164].

Particle	Mass (MeV/c^2)	Decay Channel	Branching Ratio (%)	Lifetime cτ (cm)
$\Xi^{\pm}$	1321.71 ± 0.07	$\Lambda\pi^{\pm}$	99.887 ± 0.035	4.91 ± 0.04
$\Omega^{\pm}$	1672.45 ± 0.29	$\Lambda K^{\pm}$	67.8 ± 0.7	2.46 ± 0.03
$\Lambda/\overline{\Lambda}$	1115.683 ± 0.006	$p^{\pm}\ \pi^{\mp}$	63.9 ± 0.5	7.89 ± 0.06

this distance, it will undergo a weak decay. The most likely decay, with a branching ratio of 99.887% [164], is into a Λ and a $\pi^{\pm}$ (which is referred to as the bachelor). The Λ itself is neutral so its path is not tracked by the ALICE detector. However, it then decays into a pair of particles with opposite electric charge which can be identified. This Λ is referred to as a V0 due to the distinctive V shape of the oppositely charged decay particles produced. For the $\Omega^{\pm}$, the topology is the same but the bachelor is a K instead of a π.

Due to the short decay length of the cascades, they are not measured directly in the ITS (the two layers of the SPD are at 3.9 cm and 7.6 cm from the interaction point). Therefore, they have to be reconstructed using the V0 daughter tracks and the bachelor track (the neutral Λ has no track). Firstly, the Λ is reconstructed from the V0 daughter tracks, then the Λ is associated with a bachelor track to reconstruct a cascade candidate. A combination of geometric and kinematic selection criteria are used to identify the cascades. The key topological selections are shown in figure 4.2. The V0 finder used in the analysis initially combines every secondary track with all other secondary tracks that are oppositely charged. A cut on the minimum distance of closest approach (DCA) with the primary vertex (PV) for the two tracks is applied to ensure the tracks are secondary and do not originate from the PV (DCA baryon/meson to PV in figure 4.2). A cut on the

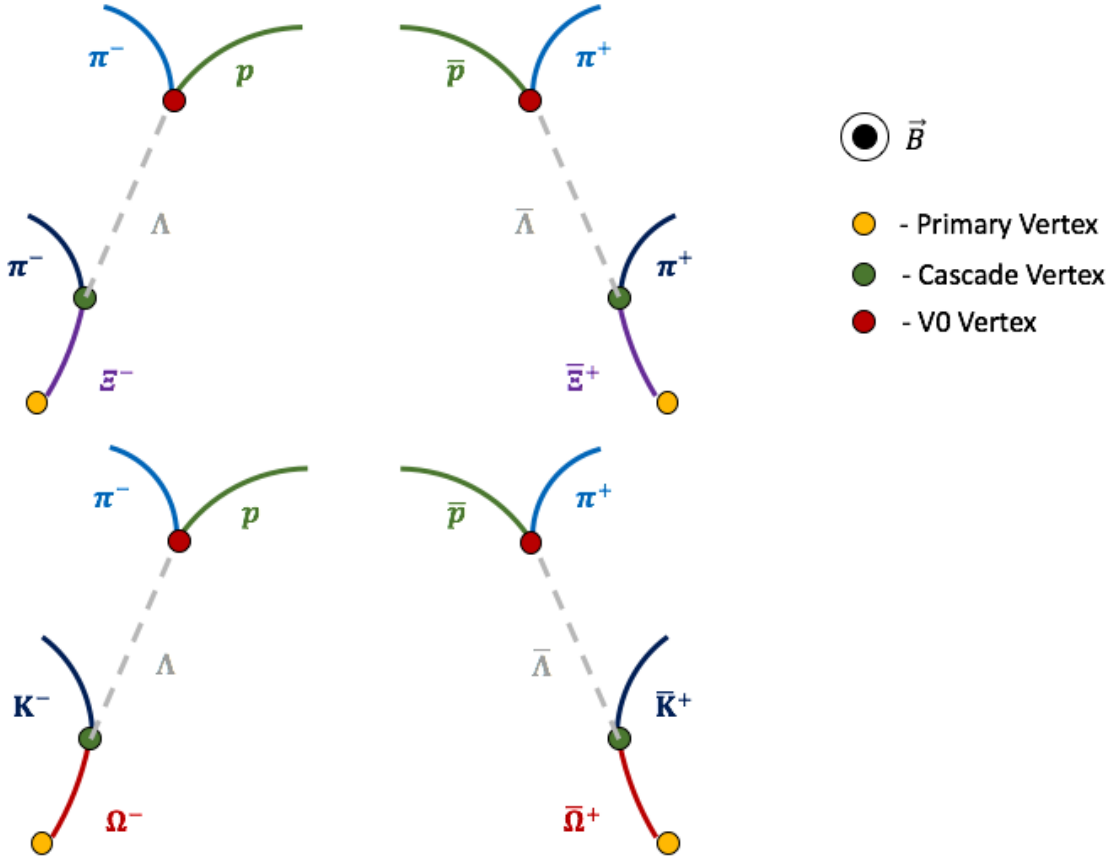

Figure 4.1: Diagram illustrating topology of decay of the four cascade particles identified in this analysis: $\Xi^{\pm}$ and $\Omega^{\pm}$.

maximum allowed DCA between the two tracks is also applied to ensure they both originate from a Λ decay (DCA V0 daughters on figure 4.2). The V0 decay vertex is taken as a point on the DCA line that connects the two daughter tracks, weighted according to the uncertainties of the positive and negative tracks. Once the vertex has been identified it is accepted if it lies at least a minimum distance from the PV (V0 decay radius on figure 4.2). The DCA between the reconstructed trajectory of the Λ and the PV is checked to pass a minimum cut to reject contributions from primary particles (DCA V0 to PV on figure 4.2). Finally, the momentum of the V0 candidate will be checked to confirm it originates from the direction of the PV, which is carried out by putting a minimum cut on the cosine of the angle (which corresponds to a maximum angle) between the V0 momentum vector and the vector that connects the PV and V0 vertex position (V0 pointing angle on figure 4.2).

The invariant mass of the V0 can then be calculated by assuming the mass of the V0 daughters to be as expected ((anti)proton and a pion). Due to finite resolution, the reconstructed mass will be a distribution with a width that is related to the detector resolution. A final selection is made by applying a window in the invariant mass distribution of the V0 candidates of ± 10 MeV/c^2 around the PDG value of 1115.68 MeV/c^2 [164]. In order to identify a cascade, the V0 candidates are associated with all possible secondary tracks which are bachelor candidates. A minimum cut is placed on the DCA of the bachelor to the primary vertex in order to reject primary particles (DCA bachelor to PV on figure 4.2). The V0-bachelor pair is accepted if the DCA between the bachelor track and the V0 is under the maximum cut value, to ensure the tracks both emerged from the same point, the cascade decay vertex (DCA cascade daughters on figure 4.2). The cascade decay vertex is determined to be halfway between the point of closest approach of the V0 and the bachelor. A minimum cut on the cosine of the pointing angle (PA) of the cascade candidate is also applied to check the candidate points back to the primary vertex (Cascade pointing angle on figure 4.2). The cascade finding is limited similarly to the V0s

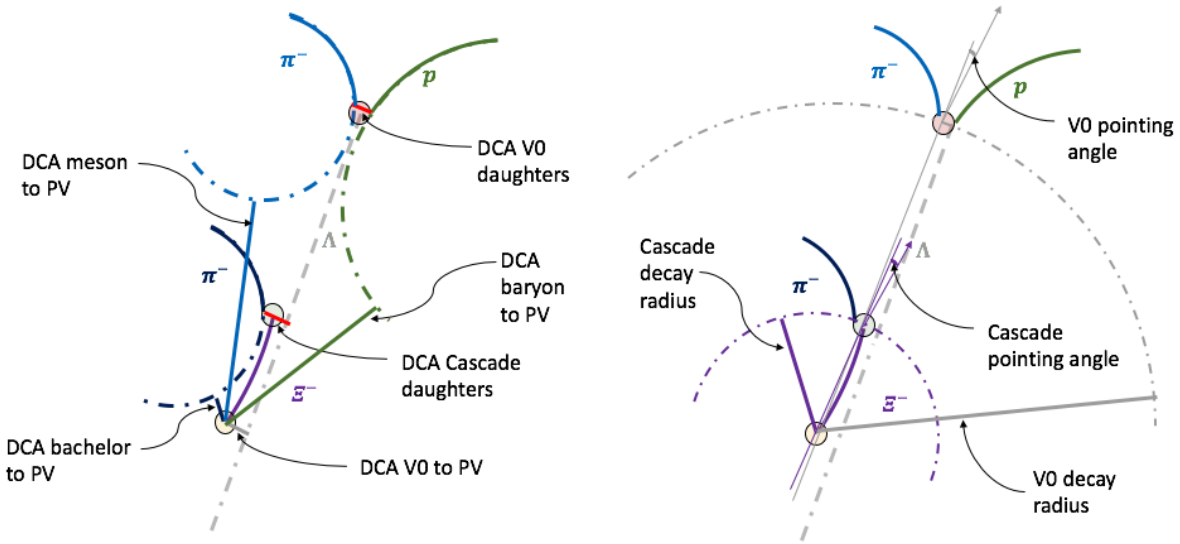

Figure 4.2: Diagram illustrating the topological selections placed on the cascades in this analysis.

by a cut on the minimum distance from the primary vertex (Cascade decay radius on figure 4.2). A check on causality is also made to ensure the V0 vertex is further from the PV than the cascade vertex. The values for all these cuts used in this analysis are shown in table 4.5.

At this stage, the two V0 daughter tracks and bachelor track, that have been identified during this procedure, are either from a real cascade or are just a combination of tracks that have a similar topology to a cascade decay. In order to separate the true signal from the underlying background, the invariant mass of the cascade is computed. This is a Lorentz invariant quantity so should equal the expected mass of the cascade particle if the tracks truly originate from the decay of the expected particle. The invariant mass is computed as $M^2 = (\sum_i E_i)^2 - |\sum_i \overrightarrow{p}_i|^2$. The formulae for Ξ^- and Ω^- are:

$$M^2(\Xi^{\mp}) = \left(\sqrt{m_{\Lambda}^2 + p_{V^0}^2} + \sqrt{m_{\pi^{\mp}}^2 + p_{bach}^2}\right)^2 - \left(\vec{p}_{V^0} + \vec{p}_{bach}\right)^2, \tag{4.2}$$

$$M^2(\Omega^{\mp}) = \left(\sqrt{m_{\Lambda}^2 + p_{V^0}^2} + \sqrt{m_{K^{\mp}}^2 + p_{bach}^2}\right)^2 - \left(\vec{p}_{V^0} + \vec{p}_{bach}\right)^2, \tag{4.3}$$

where $\vec{p}_{V^0} = \vec{p}_{bar} + \vec{p}_{mes}$. *bach*, *bar* and *mes* correspond to the bachelor, baryon V0 daughter and meson V0 daughter tracks respectively. The Λ, $\pi^{\mp}$ and $K^{\mp}$ mass values used in the calculation are the PDG values, not the measured ones in order to reduce the effect of experimental resolution on the calculated Ξ and Ω masses.

The $\Xi^-$and Ω^- baryons have the same decay topology as is shown in figure 4.1. This means it is possible for some Ξ^-candidates to be reconstructed as Ω^- candidates. As the Ξ^- yield is an order of magnitude greater than the Ω^- yield, this can have a significant effect on the resulting Ω^- yield. In order to remove this contribution, the mass of the Ω^-candidate is calculated as if it were a Ξ^-(by using the π mass for the bachelor) and a rejection window of 8 MeV/c^2 around the PDG mass of the Ξ^- is applied. This cut is referred to as the Competing Species or Mass Hypothesis cut.

A selection is also placed on the proper lifetime of the particles so low-momentum particles that originate far from the primary vertex are rejected. The cut is placed on the proper lifetime as defined in equation 4.1. As the cascades are charged particles, their path in a magnetic field will be curved. However, the amount of curvature is considered negligible for this cut and so the approximation has no significant consequences. Furthermore, the cut is consistently placed in both real and MC data, therefore, any proportion of particles removed by the approximation in real data, will also be removed in MC data and thus, efficiency corrections will account for any deviations.

Additionally, in order to remove background from combinations of tracks that are of the wrong particle species, a further selection is applied on the energy loss while traversing the TPC gas. A candidate is removed from the analysis if any of its three daughter tracks has a dE/dx value that differs by more than 4σ from the expected value. A cut on the minimum number of TPC Clusters is also applied to select good quality tracks. A minimum number of 70 clusters, out of a possible 159, is required.

The rapidity acceptance interval used for this analysis is $-0.5 < y_{lab} < 0.0$ for both data and Monte Carlo. This is chosen to largely contain the acceptance of the central barrel, which for asymmetric collisions like p–Pb is not symmetric around midrapidity. As explained in section 3.2.1, $y_{CM} = y_{lab} + 0.465$, so this approximately corresponds to a rapidity interval of $0.0 < y_{CM} < 0.5$ which is comparable to other analyses undertaken at ALICE. The detectors used in this analysis cover $|\eta|$<0.9 so a cut is also placed in the analysis on both daughter tracks at a lower value of $|\eta|$<0.8 to avoid edge effects in the detector.

4.1.1 | Data Sample and Event Selection

The analyses described in this thesis were conducted on an event sample collected at the end of 2016 on proton–lead collisions at a centre of mass energy of $\sqrt{s_{NN}} = 8.16$ TeV. The data set is referred to internally by ALICE as *LHC16r_CENT*, where *CENT* refers to the *CENT* cluster which includes all events with the slowest detector in ALICE, the SDD, in the readout (there is also a *FAST* cluster which includes events collected without the SDD when it is busy). Two different data samples were used in the analysis which had to be handled differently due to pile-up.

4.1.1.1 | Pile Up

The effect of pileup on data has to be taken into account in any physics analysis as it could bias the results. Two types of pileup can occur in the collisions at ALICE, called out-of-bunch (OOB) pileup and in-bunch pileup. In-bunch pileup occurs when two collisions occur in the same trigger window. In order to remove in-bunch pileup, events with more than one vertex reconstructed by the ITS are rejected, as described in section 4.1.1.2. However, out-of-bunch pileup, where events from different bunches are mixed together can still occur. This is due to the long drift time of the electrons in the TPC, which means tracks can still be traversing the TPC when a new collision occurs. This type of event is not removed by the rejection described previously if there is only one ITS vertex, so other conditions need to be used. The probability of pile-up events in a sample increases with the collision rate. The in-bunch pile-up probability of the data was evaluated run-by-run by calculating the average number of interactions per bunch crossing, μ, in each run. The probability for n interactions in a bunch crossing follows a Poisson distribution, as a function of μ:

$$P(n,\mu) = \frac{e^{-\mu}\mu^{n}}{n!}. \tag{4.4}$$

The probability of two or more interactions per BC can then be calculated using

$$P(n \geq 2, \mu) = 1 \; - \; P(0, \mu) \; - \; P(1, \mu) = 1 \; - \; (\mu + 1)e^{-\mu}. \tag{4.5}$$

The value of μ for each run in the *LHC16r_CENT* dataset is shown in figure 4.3. In order to avoid pile-up in the data analysed, runs with a low μ value were selected to form a subsample. The six runs selected, highlighted in red on figure 4.3, had $\mu < 0.02$. This subsample corresponded to $\approx 40\%$ of the total MB data (11.4 million out of 29 million events). The average μ of the events in this sample was 0.011, which means the probability of pileup in the sample analysed was $P(n \geq 2, 0.011)/(1 - P(0, 0.011)) = 0.6\%$. This is a significant reduction from the whole dataset which has an average μ of 0.052, which means there is a more significant probability of pileup at 2.6%.

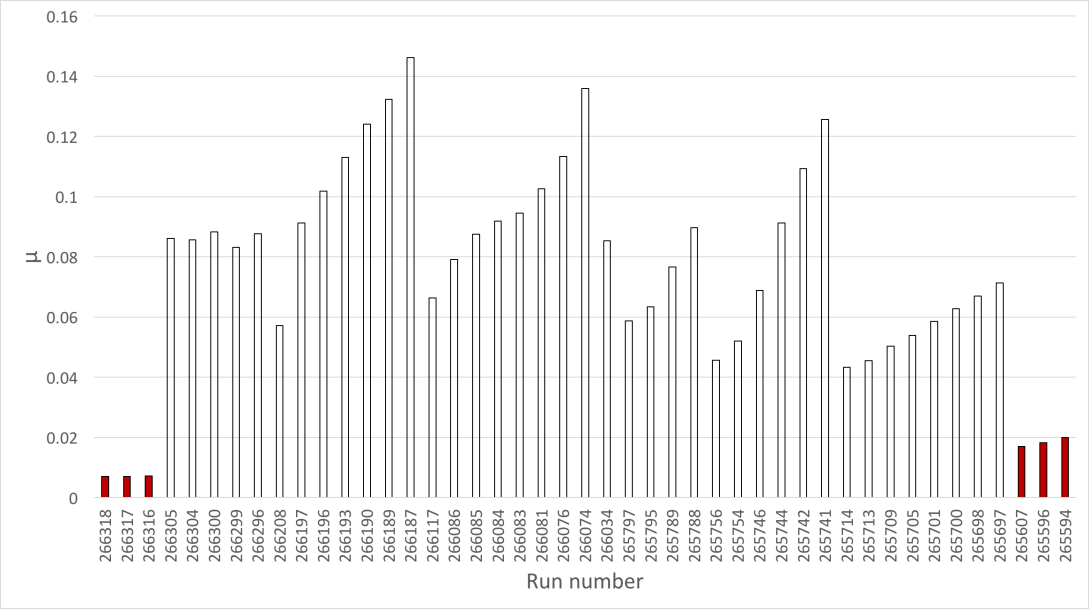

Figure 4.3: Plot showing the value of average number of interactions per BC, μ, for each run in *LHC16r_CENT*. The red runs are used in the low interaction rate dataset.

The analysis process presented in the following sections are on this subsample of data. However, new procedures were developed later within ALICE to handle the OOB pileup

in the data, so the full data set could then be analysed. The same analysis procedure was completed on both datasets and the results for both are shown in chapter 5.

4.1.1.2 | Event Selections

Basic event selections used in p–Pb collisions in ALICE were applied in this analysis. The data selected were collected using a minimum bias trigger, which requires at least one hit in both the V0A and V0C detectors. Also, a selection on the position of the PV of the interaction was made, requiring it to be within $\pm$ 10 cm from the centre of the detector along the z axis. Finally, an initial cut was placed to remove in-bunch pileup events using the SPD. Events were rejected if a secondary interaction vertex was found, separated from the first one by more than 0.8 cm along the beam (z) axis and with

- at least 3 associated tracklets for events with a total number of reconstructed tracklets, $N_{tracklets} \leq 20$,
- at least 4 associated tracklets for events with $20 < N_{tracklets} \leq 50$, or
- at least 5 associated tracklets for events with $N_{tracklets} > 50$,

where a 'tracklet' is defined as a track in the SPD between a cluster in the first layer and an accompanying cluster in the second layer that is aligned with the reconstructed PV.

In addition to the selections already mentioned, the data were also divided into classes defined by the multiplicity of the event. The multiplicity is determined from the amplitude in the V0A detector as described in section 3.2.5. As there is a particular interest in the multiplicity of the data, the classes were chosen to maximise the number of multiplicity bins that could be explored with the statistics available. The classes used in this analysis are listed in table 4.2, where the highest multiplicities are contained within the 0-5% class and the lowest multiplicities are contained within the 80-100%/60-100% class.

Table 4.2: Table showing V0A multiplicity classes used for cascades.

Particle	V0A Multiplicity Classes (%)
$\Xi^{\pm}$	0-5, 5-10, 10-15, 15-20, 20-30, 30-40, 40-50, 50-60, 60-80, 80-100
$\Omega^{\pm}$	0-5, 5-15, 15-30, 30-60, 60-100

Table 4.3 shows the number of events available for the analysis after the trigger selection and event selections have taken place for the two datasets analysed in this thesis.

Table 4.3: Table showing number of events for the two data sets analysed.

	No. Events	
	Low Interaction Dataset	Total Dataset
Total reconstructed events	15.9×10^6	60.0×10^6
Available after trigger selection	12.5×10^6	31.5×10^6
Available after event selections	11.4×10^6	29.0×10^6

4.2 | Signal Extraction

In order to extract the signal, the invariant mass of the cascades is plotted in the multiplicity classes described in table 4.2. The data are also divided into transverse momentum (p_T) bins so that spectra can be extracted. The bins used were selected to allow a spread of p_T to be studied, but ensuring the statistics are high enough for good signal extraction. In order to optimise the statistics available in this data sample, the particles and antiparticles were combined. Figure 4.4 shows the raw yields for both particles and antiparticles as a function of p_T. The results for particles and antiparticles are consistent with each other.

Previous analyses have combined particles and antiparticles when extracting yields from p_T spectra. Combining at this earlier stage allowed finer multiplicity and p_T bins to be explored and reduced the effect of statistical fluctuations. The chosen bins are described in table 4.4. The binning does not start at zero as the low momentum cascades can not be detected, as their decay products do not traverse the detectors due to the low radius

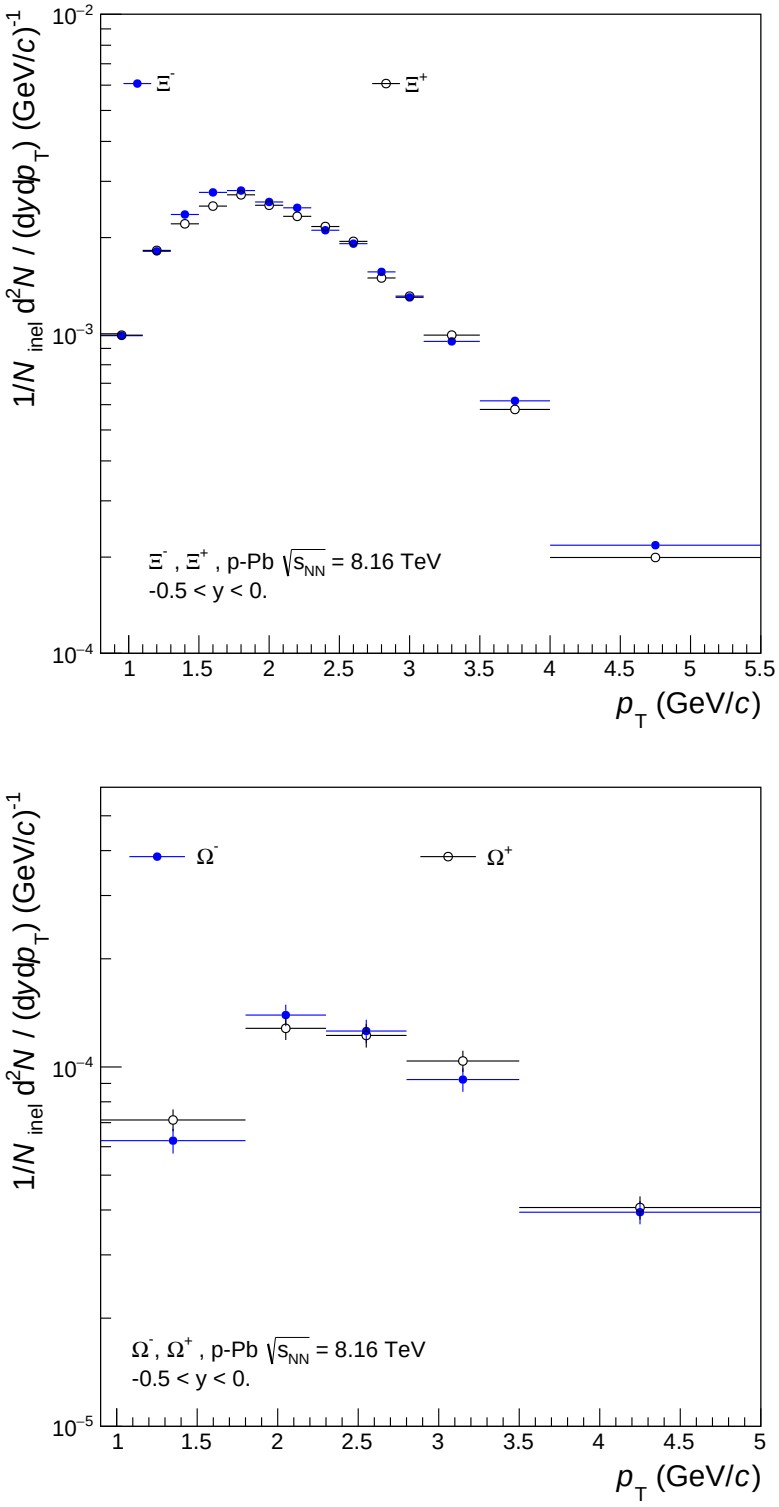

Figure 4.4: Plots showing raw yields for Ξ^- and $\overline{\Xi}^+$ (top) and Ω^- and $\overline{\Omega}^+$ (bottom). Open circles show particle results and closed circles show antiparticle results.

Table 4.4: Table showing p_T bins used for cascades.

Particle	p_T bins (GeV/c^2)
$\Xi^{\pm}$	0.8, 1.1, 1.3, 1.5, 1.7, 1.9, 2.1, 2.3, 2.5, 2.7, 2.9, 3.1, 3.5, 4, 5.5
$\Omega^{\pm}$	0.9, 1.6, 2.0, 2.4, 2.9, 3.5, 5.0

of the curvature of their path.

The binned data for each p_T and multiplicity bin are then fitted with a Gaussian plus second degree polynomial. A linear fit was not used due to the non-linear behaviour of the background in some of the invariant mass plots. A signal region is then defined as the number of σ (peak width) from the μ (mean) of the peak. For this analysis, this was chosen to be $\pm 4\sigma$ but the effect of the size of this window was explored in the systematic evaluations. The data are summed in the signal region in order to get the signal+background counts. The background fit is then integrated in the signal region in order to calculate and subtract the background and obtain the final signal value. An example of invariant mass plots for Ξ^- and Ω^- at high centrality and mid-p_T are shown in figure 4.5. The fit is shown in red and the signal region is highlighted by the vertical green lines.

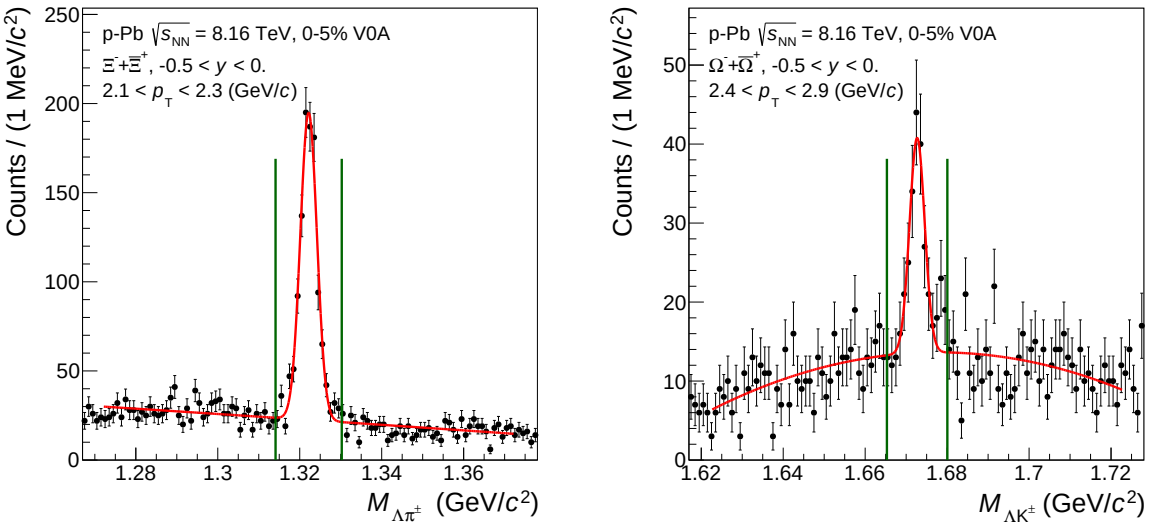

Figure 4.5: Plots showing examples of invariant mass for $\Xi^{\pm}$(left) and $\Omega^{\pm}$(right). The red line shows the gaussian + 2nd degree polynomial fit to the data and the green lines indicate the signal region.

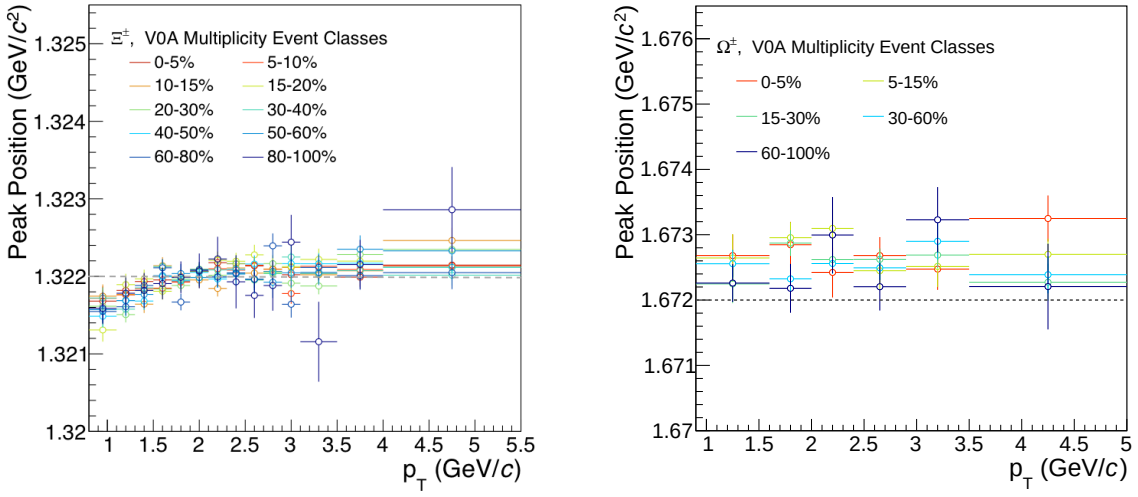

Figure 4.6: Plots showing peak position, μ, for $\Xi^{\pm}$(left) and $\Omega^{\pm}$(right) across p_T with results for different V0A multiplicity classes shown by the different colours. The dashed line shows the PDG mass.

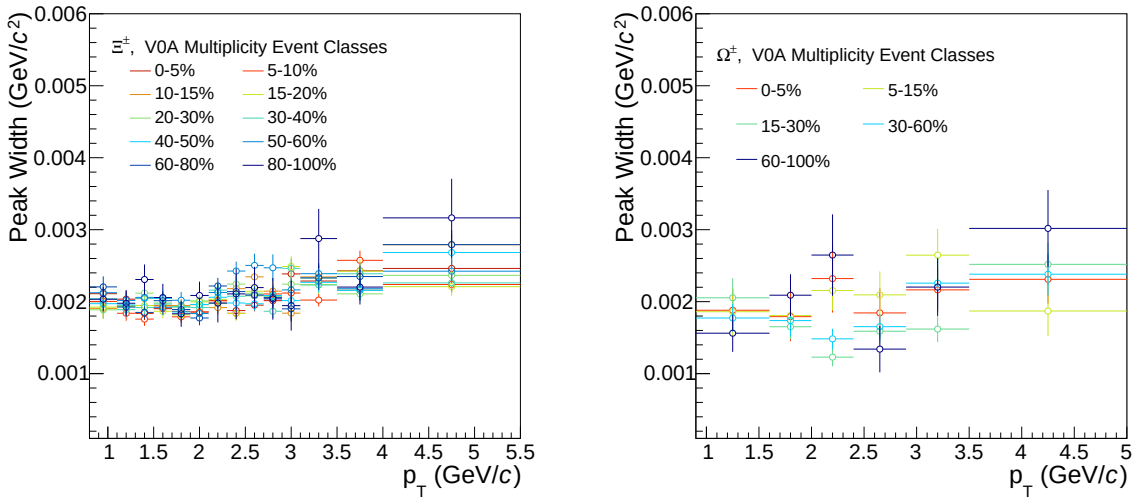

Figure 4.7: Plots showing peak width, σ, for $\Xi^{\pm}$(left) and $\Omega^{\pm}$(right) across p_T with results for different V0A multiplicity classes shown by the different colours.

In order to ensure the signal extraction is performing well in the chosen bins, μ and σ are extracted from the fits and are plotted as a function of p_T in figures 4.6 and 4.7 for $\Xi^{\pm}$ and $\Omega^{\pm}$. The position is in agreement with the PDG mass of the particles within 0.1% and the widths do not show a significant p_T dependence and are below 0.003 GeV/c^2 for both particles across all p_T.

4.3 | Monte Carlo Corrections

The signal extracted from the real data needs to be corrected in order to take into account the efficiency of the detectors, the efficiency of the reconstruction and selection methods used in the analysis, the acceptance cuts of the detector and the branching ratio of the decay channels not considered.

Samples of simulated p–Pb collisions were used for efficiency calculations. The simulated data were created using the event generators EPOS-LHC [119] (described in section 2.2.5) and DPMJET [165], which is based on the Dual Parton Model [166]. They are then propagated through the simulated ALICE detector using GEANT4 [167].

The efficiencies are estimated by repeating the same analysis on simulated data and comparing the results to the known generated cascades. The only way the analyses differ is the Monte Carlo (MC) cascade candidates are checked to ensure they are associated with a true generated cascade. The efficiency of the p_T bin is then computed as

$$\epsilon(p_T) = \frac{N_{reconstructed+associated}(p_T)}{N_{generated}(p_T)}. \tag{4.6}$$

The generated distributions can be extracted from the MC data. As the production rates of cascades are small and the generation and propagation of MC events are computationally intensive, two methods were used to increase the statistics of cascades available in the data set. In an injected sample, up to five cascade signals are injected per event before they are propagated. In a triggered sample, the event was only propagated if the event generated at least one multi-strange baryon. The efficiency values obtained with the injected and triggered samples were compared to two general purpose productions (with no injection or triggering).

Figure 4.8 shows a comparison of all MC data sets. The bottom panel shows the ratio of each data set to the fully merged sample of all the MC datasets. The injected sample is

in agreement with the general purpose MC data, however the triggered sample (shown by full turquoise circles) shows significant deviations to the other datasets, especially at low p_T, so was discarded. Deviations were attributed to errors in the MC configuration of the sample, but further investigation would be required to confirm the source of the deviations. The results for the two general purpose and injected sample are consistent, therefore, the samples were merged in order to provide the maximum statistics for efficiency calculations. After merging there were ≈ 1 million events available in the MC sample.

4.3.1 | Multiplicity Dependence

The efficiency values are calculated as a function of p_T. However, it is also important to check if there is a multiplicity dependence. This is done by dividing the Monte Carlo data into multiplicity bins and recalculating the efficiency values in the same way. Figure 4.9 shows the efficiency values plotted against p_T for different multiplicity classes, compared to the efficiency values in the whole 0-100% multiplicity-integrated data. Within uncertainties there is no significant multiplicity dependence, so the multiplicity-integrated values are used for the analysis.

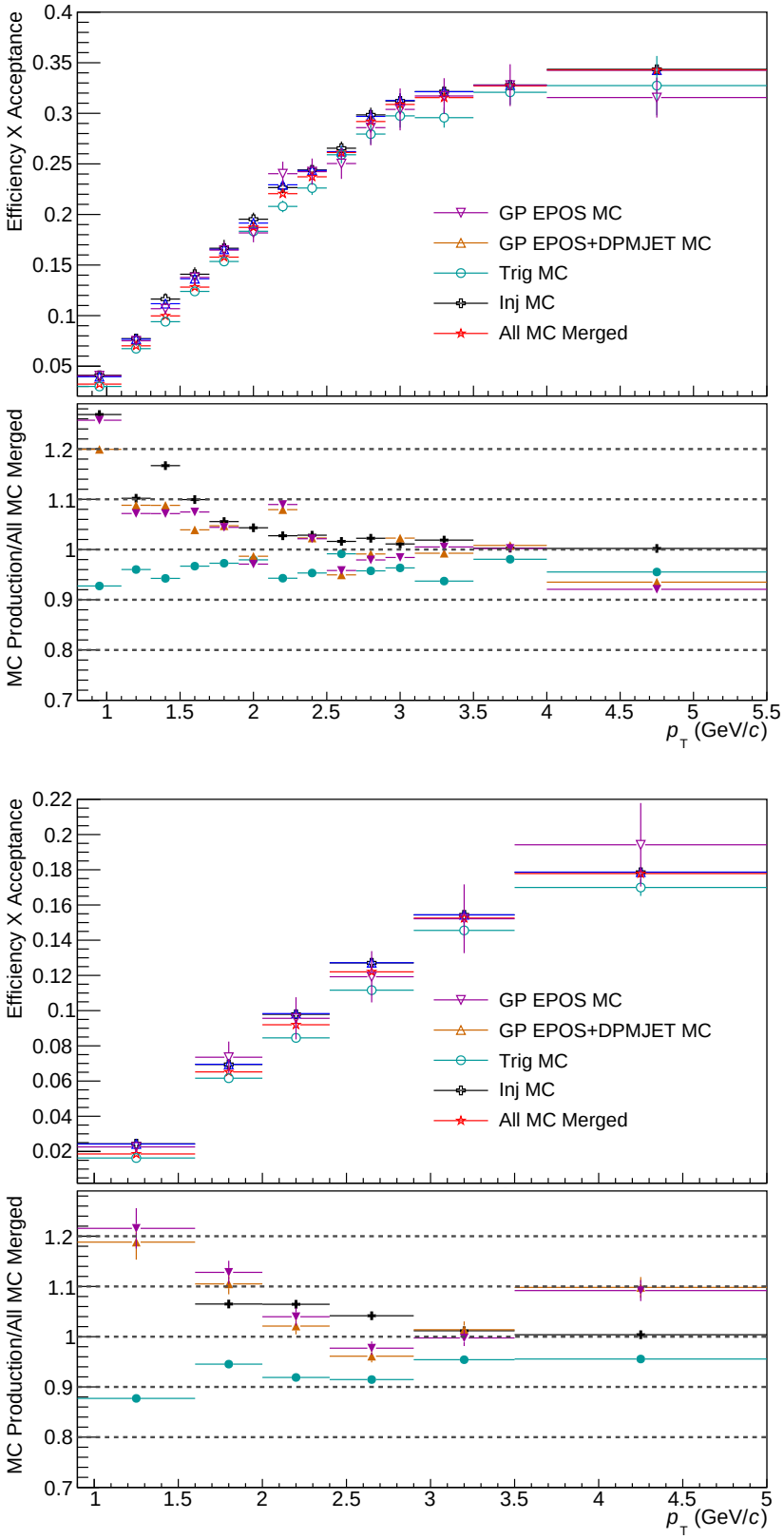

Figure 4.8: Plots showing comparison of efficiency values obtained from different MC data samples for Ξ^-(above) and Ω^-(below). The bottom panel shows the ratio of each data set to the merged sample. The only sample whose ratio deviates, indicated by the closed green circles, is the DMPJET triggered sample.

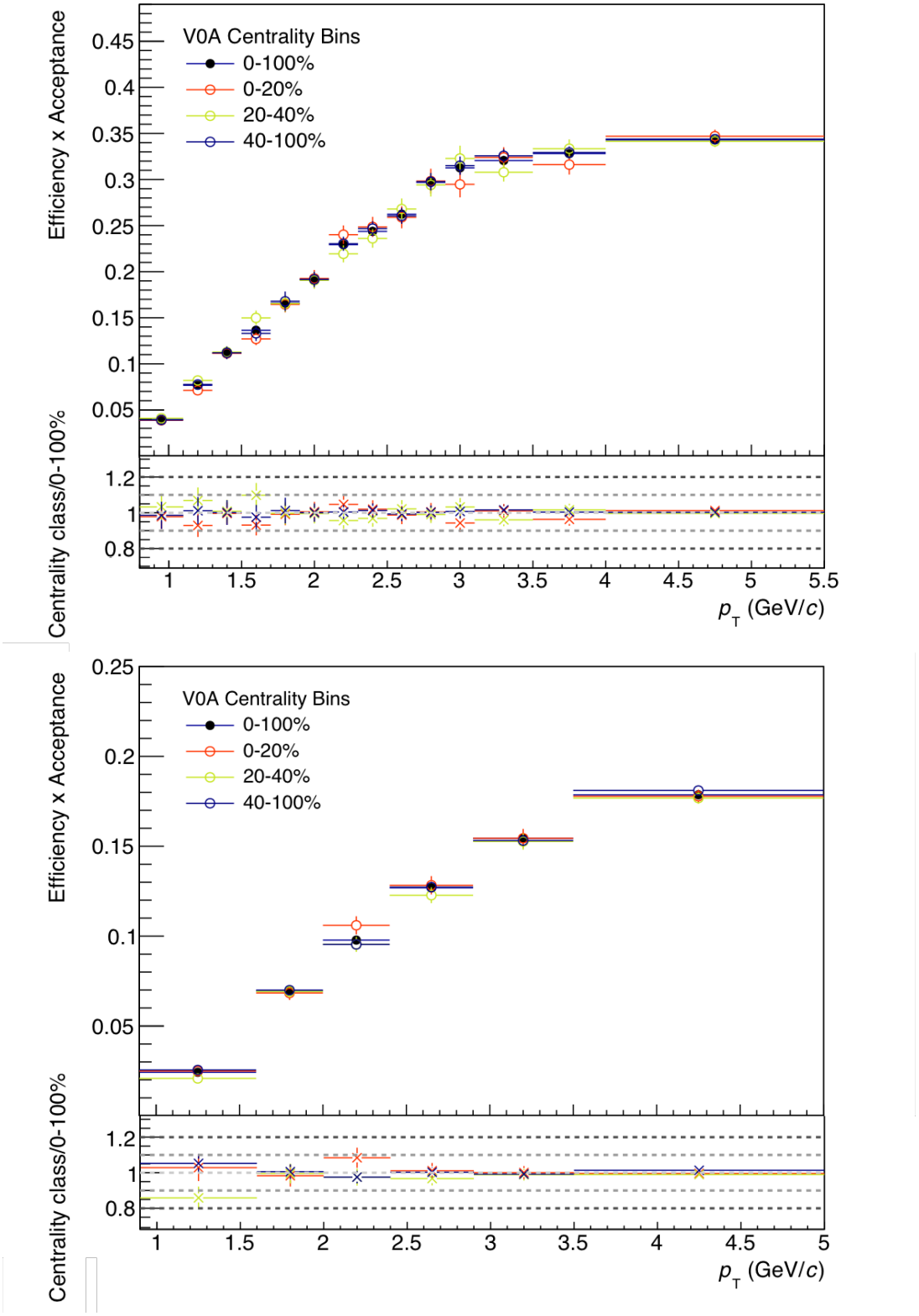

Figure 4.9: Plots showing multiplicity dependence of efficiency values for Ξ^-(above) and Ω^-(below). The bottom panel shows the ratio of each centrality class to the full 0-100% multiplicity-integrated values.

4.4 | Signal Optimisation

The initial topological and kinematic cuts, discussed in section 4.1, are placed loosely to remove a significant amount of background, and therefore reduce the size of the output data files for analysis, but still allow a study of the effect of the cuts on the signal to choose the optimum value for the default cuts and to evaluate systematic uncertainties from the cuts.

When selecting default cut values, the goal was to minimise the background while maximising the signal and therefore increasing the signal to noise ratio. This can be done by studying a few quantities in the data. Firstly, the signal significance can be calculated as

$$\text{Significance} = \frac{signal}{\sqrt{signal + background}}. \tag{4.7}$$

This value can be maximised to optimise the signal-to-noise ratio (SNR) but is safer (than SNR) as it avoids the possibility of division by zero in the case of no background.

The other quantity to be checked is

$$\text{Signal loss} = 1 - \frac{signal(chosen\ cut)}{signal(loosest\ cut)}, \tag{4.8}$$

which shows the amount of signal lost due to the applied cut with respect to the loosest value already applied in the data. This is checked while keeping all other cuts at default values for the analysis. As multiple rescatterings are more likely at low p_T, the signal significance and signal losses were checked in three different p_T bins in order to check if a p_T dependent cut was required. The default cut was chosen to maximise signal significance, while keeping signal losses below 2%. Values for the default cuts chosen for the analysis are shown in table 4.5 for $\Xi^{\pm}$ and $\Omega^{\pm}$.

Table 4.5: Values of the default cuts chosen for $\Xi^{\pm}$ and $\Omega^{\pm}$. If a different cut was used for $\Omega^{\pm}$ it is shown in brackets. If a p_T dependent cut was required, three values are shown corresponding to low, mid and high p_T corresponding to 0.8-1.9 (0.9-2.0) GeV/c, 1.9-3.1 (2.0-2.9) GeV/c and 3.1-5.5 (2.9-5.0) GeV/c.

Default Cuts	Cut value $\Xi^{\pm}(\Omega^{\pm})$
V0 cos(PA)	$>$ 0.98 (0.97,0.98,0.98)
Cascade cos(PA)	$>$ 0.96,0.97,0.97
DCA Casc daughters (cm)	$<$ 1.6,1.5,1.4
DCA V0 daughters (σ)	$<$ 1.7,1.6,1.5 (1.7,1.6,1.6)
Cascades's decay radius (cm)	$>$ 0.6 (0.5)
V0's decay radius (cm)	$>$ 1.2 (1.1)
DCA bachelor-PV (cm)	$>$ 0.04
DCA V0-PV (cm)	$>$ 0.06
DCA V0's meson daughter - PV (cm)	$>$ 0.04
DCA V0's baryon daughter - PV (cm)	$>$ 0.03
V0 mass window (MeV/c^2)	$\pm$ 0.008
Signal extraction window (σ from mass peak)	$\pm$ 4
TPC PID (σ from Bethe-Bloch curve)	$\pm$ 4
Least number of TPC clusters	$\geq$ 70
Deviation from proper lifetime (no. PDG $c\tau$)	$<$ 3

4.5 | Systematic Uncertainty Evaluations

Values for loose and tight cuts were also chosen in order to evaluate the uncertainty on the possible bias introduced from the positioning of the cuts at the default locations. Loose (and very loose) cuts were applied at looser values than the default cut if available. Tight cuts were chosen to be placed at 5% signal loss and very tight cuts were chosen to be placed at 10% signal loss. All cuts were adjusted if there were deviations in the signal loss between MC and real data of more than 2% as this would introduce bias in the corrected spectra.

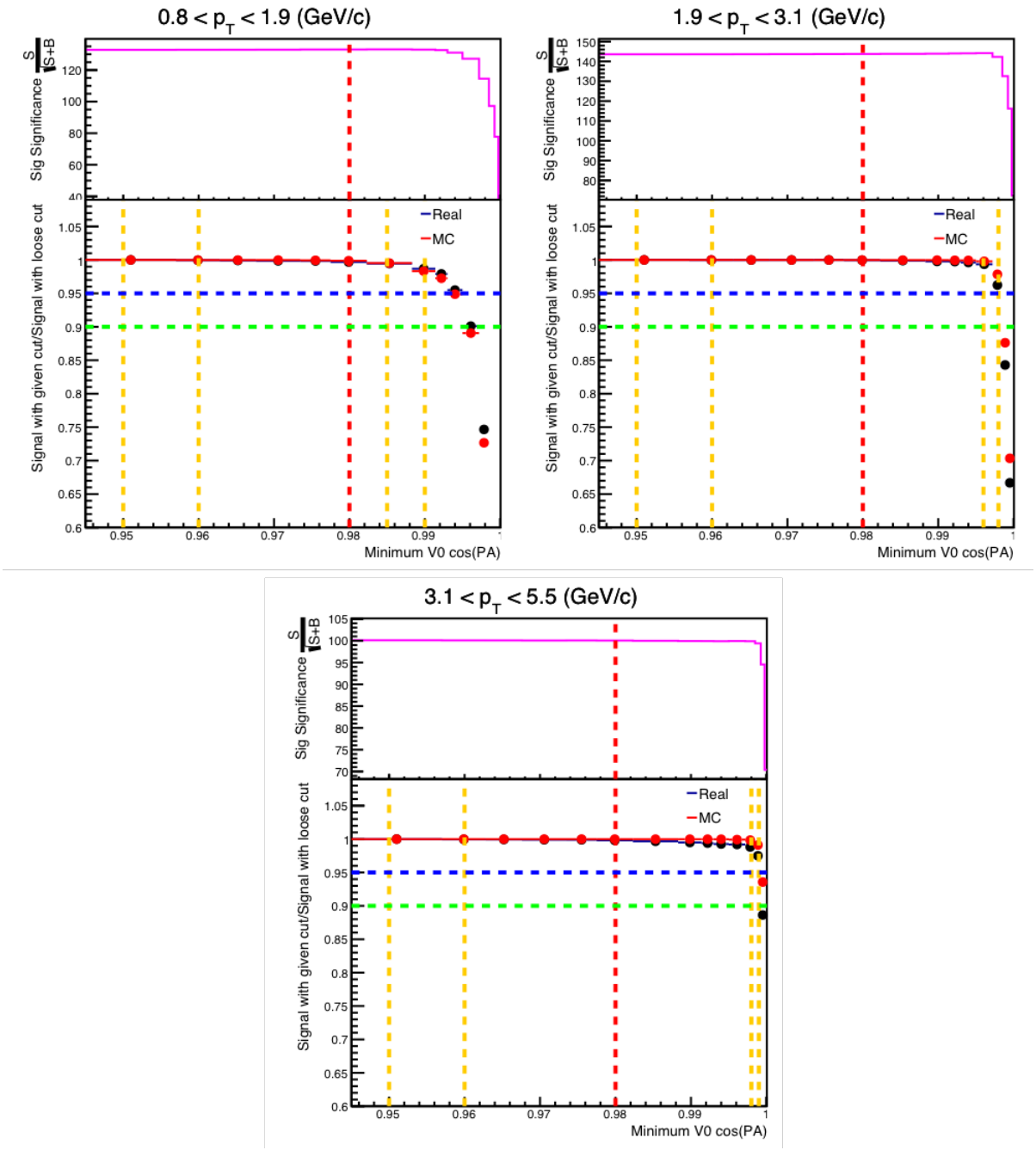

Figure 4.10: For each plot, the top shows Signal Significance and the bottom shows Signal losses, with respect to the loosest cut considered for Minimum V0 cos(PA). The $\Xi^{\pm}$data are divided into low (top-left), mid (top-right) and high (bottom) p_T bins. Black markers are for real data and red markers are for MC data. Red vertical line indicates default cut and orange vertical lines show loose/tight cuts.

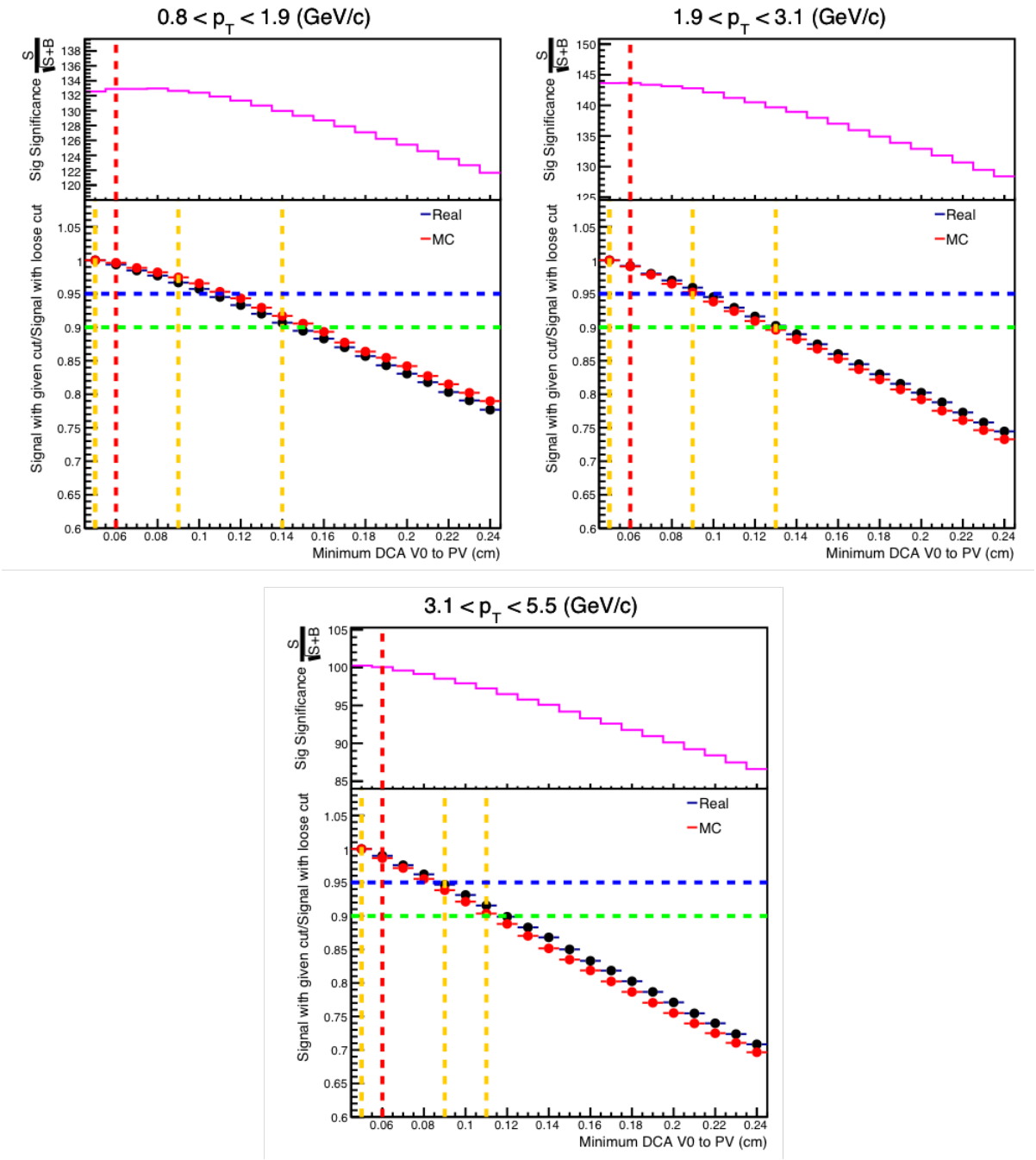

Figure 4.11: For each plot, the top shows Signal Significance and the bottom shows Signal losses, with respect to the loosest cut considered for Minimum DCA V0 to PV. The $\Xi^{\pm}$data are divided into low (top-left), mid (top-right) and high (bottom) p_T bins. Black markers are for real data and red markers are for MC data. Red vertical line indicates default cut and orange vertical lines show loose/tight cuts.

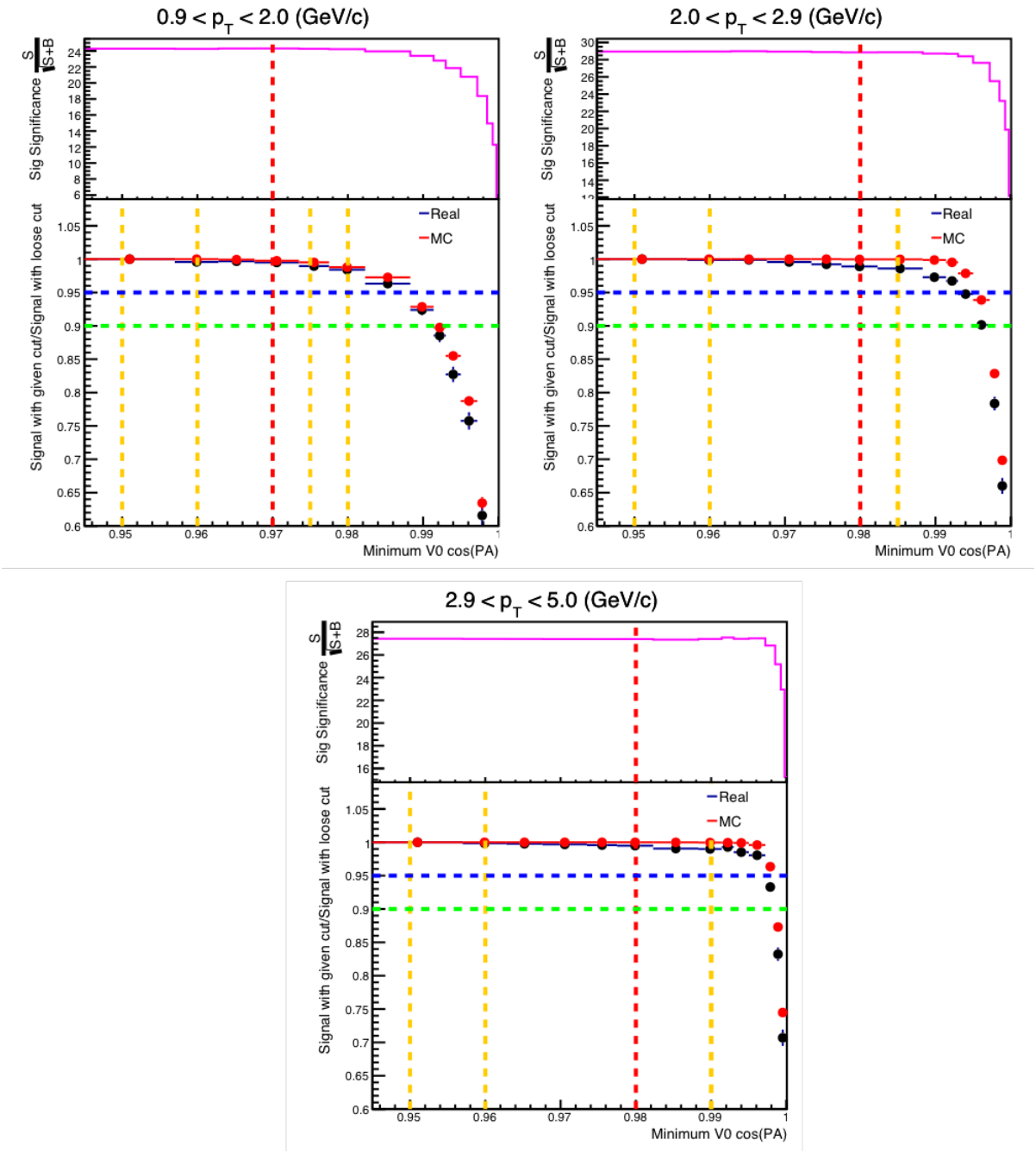

Figure 4.12: For each plot, the top shows Signal Significance and the bottom shows Signal losses, with respect to the loosest cut considered for Minimum V0 cos(PA). The $\Omega^{\pm}$data are divided into low (top-left), mid (top-right) and high (bottom) p_T bins. Black markers are for real data and red markers are for MC data. Red vertical line indicates default cut and orange vertical lines show loose/tight cuts.

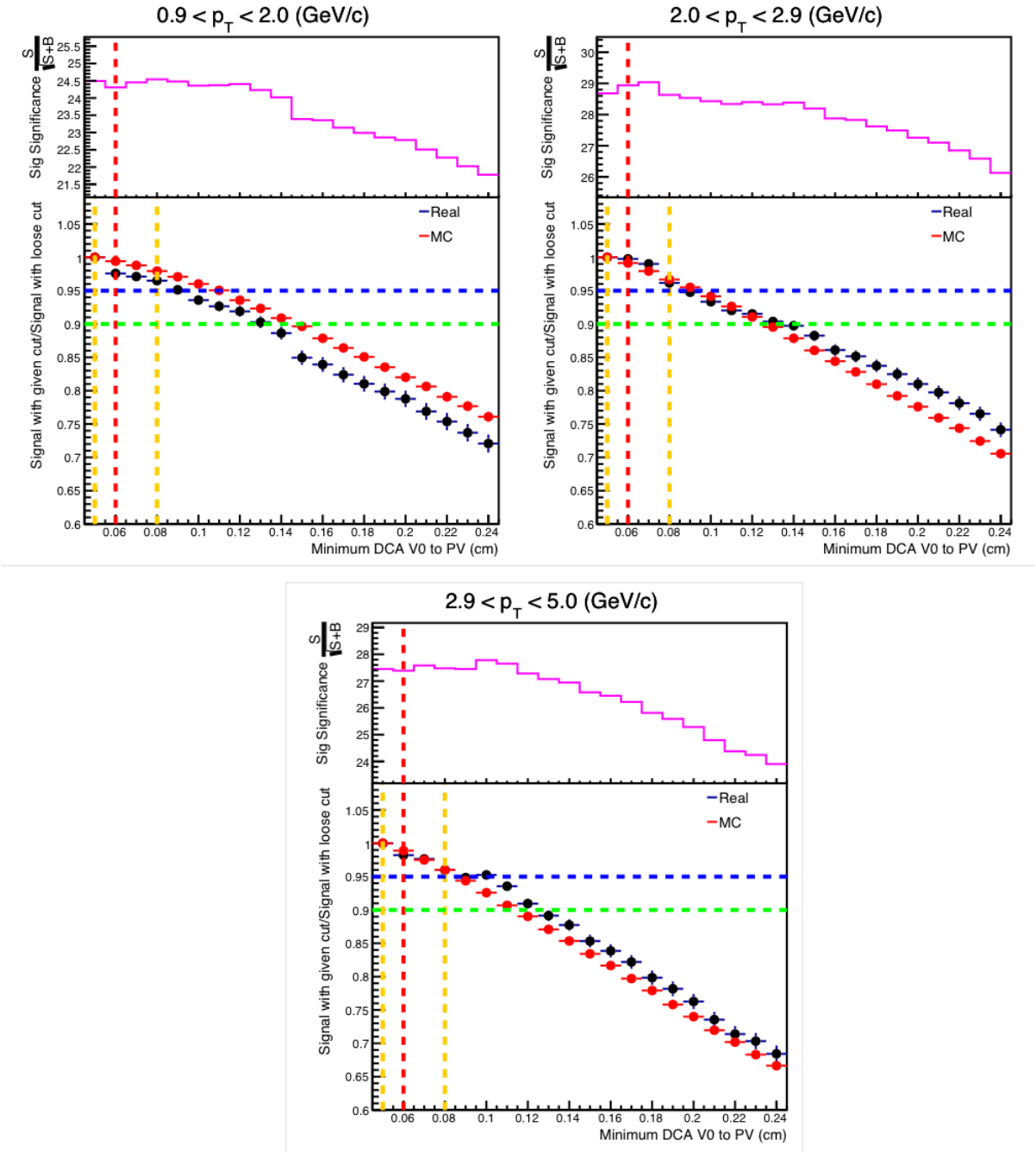

Figure 4.13: For each plot, the top shows Signal Significance and the bottom shows Signal losses, with respect to the loosest cut considered for Minimum DCA V0 to PV. The $\Omega^{\pm}$data are divided into low (top-left), mid (top-right) and high (bottom) p_T bins. Black markers are for real data and red markers are for MC data. Red vertical line indicates default cut and orange vertical lines show loose/tight cuts.

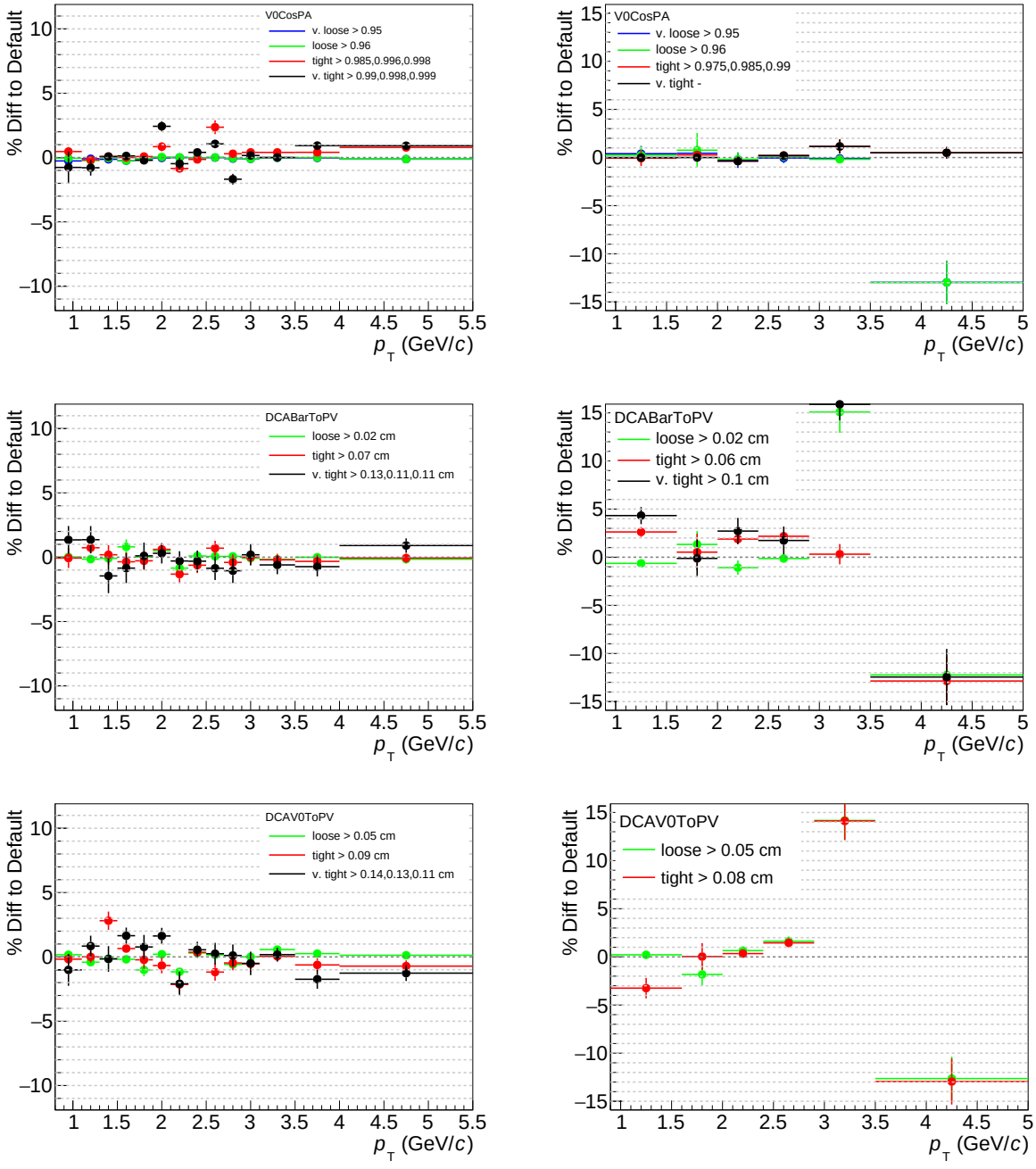

Figure 4.14: Signal deviations seen in corrected $\Xi^{\pm}$ (left) and $\Omega^{\pm}$ (right) spectra due to cut selection changes. The top row shows the results with the minimum V0 cos(PA) cuts, the middle row shows the results with the cuts on the minimum DCA between the baryon V0 daughter and the PV and the bottom row shows the results with the cuts on the minimum DCA between the V0 and the PV. Error bars are Roger-Barlow errors representing an acceptable deviation due to statistical fluctuations.

The plots used for the selection of cuts for some key variables are shown in figures 4.10 and 4.11 for $\Xi^{\pm}$ and 4.12 and 4.13 for $\Omega^{\pm}$. In each plot, the signal significance is shown in the top panel by the pink line, and the signal loss fraction is shown in the bottom panel with the black points indicating results for real data and the red points indicating results for MC data. The default cuts are shown by the vertical dashed red line and the cuts chosen for systematic studies are indicated by the orange vertical dashed lines. The final cuts used are reported in table 4.6 for $\Xi^{\pm}$and 4.7 for $\Omega^{\pm}$. The plots for all variables can be found in appendix A.

Using the cuts chosen, the signal was recomputed for each cut position and the relative deviations with respect to the default cuts are shown for the same variables shown previously as a function of p_T in figure 4.14 for $\Xi^{\pm}$and $\Omega^{\pm}$. These signal deviations for the remaining variables can be found in appendix B. The errors on the deviations are calculated as Roger Barlow errors [168], $\sigma_B^2 = \sigma_2^2 - \sigma_1^2$, where σ_2 and σ_1 are the errors on the signal calculated with the default cut and the systematic check cut. The deviations are considered significant, only if they are larger than one σ_B, which disregards statistical fluctuations that do not contribute to the systematic uncertainty.

On top of the systematic errors already discussed, a further systematic error was added due to the uncertainty of the material budget (amount of material in the detector). This was estimated using Monte Carlo productions with variations in the material budget of the detector within the MC simulation. The uncertainty on the measurement due to the uncertainty on the material budget could then be estimated. Five productions were used with a change in material budget of: +4.5%, +10%, 0%, -4.5% and -10% [146]. 4.5% corresponds to the uncertainty on the material budget in ALICE, as estimated from previous analyses of photon conversions [153, 169]. The variation was raised to 10% in two of the productions to increase the effect and better estimate the contribution to the error, however, the result were normalised to 0.45 to estimate the variation due to the

expected ±4.5% material budget uncertainty. The ratio of the efficiency values with and without a material budget change was then computed. The uncertainty was estimated to be half the deviation from one of the ratio of the yields calculated with a change in material budget to the yields without any change. The final uncertainty values used in the analysis are shown in figure 4.15.

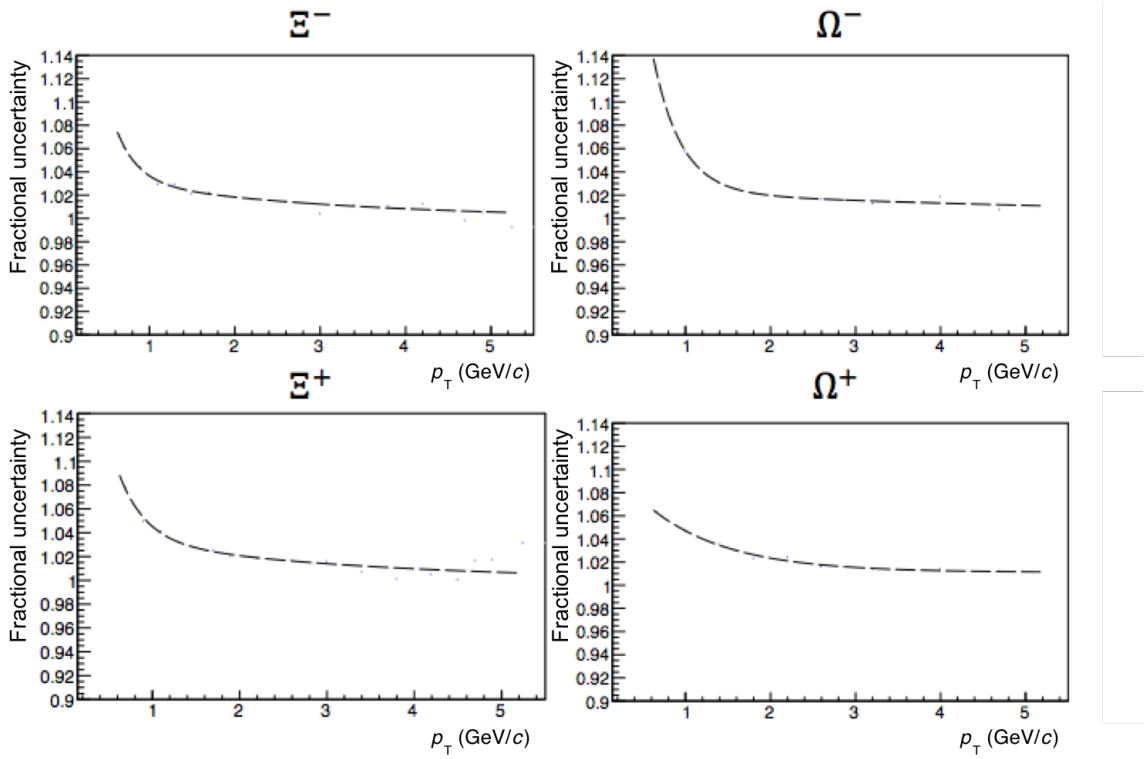

Figure 4.15: Material Budget uncertainty as a function of p_T for $\Xi^{\pm}$ and $\Omega^{\pm}$ [170].

Table 4.6: Values of the selection cuts chosen for systematic error estimation in the case of $\Xi^{\pm}$. If a p_T dependent cut was required, three values are shown corresponding to low, mid and high p_T corresponding to <1.9 GeV/c, 1.9-3.1 GeV/c and >3.1 GeV/c.

Syst Type	Cut value			
	very loose	loose	tight	very tight
V0 cos(PA)	$>$ 0.95	$>$0.96	$>$ 0.985, 0.996, 0.998	$>$ 0.99, 0.998, 0.999
Cascade cos(PA)	$>$ 0.95	$>$ 0.95, 0.96, 0.96	$>$ 0.965, 0.985, 0.985	$>$ 0.97, 0.992, 0.992
DCA bachelor-V0 (cm)	$<$ 2.0	$<$ 1.8	$<$ 1.4, 1.0, 0.9	$<$1.2, 0.8, 0.7
DCA V0 daughters (σ)	$<$ 2.0	$<$ 1.9, 1.8, 1.8	$<$ 1.5, 0.9, 0.6	$<$ 1.3, 0.8, 0.4
Cascades's decay radius (cm)	-	$>$ 0.5	$>$ 1., 1.4, 2.	$>$ 1.4, 2., 3.
V0's decay radius (cm)	-	$>$ 1.1	$>$ 3., 5.5, 7.	-
DCA bachelor-PV (cm)	-	$>$ 0.03	$>$ 0.11	$>$ 0.19
DCA V0-PV (cm)	-	$>$ 0.05	$>$ 0.09	$>$ 0.14, 0.13, 0.11
DCA V0's meson daughter - PV (cm)	$>$ 0.02	$>$ 0.03	$>$ 0.24	$>$ 0.42, 0.5, 0.5
DCA V0's baryon daughter - PV (cm)	-	$>$ 0.02	$>$ 0.07	$>$ 0.13, 0.11, 0.11
V0 mass window (MeV/c^2)	-	$\pm$0.009	$\pm$0.006	-
Signal extraction window (σ from mass peak)	-	$\pm$5.0	$\pm$3.0	-
TPC PID (σ from Bethe-Bloch curve)	-	$\pm$5	$\pm$3.5	-
Least number of TPC clusters	-	-	$\geq$75	$\geq$80
Deviation from proper lifetime (no. PDG $c\tau$)	-	$<$ 4	$<$ 2	-

Table 4.7: Values of the selection cuts chosen for systematic error estimation in the case of $\Omega^{\pm}$. If a p_T dependent cut was required, three values are shown corresponding to low, mid and high p_T corresponding to <2.0 GeV/c, 2.0-2.9 GeV/c and >2.9 GeV/c.

Syst Type	Cut value			
	very loose	loose	tight	very tight
V0 cos(PA)	>0.95	> 0.96	> 0.975, 0.994, 0.996	> 0.98, 0.994, 0.996
Cascade cos(PA)	> 0.95	> 0.95, 0.96, 0.96	> 0.965, 0.985, 0.98	>0.97,0.992,0.985
DCA bachelor-V0 (cm)	< 2.0	< 1.8	< 1.4, 1.0, 1.0	< 1.2, 0.8, 0.8
DCA V0 daughters (σ)	<2.0	< 1.9, 1.8, 1.8	< 1.5, 1.4, 1.4	< 1.3, -, -
Cascades's decay radius (cm)	-	> 0.5	> 0.6, 0.9, 1.0	-
V0's decay radius (cm)	-	> 1.1	> 2., 2.5, 5.	-
DCA bachelor-PV (cm)	-	> 0.03	> 0.06	> 0.09, 0.09, -
DCA V0-PV (cm)		> 0.05	> 0.08	> 0.1, -, -
DCA V0's meson daughter - PV (cm)	> 0.02	> 0.03	> 0.11, 0.06, 0.15	-
DCA V0's baryon daughter - PV (cm)	-	> 0.02	> 0.06	> 0.1
V0 mass window (MeV/c^2)	-	$\pm$0.009	$\pm$0.006	-
Signal extraction window (σ from mass peak)	-	$\pm$5.0	$\pm$3.0	-
TPC PID (σ from Bethe-Bloch curve)	-	$\pm$5	$\pm$3.5	-
Least number of TPC clusters	-	-	$\geq$75	$\geq$80
Deviation from proper lifetime (no. PDG $c\tau$)	-	< 4	< 2.	-
Ξ rejection (MeV/c^2 from Ξ hypothesis)	-	none	-	-

The total systematic errors were evaluated, by adding all uncertainties considered in quadrature. A smoothing procedure was then applied to the total systematic errors in order to remove any bin-by-bin fluctuations, which were not caused by the physics or the detector. A summary of the topological systematic errors for $\Xi^{\pm}$ is shown in figure 4.16 on the left, with the total systematic errors shown on the right. For $\Omega^{\pm}$, the calculated errors in the two highest p_T bins, using the procedure explained, were still significantly affected by statistical fluctuations. This can be seen in the plots of the error differences shown previously in figure 4.14, as well as the figures in appendix B. As shown in figure 4.17, the systematic errors calculated in the first four p_T bins in this analysis were consistent with those measured at $\sqrt{s_{NN}} = 5.02$ TeV, which was not as limited by statistics with ten times the events. This is expected, due to the very similar analysis procedure and experimental setup. Therefore, the systematic errors from the previous analysis were used for the final two p_T bins [171], which are approximately the same size in both analyses. A future reanalysis would combine high p_T bins to obtain better statistics that lead to more stable results in a cut study analysis. This would allow for a better estimation of the systematic errors at high p_T. The final step was to apply the same smoothing procedure used for the $\Xi^{\pm}$ to the $\Omega^{\pm}$ total errors. The topological and total errors for $\Omega^{\pm}$ are shown in figure 4.18.

The dominant source of error across all p_T bins for both $\Xi^{\pm}$ and $\Omega^{\pm}$ is the topological errors. At low p_T the material budget is another significant source which reduces at high p_T. The number of σ used for TPC PID also dominates at low p_T whereas, in the case of the $\Xi^{\pm}$, at high p_T, the signal extraction is more significant.

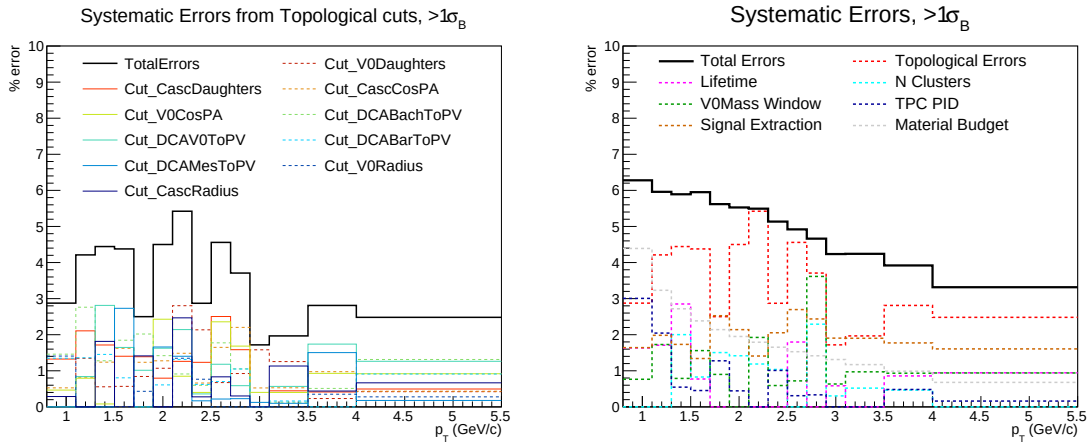

Figure 4.16: Systematic errors due to topological cuts (left) and total systematic errors (right) computed for $\Xi^{\pm}$.

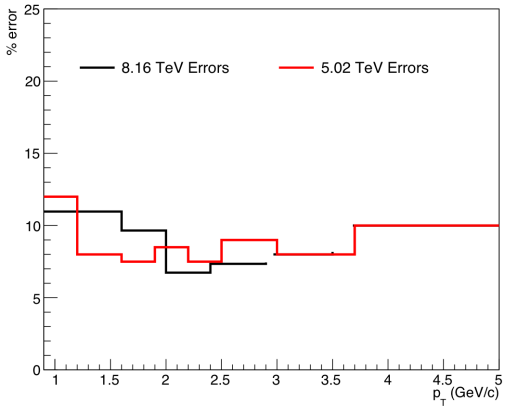

Figure 4.17: Total systematic errors for $\Omega^{\pm}$in this analysis at $\sqrt{s_{NN}} = 8.16$ TeV in black, up to $p_T = 3$ GeV/c, and the analysis at $\sqrt{s_{NN}} = 5.02$ TeV in red.

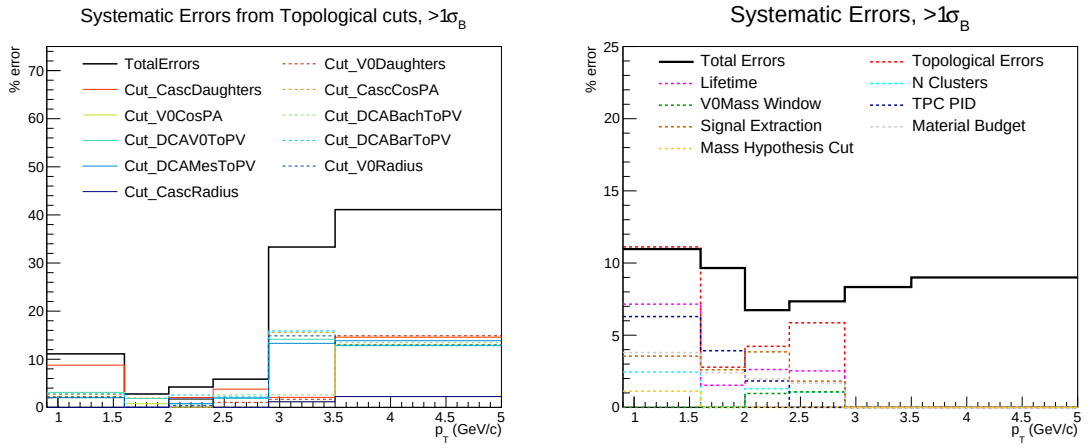

Figure 4.18: Systematic errors due to topological cuts (left) and total systematic errors (right) computed for $\Omega^{\pm}$.

Chapter 5

Results

In this chapter, the results for multi-strange baryon production in proton–lead collisions at $\sqrt{s_{NN}} = 8.16$ TeV will be presented and discussed. Results for integrated yields and mean p_T will be shown. The first section will present the initial results obtained with the low interaction rate dataset that were presented by the author at The International Conference on Strangeness in Quark Matter 2019 [172] and the International Nuclear Physics Conference 2019 [173]. In the second section, the developments achieved from analysing the full dataset will be given. The next chapter will put these results into context by making comparisons between the current analysis and analyses of other hadrons, as well as comparisons to results in other collision systems and the lower energy Run 1 results.

5.1 | Low Interaction Rate Data

5.1.1 | Transverse momentum spectra

Following the procedure described in the previous chapter, the fully corrected transverse momentum spectra for $\Xi^{\pm}$ and $\Omega^{\pm}$ were obtained and are shown in figure 5.1

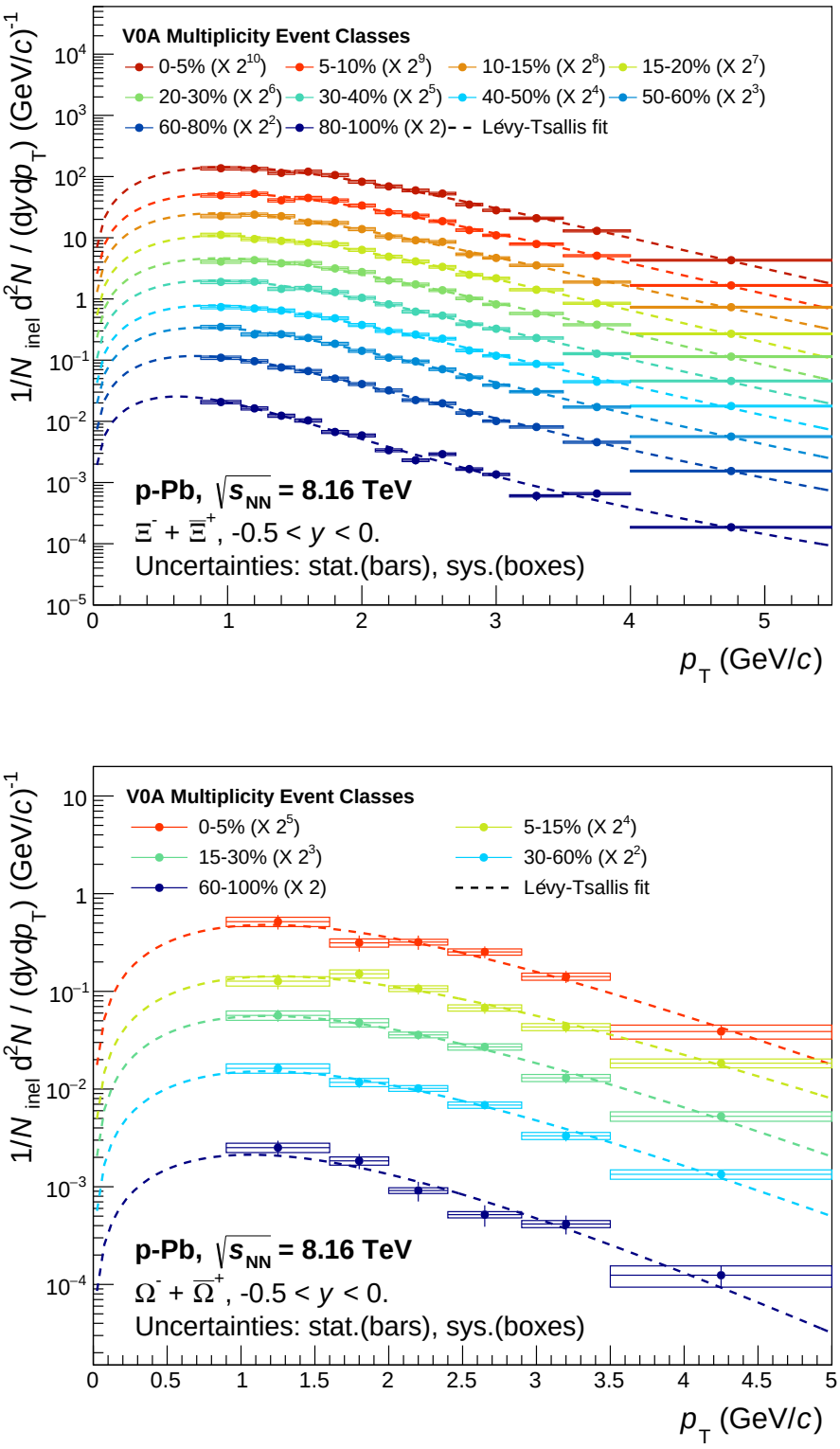

Figure 5.1: Plots showing p_T spectra for $\Xi^{\pm}$ (above) and $\Omega^{\pm}$ (below) for different V0A multiplicity classes with Lévy-Tsallis fits [133] shown by dashed lines.

for the different V0A multiplicity bins. An additional correction was applied to take into account the influence of the Monte Carlo p_T shape on the efficiency values calculated. This correction is discussed in section 5.1.1.1. The final p_T spectra are fitted with a Lévy-Tsallis function [133] which is shown in the plots by the dashed lines.

5.1.1.1 | p_T shape effect

At low and high p_T, wider p_T bins were used in order to reduce the effect of statistical fluctuations in these regions. This is most significant at low p_T, where the majority of the signal is contained, so in this region the spectra can be influenced by the p_T shape of the Monte Carlo data. If this deviates from the shape of the measured spectra, this can cause biases in the corrected spectra. The iterative procedure described here was used to correct this bias. The shape of the p_T spectra have strong multiplicity dependence, so a multiplicity-dependent correction needs to be applied.

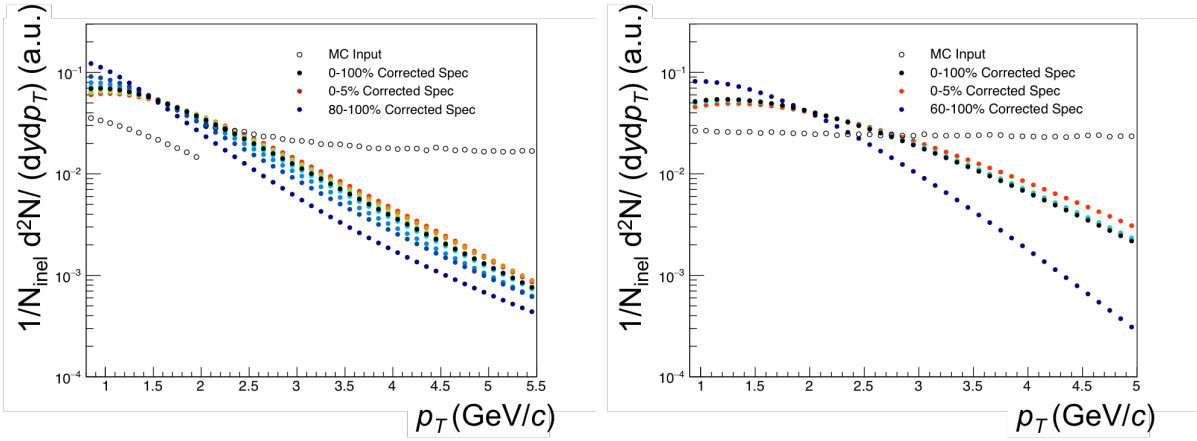

Figure 5.2: Plots showing a comparison of p_T shapes of Monte Carlo input data and a Lévy-Tsallis fit of measured data for $\Xi^{\pm}$ (left) and $\Omega^{\pm}$ (right).

The p_T shapes were initially checked for both $\Xi^{\pm}$ and $\Omega^{\pm}$ baryons by fitting the data and Monte Carlo with a Lévy-Tsallis function [133]. A p_T spectra for each multiplicity was then produced using high granularity. The resulting p_T shapes for $\Xi^{\pm}$ and $\Omega^{\pm}$ baryons are shown in figure 5.2. The black open points shows the Monte Carlo shape in

comparison to the real data, indicated by the full coloured points, in different multiplicity classes. From the plots, it is clear that the Monte Carlo p_T shape differs from the real data as a function of multiplicity. The jump at 2 GeV/c^2 in the $\Xi^{\pm}$ spectra is due to the injection procedure, which is only carried out for particles with a $p_T > 2$ GeV/c^2 for $\Xi^{\pm}$. In order to remove this bias, an iterative procedure was applied to the corrected spectra.

Firstly, the ratio of the fitted shapes of the real data over the Monte Carlo input data were computed at high granularity (higher than used in the analysis). The ratios were used to reweight the MC reconstructed and generated p_T spectra used in the analysis. The resulting new efficiency values were then recalculated by rebinning the reweighted p_T spectra into the p_T bins used in the analysis. The correction factors are calculated from the ratio of the new efficiency values to the old ones and are applied to the measured spectra.

These steps were repeated iteratively until convergence, which was achieved after two iterations. The results of this procedure for $\Xi^{\pm}$ and $\Omega^{\pm}$ are shown in figures 5.3 and 5.4, with each row showing a new iteration. The left panel shows the reweighting factors calculated in the first step and the right panel shows the correction factors applied in the final step. The correction factors approach one as the procedure is repeated.

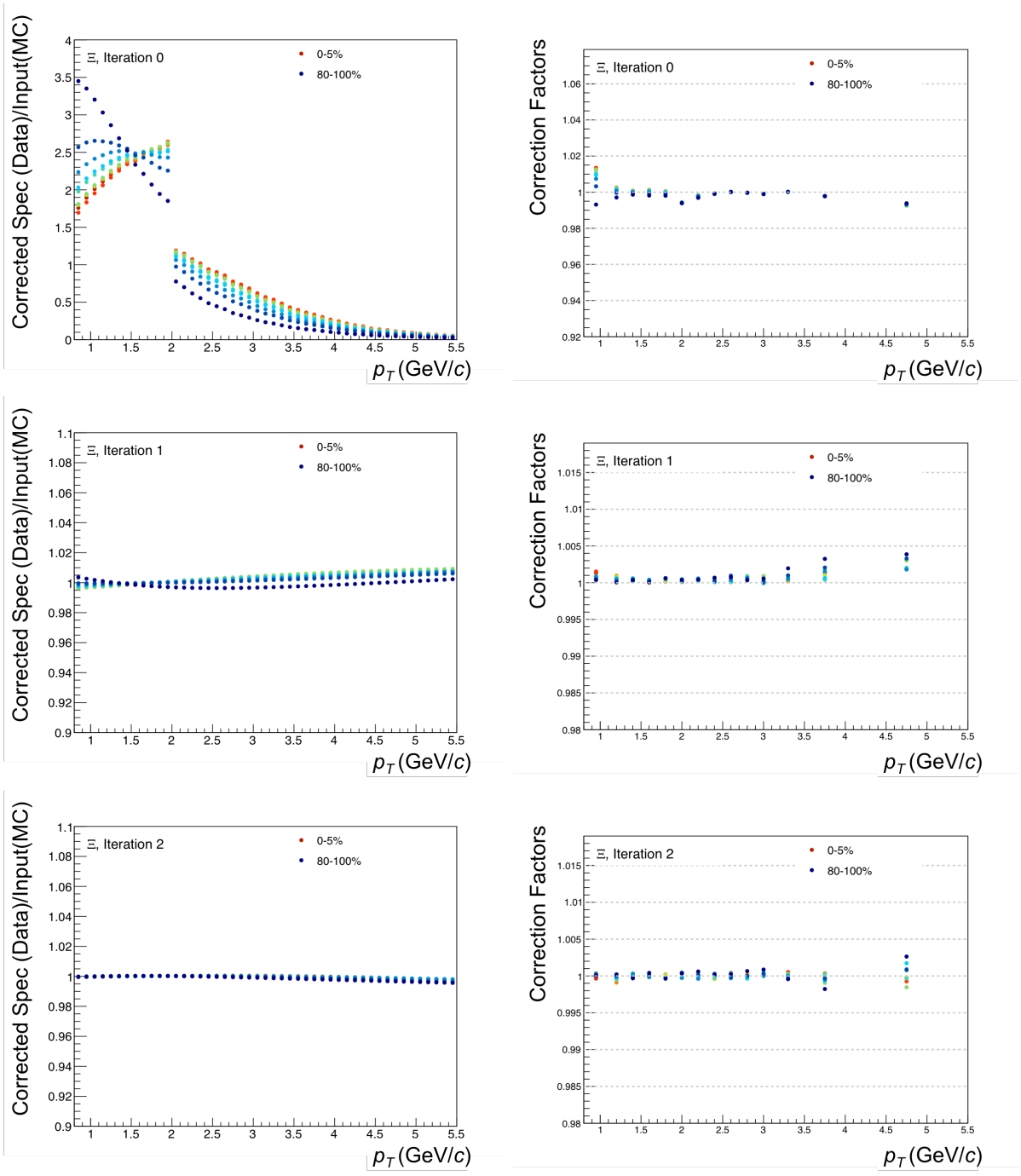

Figure 5.3: Plots showing the reweighting values (left) and correction factors (right) applied in each stage of the iterative procedure for the Ξ^- spectra.

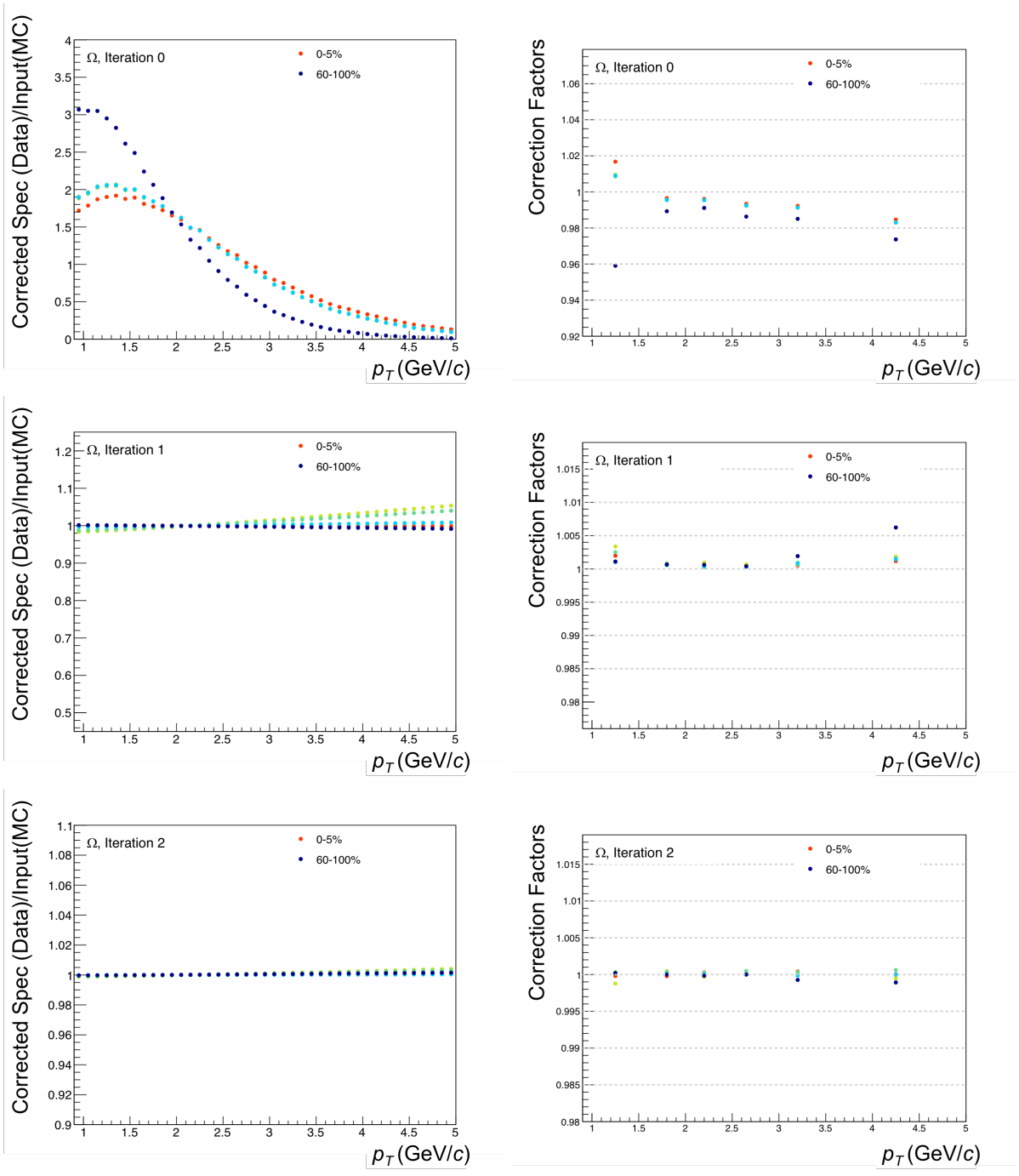

Figure 5.4: Plots showing the reweighting values (left) and correction factors (right) applied in each stage of the iterative procedure for the Ω^- spectra.

5.1.2 | Multiplicity dependence of yields and $< p_T >$

In order to calculate the integrated yields and $\langle p_{\mathrm{T}} \rangle$, two contributions were combined: the measured data points were summed together and the integral under the Lévy-Tsallis fit [133] was calculated in the unmeasured regions at low and high p_T.

5.1.2.1 | Uncertainties

To evaluate the statistical uncertainties on the yields and $\langle p_{\mathrm{T}} \rangle$, the spectra were reproduced 1000 times and each data point on the spectra was produced by mapping a Gaussian distribution with a mean equal to the original p_T bin yield and a width equal to that bin's statistical uncertainty. The yields and $\langle p_{\mathrm{T}} \rangle$ were then computed with the copied spectra and a Gaussian function was fitted to the distributions of yields/$\langle p_{\mathrm{T}} \rangle$ values obtained. The standard deviation of this distribution was taken as the statistical uncertainty.

In order to calculate the systematic uncertainties on the calculated values of yields and $\langle p_{\mathrm{T}} \rangle$, two contributions had to be considered. Firstly, the contributions from the systematic errors on the p_T spectra that were shown in section 4.5. Secondly, the uncertainty introduced by extrapolating the spectra to the unmeasured p_T regions. In order to evaluate the systematic errors from the p_T spectra, the full size of the error bands were considered by calculating the yields/$\langle p_{\mathrm{T}} \rangle$at the minimum and maximum of the error bars. The maximum deviation in the yield/$\langle p_{\mathrm{T}} \rangle$gave the systematic uncertainty. The evaluation of the second contribution is described in the next section.

5.1.2.2 | Extrapolation to unmeasured p_T regions

As mentioned in section 4.2, due to the acceptance of ALICE, particles with a very low p_T can not be measured. Therefore, in order to calculate yields and $\langle p_{\mathrm{T}} \rangle$, the p_T spectra needed to be fitted and extrapolated in unmeasured regions at high and low p_T. In

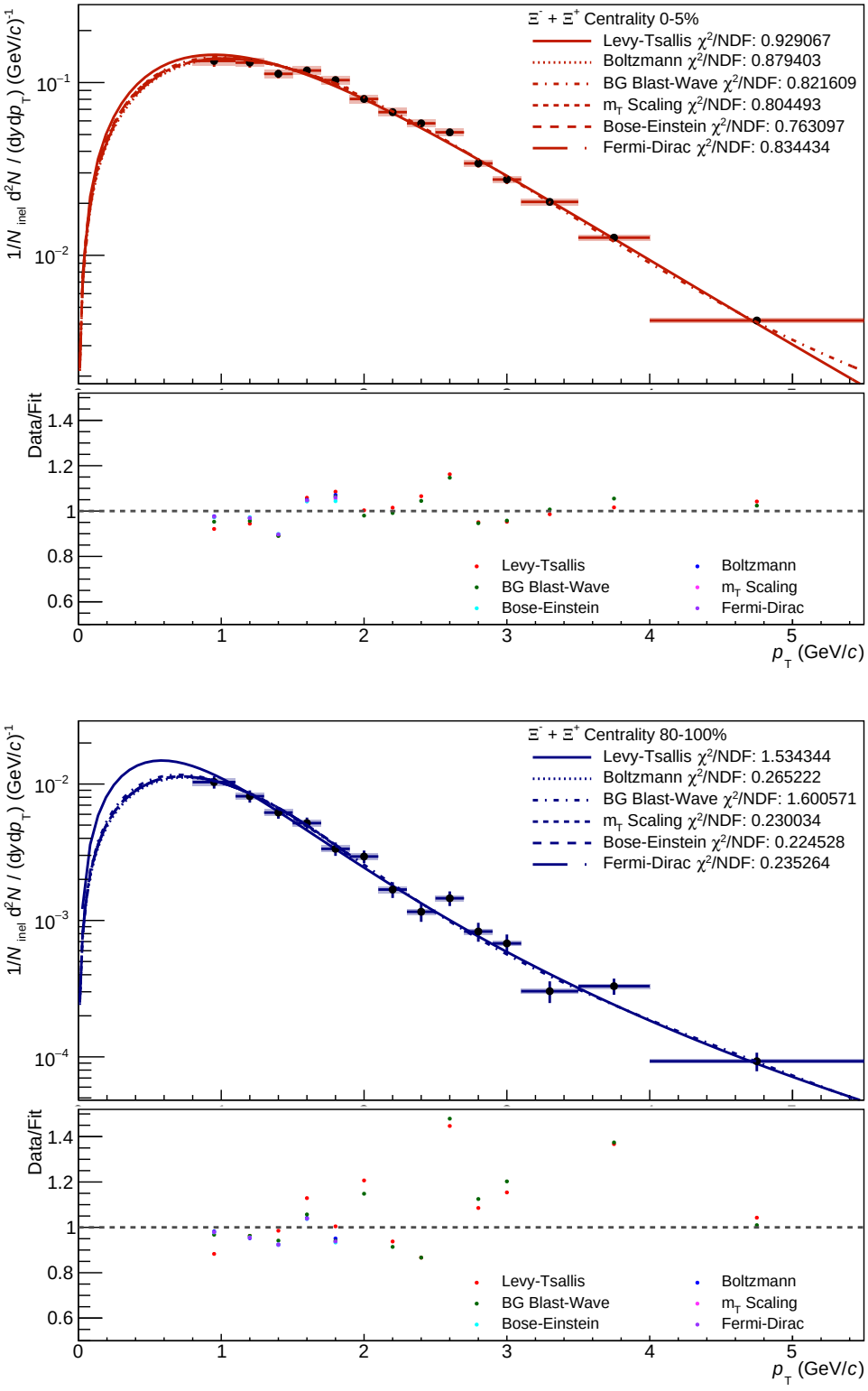

Figure 5.5: Plots showing the default Lévy-Tsallis and other fits in highest (top) and lowest (bottom) multiplicity bin for $\Xi^{\pm}$. The data and fits are shown in the top panel and the ratio of the data to the fit is shown in the bottom panel.

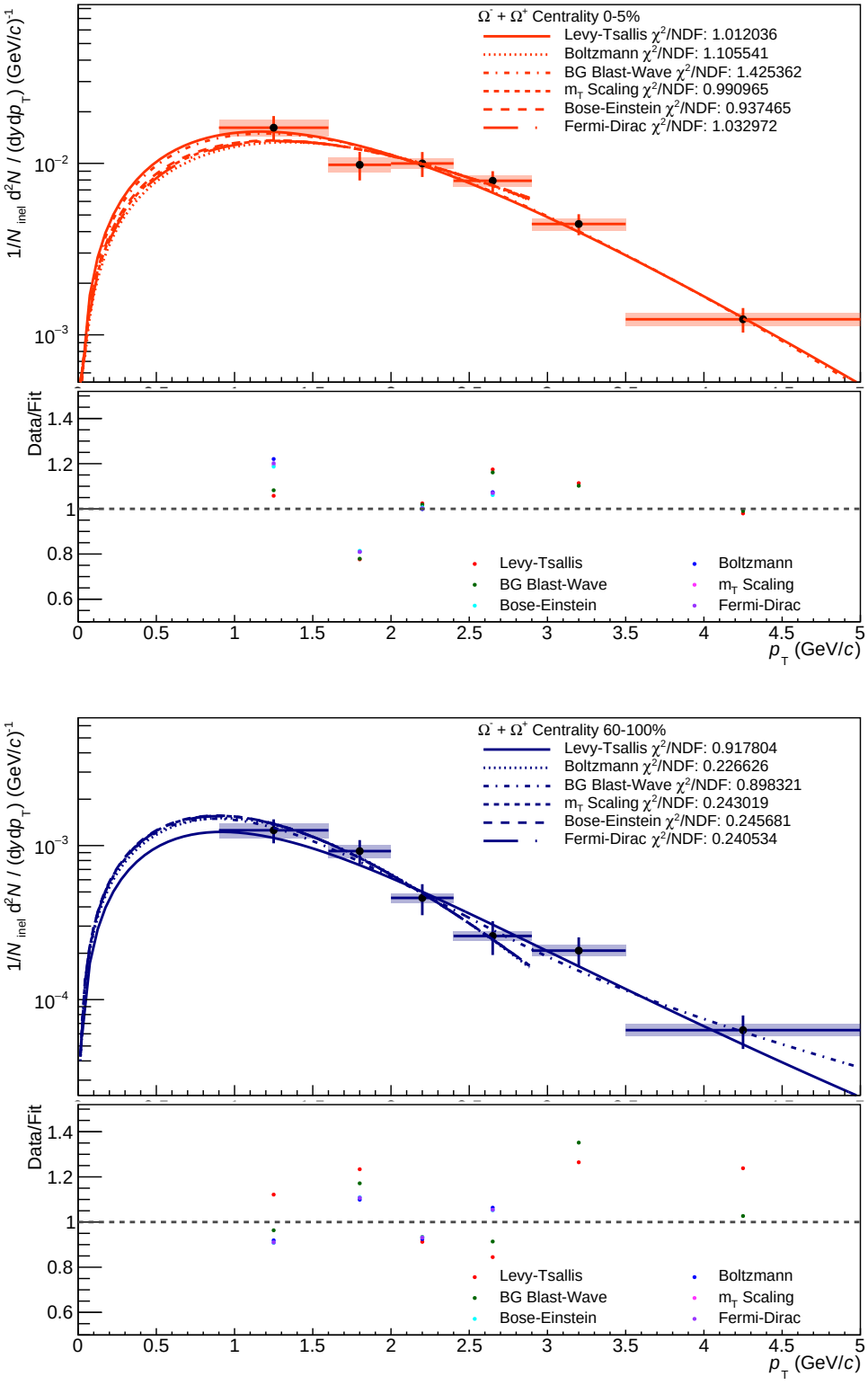

Figure 5.6: Plots showing the default Lévy-Tsallis and other fits in highest (top) and lowest (bottom) multiplicity bin for $\Omega^{\pm}$. The data and fits are shown in the top panel and the ratio of the data to the fit is shown in the bottom panel.

order to calculate the uncertainty contribution due to the extrapolated fraction of the yields, the spectra were fitted with five alternative functions instead of the reference Lévy-Tsallis [133], as outlined in section 2.2.5.2. The ranges of the fits were altered in order to achieve a $\chi^2/ndf \leq 2.5$. This means the upper p_T limit of the fit range had to be reduced in most cases.

The results of the fits for the highest and lowest multiplicity bins are shown in figure 5.5 for $\Xi^{\pm}$and figure 5.6 for $\Omega^{\pm}$, with the χ^2/ndf values shown for all fits. The results for the remaining multiplicity bins are shown in appendix C. The bottom panel of figures 5.5 and 5.6 shows the relative differences between the data in each p_T bin and the fitting function at that point. Only the low p_T extrapolation was used for uncertainty estimation as the contribution from high p_T to the yields was less than 1% for all multiplicity bins and, as already mentioned, the fit was poor at high p_T for the alternative functions used.

The measured yields and $\langle p_{\mathrm{T}} \rangle$ values obtained with different fitting functions were extracted and the ratio to the results with the default Lévy-Tsallis fit were calculated. The systematic uncertainties due to the extrapolation were calculated by taking half the maximum deviation from the Lévy-Tsallis value in each multiplicity class for both yields and $\langle p_{\mathrm{T}} \rangle$.

5.1.2.3 | Results

The total yields calculated for $\Xi^{\pm}$ and $\Omega^{\pm}$ are given in tables 5.1 and 5.2 alongside the mean charged particle multiplicities, $\mathrm{d}N_{\mathrm{ch}}/\mathrm{d}\eta$, for the corresponding multiplicity class [174]. The fraction of the extrapolated contribution is also given. For $\Xi^{\pm}$ they range from 23 to 44% and for $\Omega^{\pm}$ they range from 22 to 30%. The yields are shown in figure 5.7 as a function of $\mathrm{d}N_{\mathrm{ch}}/\mathrm{d}\eta$. An increase in the yields of both $\Xi^{\pm}$ and $\Omega^{\pm}$ can be seen relative to $\mathrm{d}N_{\mathrm{ch}}/\mathrm{d}\eta$.

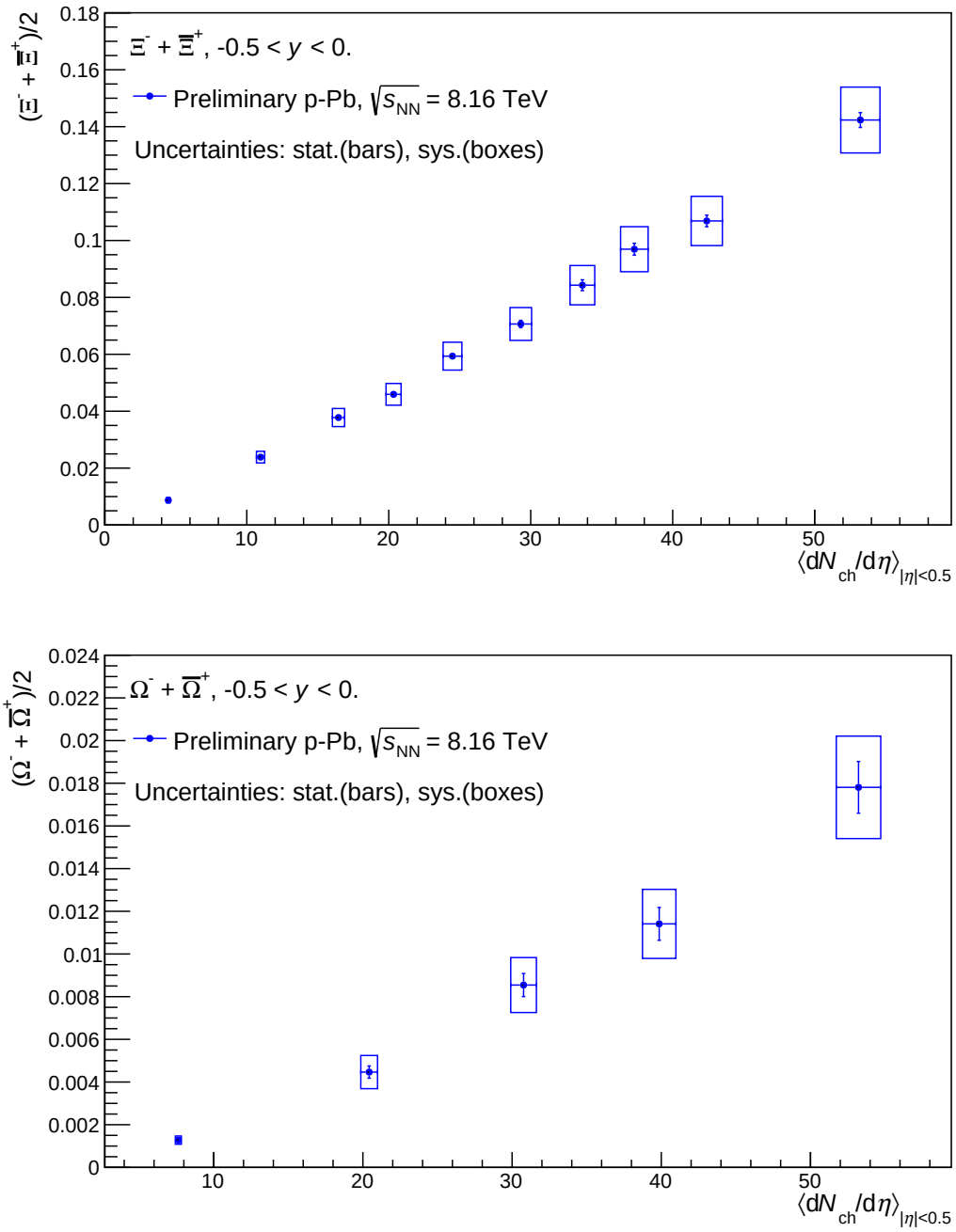

Figure 5.7: Plots showing the particle yields as a function of $\mathrm{d}N_{\mathrm{ch}}/\mathrm{d}\eta$ for $\Xi^{\pm}$(top) and $\Omega^{\pm}$(bottom).

As well as calculating integrated yields, the mean transverse momentum, $\langle p_{\mathrm{T}} \rangle$, was also calculated. The $\langle p_{\mathrm{T}} \rangle$ for each multiplicity class are also given in table 5.1 and 5.2 and shown in figure 5.8 as a function of $\mathrm{d}N_{\mathrm{ch}}/\mathrm{d}\eta$. The results show an increase as a func-

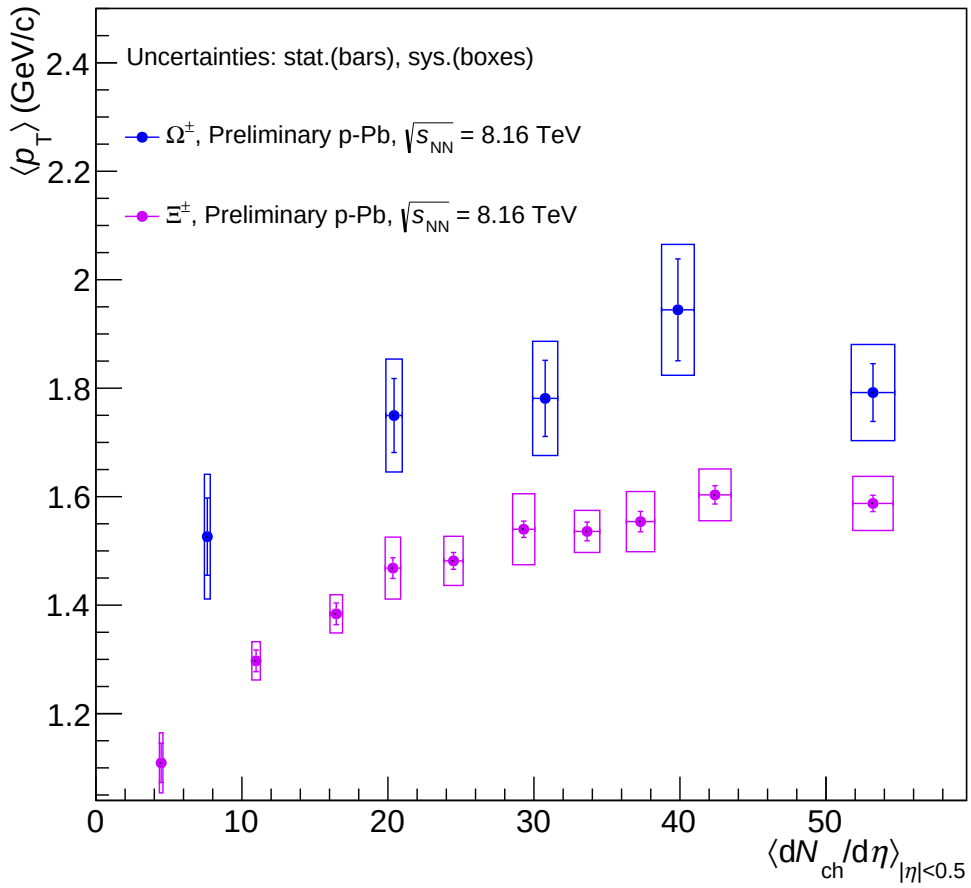

Figure 5.8: Plots showing the average transverse momentum, $\langle p_{\mathrm{T}} \rangle$, as a function of $\mathrm{d}N_{\mathrm{ch}}/\mathrm{d}\eta$ for $\Xi^{\pm}$ and $\Omega^{\pm}$. Points for $\Xi^{\pm}$ are shown in purple and points for $\Omega^{\pm}$ are shown in blue.

tion of multiplicity, although for $\Omega^{\pm}$ this is less clear given the size of the uncertainties. These results demonstrate spectrum hardening, where there is an increase in the peak of the p_T distributions towards larger values of p_T at higher multiplicities. The values are larger for $\Omega^{\pm}$ than for $\Xi^{\pm}$ across multiplicity, indicating a mass ordering of this effect, which supports the presence of radial flow [175].

In a Boltzmann distribution, as was shown in equation 2.5, the particle spectra are proportional to $\exp(-\frac{m_T}{T})$, where all particle species have a common emission temperature at freeze-out, $T = T_{kin}$. In heavy-ion collisions, measured spectra for different particle species have different slopes, breaking the predicted m_T scaling. This

Table 5.1: The $\Xi^- + \overline{\Xi}^+$ integrated yields and mean p_T in each V0A multiplicity class with the corresponding mid-rapidity $\mathrm{d}N_{\mathrm{ch}}/\mathrm{d}\eta$ values given. The statistical errors and then the systematic errors are shown. The percentage of the yields extrapolated is also given.

V0A Mult Bins, %	$\mathrm{d}N_{\mathrm{ch}}/\mathrm{d}\eta$	$(\Xi^- + \overline{\Xi}^+)/2 \times (10^{-1})$	$\langle p_{\mathrm{T}} \rangle$, GeV/$c$	Extrapolation, %
0-5	53.22 ± 1.38	$1.423 \pm 0.026 \pm 0.127$	$1.588 \pm 0.015 \pm 0.050$	24
5-10	42.40 ± 1.10	$1.069 \pm 0.020 \pm 0.094$	$1.603 \pm 0.017 \pm 0.048$	23
10-15	37.30 ± 0.97	$0.969 \pm 0.021 \pm 0.085$	$1.554 \pm 0.019 \pm 0.055$	25
15-20	33.64 ± 0.87	$0.843 \pm 0.019 \pm 0.071$	$1.536 \pm 0.017 \pm 0.039$	24
20-30	29.30 ± 0.76	$0.707 \pm 0.013 \pm 0.069$	$1.540 \pm 0.015 \pm 0.065$	25
30-40	24.49 ± 0.66	$0.594 \pm 0.011 \pm 0.054$	$1.482 \pm 0.015 \pm 0.045$	27
40-50	20.34 ± 0.53	$0.459 \pm 0.010 \pm 0.042$	$1.468 \pm 0.019 \pm 0.057$	28
50-60	16.46 ± 0.43	$0.377 \pm 0.010 \pm 0.036$	$1.384 \pm 0.020 \pm 0.035$	30
60-80	10.97 ± 0.29	$0.239 \pm 0.007 \pm 0.023$	$1.297 \pm 0.020 \pm 0.035$	34
80-100	4.47 ± 0.12	$0.087 \pm 0.005 \pm 0.014$	$1.109 \pm 0.036 \pm 0.055$	44

Table 5.2: The $\Omega^- + \overline{\Omega}^+$ integrated yields and mean p_T in each V0A multiplicity class with the corresponding mid-rapidity $\mathrm{d}N_{\mathrm{ch}}/\mathrm{d}\eta$ values given. The statistical errors and then the systematic errors are shown. The percentage of the yields extrapolated is also given.

V0A Mult Bins, %	$\mathrm{d}N_{\mathrm{ch}}/\mathrm{d}\eta$	$(\Omega^- + \overline{\Omega}^+)/2 \times (10^{-2})$	$\langle p_{\mathrm{T}} \rangle$, GeV/$c$	Extrapolation, %
0-5	53.22 ± 1.38	$1.781 \pm 0.121 \pm 0.240$	$1.792 \pm 0.053 \pm 0.089$	22
5-15	39.86 ± 1.10	$1.141 \pm 0.077 \pm 0.162$	$1.944 \pm 0.093 \pm 0.121$	23
15-30	30.77 ± 0.86	$0.854 \pm 0.054 \pm 0.129$	$1.781 \pm 0.070 \pm 0.105$	25
30-60	20.42 ± 0.56	$0.447 \pm 0.028 \pm 0.078$	$1.750 \pm 0.068 \pm 0.104$	23
60-100	7.63 ± 0.20	$0.128 \pm 0.011 \pm 0.019$	$1.526 \pm 0.071 \pm 0.115$	30

is interpreted as another component contributing to the measured emission temperature, $T = T_{kin} + \frac{1}{2}mv^2$, where $\frac{1}{2}mv^2$ corresponds to the kinetic energy acquired by the particles due to hydrodynamical collective expansion along the transverse plane *ie.* radial flow. This component modifies the particle spectra by pushing the mean transverse momentum at emission to higher values, proportional to the particles species mass. This effect has also been reported in pp collisions by ALICE [176] and CMS [177]. It supports the evidence for collective behaviour in small systems that can be described by hydrodynamic models [175], along with other features of heavy-ion collisions observed in

small systems [178–180].

5.2 | Full Data Analysis

The decision to use a sub-sample of the data available was described in section 4.1.1.1. After analysis of this subset a new procedure was developed within the ALICE collaboration to handle OOB pile-up on a cascade-by-cascade candidate basis by utilising information from the ITS and the TOF. The cut is applied by checking that out of the three detectable daughter tracks from the measured decay (the baryon and meson tracks from the V0 and the bachelor track from the cascade), at least one either satisfies a timing check on the ITS or the TOF, to ensure the track is from a triggered event. Both are checked as the efficiencies of both compensate each other in the low/high p_T regions. The ITS cut checks that the track was reconstructed with TPC and ITS hits. As the ITS has a narrower acquisition window compared to the TPC, this cut causes tracks from events from before or after the triggered event to be discarded. The TOF cut checks that there is TOF information for that track, which also discards tracks from before or after the triggered event due to its narrow acquisition window.

In order to confirm that the cuts were performing as expected, the low μ data subsample was reanalysed using the new data output with the ITS/TOF information required to apply the cuts. Some minor changes to a few of the topological cuts described in section 4.5 were made.

Once these changes were made, checks could be carried out using the $\Xi^{\pm}$ yields. This was done by calculating the new yields with and without the ITS/TOF cuts and comparing them to the previous analysis. Without the ITS/TOF cuts, the calculated yields should be identical, therefore the ratio of the yields shown by the green points in the bottom panel of figure 5.9 should be one. Deviations can be seen due to fluctuations

in the data that is analysed on the LEGO train system used by ALICE [1] and the small changes in some of the topological cuts between the two analyses. The points are within 3% in agreement with each other so these appear to be consistent as expected.

The application of the ITS/TOF cuts should have minimal effect on this data set as it has a low probability of pileup. Therefore the yields calculated should still be consistent. The ratio of the yields with the ITS/TOF cuts compared to the original analysis is shown by the red points in the bottom panel of figure 5.9. These are also below 3% for nearly all multiplicities. The lowest multiplicity shows a deviation of 6% but this may be attributed to some pile-up removal at the lowest multiplicity, where pileup is

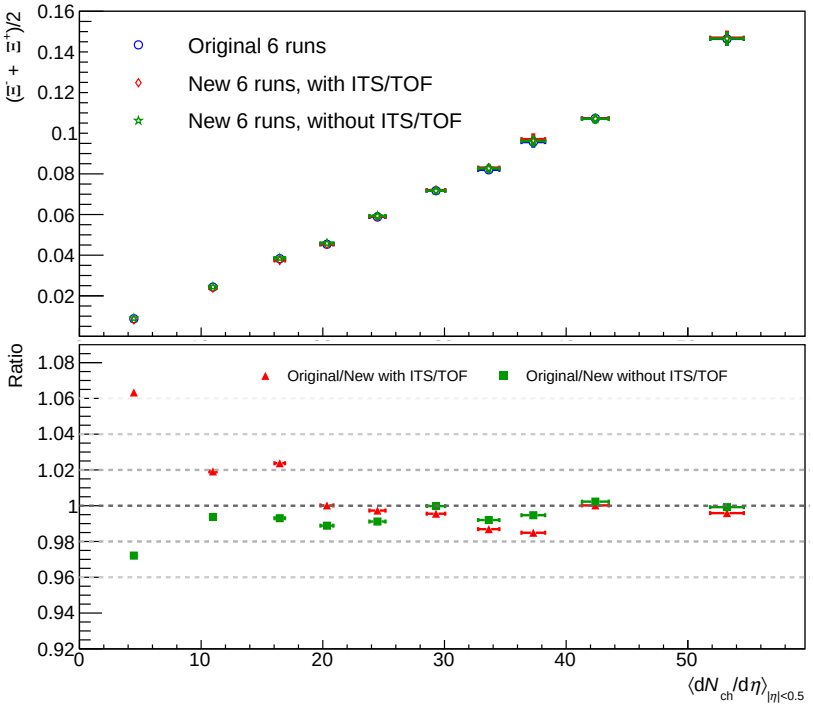

Figure 5.9: Plots showing the integrated yields for $\Xi^{\pm}$calculated using the original analysed data (open blue circles), the new dataset with ITS/TOF cuts (open red diamonds), the new dataset without ITS/TOF cuts (open green stars). The bottom panel shows the ratio of the original data set to the new dataset with (red) and without (green) the ITS/TOF cuts.

[1] Due to the large size of the data sets that are being analysed, analysis code can be run centrally via the so-called LEGO trains on the ALICE Grid system. At run-time a small number of failures can occur so the complete data set analysed on any one train will differ slightly to that of a train run at a different time.

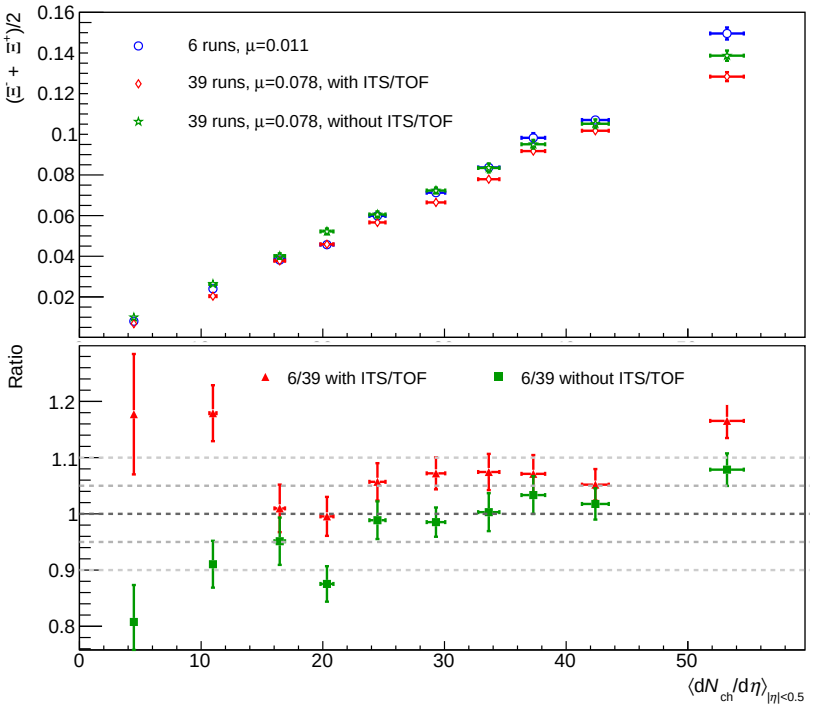

Figure 5.10: Plots showing the integrated yields for $\Xi^{\pm}$calculated using the low μ data (open blue circles) and the high μ data with ITS/TOF cuts (open red diamonds) and without ITS/TOF cuts (open green stars). The bottom panel shows the ratio of the low μ data to the high μ data with (red) and without (green) the ITS/TOF cuts.

most probable. (Low multiplicity events with few tracks are more prone to OOB pileup affecting reconstruction). As no significant deviations were found with this check the analysis proceeded to the full data set.

Firstly, the yields of the 39 runs with high μ cuts were evaluated in order to make a comparison to the low μ results already obtained. The 39 runs have an average μ of 0.078, compared to the 0.011 of the original dataset so are much more effected by pileup. The results for the yields with the 39 runs are shown in figure 5.10 compared to the six runs. Differences can be seen in the results for low and high μ runs even once ITS/TOF cuts have been applied. These differences are significant, especially at high and low multiplicity. In order to take this effect from μ into account a systematic error was estimated. This was done by comparing the results in the two sub-samples to the full data set (including all 45 runs) as shown in figure 5.11 for $\Xi^{\pm}$ and $\Omega^{\pm}$. The maximum deviation

in each multiplicity bin, halved, was added to the systematic errors of the final yields. Table 5.3 shows the systematic contributions from this effect. The final yields using this data set with the new systematic error for $\Xi^{\pm}$ and $\Omega^{\pm}$ are shown in figure 5.12.

Table 5.3: Systematic errors due to μ for $\Xi^{\pm}$ and $\Omega^{\pm}$

V0A Mult Bins, % ($\Xi^{\pm}$)	Systematic Error ($\Xi^{\pm}$)	V0A Mult Bins, % ($\Omega^{\pm}$)	Systematic Error ($\Omega^{\pm}$)
0-5	5%	0-5	29%
5-10	5%	5-15	5%
10-15	1%	15-30	5%
15-20	1%	30-60	4%
20-30	2%	60-100	5%
30-40	2%		
40-50	2%		
50-60	2%		
60-80	2%		
80-100	4%		

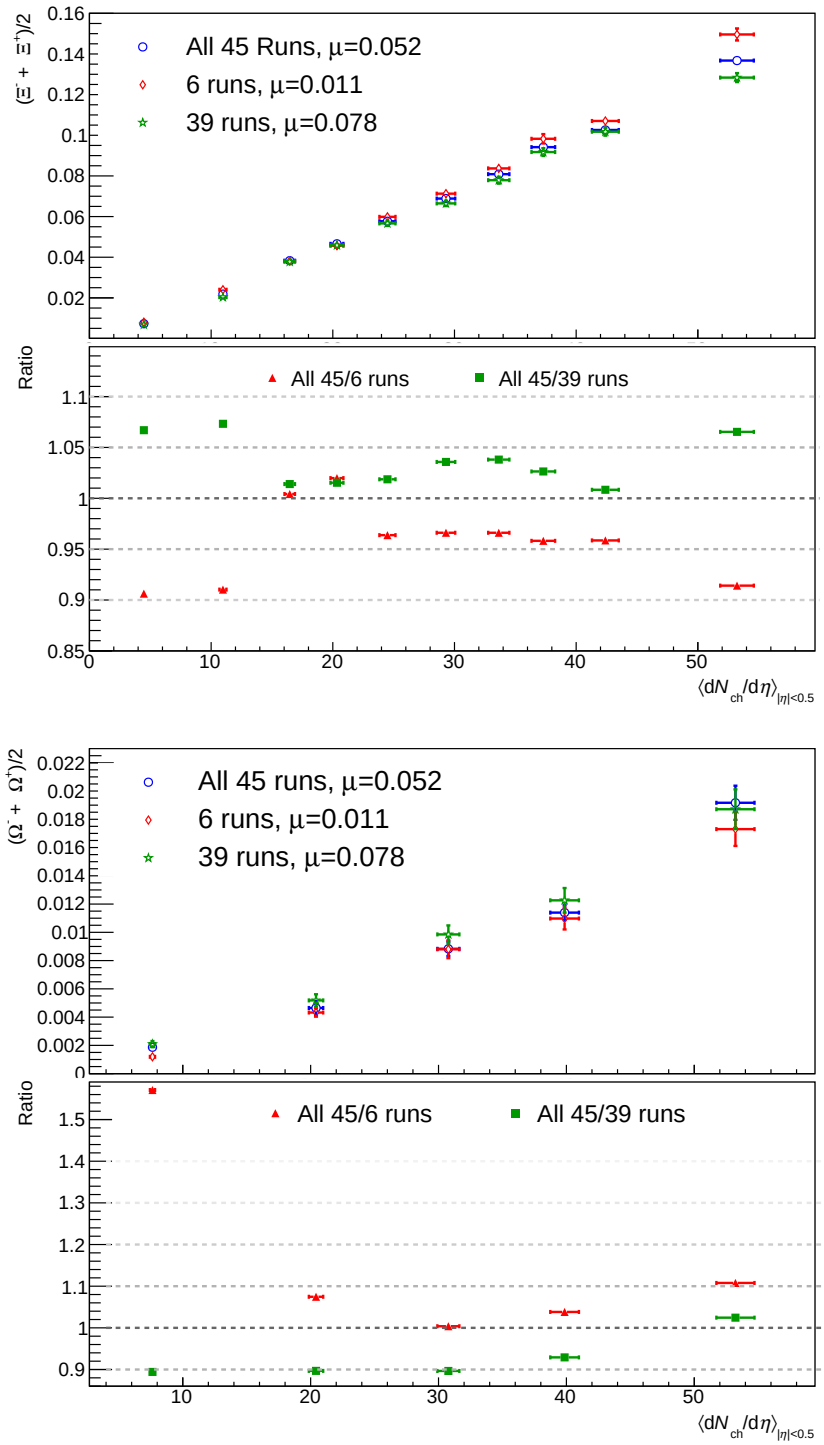

Figure 5.11: Plots showing the integrated yields for $\Xi^{\pm}$ calculated using all the data (open blue circles), the low μ data (open red diamonds) and the high μ data (open green stars). The bottom panel shows the ratio of the whole data set to the low μ dataset (red) and high μ dataset (green).

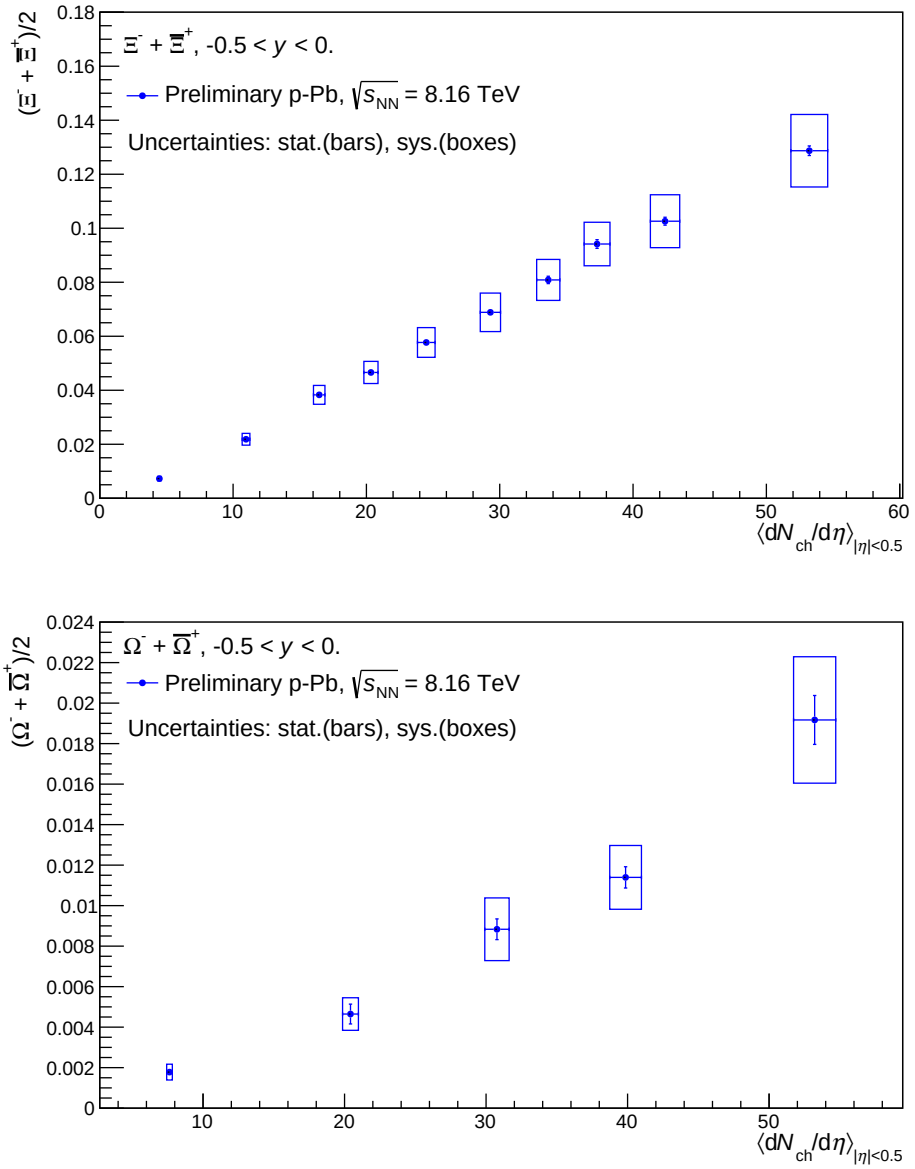

Figure 5.12: Plots showing the integrated yields for $\Xi^{\pm}$ (top) and $\Omega^{\pm}$(bottom) calculated using the full data set with a systematic error contribution from μ included.

5.2.1 | Extended multiplicity reach

Due to the increased statistics available in the whole data set it was realised that a further multiplicity bin could be extracted from the $\Xi^{\pm}$data by splitting the 0-5% bin into a 0-1% bin and a 1-5% bin. This meant the multiplicity reach of the final results could be extended even further, with the highest value of $\mathrm{d}N_{\mathrm{ch}}/\mathrm{d}\eta$ being increased 20% from 53.2 to 64.0. The yields with this extra multiplicity bin are shown in figure 5.13, with the systematic uncertainty for the μ variation included, which shows the yields continuing to increase at this higher value of $\mathrm{d}N_{\mathrm{ch}}/\mathrm{d}\eta$. The data used to produce figures 5.12 and 5.13 are included in appendix D.

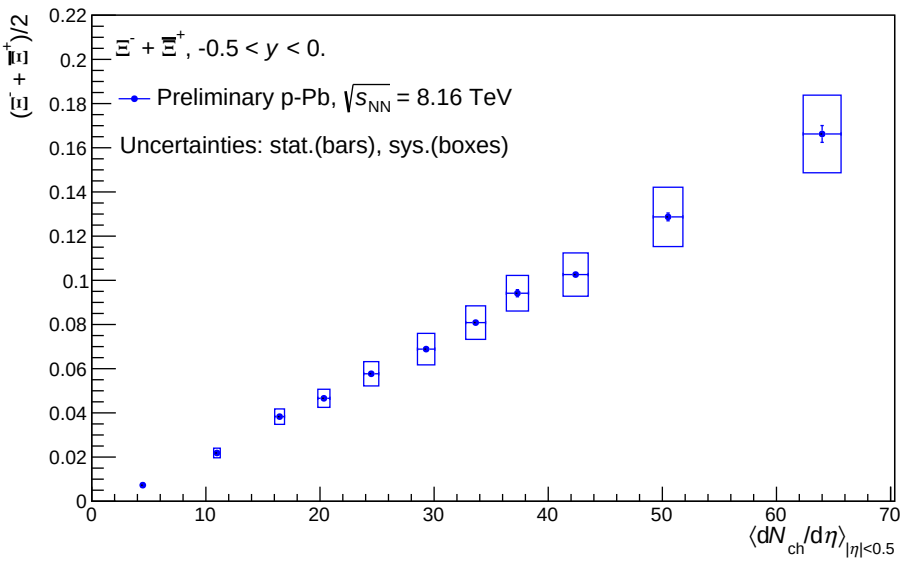

Figure 5.13: Plots showing the integrated yields for $\Xi^{\pm}$with an extra multiplicity bin.

Chapter 6

Conclusions

In the previous chapter the results obtained for multi-strange baryon yields and $\langle p_{\mathrm{T}} \rangle$ were presented. In this final chapter, the results will be put into context by comparing to other results obtained by ALICE at different collision energies, with other collision systems and with other hadron measurements.

6.1 | Discussion of Results

6.1.1 | Energy Dependence

In order to establish if the results for multi-strange baryon yields found in the previous chapter are consistent with those measured in Run 1 at $\sqrt{s_{NN}} = 5.02$ TeV[117], a direct comparison was made as shown in figure 6.1. These results show that the yields at both energies are in agreement, indicating the multiplicity dependence is independent of the initial collision energy. This was also found when Run 2 pp data at $\sqrt{s} = 13$ TeV were compared to Run 1 pp data at $\sqrt{s} = 7$ TeV [181]. The values for $\langle p_{\mathrm{T}} \rangle$ were also compared to the results at lower energy and figure 6.2 indicate that these are also consistent with Run 1 results.

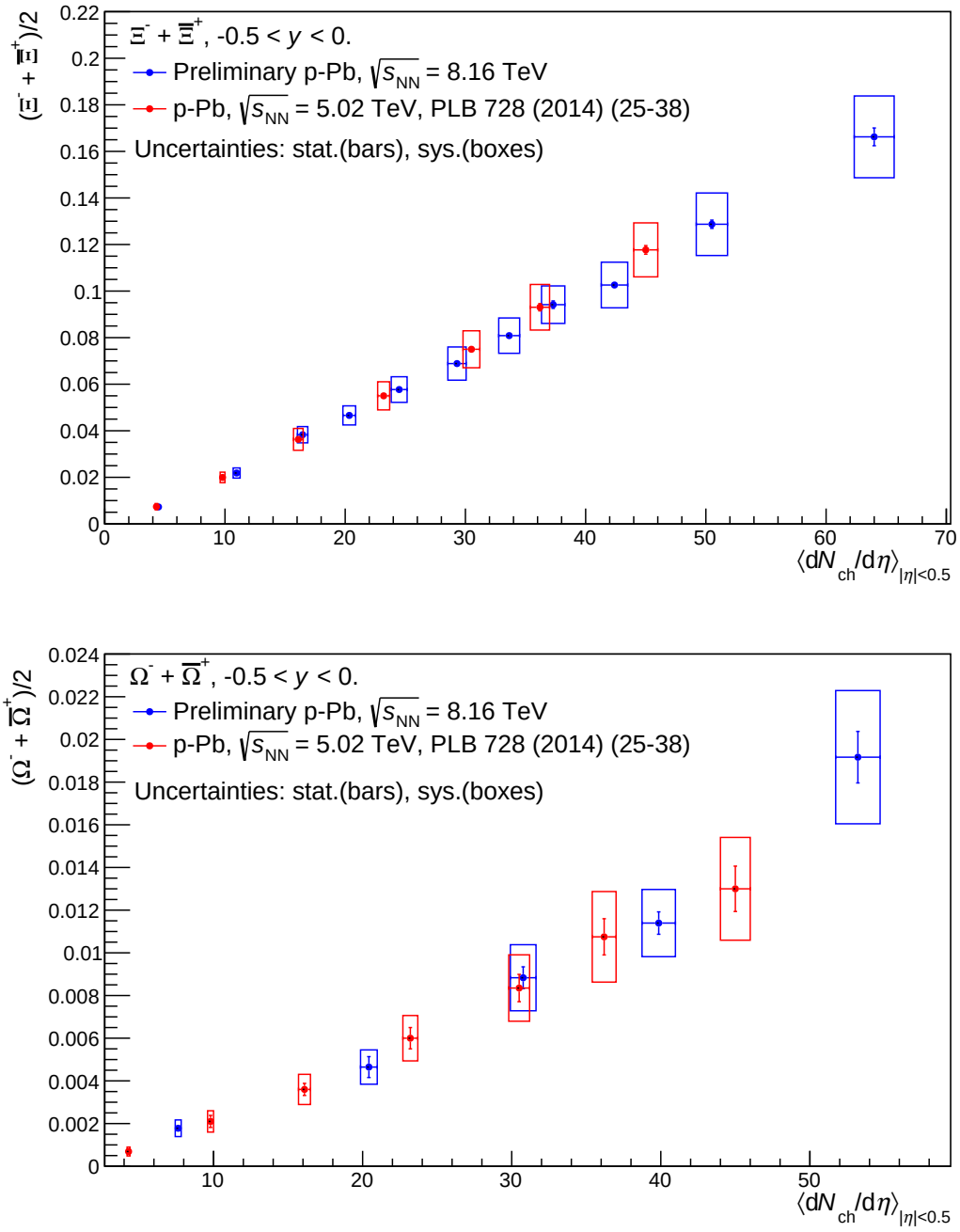

Figure 6.1: Plots showing the particle yields as a function of $\langle dN_{ch}/d\eta \rangle_{|\eta|<0.5}$ for $\Xi^{\pm}$(top) and $\Omega^{\pm}$(bottom).

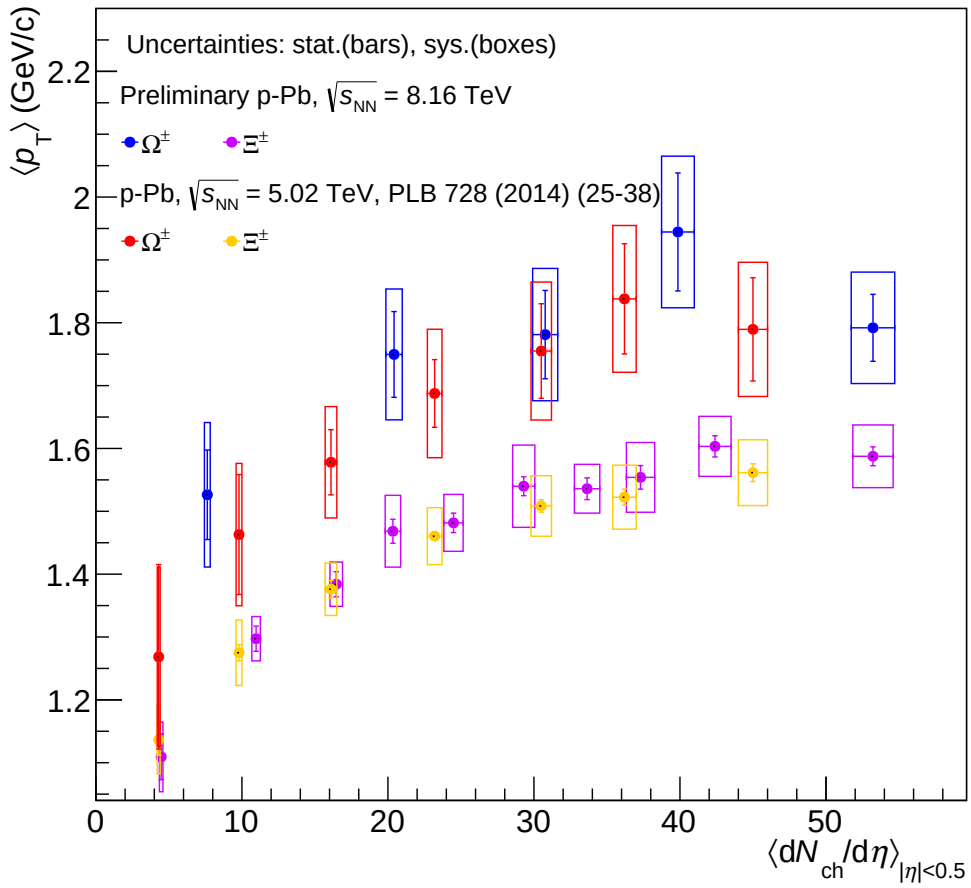

Figure 6.2: Plots showing the average transverse momentum, $\langle p_{\mathrm{T}} \rangle$, as a function of $\langle \mathrm{d}N_{\mathrm{ch}}/\mathrm{d}\eta \rangle_{|\eta|<0.5}$ for $\Xi^{\pm}$ and $\Omega^{\pm}$. Points for $\Xi^{\pm}$ are shown in purple for $\sqrt{s_{NN}}$ = 8.16 TeV and orange for $\sqrt{s_{NN}}$ = 5.02 TeV. Points for $\Omega^{\pm}$ are shown in blue for $\sqrt{s_{NN}}$ = 8.16 TeV and red for $\sqrt{s_{NN}}$ = 5.02 TeV.

6.1.2 | Hyperon-to-pion yields

The previous section demonstrated that the yields of multi-strange baryons increase as a function of multiplicity. However, in order to establish if there is an actual enhancement of strangeness in this system, a comparison has to be made to the yields of non-strange particles. As mentioned in section 2.2.5, pions are used to normalise the hyperon yields. The hyperon-to-pion yields in p–Pb collisions at both $\sqrt{s_{NN}}$ = 8.16 TeV and $\sqrt{s_{NN}}$ = 5.02 TeV are shown in figure 6.3, using recent results for pions in p–Pb collisions to calculate the ratios [182]. The statistical and systematic errors of the hyperon

yields, Y_h, and pion yields, Y_p, were propagated to the hyperon-to-pion yield ratios, R, using the formula, $\sigma_R = R\sqrt{\left(\frac{\sigma_{Yh}}{Y_h}\right)^2 + \left(\frac{\sigma_{Yp}}{Y_p}\right)^2}$. The results show that, as for Run 1 data, an enhancement can be seen in the higher energy results. The enhancement, E, seen from the lowest to the highest multiplicity measured for $\Xi^{\pm}$ is **81**$\pm$7$\pm$23% and **66**$\pm$13$\pm$35% for $\Omega^{\pm}$, using $E = (R_{max} - R_{min})/R_{min}$, with statistical and systematic errors shown.

6.1.2.1 | Colliding particle comparison

In order to put the p–Pb hyperon-to-pion ratio results into context, a comparison of the ratios in other collision systems can be made, as shown in figure 6.4. This shows the hyperon-to-pion yields for pp and Pb–Pb alongside the p–Pb values. The smooth evolution of the ratios supports the growing evidence that the hyperon-to-pion yields are also independent of the initial colliding system. The low multiplicity p–Pb results are consistent with the high-multiplicity pp results and the high multiplicity p–Pb results are consistent with the lowest multiplicity bin in the Pb–Pb data.

6.1.2.2 | Comparison with results of other hadrons

The results can also be compared to other hadrons that have been measured. Figure 6.5 shows the results for $\Xi^{\pm}$ and $\Omega^{\pm}$ alongside other particles, such as the singly strange Λ and the K^0_S, as well as the ϕ with hidden strangeness and the non-strange proton. The proton has been measured at $\sqrt{s_{NN}} = 8.16$ TeV as well, however for the other particles only the Run 1 results for p–Pb are shown. As expected, the proton and pion yields increase at the same rate with multiplicity so the ratio is flat. The rate of enhancement for the strange particles is dependent on the number of strange quarks in the particle with the $\Omega^{\pm}$ with three quarks showing the greatest enhancement.

This figure also shows the results that have been obtained for the Xe–Xe data [185]. The Xe–Xe collisions produce multiplicities intermediate between p–Pb and Pb–Pb. The

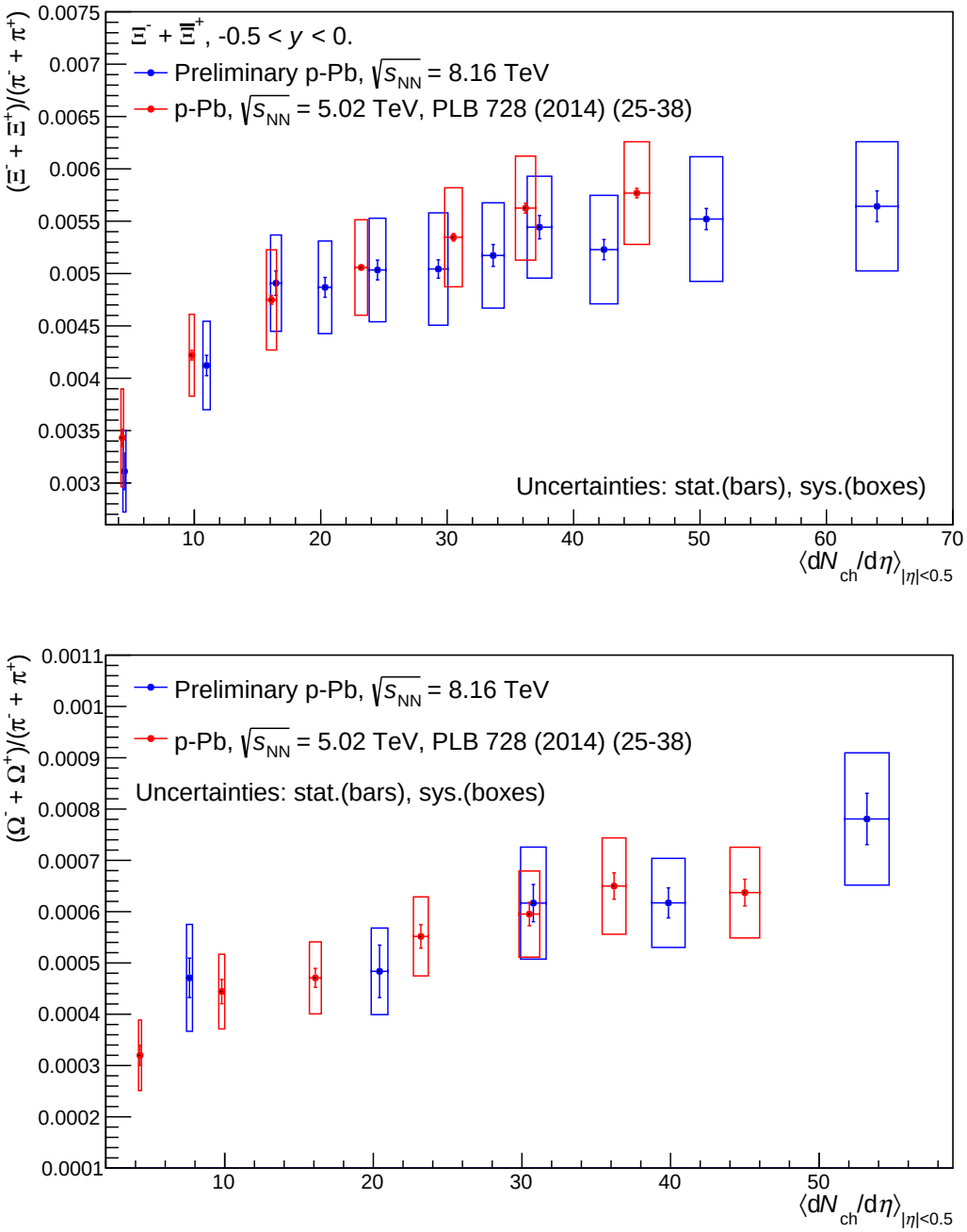

Figure 6.3: Plots showing the hyperon-to-pion ratios as a function of $\langle dN_{ch}/d\eta \rangle_{|\eta|<0.5}$ for $\Xi^{\pm}$(top) and $\Omega^{\pm}$(bottom) with $\sqrt{s_{NN}} = 8.16$ TeV results from this analysis in blue and previous $\sqrt{s_{NN}} = 5.02$ TeV results in red.

results for Xe–Xe are consistent with the picture of a ratio that smoothly increases independent of collisions system and energy.

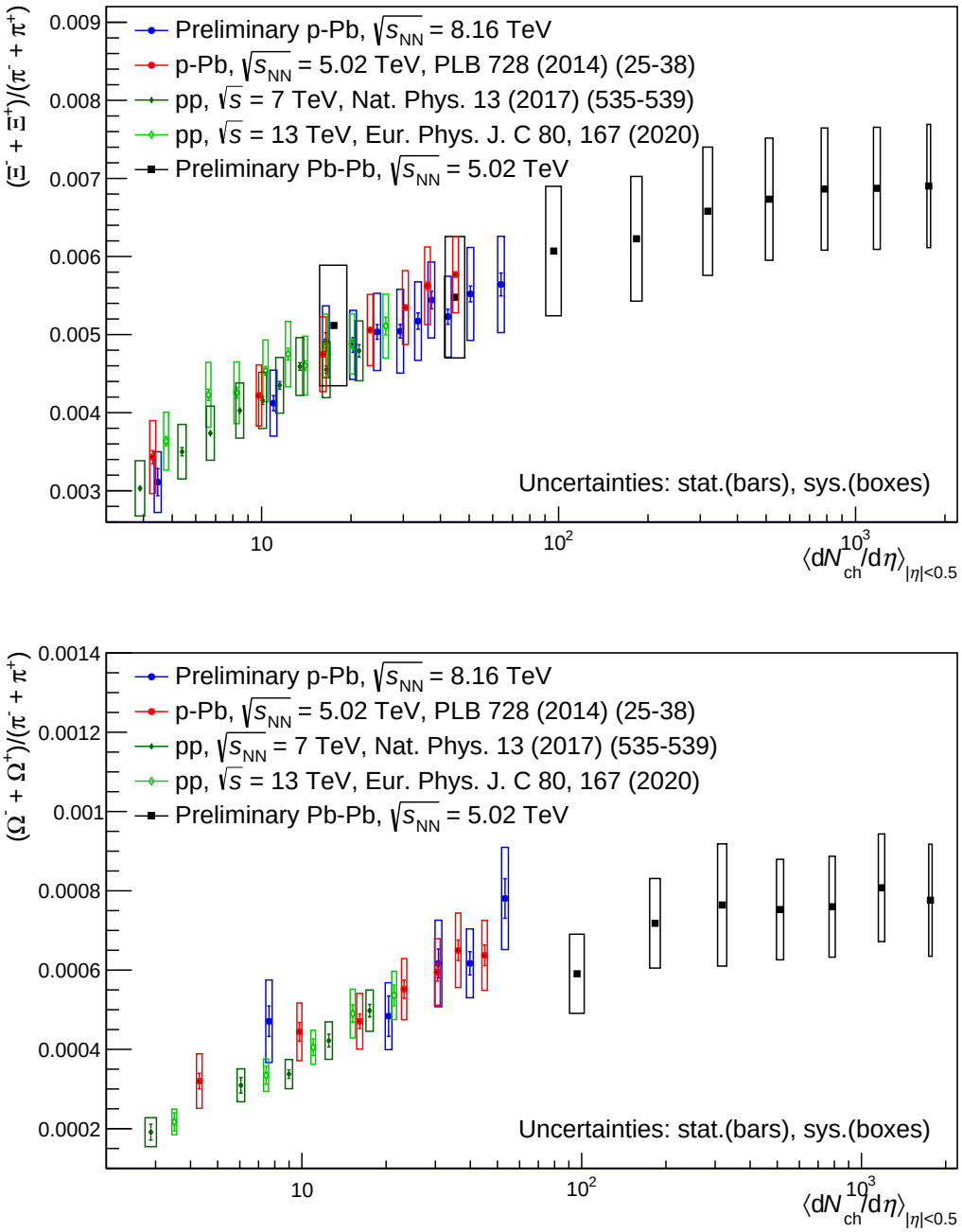

Figure 6.4: Plots showing the hyperon-to-pion ratios as a function of $\langle \mathrm{d}N_{\mathrm{ch}}/\mathrm{d}\eta \rangle_{|\eta|<0.5}$ for $\Xi^{\pm}$(top) and $\Omega^{\pm}$(bottom) in pp, p–Pb and Pb–Pb collision systems. Data are from [117] (p–Pb $\sqrt{s_{NN}} = 5.02$ TeV), [183] (p–p $\sqrt{s} = 13$ TeV), [184] (p–p $\sqrt{s} = 7$ TeV) and [185] (Pb–Pb $\sqrt{s_{NN}} = 5.02$ TeV).

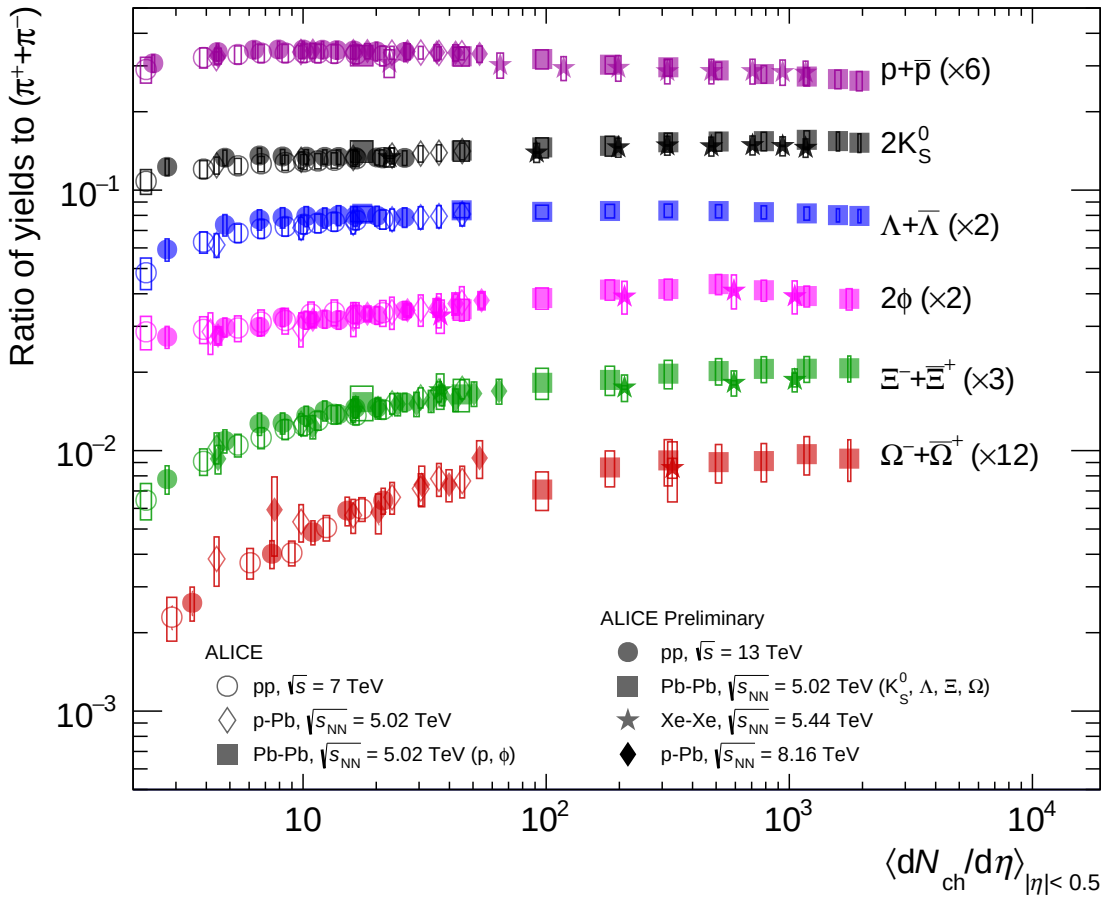

Figure 6.5: Plot showing the particle-to-pion yield ratios as a function of $dN_{ch}/d\eta$ for protons (purple), K^0_S (black), Λ (blue), ϕ (pink), $\Xi^{\pm}$(green) and $\Omega^{\pm}$(red). Results for pp are shown by circles at $\sqrt{s}$ = 7 TeV [184] (open) and $\sqrt{s}$ = 13 TeV [183] (full), p–Pb are shown by diamonds at $\sqrt{s_{NN}}$ = 5.02 TeV [117] (open) and $\sqrt{s_{NN}}$ = 8.16 TeV (full), Pb–Pb at $\sqrt{s_{NN}}$ = 5.02 TeV [185] are shown by squares and Xe–Xe at $\sqrt{s_{NN}}$ = 5.44 TeV [185] are shown by stars.

6.2 | Future Work

Future work will involve increasing the range of $\mathrm{d}N_{\mathrm{ch}}/\mathrm{d}\eta$ studied in p–Pb collisions by analysing a data set taken using a high multiplicity trigger, as opposed to the minimum bias data used in the analysis in this thesis. The high-multiplicity trigger saves events with simultaneous signals in the two V0 detectors above a set threshold. This means the data have very large statistics in the 0-5% multiplicity bin, allowing it to be split into many different finer multiplicity bins. This should allow the p–Pb data to cross over with the multiplicities reached in Pb–Pb data in order to understand if the p–Pb yield ratios continue to increase at these higher multiplicities or if they reach saturation levels similar to Pb–Pb results. These further results will contribute to the understanding of strangeness production in high-energy collisions and help answer the open question if a quark-gluon plasma can be produced in small collision systems.

6.3 | Conclusion

In this thesis, the measurements of multi-strange baryons, Ξ^-, $\overline{\Xi}^+$, Ω^- and $\overline{\Omega}^+$, in p–Pb collisions at centre-of-mass energy $\sqrt{s_{NN}} = 8.16$ TeV using ALICE at the LHC have been presented. The identification of the cascades using the topology of their weak decays into charged particles was explained. This method is possible due to the excellent particle identification and tracking capabilities of the ALICE detectors that were also described.

The p_T spectra for both $\Xi^{\pm}$ and $\Omega^{\pm}$ were evaluated in multiplicity bins and the $\langle p_{\mathrm{T}} \rangle$ were also reported. A hardening of the p_T spectra was observed with multiplicity for $\Omega^{\pm}$ and $\Xi^{\pm}$, although the results for $\Omega^{\pm}$ were limited by statistics, however, the $\langle p_{\mathrm{T}} \rangle$ were observed to be higher in $\Omega^{\pm}$ than for $\Xi^{\pm}$, as was also reported in p–Pb at $\sqrt{s_{NN}} = 5.02$ TeV. These observations are consistent with the presence of collective behaviour which can be described by hydrodynamic models of the medium.

The total yields of the cascades were also calculated and the strangeness enhancement effect was studied by comparing the relative strangeness production rate. This was done by evaluating the hyperon-to-pion ratio in each multiplicity bin. The results for strangeness enhancement were presented and compared with results obtained at different energies and in different collision systems. The results extended the $\mathrm{d}N_{\mathrm{ch}}/\mathrm{d}\eta$ reach of the previous $\sqrt{s_{NN}} = 5.02$ TeV p–Pb results and are consistent with a smooth evolution across multiplicity from low multiplicity pp to central Pb–Pb collisions, where a saturation of the enhancements can be seen.

These measurements provide further data to help constrain models of strangeness production in these collision systems. The MC models described in section 2.2.5 are currently used to model pp collisions, however, hopefully future developments will allow p–Pb collisions to also be modelled in a similar way, so a comparison to data can be made. These results also set the stage for future measurements that will extend the work presented in this thesis and take advantage of a high-multiplicity trigger to increase the data in the p–Pb and Pb–Pb crossover region and investigate if strangeness production saturates in p–Pb or continues to increase.

Bibliography

[1] Rene Brun and Fons Rademakers. ROOT - An Object Oriented Data Analysis Framework. *Nucl. Inst. Meth. in Phys. Res.*, A 389:81–86, Jan 1997. doi:10.1016/S0168-9002(97)00048-X.

[2] Emily Willsher. Hadrochemistry of Particle Production in Small Systems with ALICE at the LHC. *Springer Proceedings in Physics*, 250:233–237, Oct 2020. doi:https://doi.org/10.1007/978-3-030-53448-6_35.

[3] John Dalton. A New System of Chemical Philosophy (v. 1; pt. 2). 1808. doi:10.5479/sil.324338.39088000885681.

[4] Joseph J. Thomson. XL. Cathode Rays. *Philosophical Magazine and Journal of Science*, 44(269), Oct 1897. doi:10.1080/09500830701306165.

[5] Ernest Rutherford. The Scattering of α and β Particles by Matter and the Structure of the Atom. *Philosophical Magazine*, 21:669–688, May 1911. doi:10.1080/14786440508637080.

[6] James Chadwick. The Existence of a Neutron. *Proceedings of the Royal Society A*, 136(830), 1932. doi:10.1098/rspa.1932.0112.

[7] Niels Bohr. On the Constitution of Atoms and Molecules. *Philosophical Magazine and Journal of Science*, 26(151), Jul 1913. doi:10.1080/14786441308634955.

[8] Wikipedia. Standard Model of Particle Physics. URL `https://en.wikipedia.org/wiki/Standard_Model`. Accessed: 22-01-2021.

[9] Yuji Fukuda and Tomohiko et al. Hayakawa. Evidence for Oscillation of Atmospheric Neutrinos. *Physical Review Letters*, 81(8):1562–1567, Aug 1998. ISSN 1079-7114. doi:10.1103/physrevlett.81.1562.

[10] Shin'ichirō Tomonaga. On a Relativistically Invariant Formulation of the Quantum Theory of Wave Fields. *Progress of Theoretical Physics*, 1(2):27–42, Aug 1946. doi:10.1143/PTP.1.27.

[11] Julian Schwinger. Quantum Electrodynamics. I. A Covariant Formulation. *Phys. Rev.*, 74:1439–1461, Nov 1948. doi:10.1103/PhysRev.74.1439.

[12] Julian Schwinger. On Quantum-Electrodynamics and the Magnetic Moment of the Electron. *Phys. Rev.*, 73:416–417, Feb 1948. doi:10.1103/PhysRev.73.416.

[13] R. P. Feynman. Space-Time Approach to Quantum Electrodynamics. *Phys. Rev.*, 76:769–789, Sep 1949. doi:10.1103/PhysRev.76.769.

[14] Richard P. Feynman. Mathematical Formulation of the Quantum Theory of Electromagnetic Interaction. *Phys. Rev.*, 80:440–457, Nov 1950. doi:10.1103/PhysRev.80.440.

[15] Sheldon L. Glashow. The Renormalizability of Vector Meson Interactions. *Nucl. Phys.*, 10:107–117, May 1959. doi:10.1016/0029-5582(59)90196-8.

[16] Abdus Salam and J. C. Ward. Weak and Electromagnetic Interactions. *Il Nuovo Cimento*, 11(4): 568–577, Feb 1959. doi:10.1007/BF02726525.

[17] Steven Weinberg. A Model of Leptons. *Phys. Rev. Lett.*, 19:1264–1266, Nov 1967. doi:10.1103/PhysRevLett.19.1264.

[18] UA2 Collaboration. Observation of Single Isolated Electrons of High Transverse Momentum in Events with Missing Transverse Energy at the CERN pp Collider. *Physics Letters B*, 122(5):476 – 485, Mar 1983. ISSN 0370-2693. doi:10.1016/0370-2693(83)91605-2.

[19] UA2 Collaboration. Evidence for $Z^0 \to e^+e$ at the CERN pp Collider. *Physics Letters B*, 129(1):130 – 140, Mar 1983. ISSN 0370-2693. doi:10.1016/0370-2693(83)90744-X.

[20] UA1 Collaboration. Experimental observation of Lepton Pairs of Invariant Mass Around 95 GeV/c^2 at the CERN SPS Collider. *Physics Letters B*, 126(5):398 – 410, Jul 1983. ISSN 0370-2693. doi:10.1016/0370-2693(83)90188-0.

[21] UA1 Collaboration. Experimental Observation of Isolated Large Transverse Energy Electrons with Associated Missing Energy at $\sqrt{s}$=540 GeV. *Physics Letters B*, 122(1):103 – 116, 1983. ISSN 0370-2693. doi:10.1016/0370-2693(83)91177-2.

[22] Carl D. Anderson. The Positive Electron. *Phys. Rev.*, 43:491–494, Mar 1933. doi:10.1103/PhysRev.43.491.

[23] Dmitri Mendeleev. The Periodic Law of the Chemical Elements. *Journal of the Chemical Society*, 55: 634–656, 1889. doi:10.1098/rsta.2019.0537.

[24] Murray Gell-Mann. The Eightfold Way: A Theory of Strong Interaction Symmetry. Mar 1961. doi:10.2172/4008239.

[25] Yuval Ne'eman. Derivation of Strong Interactions from a Gauge Invariance. *Nuclear Physics*, 26 (2):222 – 229, Aug 1961. ISSN 0029-5582. doi:10.1016/0029-5582(61)90134-1.

[26] George Zweig. An SU(3) Model for Strong Interaction Symmetry and its Breaking. Version 2. In *Developments in the Quark Theory of Hadrons. Vol. 1.*, pages 22–101. Feb 1964.

[27] Murray Gell-Mann. A Schematic Model of Baryons and Mesons. *Phys. Lett.*, 8:214–215, 1964. doi:10.1016/S0031-9163(64)92001-3.

[28] Wolfgang Pauli. Über den Zusammenhang des Abschlusses der Elektronengruppen im Atom mit der Komplexstruktur der Spektren. *Zeitschrift für Physik*, 31:765–783, 1925. doi:10.1007/BF02980631.

[29] Moo-Young Han and Yoichiro Nambu. Three-Triplet Model with Double SU(3) Symmetry. *Phys. Rev.*, 139:B1006–B1010, Aug 1965. doi:10.1103/PhysRev.139.B1006.

[30] Oscar W. Greenberg. Spin and Unitary-Spin Independence in a Paraquark Model of Baryons and Mesons. *Phys. Rev. Lett.*, 13:598–602, Nov 1964. doi:10.1103/PhysRevLett.13.598.

[31] K. Yagi, T. Hatsuda, and Y. Miake. *Quark-Gluon Plasma: From Big Bang to Little Bang*, page 32. Cambridge University Press, 2008.

[32] Michiel Botje. Lecture Notes On Particle Physics II: Quantum Chromo Dynamics. `https://www.nikhef.nl/~h24/qcdcourse/section-5.pdf`, December 2013. Accessed: 08-05-2020.

[33] Guang-jiong Ni, Guo-hong Yang, Rong-tang Fu and Haibin Wang. Running Coupling Constants of Fermions with Masses in Quantum Electro Dynamics and Quantum Chromo Dynamics. *International Journal of Modern Physics A*, 16(16):2873–2894, Feb 2000. doi:10.1142/S0217751X01001756.

[34] Raymond Brock et al. Handbook of Perturbative QCD: Version 1.0. *Rev. Mod. Phys.*, 67:157–248, Jan 1995. doi:10.1103/RevModPhys.67.157.

[35] Hugh D. Politzer. Reliable Perturbative Results for Strong Interactions? *Phys. Rev. Lett.*, 30:1346–1349, Jun 1973. doi:10.1103/PhysRevLett.30.1346.

[36] David J. Gross and Frank Wilczek. Asymptotically Free Gauge Theories. I. *Phys. Rev. D*, 8:3633–3652, Nov 1973. doi:10.1103/PhysRevD.8.3633.

[37] David J. Gross and Frank Wilczek. Asymptotically Free Gauge Theories. II. *Phys. Rev. D*, 9:980–993, Feb 1974. doi:10.1103/PhysRevD.9.980.

[38] John C. Collins and Malcolm J. Perry. Superdense Matter: Neutrons or Asymptotically Free Quarks? *Phys. Rev. Lett.*, 34:1353–1356, May 1975. doi:10.1103/PhysRevLett.34.1353.

[39] Masaharu Tanabashi et al. (Particle Data Group). Review of Particle Physics. *Phys. Rev. D*, 98 (030001), 2018. doi:10.1103/PhysRevD.98.030001.

[40] Helmut Satz. Colour Deconfinement and Quarkonium Binding. *Journal of Physics G: Nuclear and Particle Physics*, 32(3):R25–R69, Feb 2006. ISSN 1361-6471. doi:10.1088/0954-3899/32/3/r01.

[41] ALICE Collaboration. The ALICE experiment at the CERN LHC. *Journal of Instrumentation*, 3(08): S08002–S08002, Aug 2008. doi:10.1088/1748-0221/3/08/s08002.

[42] Lyndon Evans and Philip Bryant. LHC Machine. *Journal of Instrumentation*, 3(08):S08001–S08001, Aug 2008. doi:10.1088/1748-0221/3/08/s08001.

[43] Gines Martinez. Advances in Quark Gluon Plasma. `https://arxiv.org/abs/1304.1452`, Apr 2013. Accessed: 13-04-2020.

[44] Alan Chodos, Robert L. Jaffe, Kenneth Johnson, Charles B. Thorn, and Victor F. Weisskopf. New Extended Model of Hadrons. *Phys. Rev. D*, 9:3471–3495, Jun 1974. doi:10.1103/PhysRevD.9.3471.

[45] Frithjof Karsch and Edwin Laermann. Thermodynamics and in-medium Hadron Properties from Lattice QCD. *Quark–Gluon Plasma 3*, pages 1–59, 2004. doi:doi.org/10.1142/9789812795533_0001.

[46] Frithjof Karsch. Lattice QCD at High Temperature and Density. *Lect. Notes Phys.*, 583:209–249, Apr 2002. doi:10.1007/3-540-45792-5_6.

[47] Tapan K. Nayak. Heavy Ions: Results from the Large Hadron Collider. *Pramana*, 79:719–735, 2012. doi:10.1007/s12043-012-0373-7.

[48] Particles and Friends. Evolution of Collisions and QGP. `https://particlesandfriends.wordpress.com/2016/10/14/evolution-of-collisions-and-qgp/`, October 2016. Accessed: 13-04-2020.

[49] Brookhaven National Lab. Alternating Gradient Synchrotron Project: Construction Completion Report. Dec 1966. URL https://www.bnl.gov/cad/accelerator/docs/pdf/AGSDesignReport.pdf. Accessed: 22-01-2021.

[50] Brookhaven National Lab. About Brookhaven. URL https://www.bnl.gov/about/. Accessed: 03-01-2021].

[51] CERN. The Super Proton Synchrotron, . URL https://home.cern/science/accelerators/super-proton-synchrotron. Accessed: 03-01-2021.

[52] Peter Braun-Munzinger and Johanna Stachel. The Quest for the Quark-Gluon Plasma. *Nature*, 448:302–309, Jul 2007. doi:10.1038/nature06080.

[53] WA94 Collaboration WA85 Collaboration. Enhancement of Strange and Multi-strange Hyperons and Anti-Hyperons in S-S and S-W interactions at 200 GeV/c. *Journal of Physics G: Nuclear and Particle Physics*, 25:209, Jan 1999. doi:10.1088/0954-3899/25/2/008.

[54] Ulrich Heinz and Maurice Jacob. Evidence for a New State of Matter: An Assessment of the Results from the CERN Lead Beam Programme. https://arxiv.org/abs/nucl-th/0002042, 2000. Accessed: 13-04-2020.

[55] CERN. New State of Matter created at CERN. https://home.cern/news/press-release/cern/new-state-matter-created-cern, . Accessed: 25-11-2019.

[56] NA44 Collaboration. Strange Meson Enhancement in Pb–Pb Collisions. *Phys. Lett. B*, 471:6–12, 1999. doi:10.1016/S0370-2693(99)01327-1.

[57] NA44 Collaboration. Collective Expansion in High-Energy Heavy Ion Collisions. *Phys. Rev. Lett.*, 78:2080–2083, 1997. doi:10.1103/PhysRevLett.78.2080.

[58] NA45 Collaboration. Recent Results from Pb-Au Collisions at 158 GeV/c per Nucleon Obtained with the CERES Spectrometer. *Nuclear Physics A*, 661(1):23 – 32, 1999. ISSN 0375-9474. doi:10.1016/S0375-9474(99)85005-2.

[59] NA45 Collaboration. Low-mass e^+e^- Pair Production in 158 A GeV Pb–Au Collisions at the CERN SPS, its Dependence on Multiplicity and Transverse Momentum. *Physics Letters B*, 422 (1-4):405–412, Mar 1998. ISSN 0370-2693. doi:10.1016/s0370-2693(98)00083-5.

[60] NA49 Collaboration. Hadron Production in Nuclear Collisions from the NA49 experiment at 158-GeV/c/A. *Nucl. Phys. A*, 661:45–54, 1999. doi:10.1016/S0375-9474(99)85007-6.

[61] NA49 Collaboration. Hadronic Expansion Dynamics in Central Pb+Pb Collisions at 158 GeV per Nucleon. *The European Physical Journal C*, 2(4):661–670, May 1998. ISSN 1434-6052. doi:10.1007/s100529800866.

[62] NA50 Collaboration. Observation of a Threshold Effect in the Anomalous J/Ψ Suppression. *Phys. Lett. B*, 450:456–466, 1999. doi:10.1016/S0370-2693(99)00178-1.

[63] NA50 Collaboration. Anomalous J /Ψ Suppression in Pb–Pb Interactions at 158 GeV/c per Nucleon. *Phys. Lett. B*, 410:337–343, 1997. doi:10.1016/S0370-2693(97)00915-5.

[64] NA52 Collaboration. Impact Parameter Dependence of $K^{\pm}$, p, $\bar{p}$, d and $\bar{d}$ production in fixed target Pb + Pb Collisions at 158-GeV per Nucleon. *New J. Phys.*, 1:22, 1999. doi:10.1088/1367-2630/1/1/322.

[65] NA52 Collaboration. Baryon and Antibaryon Production in lead-lead Collisions at 158 A GeV/c. *Physics Letters B*, 417(1-2):202–210, January 1998. doi:10.1016/S0370-2693(97)01383-X.

[66] WA97 Collaboration. Transverse Mass Spectra of Strange and Multistrange Particles in Pb–Pb Collisions at 158-A-GeV/c. *Eur. Phys. J. C*, 14:633–641, 2000. doi:10.1007/s100520000386.

[67] WA97 Collaboration. Production of Strange and Multistrange Hadrons in Nucleus Nucleus Collisions at the SPS. *Nucl. Phys. A*, 661:130–139, 1999. doi:10.1016/S0375-9474(99)85015-5.

[68] M. M. Aggarwal et al. Centrality Dependence of Neutral Pion Production in 158-A-GeV ^{208}Pb + ^{208}Pb Collisions. *Phys. Rev. Lett.*, 81:4087–4091, 1998. doi:10.1103/PhysRevLett.81.4087. [Erratum: Phys.Rev.Lett. 84, 578–579 (2000)].

[69] WA98 Collaboration. Freeze-out parameters in central 158A gev $^{208}pb + pb$ collisions. *Phys. Rev. Lett.*, 83:926–930, Aug 1999. doi:10.1103/PhysRevLett.83.926.

[70] BRAHMS Collaboration. Quark Gluon Plasma and Color Glass Condensate at RHIC? The Perspective from the BRAHMS Experiment. *Nucl. Phys.*, A757:1–27, 2005. doi:10.1016/j.nuclphysa.2005.02.130.

[71] PHENIX Collaboration. Formation of Dense Partonic Matter in Relativistic Nucleus-Nucleus Collisions at RHIC: Experimental Evaluation by the PHENIX Collaboration. *Nucl. Phys.*, A757:184–283, 2005. doi:10.1016/j.nuclphysa.2005.03.086.

[72] STAR Collaboration. Experimental and Theoretical Challenges in the Search for the Quark Gluon Plasma: The STAR Collaboration's Critical Assessment of the Evidence from RHIC Collisions. *Nucl. Phys.*, A757:102–183, 2005. doi:10.1016/j.nuclphysa.2005.03.085.

[73] PHOBOS Collaboration. The PHOBOS Perspective on Discoveries at RHIC. *Nucl. Phys.*, A757: 28–101, 2005. doi:10.1016/j.nuclphysa.2005.03.084.

[74] ALICE Collaboration. Direct Photon Production in Pb–Pb Collisions at $\sqrt{s_{NN}}$ = 2.76 TeV. *Physics Letters B*, 754:235–248, Mar 2016. ISSN 0370-2693. doi:10.1016/j.physletb.2016.01.020.

[75] PHENIX Collaboration. Enhanced Production of Direct Photons in Au+Au Collisions at $\sqrt{s_{NN}}$ =200 GeV and Implications for the Initial Temperature. *Physical Review Letters*, 104(13), Mar 2010. ISSN 1079-7114. doi:10.1103/physrevlett.104.132301.

[76] James D. Bjorken. Highly Relativistic Nucleus-Nucleus Collisions: The Central Rapidity Region. *Phys. Rev. D*, 27:140–151, Jan 1983. doi:10.1103/PhysRevD.27.140.

[77] James D. Bjorken. Energy Loss of Energetic Partons in Quark - Gluon Plasma: Possible Extinction of High p_T Jets in Hadron - Hadron Collisions. `https://lss.fnal.gov/archive/preprint/fermilab-pub-82-059-t.shtml`, Aug 1982. Accessed: 13-04-202.

[78] J Casalderrey-Solana, J G Milhano, and U Wiedemann. Jet Quenching via Jet Collimation. *Journal of Physics G: Nuclear and Particle Physics*, 38(12):124086, Nov 2011. ISSN 1361-6471. doi:10.1088/0954-3899/38/12/124086.

[79] Michael L. Miller, Klaus Reygers, Stephen J. Sanders, and Peter Steinberg. Glauber Modeling in High Energy Nuclear Collisions. *Ann. Rev. Nucl. Part. Sci.*, 57:205–243, Nov 2007. doi:10.1146/annurev.nucl.57.090506.123020.

[80] Emily Willsher. Investigating Quark-Gluon Plasma Effects With Jets Using Data from ALICE at the LHC, 2016. Unpublished Master's Thesis. University of Birmingham.

[81] ALICE Collaboration. Suppression of Charged Particle Production at Large Transverse Momentum in Central Pb-Pb Collisions at $\sqrt{s_{NN}}$ = 2.76 TeV. *Phys. Lett.*, B696:30–39, 2011. doi:10.1016/j.physletb.2010.12.020.

[82] ALICE Collaboration. Transverse Momentum Distribution and Nuclear Modification Factor of Charged Particles in p+Pb Collisions at $\sqrt{s_{NN}}$ = 5.02 TeV. *Physical Review Letters*, 110(8), Feb 2013. ISSN 1079-7114. doi:10.1103/physrevlett.110.082302.

[83] CMS Collaboration. Observation of Long-Range Near-Side Angular Correlations in Proton-Proton Collisions at the LHC. *JHEP*, 09:091, 2010. doi:10.1007/JHEP09(2010)091.

[84] CMS Collaboration. Measurement of Long-Range Near-Side Two-Particle Angular Correlations in pp Collisions at $\sqrt{s} = 13$ TeV. *Physical Review Letters*, 116(17), Apr 2016. ISSN 1079-7114. doi:10.1103/physrevlett.116.172302.

[85] CMS Collaboration. Observation of Long-range, Near-side Angular Correlations in pPb Collisions at the LHC. *Physics Letters B*, 718(3):795–814, Jan 2013. ISSN 0370-2693. doi:10.1016/j.physletb.2012.11.025.

[86] Jiangyong Jia. Long-range Correlations in Proton-lead Collisions at = 5.02 TeV from ATLAS. *Journal of Physics: Conference Series*, 458:012023, Aug 2013. ISSN 1742-6596. doi:10.1088/1742-6596/458/1/012023.

[87] ALICE Collaboration. Particle-Yield Modification in Jetlike Azimuthal Dihadron Correlations in Pb-Pb Collisions at $\sqrt{s_{\mathrm{NN}}} = 2.76$ TeV. *Phys. Rev. Lett.*, 108:092301, Mar 2012. doi:10.1103/PhysRevLett.108.092301.

[88] Taku Matsui and Helmut Satz. J/Ψ Suppression by Quark-Gluon Plasma Formation. *Physics Letters B*, 178(4):416 – 422, Oct 1986. ISSN 0370-2693. doi:10.1016/0370-2693(86)91404-8.

[89] ALICE Collaboration. Centrality, Rapidity and Transverse Momentum Dependence of J/Ψ Suppression in Pb–Pb Collisions at $\sqrt{s_{NN}}$ = 2.76 TeV. *Physics Letters B*, 734:314–327, Jun 2014. ISSN 0370-2693. doi:10.1016/j.physletb.2014.05.064.

[90] PHENIX Collaboration. J/Ψ Suppression at Forward Rapidity in Au+Au Collisions at $\sqrt{s_{NN}}$ = 200 GeV. *Physical Review C*, 84(5), Nov 2011. ISSN 1089-490X. doi:10.1103/physrevc.84.054912.

[91] NA50 Collaboration. Quarkonium Production and Suppression in Pb+Pb and p+A Collisions at SPS Energies. *Nuclear Physics A*, 774:59–66, 2006. ISSN 0375-9474. doi:10.1016/j.nuclphysa.2006.06.029.

[92] NA50 Collaboration. Transverse Momentum Dependence of Charmonium Suppression in Pb-Pb Collisions at the CERN SPS. *Nuclear Physics A*, 749:243–250, 2005. ISSN 0375-9474. doi:10.1016/j.nuclphysa.2004.12.046.

[93] NA50 Collaboration. A New Measurement of J/psi Suppression in Pb-Pb Collisions at 158-GeV per Nucleon. *Eur. Phys. J. C*, 39:335–345, 2005. doi:10.1140/epjc/s2004-02107-9.

[94] PHENIX Collaboration. J/Ψ Production versus Centrality, Transverse Momentum, and Rapidity in Au+Au Collisions at $\sqrt{s_{NN}}$ = 200 GeV. *Physical Review Letters*, 98(23), Jun 2007. ISSN 1079-7114. doi:10.1103/physrevlett.98.232301.

[95] PHENIX Collaboration. J/Ψ Production at RHIC-PHENIX. *Journal of Physics G: Nuclear and Particle Physics*, 35(10):104134, Sep 2008. ISSN 1361-6471. doi:10.1088/0954-3899/35/10/104134.

[96] Jean-Yves Ollitrault. Anisotropy as a Signature of Transverse Collective Flow. *Phys. Rev. D*, 46: 229–245, Jul 1992. doi:10.1103/PhysRevD.46.229.

[97] E877 Collaboration. Energy and Charged Particle Flow in 10.8 A GeV/c Au+Au Collisions. *Phys. Rev. C*, 73(19):2532–2535, Nov 1994. ISSN 0031-9007. doi:10.1103/physrevlett.73.2532.

[98] NA49 Collaboration. Directed and Elliptic Flow of Charged Pions and Protons in Pb+Pb Collisions at 40A and 158A GeV. *Physical Review C*, 68(3), Sep 2003. ISSN 1089-490X. doi:10.1103/physrevc.68.034903.

[99] STAR Collaboration. Elliptic Flow in Au+Au Collisions at $\sqrt{s_{NN}}$ = 130 GeV. *Physical Review Letters*, 86(3):402–407, Jan 2001. ISSN 1079-7114. doi:10.1103/physrevlett.86.402.

[100] Sergei Voloshin and Y. Zhang. Flow Study in Relativistic Nuclear Collisions by Fourier Expansion of Azimuthal Particle Distributions. *Zeitschrift fur Physik C Particles and Fields*, 70(4):665–671, May 1996. ISSN 1431-5858. doi:10.1007/s002880050141.

[101] Arthur M. Poskanzer and Sergei A. Voloshin. Methods for Analyzing Anisotropic Flow in Relativistic Nuclear Collisions. *Physical Review C*, 58(3):1671–1678, Sep 1998. ISSN 1089-490X. doi:10.1103/physrevc.58.1671.

[102] Sergei A. Voloshin, Arthur M. Poskanzer, and Raimond Snellings. Collective Phenomena in Non-Central Nuclear Collisions. `https://arxiv.org/abs/0809.2949`, Sep 2008. Accessed: 13-04-2020.

[103] Pavel K. Kovtun, Dan T. Son, and Andrei O. Starinets. Viscosity in Strongly Interacting Quantum Field Theories from Black Hole Physics. *Phys. Rev. Lett.*, 94:111601, Mar 2005. doi:10.1103/PhysRevLett.94.111601.

[104] Charles Gale, Sangyong Jeon, Björn Schenke, Prithwish Tribedy, and Raju Venugopalan. Event-by-Event Anisotropic Flow in Heavy-ion Collisions from Combined Yang-Mills and Viscous Fluid Dynamics. *Phys. Rev. Lett.*, 110:012302, Jan 2013. doi:10.1103/PhysRevLett.110.012302.

[105] Johann Rafelski and Berndt Müller. Strangeness Production in the Quark-Gluon Plasma. *Phys. Rev. Lett.*, 48:1066–1069, Apr 1982. doi:10.1103/PhysRevLett.48.1066.

[106] E-802 Collaboration. Centrality Dependence of Kaon Yields in Si + A and $Au + Au$ Collisions at Relativistic Energies. *Phys. Rev. C*, 60:044904, Sep 1999. doi:10.1103/PhysRevC.60.044904.

[107] The WA97 Collaboration. Strangeness Enhancement at Midrapidity in Pb-Pb Collisions at 158 A GeV/c: A Comparison with VENUS and RQMD Models. *Eur. Phys. J. C*, 11(1):79–88, Oct 1999. doi:10.1007/s100529900157.

[108] NA44 Collaboration. Strange Meson Enhancement in PbPb Collisions. *Physics Letters B*, 471(1):6 – 12, Dec 1999. ISSN 0370-2693. doi:10.1016/S0370-2693(99)01327-1.

[109] NA35 Collaboration. A Study of K^0_S, Λ and $\bar{\Lambda}$ Production in 60 GeV and 200 GeV per Nucleon O-Au and p-Au Collisions With a Streamer Chamber Detector at the CERN SPS. *Z. Phys.*, C43:25, Jan 1989. doi:10.1007/BF02430607.

[110] WA85 Collaboration. Ξ^-, Ξ^+, Λ and $\bar{\Lambda}$ Production in Sulphur-Tungsten Interactions at 200 GeV/c per Nucleon. *Physics Letters B*, 270(1):123 – 127, Nov 1991. ISSN 0370-2693. doi:10.1016/0370-2693(91)91548-A.

[111] WA85 Collaboration. Observation of Ω^- and Ω^+ in Sulphur-Tungsten Interactions at 200 GeV/c per Nucleon. *Physics Letters B*, 316(4):615 – 619, Oct 1993. ISSN 0370-2693. doi:10.1016/0370-2693(93)91052-O.

[112] NA57 Collaboration. Energy Dependence of Hyperon Production in Nucleus–Nucleus Collisions at SPS. *Physics Letters B*, 595(1):68 – 74, Aug 2004. ISSN 0370-2693. doi:10.1016/j.physletb.2004.05.025.

[113] NA57 Collaboration. Enhancement of Hyperon Production at Central Rapidity in 158A GeV/c Pb–Pb Collisions. *Journal of Physics G: Nuclear and Particle Physics*, 32(4):427–441, Feb 2006. doi:10.1088/0954-3899/32/4/003.

[114] NA57 Collaboration. Strangeness Enhancements at Central Rapidity in 40 A GeV/c Pb–Pb Collisions. *Journal of Physics G: Nuclear and Particle Physics*, 37(4):045105, Mar 2010. ISSN 1361-6471. doi:10.1088/0954-3899/37/4/045105.

[115] STAR Collaboration. Strangeness Enhancement in Cu-Cu and Au-Au Collisions at $\sqrt{s_{NN}} =$ 200 GeV. *Phys. Rev. Lett.*, 108:072301, Feb 2012. doi:10.1103/PhysRevLett.108.072301.

[116] ALICE Collaboration. Multi-strange Baryon Production at Mid-Rapidity in Pb–Pb Collisions at $\sqrt{s_{NN}}$ 0 =2.76 TeV. *Physics Letters B*, 728:216 – 227, Jan 2014. ISSN 0370-2693. doi:10.1016/j.physletb.2013.11.048.

[117] ALICE Collaboration. Multi-strange Baryon Production in p-Pb Collisions at $\sqrt{s_{\mathbf{NN}}} = 5.02$ TeV. *Phys. Lett.*, B758:389–401, Jul 2016. doi:10.1016/j.physletb.2016.05.027.

[118] Torbjörn Sjöstrand, Stephen Mrenna, and Peter Skands. A Brief Introduction to PYTHIA 8.1. *Computer Physics Communications*, 178(11):852–867, Jun 2008. ISSN 0010-4655. doi:10.1016/j.cpc.2008.01.036.

[119] Tanguy Pierog, Iu. Karpenko, Judith M. Katzy, Elena Yatsenko, and Klaus Ulrich Werner. EPOS LHC : Test of Collective Hadronization with LHC Data. `https://arxiv.org/abs/1306.0121v2`, Dec 2013. Accessed: 13-04-2020.

[120] Christian Bierlich and Jesper Roy Christiansen. Effects of Color Reconnection on Hadron Flavor Observables. *Phys. Rev. D*, 92:094010, Nov 2015. doi:10.1103/PhysRevD.92.094010. URL `https://link.aps.org/doi/10.1103/PhysRevD.92.094010`.

[121] Bo Andersson, Gösta Gustafson, Gunnar Ingelman, and Torbjörn Sjöstrand. Parton Fragmentation and String Dynamics. *Physics Reports*, 97(2):31 – 145, 1983. ISSN 0370-1573. doi:10.1016/0370-1573(83)90080-7.

[122] ALICE Collaboration. Enhanced production of multi-strange hadrons in high-multiplicity proton–proton collisions. *Nature Physics*, 13(6):535–539, Apr 2017. ISSN 1745-2481. doi:10.1038/nphys4111.

[123] Francesco Becattini. An Introduction to the Statistical Hadronization Model. `https://arxiv.org/abs/0901.3643`, Jan 2009. Accessed: 13-04-202.

[124] Enrico Fermi. High Energy Nuclear Events. *Progress of Theoretical Physics*, 5(4):570–583, Jul 1950. ISSN 0033-068X. doi:10.1143/ptp/5.4.570.

[125] Rolf Hagedorn. Statistical Thermodynamics of Strong Interactions at High-Energies. *Nuovo Cim. Suppl.*, 3:147–186, Jan 1965.

[126] Michal Petráň, Jean Letessier, Vojtěch Petráček, and Johann Rafelski. Hadron Production and Quark-Gluon Plasma Hadronization in Pb-Pb Collisions at $\sqrt{s_{NN}}$ = 2.76 TeV. *Physical Review C*, 88(3), Sep 2013. ISSN 1089-490X. doi:10.1103/physrevc.88.034907.

[127] Spencer Wheaton, Jean Cleymans, and Michael Hauer. THERMUS — A Thermal Model Package for ROOT. *Computer Physics Communications*, 180(1):84–106, Jan 2009. ISSN 0010-4655. doi:10.1016/j.cpc.2008.08.001.

[128] Anton Andronic, Peter Braun-Munzinger, and Johanna Stachel. Thermal Hadron Production in Relativistic Nuclear Collisions: The Hadron Mass Spectrum, the Horn, and the

QCD Phase Transition. *Physics Letters B*, 673(2):142 – 145, Mar 2009. ISSN 0370-2693. doi:10.1016/j.physletb.2009.02.014.

[129] ALICE Collaboration. Production of ^{4}He and ^{4}He$^-$ in Pb–Pb collisions at $\sqrt{s_{MM}}$ = 2.76 TeV at the LHC. *Nuclear Physics A*, 971:1 – 20, Mar 2018. ISSN 0375-9474. doi:10.1016/j.nuclphysa.2017.12.004.

[130] Francesco Becattini, Paolo Castorina, Alexander Milov, and Helmut Satz. A Comparative Analysis of Statistical Hadron Production. *Eur. Phys. J. C*, 66:377–386, Feb 2010. doi:10.1140/epjc/s10052-010-1265-y.

[131] ALICE Collaboration. Multiplicity Dependence of Light-Flavor Hadron Production in pp Collisions at $\sqrt{s} = 7$ TeV. *Phys. Rev. C*, 99:024906, Feb 2019. doi:10.1103/PhysRevC.99.024906.

[132] Yuuka Kanakubo, Michito Okai, Yasuki Tachibana, and Tetsufumi Hirano. Strangeness Enhancement in p + p, p + Pb, and Pb + Pb Collisions at LHC Energies. *Proceedings of the 8th International Conference on Quarks and Nuclear Physics (QNP2018)*, Nov 2019. doi:10.7566/jpscp.26.031021.

[133] Constantino Tsallis. Possible Generalization of Boltzmann-Gibbs Statistics. *J. Statist. Phys.*, 52: 479–487, Jul 1988. doi:10.1007/BF01016429.

[134] Ekkard Schnedermann, Josef Sollfrank, and Ulrich Heinz. Thermal Phenomenology of Hadrons from 200A GeV S+S Collisions. *Physical Review C*, 48(5):2462–2475, Nov 1993. ISSN 1089-490X. doi:10.1103/physrevc.48.2462.

[135] Oliver Sim Brüning, Paul Collier, P Lebrun, et al. *LHC Design Report*. CERN Yellow Reports: Monographs. CERN, Geneva, Jun 2004. doi:10.5170/CERN-2004-003-V-1.

[136] Ralph Amann, Mike Lamont, and Steve Myers. A Brief History of the LEP Collider. *Nuclear Physics B - Proceedings Supplements*, 109(2):17 – 31, Jun 2002. ISSN 0920-5632. doi:10.1016/S0920-5632(02)90005-8. Proceedings of the 7th Topical Seminar.

[137] CERN. The Super Proton Synchrotron, 2021. URL `https://home.cern/science/accelerators/super-proton-synchrotron`. Accessed: 22-01-2021.

[138] CERN. The Low Energy Ion Ring. `https://home.cern/science/accelerators/low-energy-ion-ring`, 2020. Accessed: 13-04-2020.

[139] Esma Mobs. The CERN Accelerator Complex. Complexe des Accélérateurs du CERN. `https://cds.cern.ch/record/2197559`, Jul 2016. Accessed: 13-04-2020.

[140] The ATLAS Collaboration. The ATLAS Experiment at the CERN Large Hadron Collider. *Journal of Instrumentation*, 3(08):S08003–S08003, aug 2008. doi:10.1088/1748-0221/3/08/s08003.

[141] CMS Collaboration. The CMS Experiment at the CERN LHC. *JINST*, 3:S08004, 2008. doi:10.1088/1748-0221/3/08/S08004.

[142] LHCb Collaboration. The LHCb Detector at the LHC. *JINST*, 3:S08005, 2008. doi:10.1088/1748-0221/3/08/S08005.

[143] ATLAS Collaboration. Observation of a New Particle in the Search for the Standard Model Higgs Boson with the ATLAS Detector at the LHC. *Physics Letters B*, 716(1):1–29, Sep 2012. ISSN 0370-2693. doi:10.1016/j.physletb.2012.08.020.

[144] CMS Collaboration. Observation of a New Boson at a Mass of 125 GeV with the CMS Experiment at the LHC. *Physics Letters B*, 716(1):30–61, Sep 2012. ISSN 0370-2693. doi:10.1016/j.physletb.2012.08.021.

[145] Jean-Luc Caron. LHC Layout.. Schema general du LHC. `http://cds.cern.ch/record/841573`, Sep 1997. Accessed: 13-04-2020.

[146] Danilo Silva de Albuquerque. Multi-strange Hadrons in Pb–Pb collisions at the LHC with ALICE. PhD Thesis, Aug 2019.

[147] Raghunath Sahoo. Relativistic kinematics. `https://arxiv.org/abs/1604.02651`, 2016. Accessed:13-04-2020.

[148] ALICE Collaboration. ALICE Technical Design Report of the Inner Tracking System (ITS). `http://cds.cern.ch/record/391175`, Jun 1999. Accessed: 13-04-2020.

[149] J. Alme, Y. Andres, H. Appelshäuser, et al. The ALICE TPC, a Large 3-dimensional Tracking Device with Fast Readout for Ultra-high Multiplicity Events. *Nuclear Instruments and Methods in Physics Research Section A: Accelerators, Spectrometers, Detectors and Associated Equipment*, 622(1):316 – 367, Oct 2010. ISSN 0168-9002. doi:10.1016/j.nima.2010.04.042.

[150] Hans Bethe. Theory of the Passage of Fast Corpuscular Rays Through Matter. *Annalen Phys.*, 5: 325–400, 1930. doi:10.1002/andp.19303970303.

[151] Felix Bloch. Zur Bremsung Rasch Bewegter Teilchen beim Durchgang durch Materie. *Annalen Phys.*, 408:285–320, 1933. doi:10.1002/andp.19334080303. UCRL-TRANS-1367, UC-34-4.

[152] K. Yagi, T. Hatsuda, and Y. Miake. *Quark-Gluon Plasma: From Big Bang to Little Bang*, page 381. Cambridge University Press, 2008.

[153] ALICE Collaboration. Performance of the ALICE Experiment at the CERN LHC. *Int. J. Mod. Phys.*, A29:1430044, Sep 2014. doi:10.1142/S0217751X14300440.

[154] ALICE Collaboration. Charged-particle Pseudorapidity Density at Mid-rapidity in p–Pb Collisions at $\sqrt{s_{NN}} = 8.16$ TeV. *The European Physical Journal C*, 79(4):307, Apr 2019. ISSN 1434-6052. doi:10.1140/epjc/s10052-019-6801-9.

[155] ALICE Collaboration. Performance of the ALICE VZERO System. *Journal of Instrumentation*, 8 (10):P10016–P10016, Oct 2013. ISSN 1748-0221. doi:10.1088/1748-0221/8/10/p10016.

[156] O. Villalobos Baillie, D. Evans, G.T. Jones, et al. The ALICE Central Trigger Processor. In *11th Workshop on Electronics for LHC and Future Experiments (LECC 2005)*, page 51, Sep 2005.

[157] Haarvard Helstrup and Volker Lindenstruth et al. The ALICE high level trigger. *Journal of Physics G: Nuclear and Particle Physics*, 30(8):S1097–S1100, jul 2004. doi:10.1088/0954-3899/30/8/066.

[158] ALICE Collaboration. Upgrade of the ALICE Readout & Trigger System. 2013. CERN-LHCC-2013-019, ALICE-TDR-015.

[159] Marian et al. Krivda. ALICE Trigger System for LHC Run 3. *PoS*, TWEPP2018:119, 2019. doi:10.22323/1.343.0119.

[160] Gil Sharon and Greg Caswell. Temperature Cycling and Fatigue in Electronics. *Advancing Microelectronics*, 42:18–24, 01 2015.

[161] Wissam Sabbah, Faical Arabi, Oriol Avino-Salvado, et al. Lifetime of Power Electronics Interconnections in Accelerated Test Conditions: High Temperature Storage and Thermal Cycling. *Microelectronics Reliability*, 76-77:444 – 449, 2017. ISSN 0026-2714. doi:10.1016/j.microrel.2017.06.091.

[162] Pierre Billoir. Progressive Track Recognition with a Kalman-like Fitting Procedure. *Computer Physics Communications*, 57(1):390 – 394, Dec 1989. ISSN 0010-4655. doi:10.1016/0010-4655(89)90249-X.

[163] Belikov, Iouri. Event Reconstruction and Particle Identification in the ALICE Experiment at the LHC. *EPJ Web of Conferences*, 70:00029, Apr 2014. doi:10.1051/epjconf/20147000029.

[164] M. Tanabashi, K. Hagiwara, K. Hikasa, et al. Review of Particle Physics. *Phys. Rev. D*, 98:030001, Aug 2018. doi:10.1103/PhysRevD.98.030001.

[165] Stefan Roesler, Ralph E. Engel, and Johannes Ranft. The Monte Carlo Event Generator DPMJET-III. https://arxiv.org/abs/hep-ph/0012252, Dec 2000. Accessed: 13-04-2020.

[166] Alphonse Capella, Uday Sukhatme, Chung-I. Tan, and Jean Trân Thanh Vân. Dual parton model. *Physics Reports*, 236(4):225 – 329, 1994. ISSN 0370-1573. doi:10.1016/0370-1573(94)90064-7.

[167] GEANT4 Collaboration. GEANT4 — a Simulation Toolkit. *Nuclear Instruments and Methods in Physics Research Section A: Accelerators, Spectrometers, Detectors and Associated Equipment*, 506(3):250 – 303, Jul 2003. ISSN 0168-9002. doi:10.1016/S0168-9002(03)01368-8.

[168] Roger Barlow. Systematic Errors: Facts and Fictions. https://arxiv.org/abs/hep-ex/0207026, Jul 2002. Accessed: 13-04-2020.

[169] Kathrin Koch and ALICE Collaboration. π^0 and η measurement with photon conversions in alice in proton-proton collisions at $\sqrt{s} = 7$ TeV. *Nuclear Physics A*, 855(1):281–284, Apr 2011. ISSN 0375-9474. doi:10.1016/j.nuclphysa.2011.02.059.

[170] Danilo Silva de Albuquerque. Multi-strange Hadrons in Pb–Pb collisions at the LHC with ALICE. PhD Thesis, Aug 2019.

[171] Didier Alexandre. Hyperon Production in p-Pb Collisions with ALICE at the LHC. https://etheses.bham.ac.uk/id/eprint/6924/, Jun 2016. Accessed: 13-04-2020.

[172] Emily Willsher. Hadrochemistry of Particle Production in Small Systems with ALICE at the LHC. Strangeness in Quark Matter, 2019. URL https://indico.cern.ch/event/755366/contributions/3396479/.

[173] Emily Willsher. Multi-strange Particle Production in p-Pb Collisions at $\sqrt{s_{NN}} = 8.16$ TeV TeV Measured with ALICE at the LHC. International Nuclear Physics Conference, 2019. URL https://www.iopconferences.org/iop/frontend/reg/absViewDocumentFE.csp?documentID=27237&eventID=1303.

[174] ALICE Collaboration. Charged-particle Pseudorapidity Density at Mid-rapidity in p–Pb collisions at $\sqrt{s_{NN}} = 8.16$ TeV. *The European Physical Journal C*, 79(4), Apr 2019. ISSN 1434-6052. doi:10.1140/epjc/s10052-019-6801-9.

[175] Urich Heinz. Concepts of Heavy-Ion Physics. https://arxiv.org/abs/hep-ph/0407360, Jun 2003. Accessed: 08-05-2020.

[176] Domenico Elia. Strange and identified particle production with ALICE at the LHC. *EPJ Web Conf.*, 95:03008, 2015. doi:10.1051/epjconf/20149503008.

[177] CMS Collaboration. Multiplicity and Rapidity Dependence of Strange Hadron Production in pp, pPb, and PbPb Collisions at the LHC. *Physics Letters B*, 768:103–129, May 2017. ISSN 0370-2693. doi:10.1016/j.physletb.2017.01.075.

[178] ALICE Collaboration. Long-range Angular Correlations on the Near and Away Side in p–Pb Collisions at $\sqrt{s_{NN}}$ = 5.02 TeV. *Physics Letters B*, 719(1-3):29–41, Feb 2013. ISSN 0370-2693. doi:10.1016/j.physletb.2013.01.012.

[179] ATLAS Collaboration. Observation of Associated Near-Side and Away-Side Long-Range Correlations in $\sqrt{s_{NN}}$=5.02 TeV Proton-Lead Collisions with the ATLAS Detector. *Phys. Rev. Lett.*, 110: 182302, May 2013. doi:10.1103/PhysRevLett.110.182302.

[180] ALICE Collaboration. Long-range Angular Correlations of π, K and p in p–Pb Collisions at $\sqrt{s_{NN}}$ = 5.02 TeV. *Physics Letters B*, 726(1-3):164–177, Oct 2013. ISSN 0370-2693. doi:10.1016/j.physletb.2013.08.024.

[181] ALICE Collaboration. Multiplicity Dependence of (Multi-)Strange Hadron Production in proton-proton Collisions at $\sqrt{s}$ = 13 TeV. *Eur. Phys. J.*, C80(2):167, Feb 2020. doi:10.1140/epjc/s10052-020-7673-8.

[182] Michal Šefčík. Strange and Non-strange Light-Flavour Hadron Production in Pb–Pb and p–Pb Collisions at LHC Energies with ALICE. *Springer Proceedings in Physics*, 250:173–176, Oct 2020. doi:10.1007/978-3-030-53448-6_25.

[183] ALICE Collaboration. Multiplicity Dependence of (Multi-)Strange Hadron Production in Proton-Proton Collisions at $\sqrt{s}$=13 TeV. *The European Physical Journal C*, 80(2), Feb 2020. ISSN 1434-6052. doi:10.1140/epjc/s10052-020-7673-8.

[184] ALICE Collaboration. Multi-strange Baryon Production in pp Collisions at $\sqrt{s}$=7 TeV with ALICE. *Physics Letters B*, 712(4-5):309–318, Jun 2012. ISSN 0370-2693. doi:10.1016/j.physletb.2012.05.011.

[185] D.S.D. Albuquerque. Hadronic Resonances, Strange and Multi-strange Particle Production in Xe-Xe and Pb-Pb Collisions with ALICE at the LHC. *Nuclear Physics A*, 982:823 – 826, 2019. doi:10.1016/j.nuclphysa.2018.08.033.

Appendix A

Plots used for the selection of cuts

The plots included here show the signal significance and signal loss for the remaining cuts not shown in the text in chapter 4. These plots were used in the selection of the default cut positions in the analysis as well as the tight and loose cuts used in the evaluation of the systematic errors.

The signal significance is shown in the top panel of each plot by the pink line and the signal loss fraction is shown in the bottom panel. The black points show the results for real data and the red points show the results with Monte Carlo data. The default cuts selected are indicated by the vertical dashed red lines and the cuts used for systematic studies are shown by the vertical dashed orange lines. Figures A.1, A.2 and A.3, A.4, A.5, A.6, A.7 and A.8 show the results for $\Xi^{\pm}$ and figures A.9, A.10 and A.11, A.12, A.13, A.14, A.15 and A.16 show the results for $\Omega^{\pm}$.

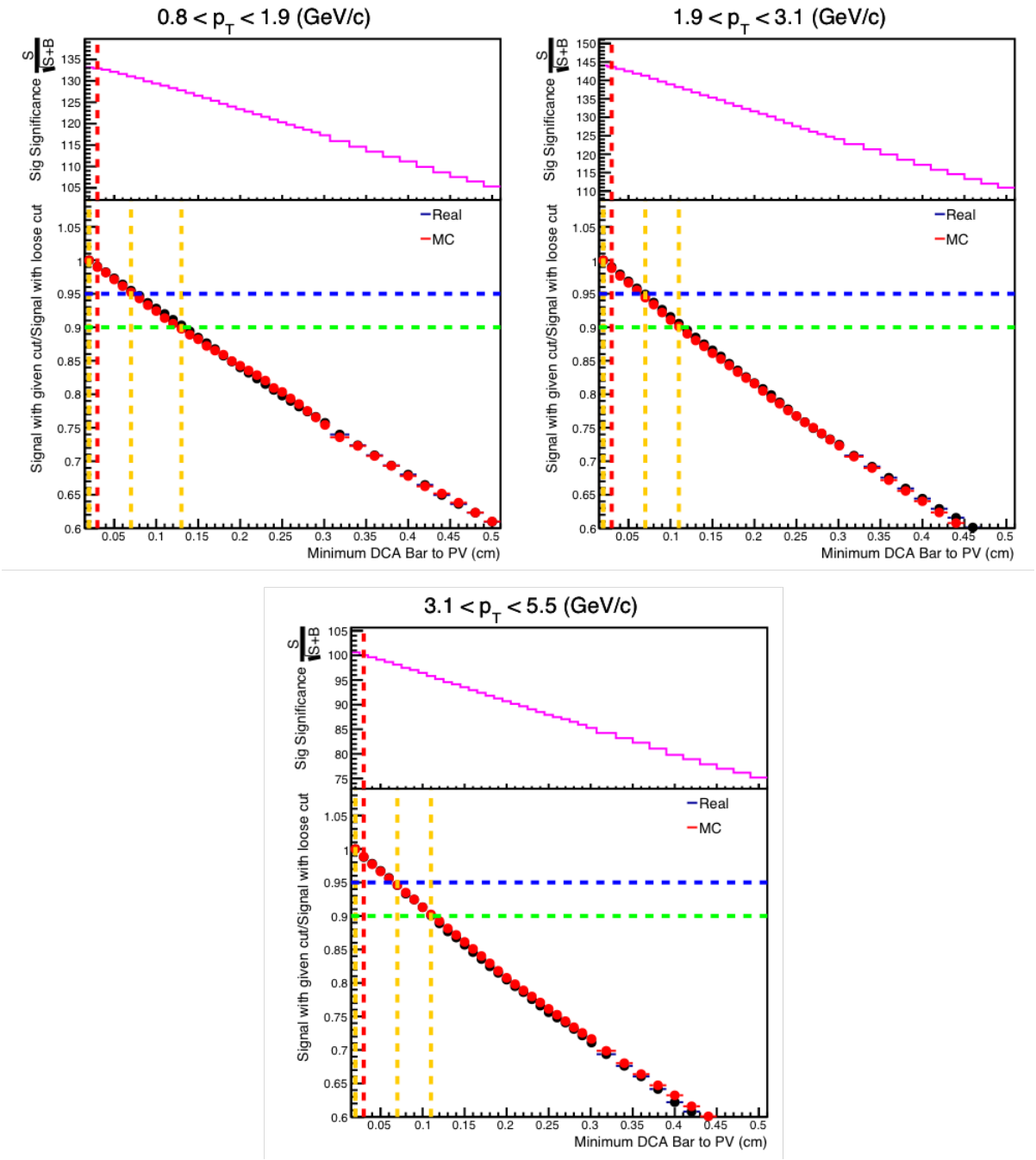

Figure A.1: For each plot, the top shows Signal Significance and the bottom shows Signal losses, with respect to the loosest cut considered for Minimum DCA Baryon to PV. The $\Xi^{\pm}$data are divided into low (top-left), mid (top-right) and high (bottom) p_T bins. Black markers are for real data and red markers are for MC data. Red vertical line indicates default cut and orange vertical lines show loose/tight cuts.

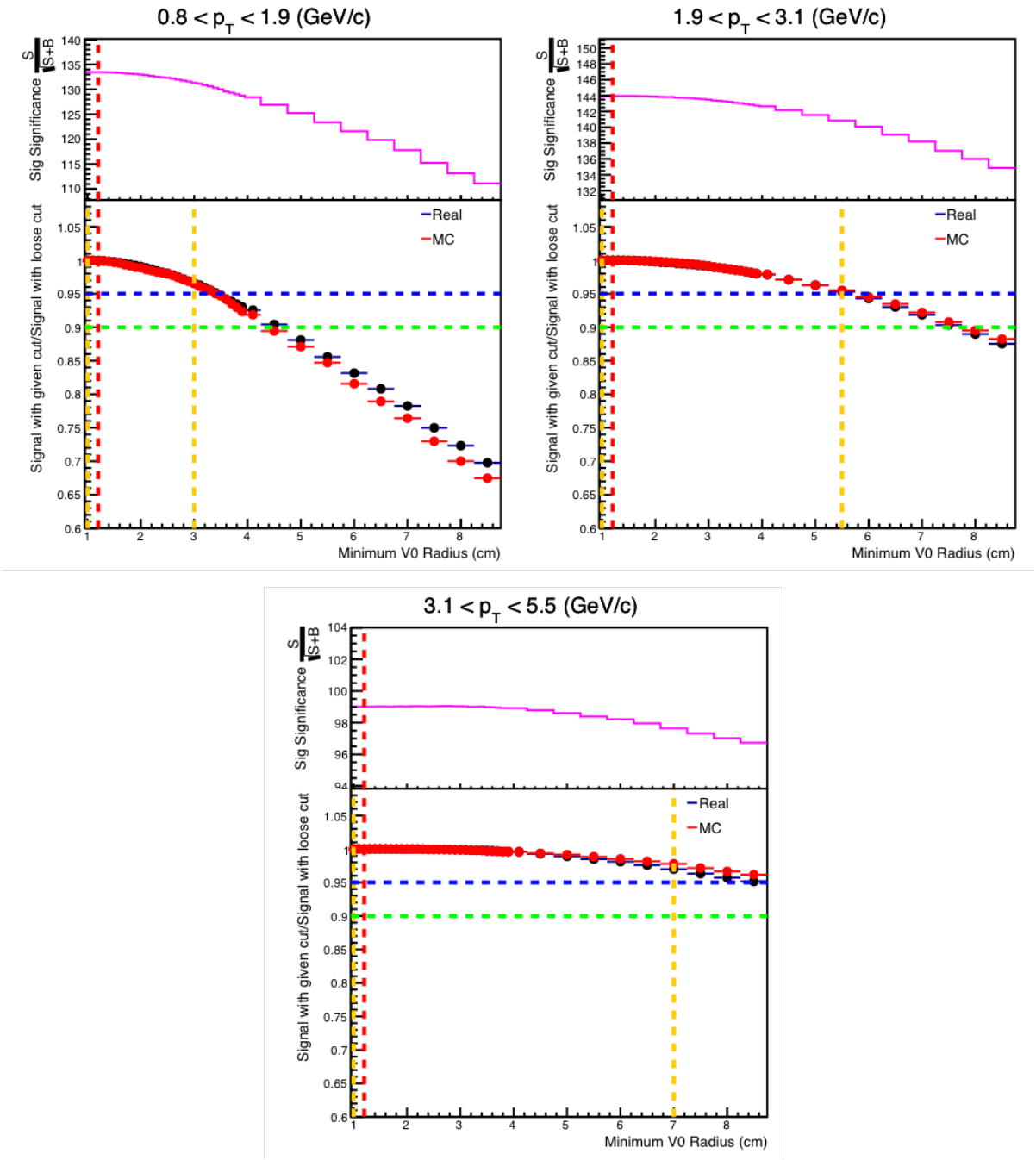

Figure A.2: For each plot, the top shows Signal Significance and the bottom shows Signal losses, with respect to the loosest cut considered for Minimum V0 Radius. The $\Xi^{\pm}$data are divided into low (top-left), mid (top-right) and high (bottom) p_T bins. Black markers are for real data and red markers are for MC data. Red vertical line indicates default cut and orange vertical lines show loose/tight cuts.

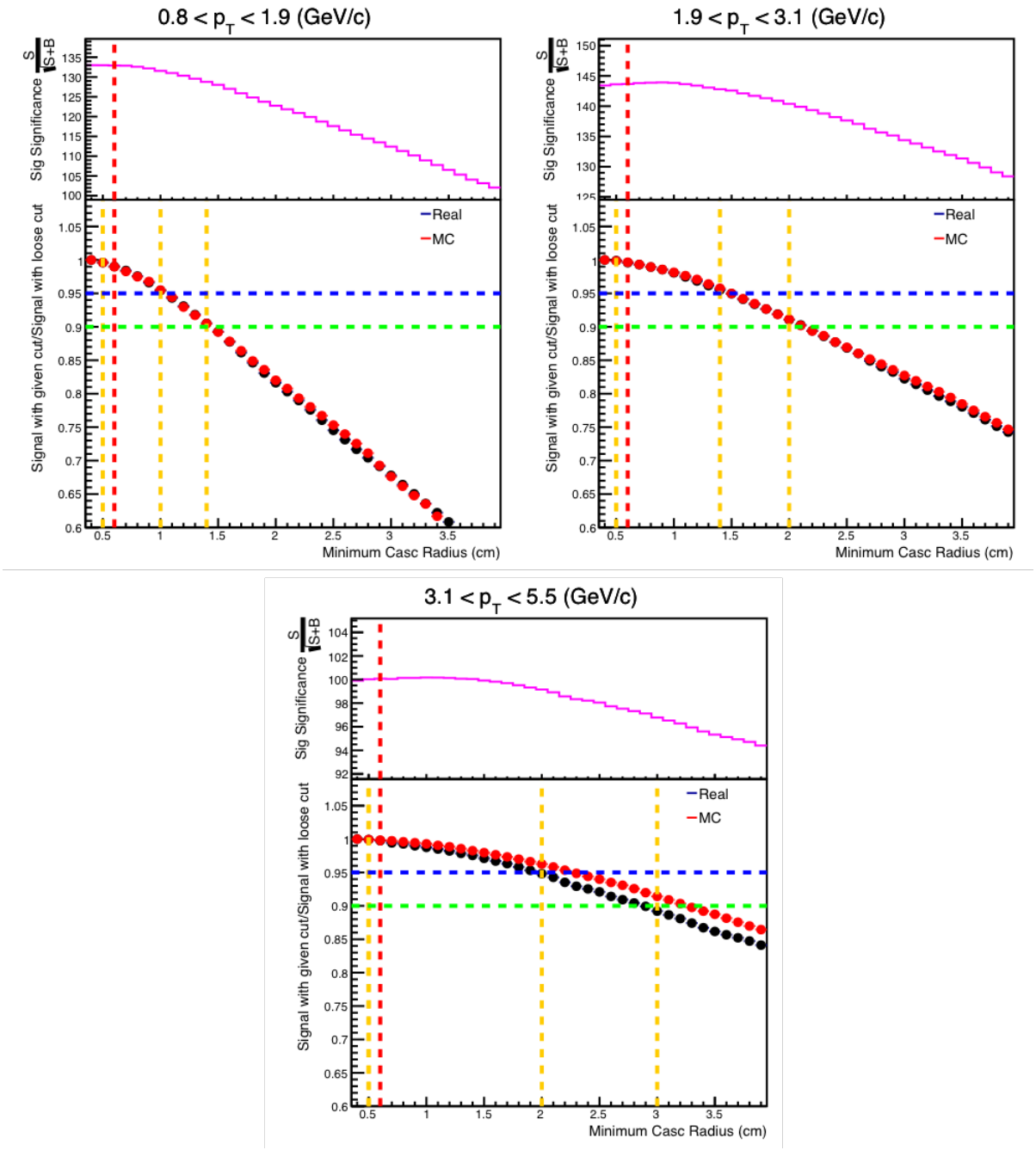

Figure A.3: For each plot, the top shows Signal Significance and the bottom shows Signal losses, with respect to the loosest cut considered for Minimum Cascade Radius. The $\Xi^{\pm}$data are divided into low (top-left), mid (top-right) and high (bottom) p_T bins. Black markers are for real data and red markers are for MC data. Red vertical line indicates default cut and orange vertical lines show loose/tight cuts.

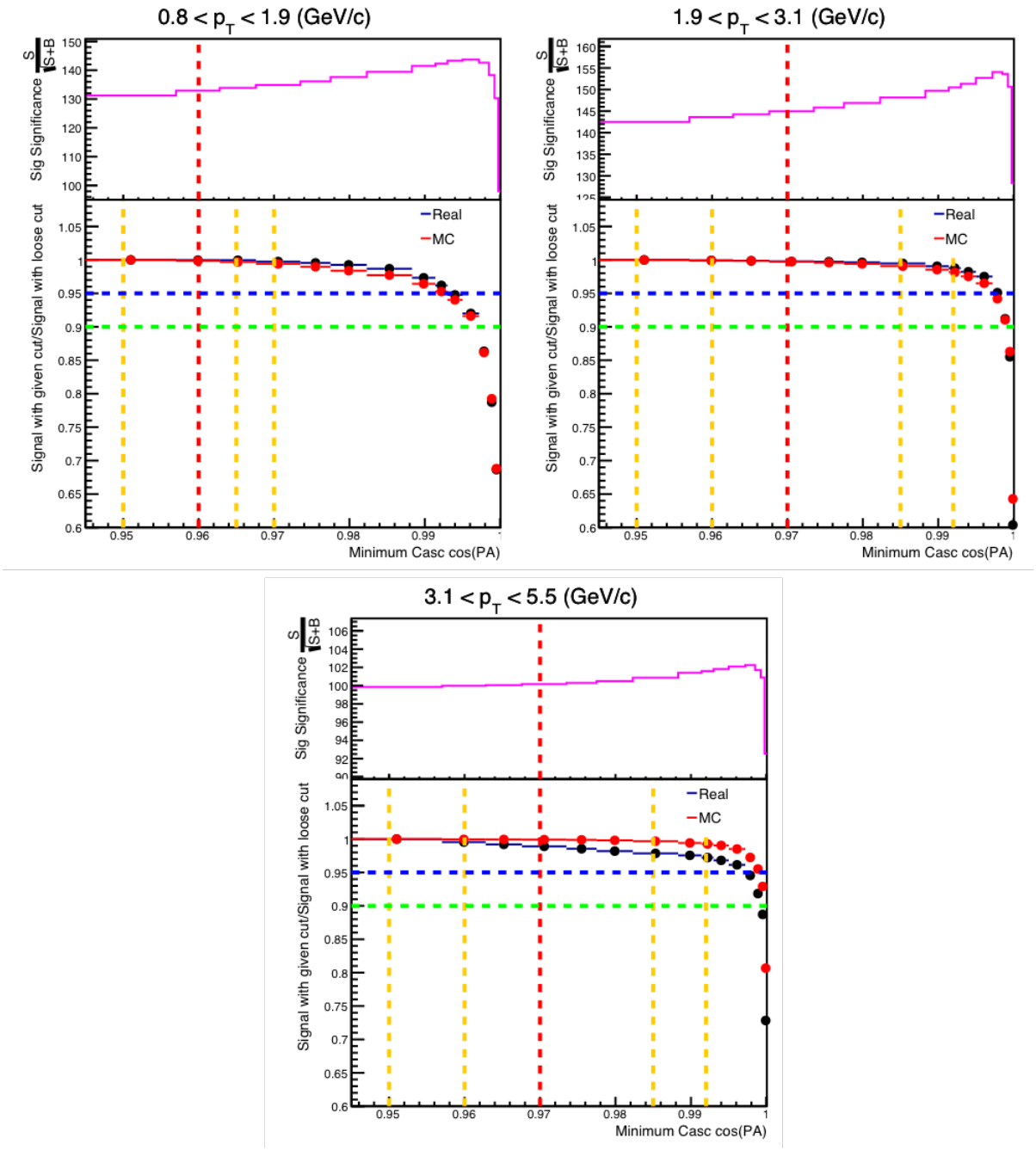

Figure A.4: For each plot, the top shows Signal Significance and the bottom shows Signal losses, with respect to the loosest cut considered for Minimum Cascade cos(PA). The $\Xi^{\pm}$data are divided into low (top-left), mid (top-right) and high (bottom) p_T bins. Black markers are for real data and red markers are for MC data. Red vertical line indicates default cut and orange vertical lines show loose/tight cuts.

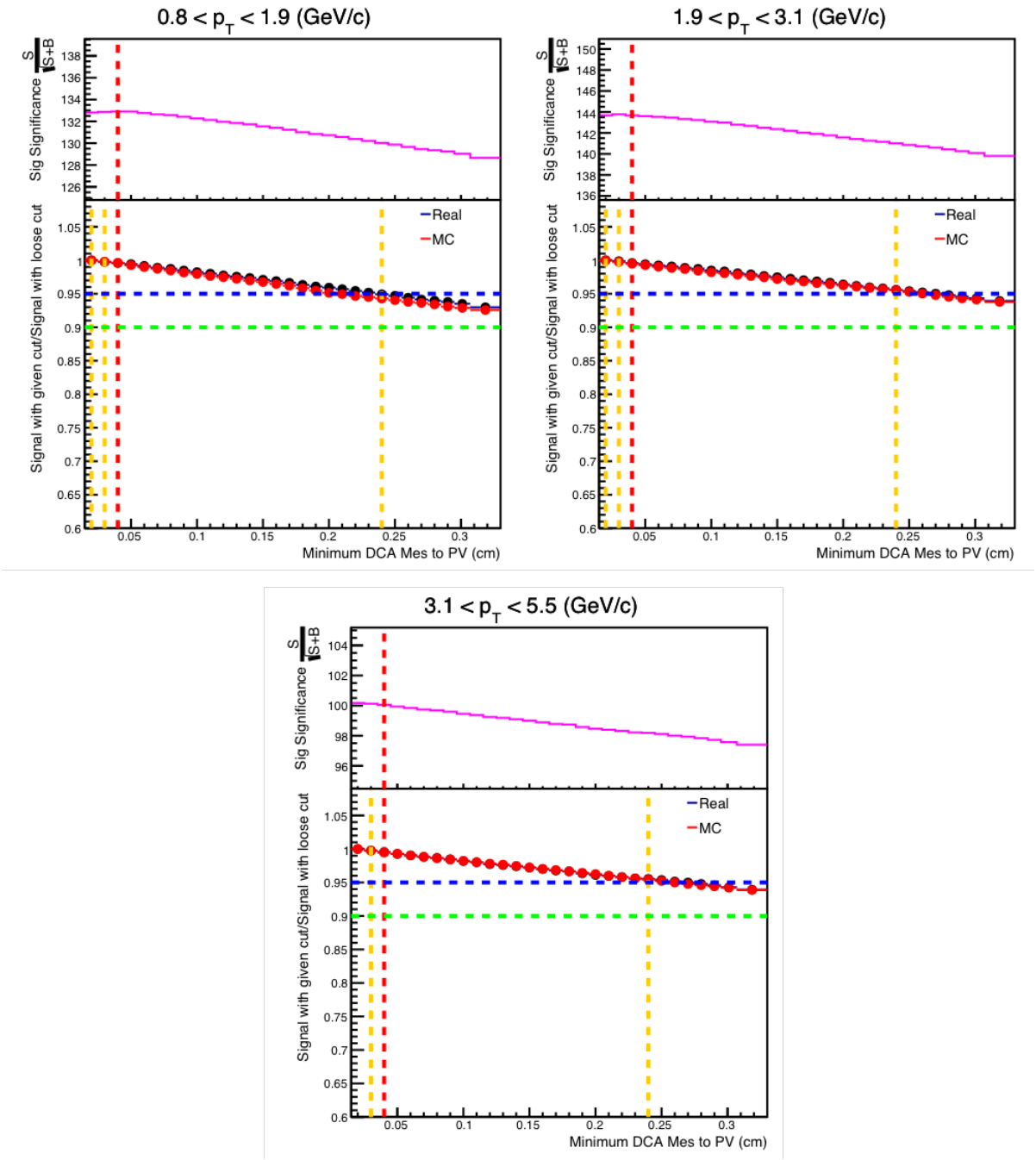

Figure A.5: For each plot, the top shows Signal Significance and the bottom shows Signal losses, with respect to the loosest cut considered for Minimum DCA Meson to PV. The $\Xi^{\pm}$data are divided into low (top-left), mid (top-right) and high (bottom) p_T bins. Black markers are for real data and red markers are for MC data. Red vertical line indicates default cut and orange vertical lines show loose/tight cuts.

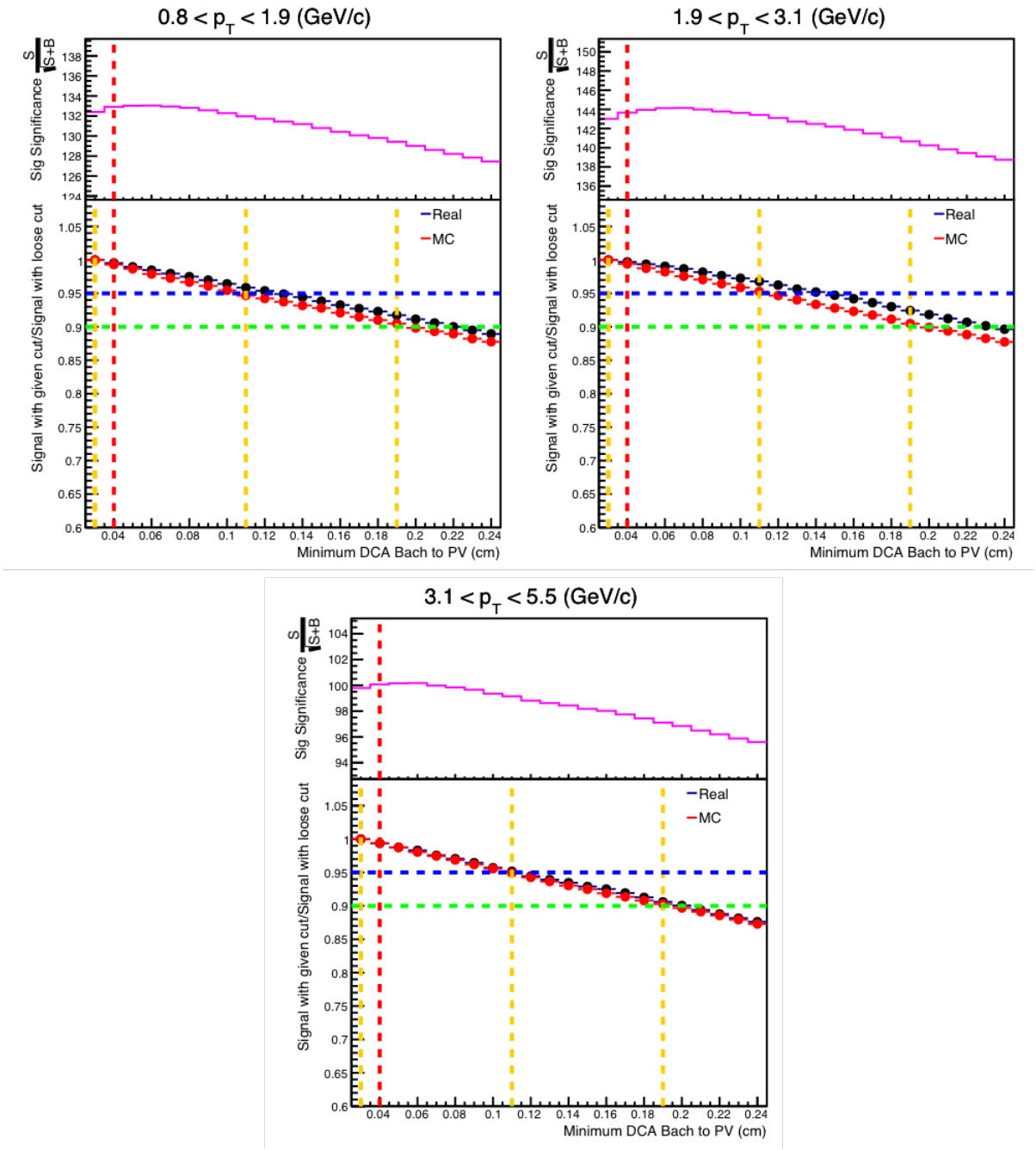

Figure A.6: For each plot, the top shows Signal Significance and the bottom shows Signal losses, with respect to the loosest cut considered for Minimum DCA Bachelor to PV. The $\Xi^{\pm}$data are divided into low (top-left), mid (top-right) and high (bottom) p_T bins. Black markers are for real data and red markers are for MC data. Red vertical line indicates default cut and orange vertical lines show loose/tight cuts.

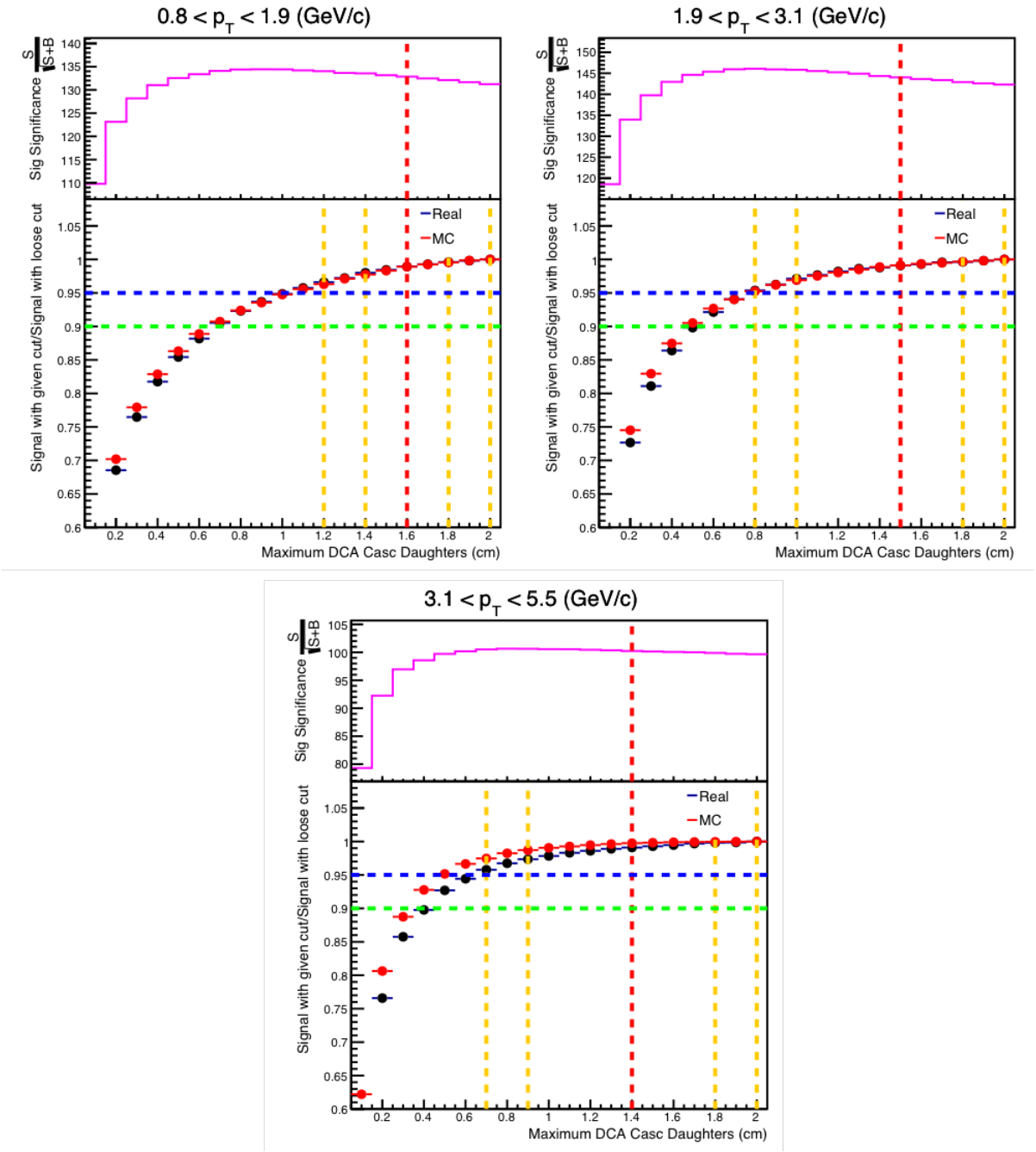

Figure A.7: For each plot, the top shows Signal Significance and the bottom shows Signal losses, with respect to the loosest cut considered for Maximum DCA Cascade Daughters. The $\Xi^{\pm}$data are divided into low (top-left), mid (top-right) and high (bottom) p_T bins. Black markers are for real data and red markers are for MC data. Red vertical line indicates default cut and orange vertical lines show loose/tight cuts.

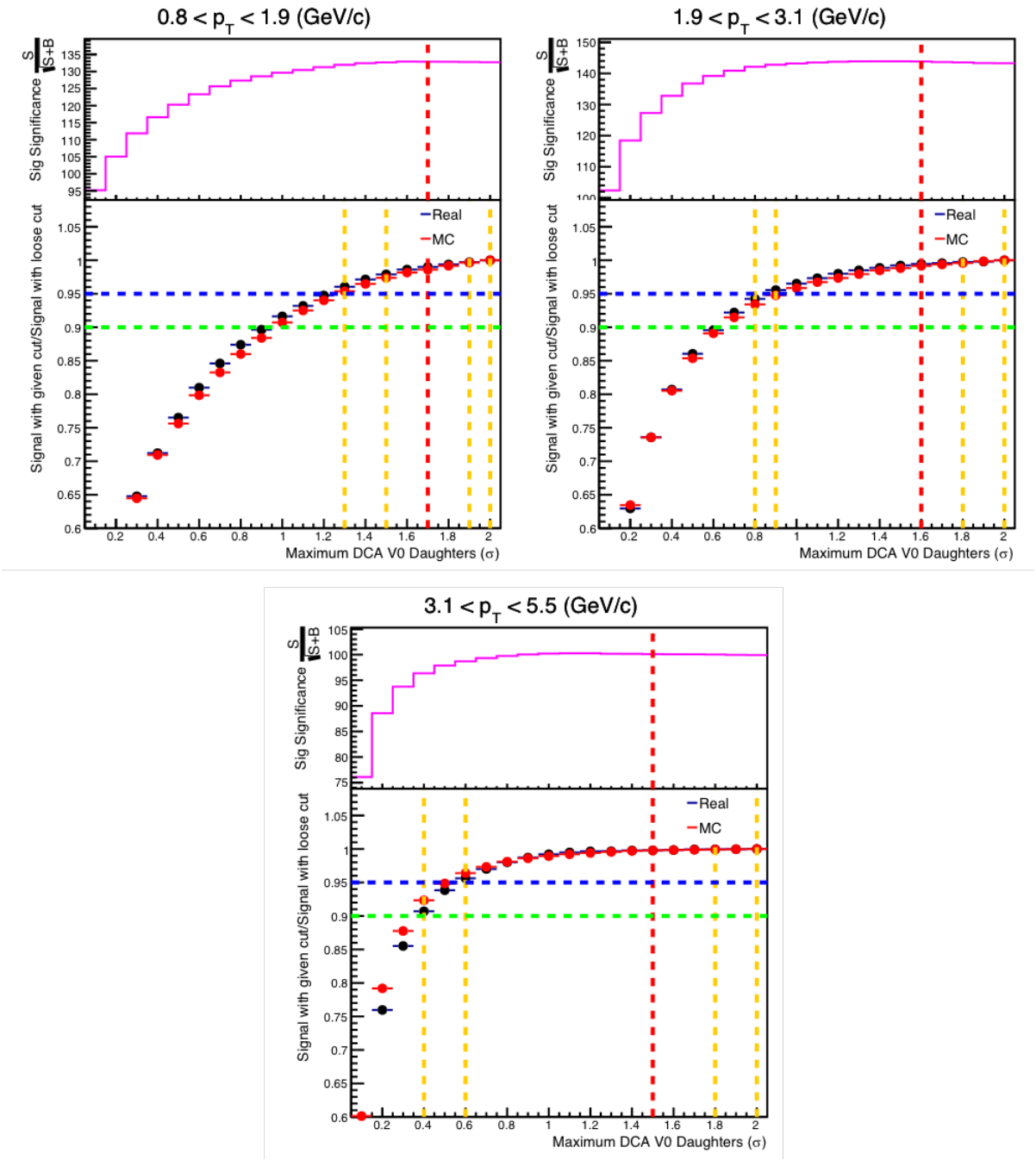

Figure A.8: For each plot, the top shows Signal Significance and the bottom shows Signal losses, with respect to the loosest cut considered for Maximum DCA V0 Daughters. The $\Xi^{\pm}$data are divided into low (top-left), mid (top-right) and high (bottom) p_T bins. Black markers are for real data and red markers are for MC data. Red vertical line indicates default cut and orange vertical lines show loose/tight cuts.

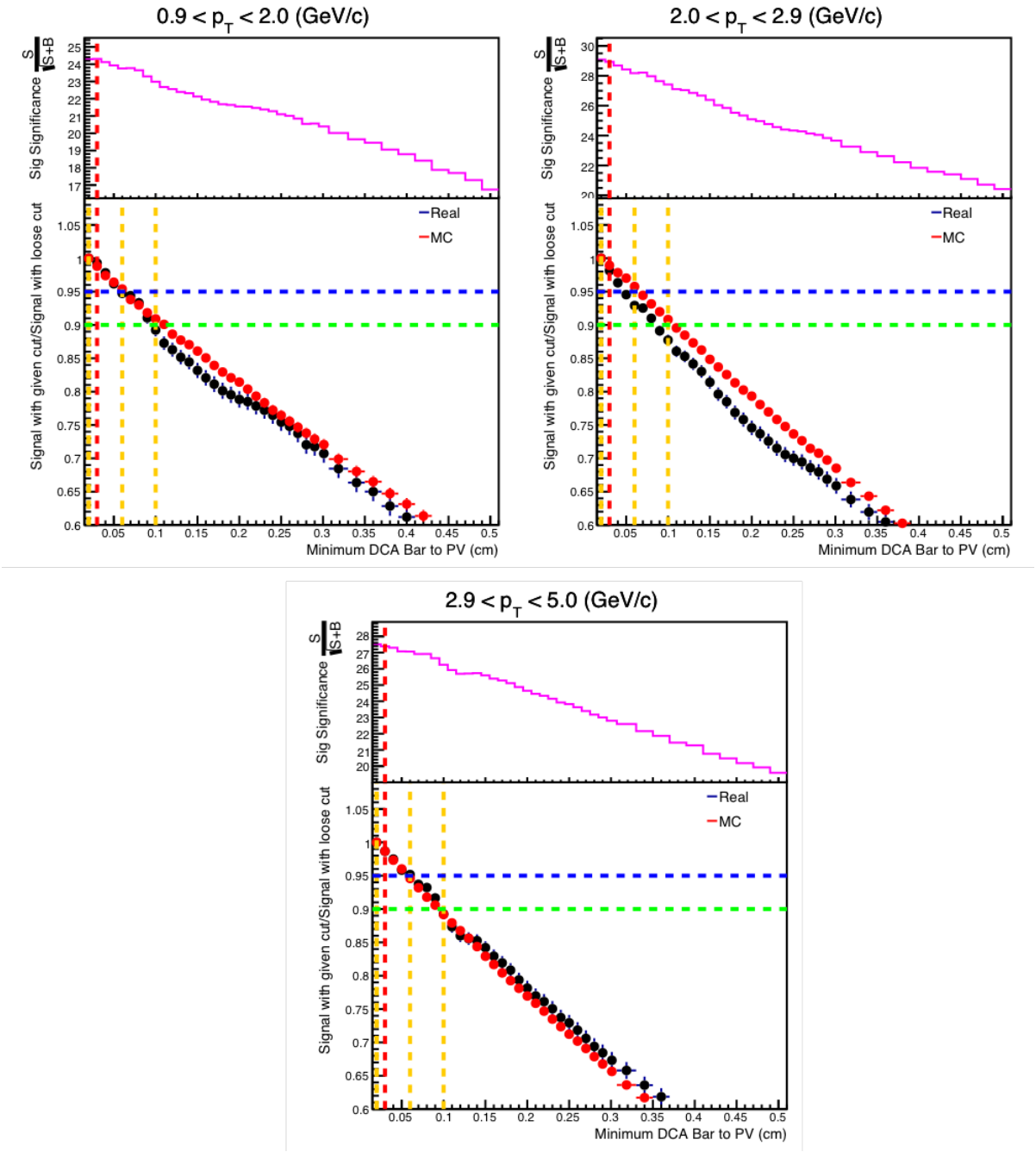

Figure A.9: For each plot, the top shows Signal Significance and the bottom shows Signal losses, with respect to the loosest cut considered for Minimum DCA Baryon to PV. The $\Omega^{\pm}$data are divided into low (top-left), mid (top-right) and high (bottom) p_T bins. Black markers are for real data and red markers are for MC data. Red vertical line indicates default cut and orange vertical lines show loose/tight cuts.

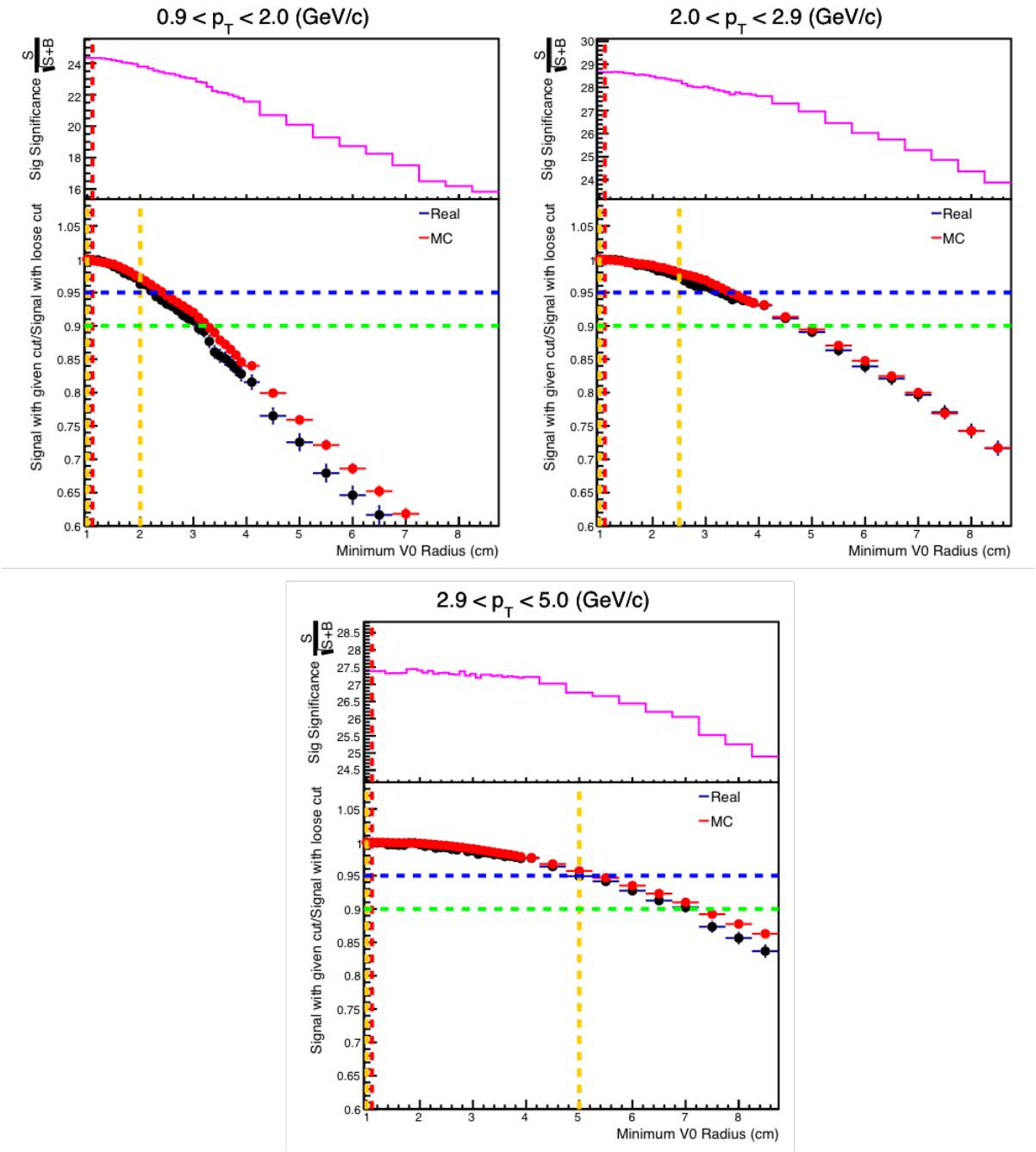

Figure A.10: For each plot, the top shows Signal Significance and the bottom shows Signal losses, with respect to the loosest cut considered for Minimum V0 Radius. The $\Omega^{\pm}$data are divided into low (top-left), mid (top-right) and high (bottom) p_T bins. Black markers are for real data and red markers are for MC data. Red vertical line indicates default cut and orange vertical lines show loose/tight cuts.

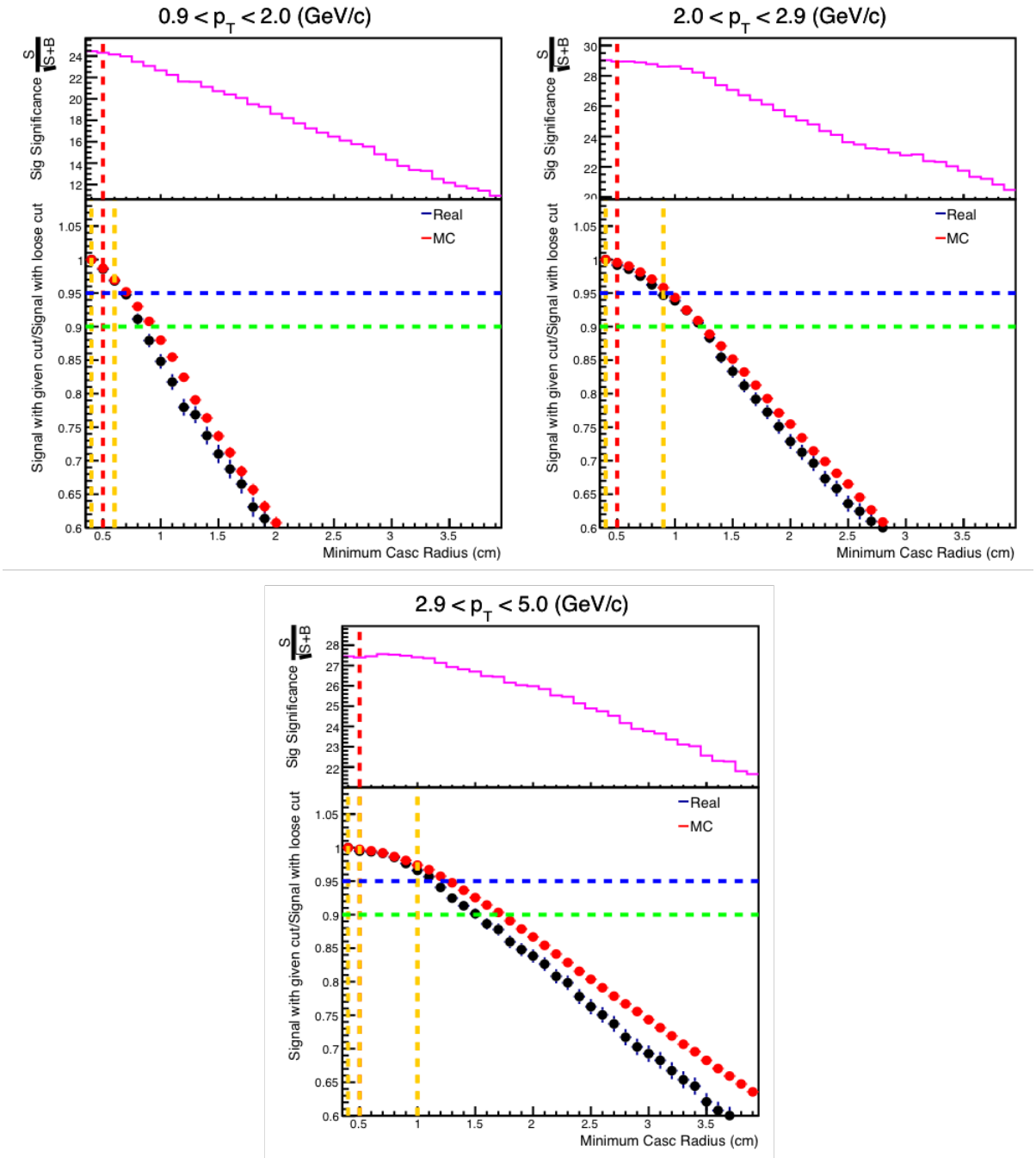

Figure A.11: For each plot, the top shows Signal Significance and the bottom shows Signal losses, with respect to the loosest cut considered for Minimum Cascade Radius. The $\Omega^{\pm}$data are divided into low (top-left), mid (top-right) and high (bottom) p_T bins. Black markers are for real data and red markers are for MC data. Red vertical line indicates default cut and orange vertical lines show loose/tight cuts.

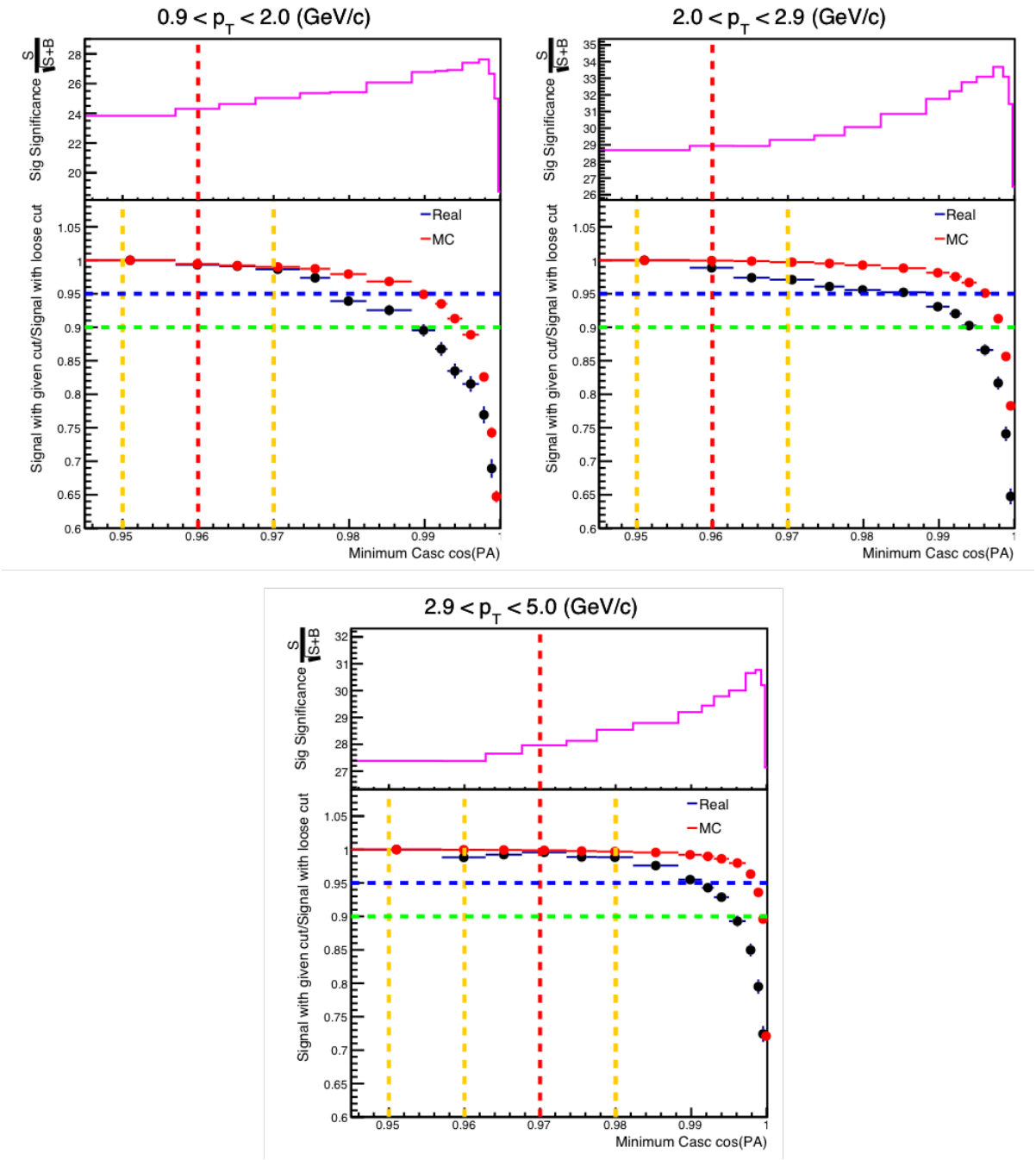

Figure A.12: For each plot, the top shows Signal Significance and the bottom shows Signal losses, with respect to the loosest cut considered for Minimum Cascade cos(PA). The $\Omega^{\pm}$data are divided into low (top-left), mid (top-right) and high (bottom) p_T bins. Black markers are for real data and red markers are for MC data. Red vertical line indicates default cut and orange vertical lines show loose/tight cuts.

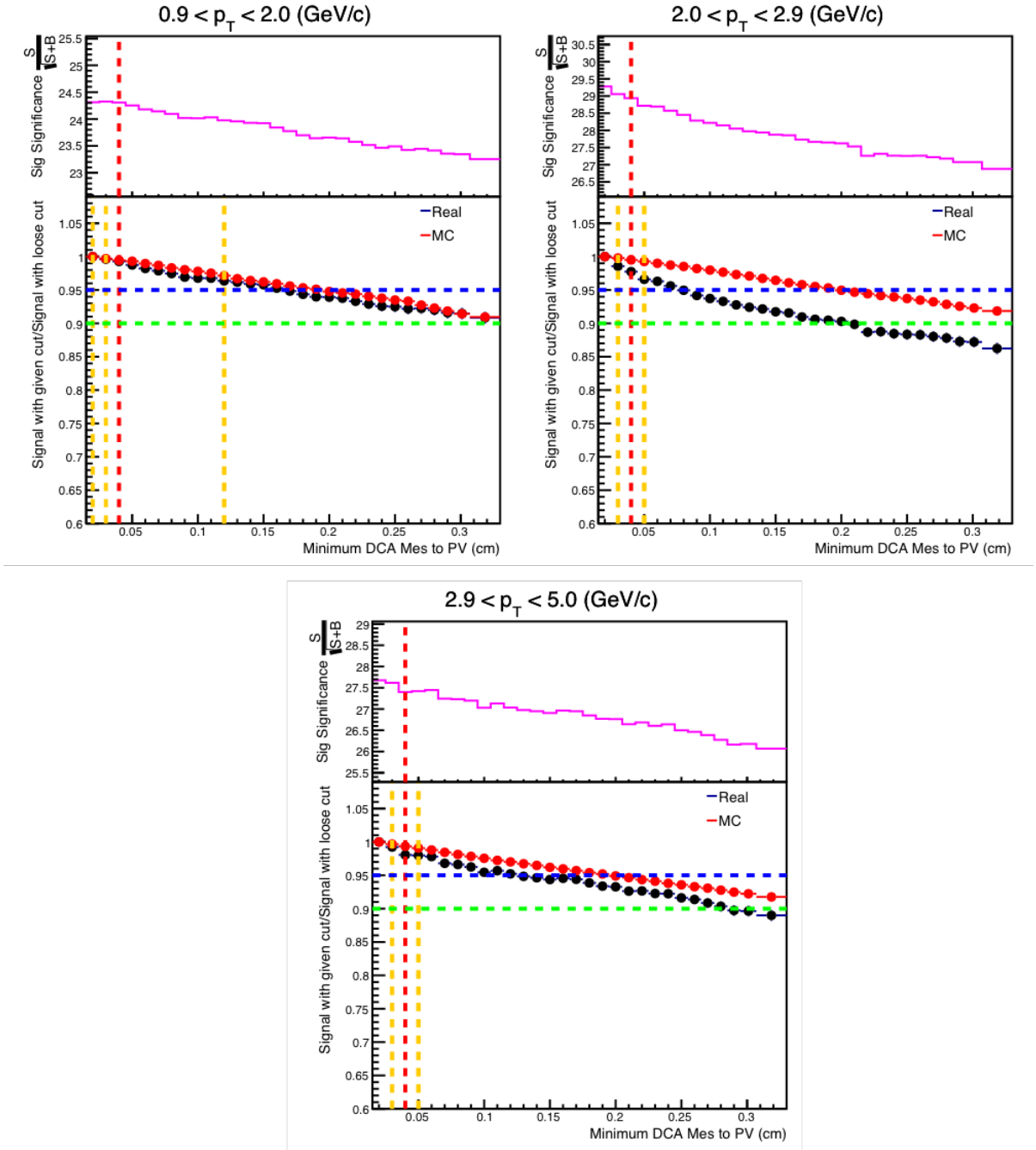

Figure A.13: For each plot, the top shows Signal Significance and the bottom shows Signal losses, with respect to the loosest cut considered for Minimum DCA Meson to PV. The $\Omega^{\pm}$data are divided into low (top-left), mid (top-right) and high (bottom) p_T bins. Black markers are for real data and red markers are for MC data. Red vertical line indicates default cut and orange vertical lines show loose/tight cuts.

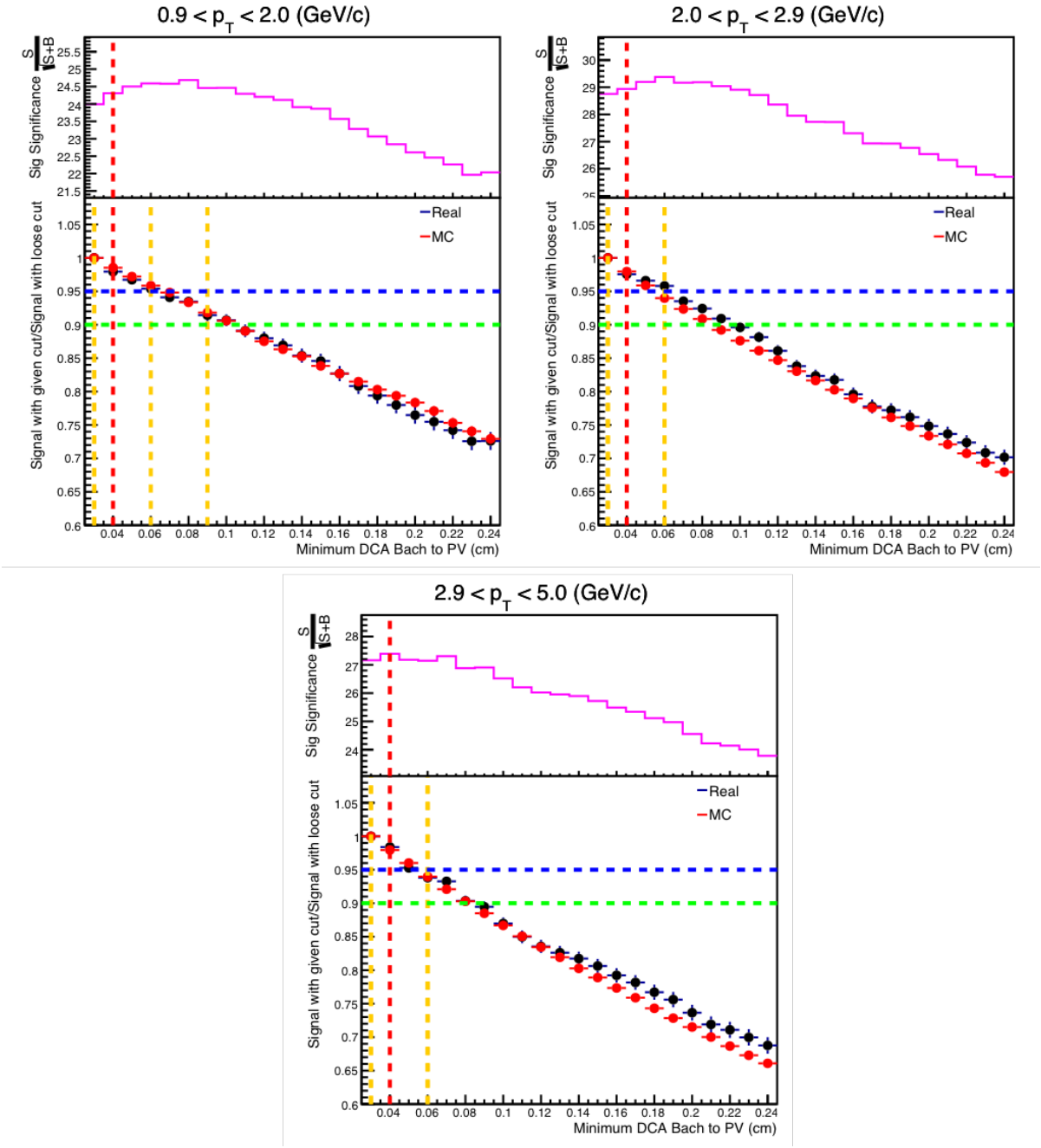

Figure A.14: For each plot, the top shows Signal Significance and the bottom shows Signal losses, with respect to the loosest cut considered for Minimum DCA Bachelor to PV. The $\Omega^{\pm}$data are divided into low (top-left), mid (top-right) and high (bottom) p_T bins. Black markers are for real data and red markers are for MC data. Red vertical line indicates default cut and orange vertical lines show loose/tight cuts.

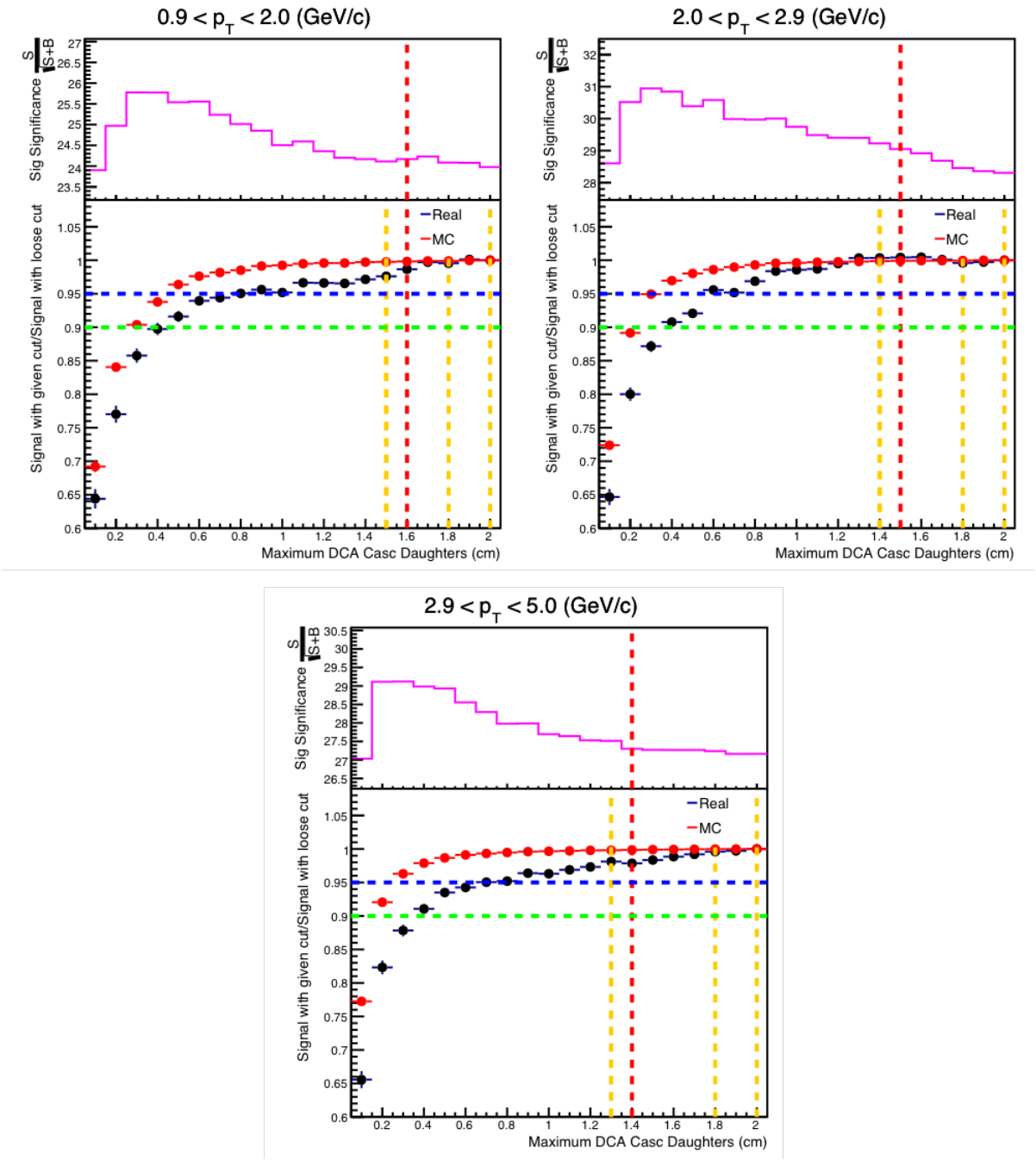

Figure A.15: For each plot, the top shows Signal Significance and the bottom shows Signal losses, with respect to the loosest cut considered for Maximum DCA Cascade Daughters. The $\Omega^{\pm}$data are divided into low (top-left), mid (top-right) and high (bottom) p_T bins. Black markers are for real data and red markers are for MC data. Red vertical line indicates default cut and orange vertical lines show loose/tight cuts.

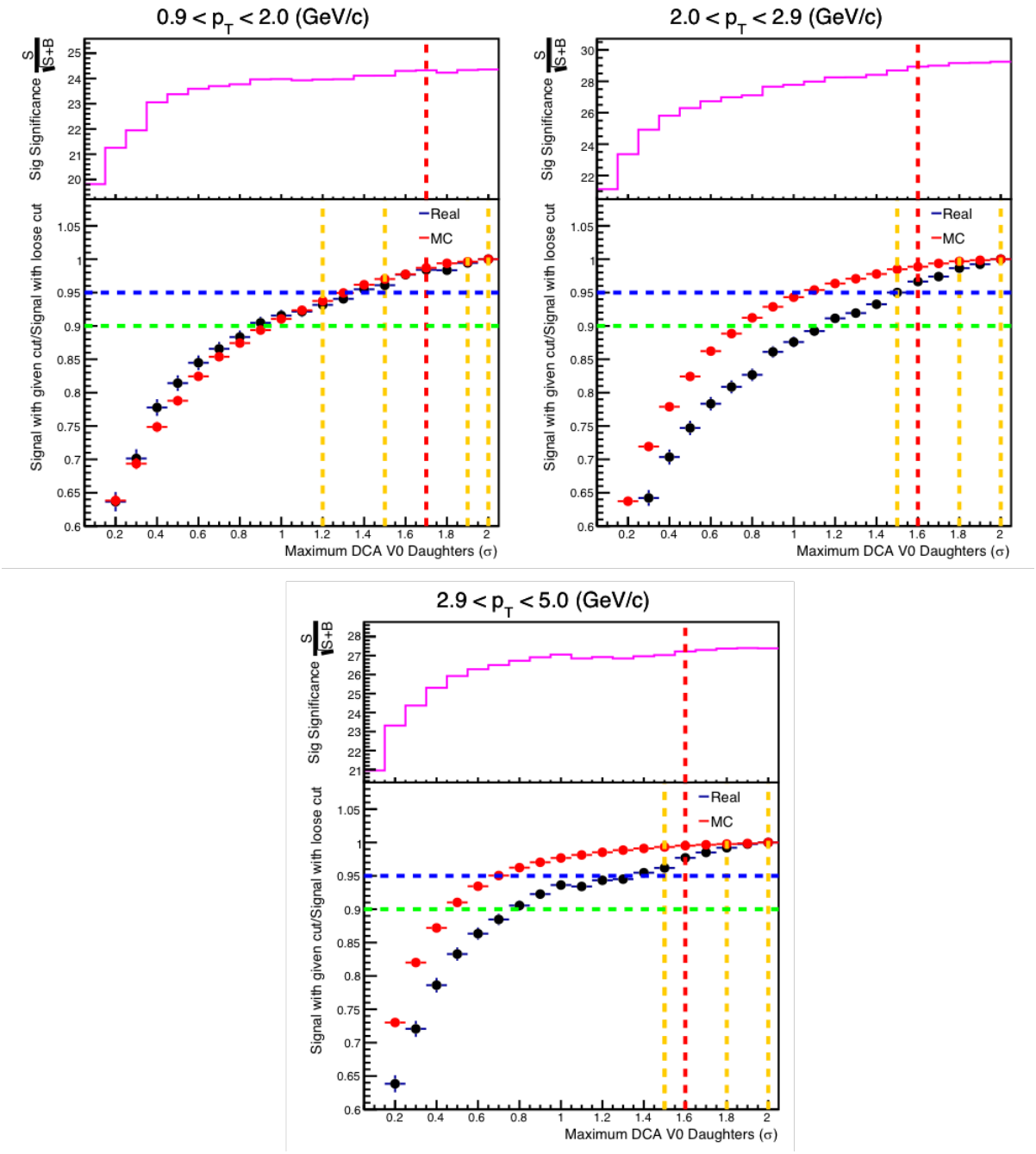

Figure A.16: For each plot, the top shows Signal Significance and the bottom shows Signal losses, with respect to the loosest cut considered for Maximum DCA V0 Daughters. The $\Omega^{\pm}$data are divided into low (top-left), mid (top-right) and high (bottom) p_T bins. Black markers are for real data and red markers are for MC data. Red vertical line indicates default cut and orange vertical lines show loose/tight cuts.

Appendix **B**

Plots used for systematic studies

Plots here showing the deviations in signal for variables not shown in the text in chapter 4. The plots show the ratio of yields with the different cuts to the yield with the default value as a function of p_T. These are used to calculate the systematic errors by taking the maximum deviation in each p_T bin if it is larger than one Roger Barlow's sigma [168], which disregards statistical fluctuations that do not contribute to the systematic uncertainty.

The results for $\Xi^{\pm}$ are shown in figures B.1 and B.2 and the results for $\Omega^{\pm}$ are shown in figures B.3, B.4 and B.5.

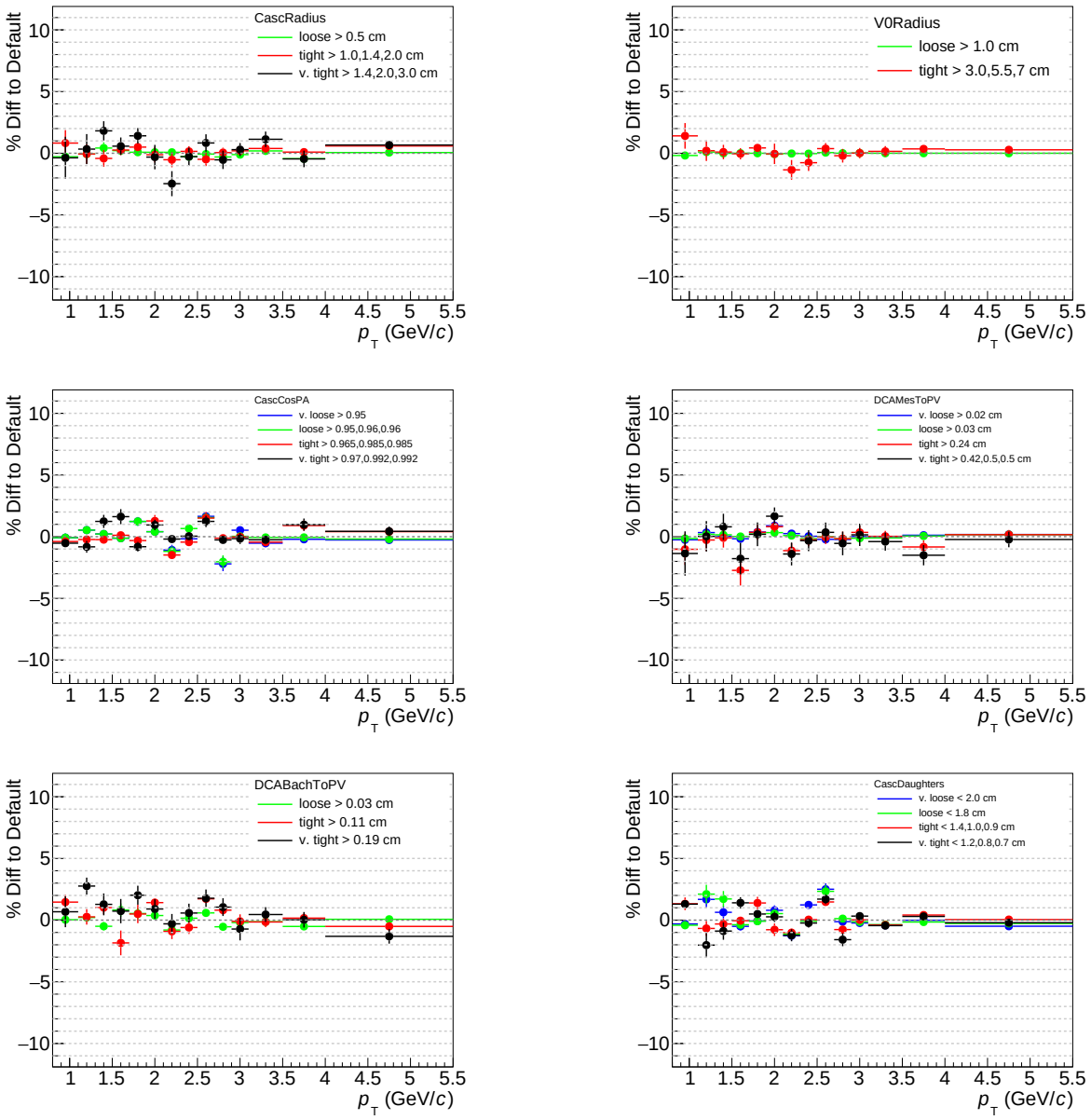

Figure B.1: Signal deviations seen in corrected $\Xi^{\pm}$ spectra due to cut selection changes. Results are shown for cascade radius cuts (top left), V0 radius cuts (top right), cascade cos(PA) cuts (middle left), DCA between meson V0 daughter and PV cuts (middle right), DCA between bachelor and PV cuts (bottom left) and cascade daughter cuts (bottom right). Error bars are Roger-Barlow errors representing an acceptable deviation due to statistical fluctuations.

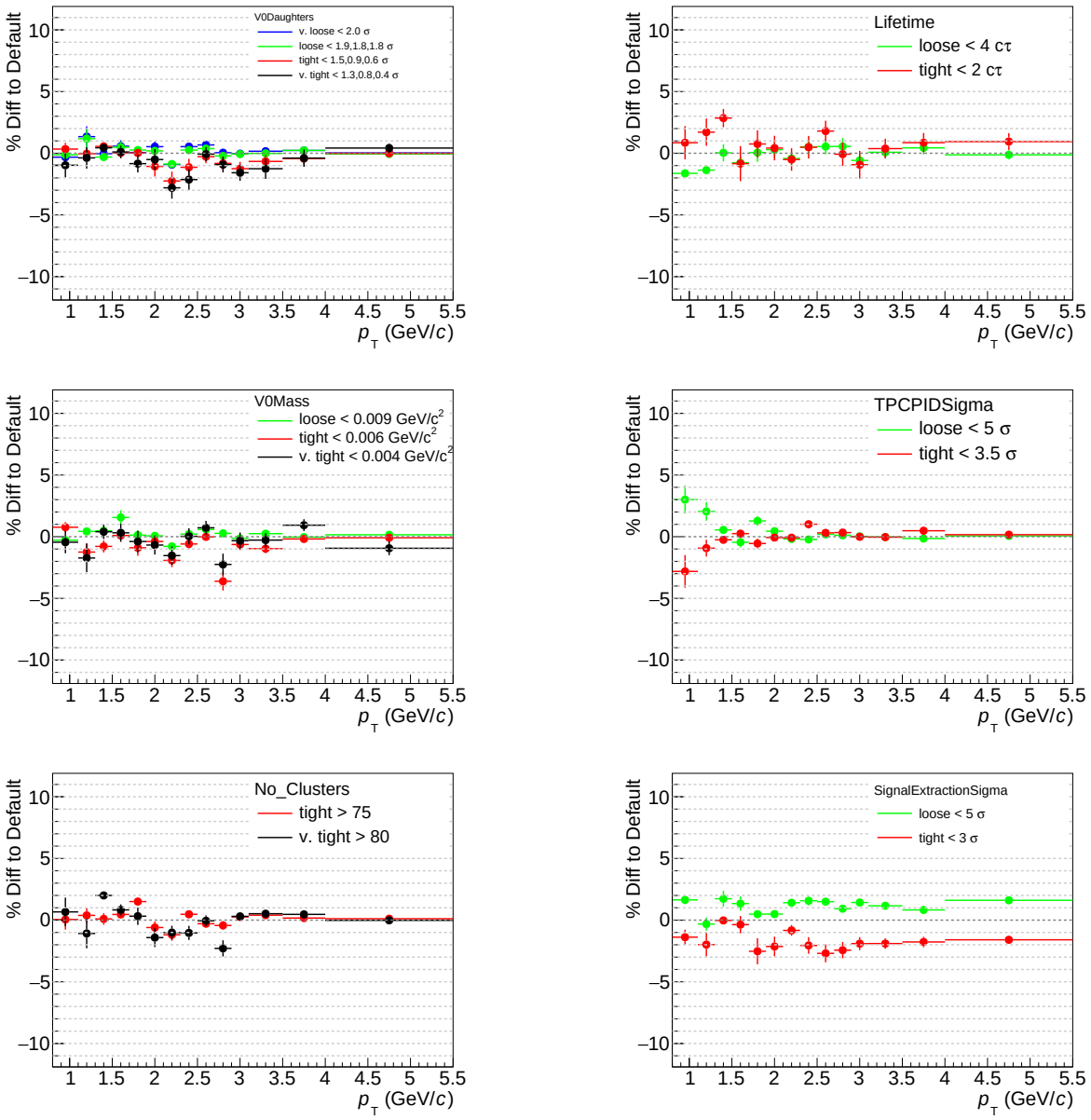

Figure B.2: Signal deviations seen in corrected $\Xi^{\pm}$ spectra due to cut selection changes. Results are shown for V0 daughter cuts (top left), lifetime cuts (top right), V0 mass cuts (middle left), number of TPC PID sigma cuts (middle right), number of TPC cluster cuts (bottom left) and number of sigma used in signal extraction cuts (bottom right). Error bars are Roger-Barlow errors representing an acceptable deviation due to statistical fluctuations.

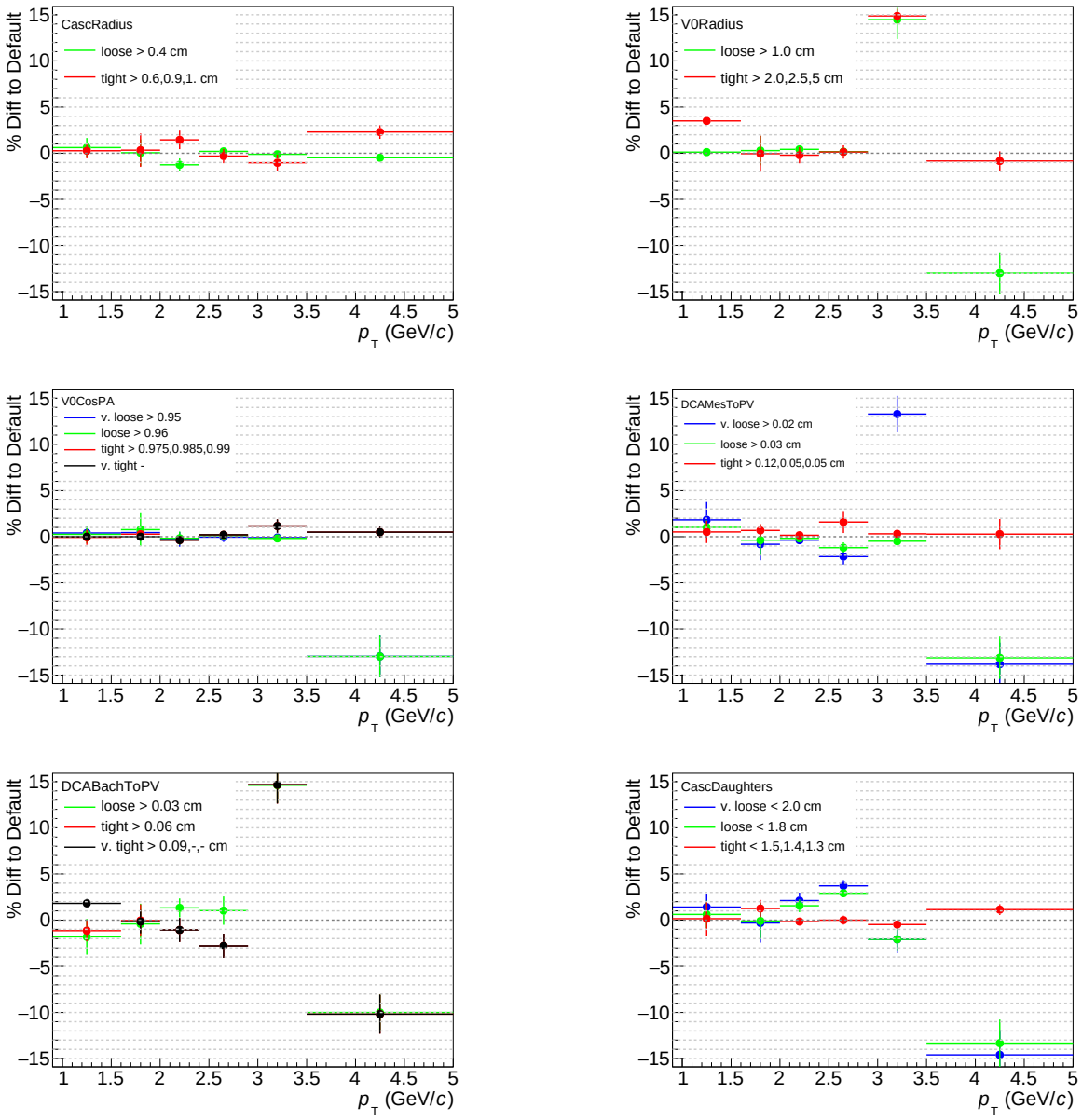

Figure B.3: Signal deviations seen in corrected $\Omega^{\pm}$ spectra due to cut selection changes. Results are shown for cascade radius cuts (top left), V0 radius cuts (top right), cascade cos(PA) cuts (middle left), DCA between meson V0 daughter and PV cuts (middle right), DCA between bachelor and PV cuts (bottom left) and cascade daughter cuts (bottom right). Error bars are Roger-Barlow errors representing an acceptable deviation due to statistical fluctuations.

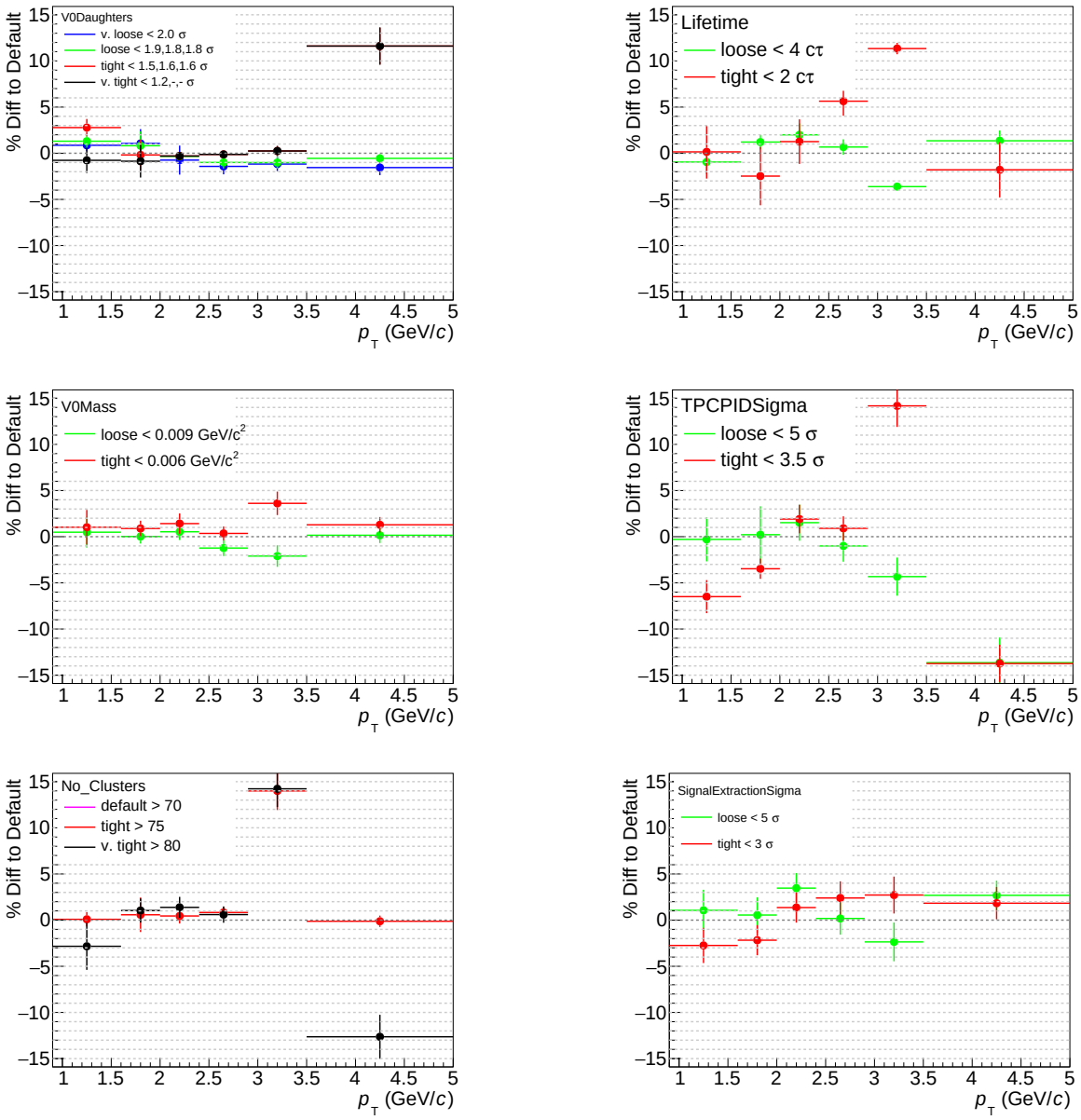

Figure B.4: Signal deviations seen in corrected $\Omega^{\pm}$ spectra due to cut selection changes. Results are shown for V0 daughter cuts (top left), lifetime cuts (top right), V0 mass cuts (middle left), number of TPC PID sigma cuts (middle right), number of TPC cluster cuts (bottom left) and number of sigma used in signal extraction cuts (bottom right). Error bars are Roger-Barlow errors representing an acceptable deviation due to statistical fluctuations.

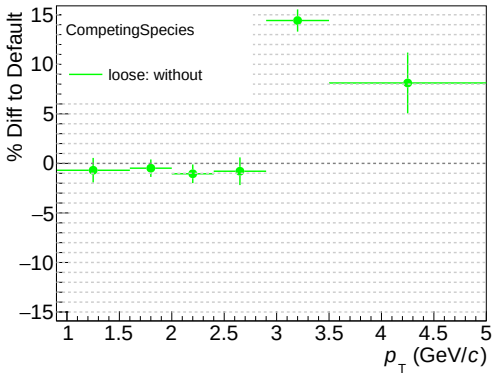

Figure B.5: Signal deviations seen in corrected $\Omega^{\pm}$ spectra due to cut selection changes. Results are shown for the mass hypothesis cut used only in the case of $\Omega^{\pm}$. Error bars are Roger-Barlow errors representing an acceptable deviation due to statistical fluctuations.

Appendix C

Fits used for extrapolation errors

Plots shown here include the Lévy-Tsallis fits for the multiplicity bins not shown in the text in chapter 5. The points indicate the data and the lines show the results of different fitting functions as outlined in section 2.2.5.2. These alternative functions were used to estimate the systematic error in the extrapolation of the data to low and high p_T as described in section . The bottom panel on each figure shows the deviation between the data and the fitting function used.

The results for $\Xi^{\pm}$ are shown in figures C.1, C.2, C.3 and C.4 and the results for $\Omega^{\pm}$ are shown in figures C.5 and C.6.

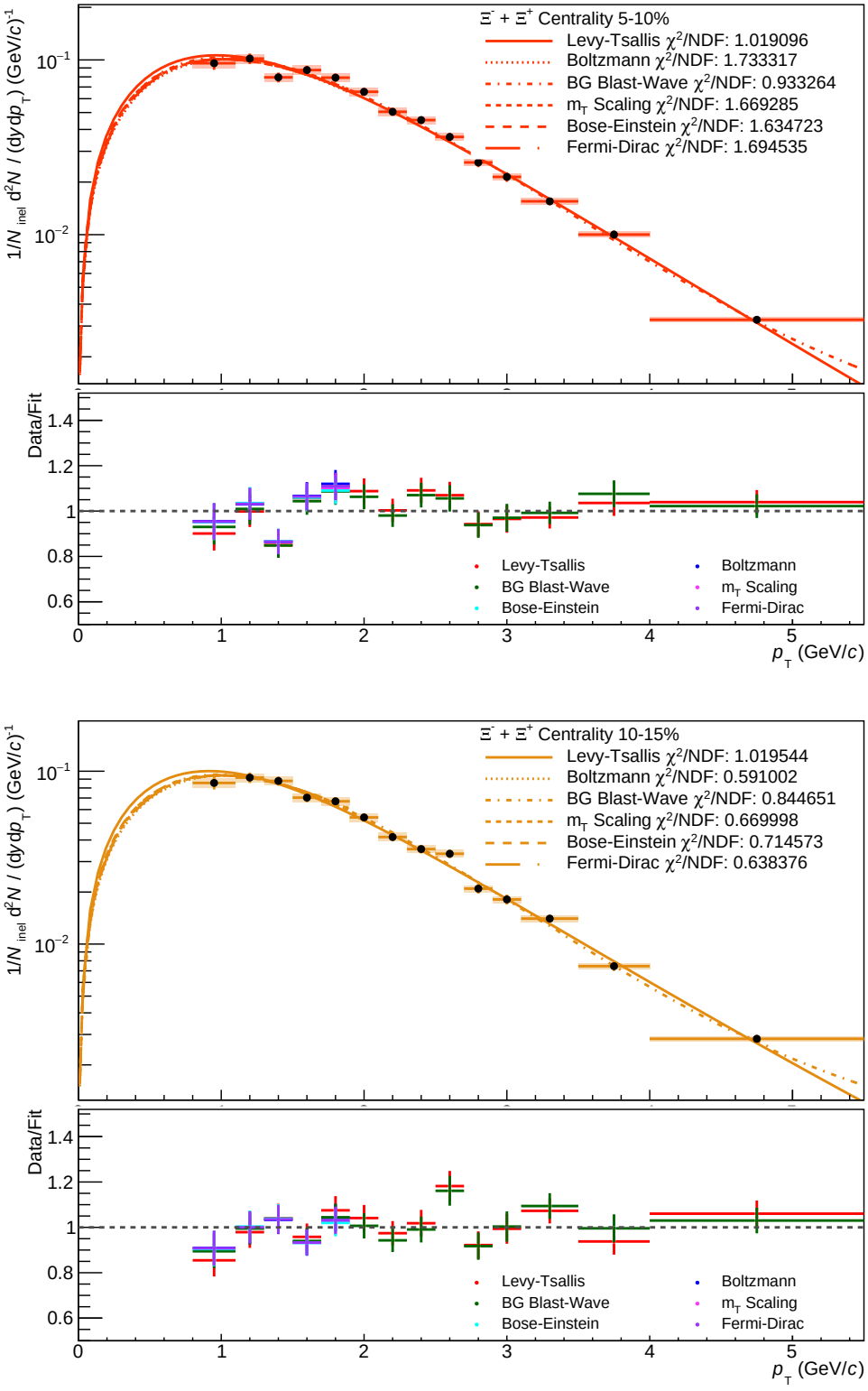

Figure C.1: Plots showing the default Lévy-Tsallis and other fits in different multiplicity bin for $\Xi^{\pm}$. The bottom panel indicates the relative deviations between the data in each p_T bin and the fitting function used. The top plot shows the 5-10% V0 multiplicity bin and the bottom plot shows the 10-15% multiplicity bin.

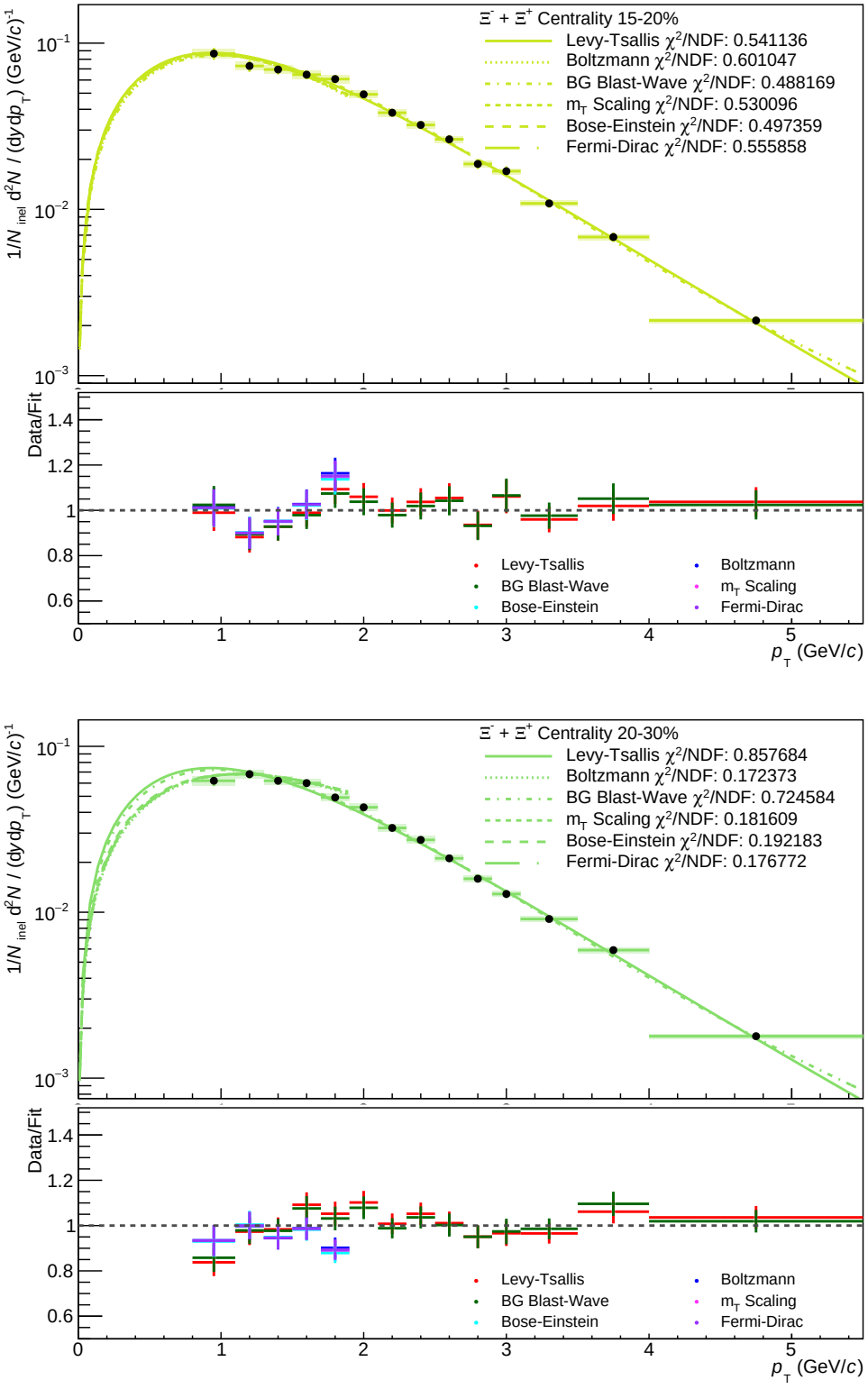

Figure C.2: Plots showing the default Lévy-Tsallis and other fits in different multiplicity bin for $\Xi^{\pm}$. The bottom panel indicates the relative deviations between the data in each p_T bin and the fitting function used. The top plot shows the 15-20% V0 multiplicity bin and the bottom plot shows the 20-30% multiplicity bin.

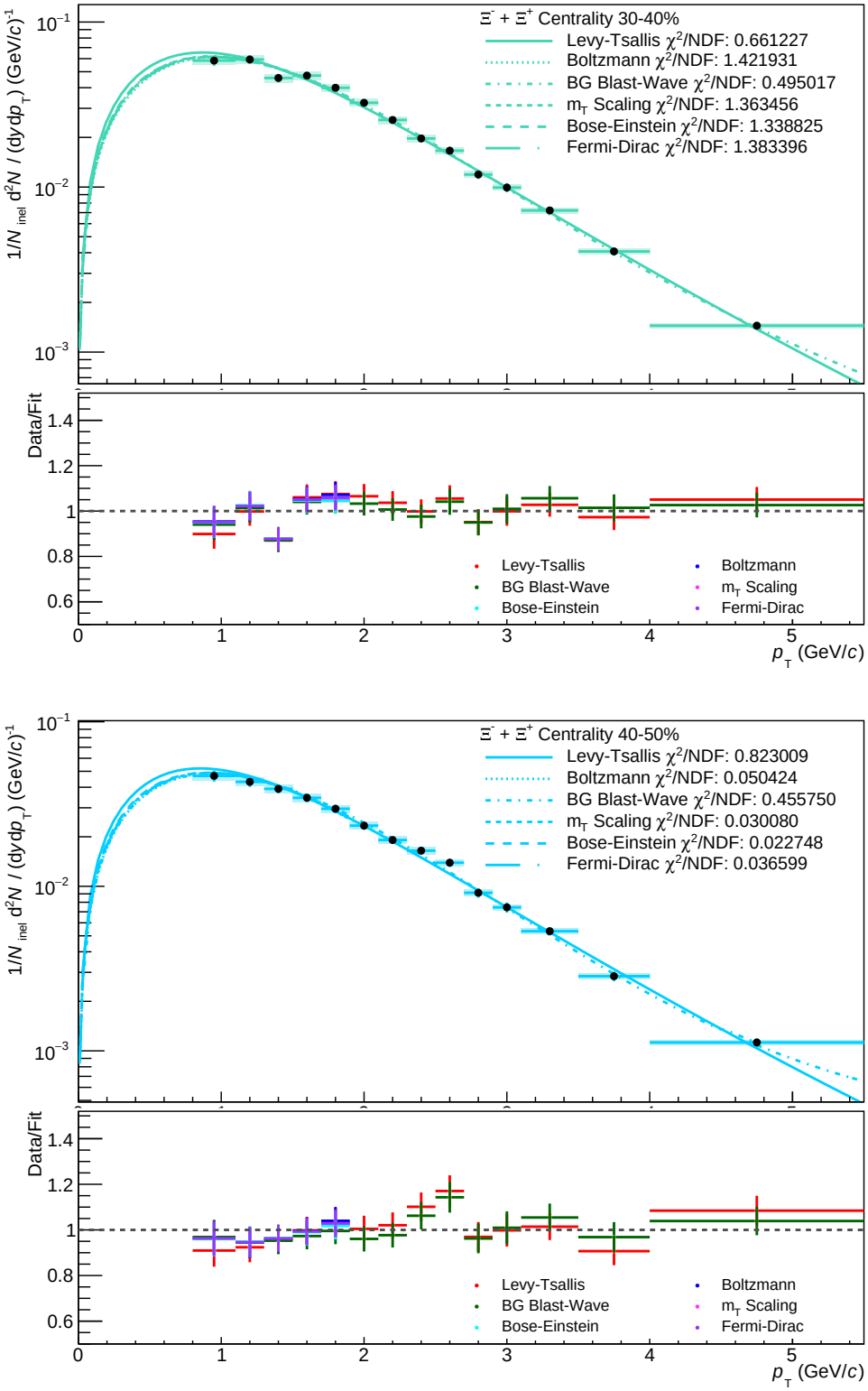

Figure C.3: Plots showing the default Lévy-Tsallis and other fits in different multiplicity bin for $\Xi^{\pm}$. The bottom panel indicates the relative deviations between the data in each p_T bin and the fitting function used. The top plot shows the 30-40% V0 multiplicity bin and the bottom plot shows the 40-50% multiplicity bin.

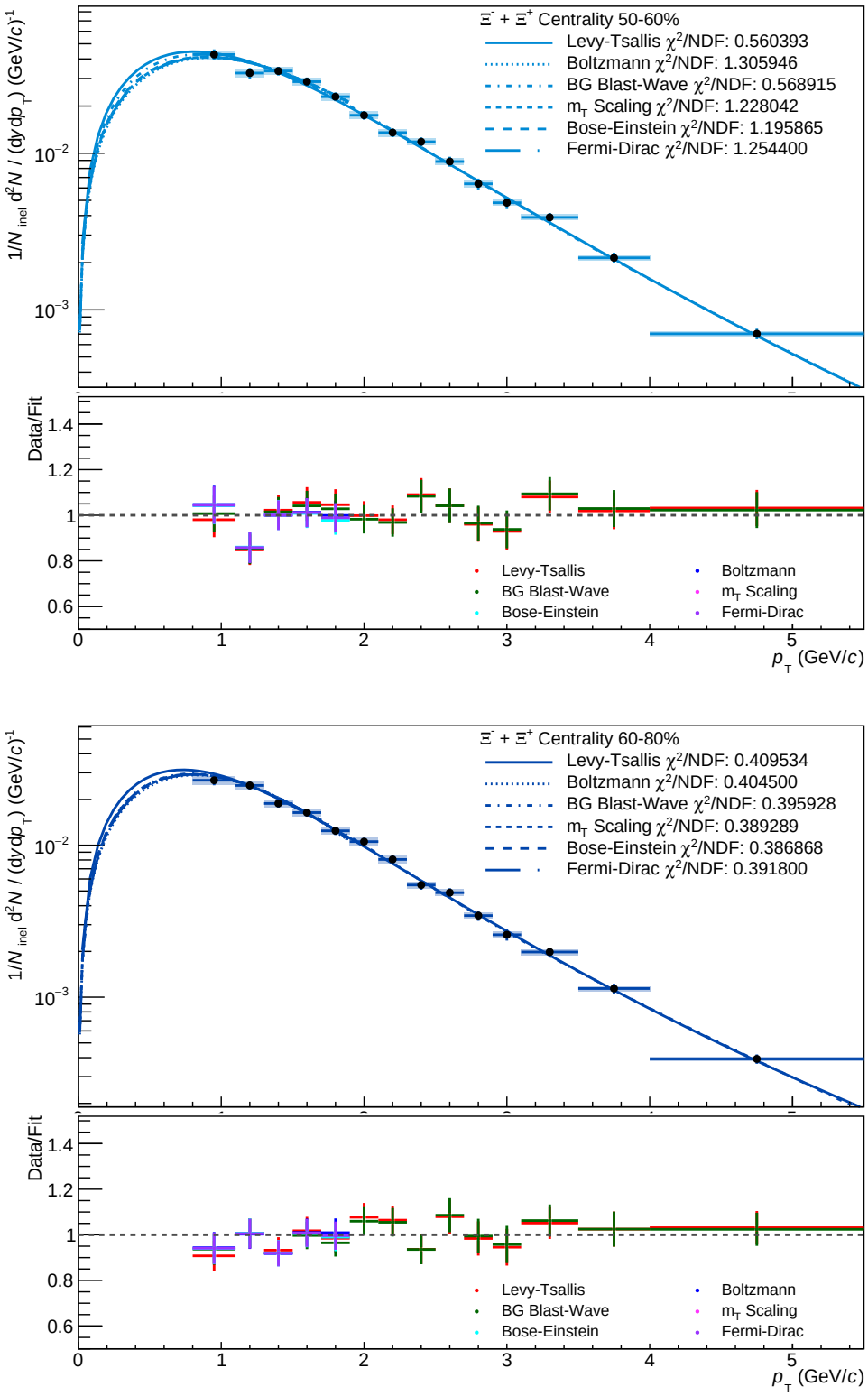

Figure C.4: Plots showing the default Lévy-Tsallis and other fits in different multiplicity bin for $\Xi^{\pm}$. The bottom panel indicates the relative deviations between the data in each p_T bin and the fitting function used. The top plot shows the 50-60% V0 multiplicity bin and the bottom plot shows the 60-80% multiplicity bin.

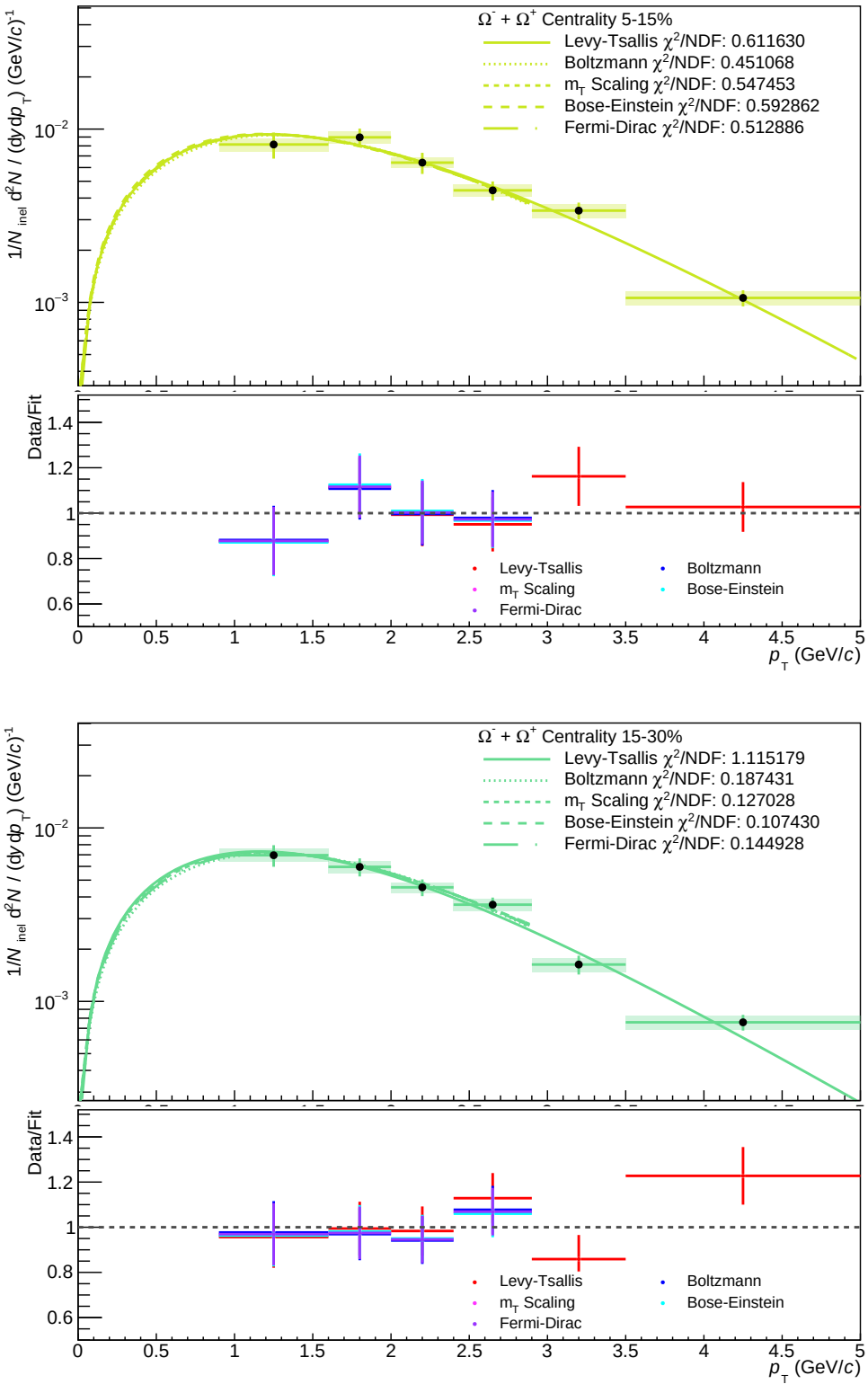

Figure C.5: Plots showing the default Lévy-Tsallis and other fits in different multiplicity bin for $\Omega^{\pm}$. The bottom panel indicates the relative deviations between the data in each p_T bin and the fitting function used. The top plot shows the 5-15% V0 multiplicity bin and the bottom plot shows the 15-30% multiplicity bin.

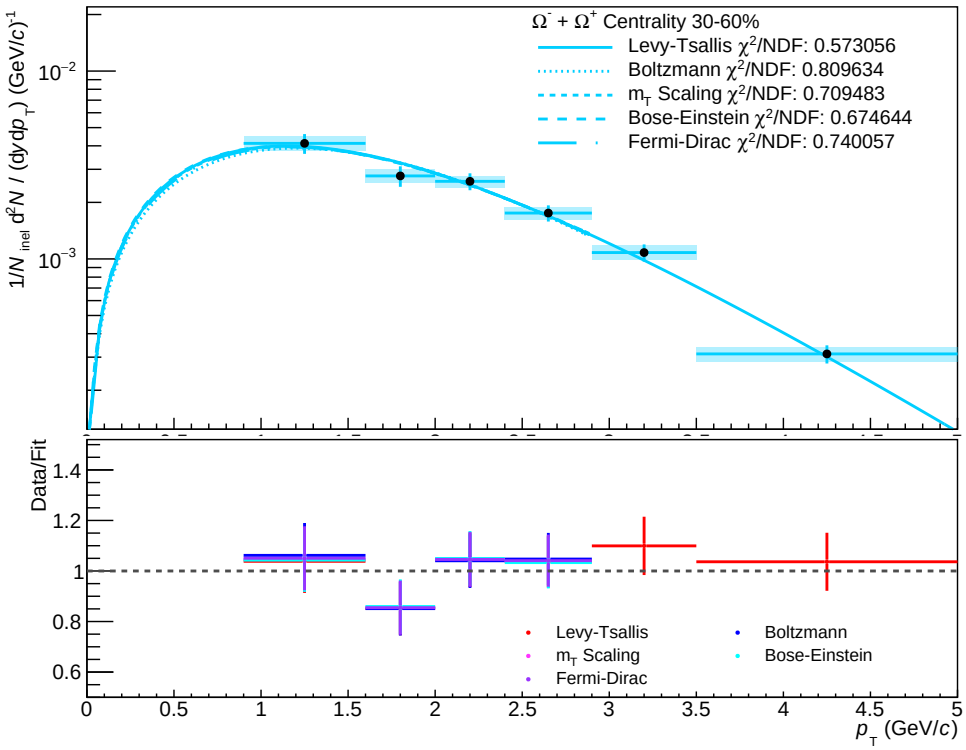

Figure C.6: Plots showing the default Lévy-Tsallis and other fits in different multiplicity bin for $\Omega^{\pm}$. The bottom panel indicates the relative deviations between the data in each p_T bin and the fitting function used. The plot shows the results for the 30-60% V0 multiplicity bin.

Appendix D

Yield Results

The following tables include the integrated yield results for $\Xi^{\pm}$ and $\Omega^{\pm}$ that produced the results found in figures 5.12 and 5.13 in chapter 5. The systematic errors include the systematic estimated from the effect of μ on the results as described in section 5.2. The $\Xi^{\pm}$results include the extra multiplicity bin that was extracted by splitting the 0-5% bin into two.

Table D.1: The $\Xi^{-}+\overline{\Xi}^{+}$ integrated yields in each V0A multiplicity class with the corresponding mid-rapidity $\mathrm{d}N_{\mathrm{ch}}/\mathrm{d}\eta$ values given. The statistical errors and then the systematic errors are shown.

V0A Mult Bins, %	$\mathrm{d}N_{\mathrm{ch}}/\mathrm{d}\eta$	$(\Xi^{-}+\overline{\Xi}^{+})/2\times(10^{-1})$
0-1	64.00 ± 1.66	$1.662 \pm 0.038 \pm 0.176$
1-5	50.50 ± 1.30	$1.287 \pm 0.018 \pm 0.134$
5-10	42.40 ± 1.10	$1.026 \pm 0.015 \pm 0.098$
10-15	37.30 ± 0.97	$0.942 \pm 0.016 \pm 0.081$
15-20	33.64 ± 0.87	$0.809 \pm 0.014 \pm 0.076$
20-30	29.30 ± 0.76	$0.689 \pm 0.009 \pm 0.071$
30-40	24.49 ± 0.66	$0.577 \pm 0.009 \pm 0.055$
40-50	20.34 ± 0.53	$0.466 \pm 0.008 \pm 0.041$
50-60	16.46 ± 0.43	$0.383 \pm 0.008 \pm 0.035$
60-80	10.97 ± 0.29	$0.219 \pm 0.005 \pm 0.022$
80-100	4.47 ± 0.12	$0.073 \pm 0.004 \pm 0.008$

Table D.2: The $\Omega^- + \overline{\Omega}^+$ integrated yields and mean p_T in each V0A multiplicity class with the corresponding mid-rapidity $\mathrm{d}N_{\mathrm{ch}}/\mathrm{d}\eta$ values given. The statistical errors and then the systematic errors are shown.

V0A Mult Bins, %	$\mathrm{d}N_{\mathrm{ch}}/\mathrm{d}\eta$	$(\Omega^- + \overline{\Omega}^+)/2 \times (10^{-2})$
0-5	53.22 ± 1.38	$1.917 \pm 0.120 \pm 0.312$
5-15	39.86 ± 1.10	$1.139 \pm 0.053 \pm 0.157$
15-30	30.77 ± 0.86	$0.883 \pm 0.051 \pm 0.154$
30-60	20.42 ± 0.56	$0.465 \pm 0.049 \pm 0.080$
60-100	7.63 ± 0.20	$0.178 \pm 0.014 \pm 0.039$

Appendix E

Hadrochemistry of Particle Production in Small Systems with ALICE at the LHC

This is a pre-print version of a contribution published in The XVIII International Conference on Strangeness in Quark Matter (SQM 2019), edited by D. Elia, G. E. Bruno, P. Colangelo and L. Cosmai, published by Springer Proceedings in Physics. The definitive authenticated version is available online via "https://doi.org/10.1007/978-3-030-53448-6_35" [2].

Hadrochemistry of Particle Production in Small Systems with ALICE at the LHC

Emily Willsher for the ALICE Collaboration

University of Birmingham, UK

Abstract. The results of multi-strange particle production as a function of transverse momentum and event multiplicity in p–Pb collisions at $\sqrt{s_{NN}} = 8.16$ TeV measured with ALICE [1] at the LHC are reported. These measurements are compared to earlier results obtained at $\sqrt{s_{NN}} = 5.02$ TeV [2], and the trend at both energies is found to be the same. A comparison to other collision systems such as pp, Pb–Pb and Xe–Xe is also made. These measurements help further the understanding of the differences and similarities between small and large colliding systems.

Keywords: Identified Hadrons · Strangeness · Multi-Strange · Small Systems · Particle Ratios · Yields

1 Introduction

Historically, small collision systems, such as proton-proton and proton-lead, have been used as a reference for measurements in heavy-ion collisions in order to separate true final state effects from QCD or cold nuclear matter effects. However, recent measurements of high-multiplicity events at the LHC have led to the observation of heavy-ion effects in small systems [3, 4]. This includes results of strange particle production as a function of charged-particle multiplicity [5]. In these proceedings, new results on the production of $\Xi^{\pm}$ and $\Omega^{\pm}$ in p–Pb collisions at the energy of $\sqrt{s_{NN}} = 8.16$ TeV are presented.

1.1 Strangeness Production

The enhanced production of strange hadrons was one of the earliest proposed signatures of Quark-Gluon Plasma (QGP) formation [6], as higher rates of thermal quark production are possible in a partonic medium. This enhancement was predicted to follow a hierarchy dependent on the strangeness content of the particle meaning the level of enhancement is stronger for multi-strange particles. This has been observed in heavy-ion collisions at SPS, RHIC, and the LHC [7–9].

ALICE has also measured this effect in small systems, where the enhancement measured is observed to be strongly dependent on charged-particle multiplicity and independent of the colliding system [5]. This smooth strange particle

enhancement across colliding systems can be explained with statistical hadronisation models as canonical suppression of strange quark production which gradually subsides as the system size increases [10]. The trend has also been described well in all systems by using the initial energy density as a universal scaling constant [11]. However, particle production mechanisms in these small collision systems are still unclear. The latest measurements presented here will compare the most recent data from p–Pb collisions to those at lower energies in order to study the centre-of-mass energy dependence of this effect.

2 Multi-strange hadron detection with ALICE

The ALICE apparatus and its performance are described in detail in [1]. The main detectors used in this analysis were: the inner tracking system (ITS), which provides tracking and vertex information, the time projection chamber (TPC), which provides further tracking information and particle identification (PID) and the V0 detectors which are used for triggering, as well as estimating the multiplicity of charged particles in the events as described in [12].

Multi-strange hadrons ($\Xi^{\pm}$ and $\Omega^{\pm}$) are reconstructed by utilising the characteristic topology of their weak decays into three identifiable charged particles. The charged particle tracks are combined in order to extract the invariant mass of the cascade candidates. The signal is optimised by applying cuts on certain topological quantities. The data are divided into different transverse momentum (p_T) and multiplicity bins and the yields are extracted by using bin counting in the signal region and a fit of the background. The results are corrected with acceptance and efficiency values which are calculated using Monte Carlo simulations of the ALICE detector using DPMJET and EPOS-LHC.

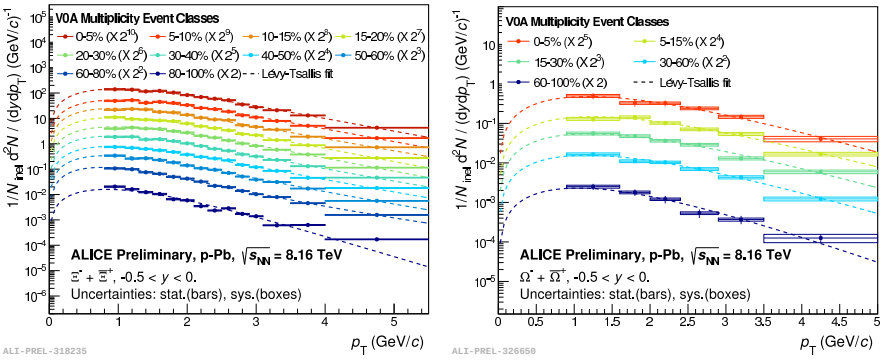

Fig. 1. Tranverse momentum spectra for $\Xi^{\pm}$ (left) and $\Omega^{\pm}$ (right) for different multiplicity intervals in p–Pb collisions at $\sqrt{s_{NN}}$ = 8.16 TeV.

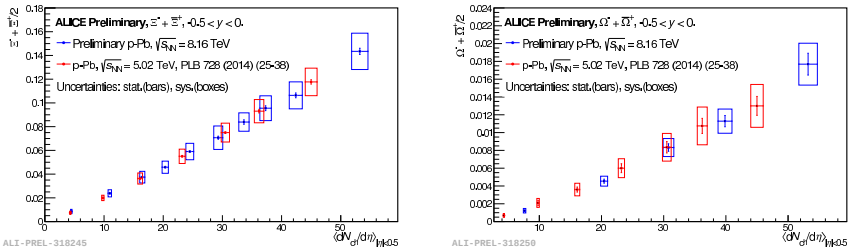

Fig. 2. Yields of $\Xi^{\pm}$ (left) and $\Omega^{\pm}$ (right) as a function of $\mathrm{d}N_{\mathrm{ch}}/\mathrm{d}\eta$ in p–Pb collisions at $\sqrt{s_{NN}} = 8.16$ TeV are shown in blue. Results from the lower energy analysis at $\sqrt{s_{NN}} = 5.02$ TeV are shown in red.

3 Results

This analysis used a 16M Minimum Bias (MB) triggered event sample of p–Pb collisions at $\sqrt{s_{NN}} = 8.16$ TeV, where the MB trigger is given by a hit in both V0 detectors. The transverse momentum distributions for $\Xi^{\pm}$ and $\Omega^{\pm}$ in different multiplicity classes are shown in Fig. 1. The yields can be extracted from the spectra by integrating the data points and using a Lévy-Tsallis [13] fit to extrapolate down to the unmeasured low p_T region.

The corrected yields plotted as a function of $\mathrm{d}N_{\mathrm{ch}}/\mathrm{d}\eta$ are shown in Fig. 2. The results at $\sqrt{s_{NN}} = 8.16$ TeV are compared to the previous results obtained at $\sqrt{s_{NN}} = 5.02$ TeV. It can be observed that the multiplicity dependence of these yields follows a linear trend at both energies, as was seen in pp results [14]. The multiplicity reach of the results has also been extended to higher values of $\mathrm{d}N_{\mathrm{ch}}/\mathrm{d}\eta$.

In order to study the level of strangeness enhancement in this system, the ratio of the strange particle yields to non-strange particle yields is calculated, where pions measured at $\sqrt{s_{NN}} = 8.16$ TeV have been used for this analysis. The results are shown in Fig. 3 for $\Xi^{\pm}$ and $\Omega^{\pm}$ in p–Pb collisions at $\sqrt{s_{NN}} = 8.16$ TeV by the filled in circle points. The results support the evidence that charged-particle multiplicity is the driving quantity behind strangeness enhancement and the results are independent of the initial collision energy and the colliding system.

4 Conclusion

In summary, measurements of multi-strange hadrons as a function of charged-particle multiplicity in p–Pb collisions at ALICE have been reported. The results add to the picture of a smooth evolution of strangeness enhancement across

colliding systems. The latest data shown here also show there is no significant change in the results from p–Pb at $\sqrt{s_{NN}} = 5.02$ TeV and $\sqrt{s_{NN}} = 8.16$ TeV. These results are important in helping improve current understanding of the microscopic mechanisms behind particle production in small systems and moving towards a unified description of nuclear collisions. Future measurements will extend pp and p–Pb results to $\mathrm{d}N_{\mathrm{ch}}/\mathrm{d}\eta$ values reached in central Pb–Pb collisions so we can understand if the grand-canonical limit for particle production is achieved in these small systems.

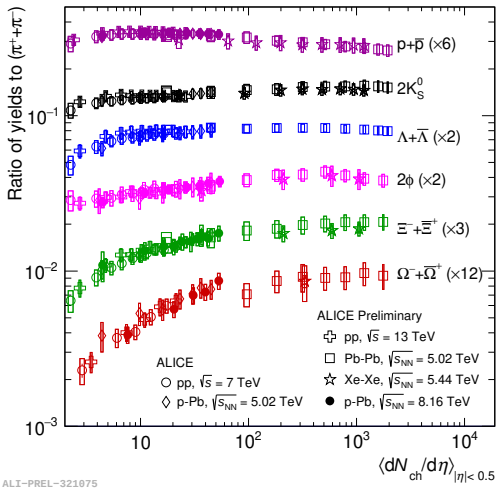

Fig. 3. Ratio of particle yields to pion yields at as a function of $\mathrm{d}N_{\mathrm{ch}}/\mathrm{d}\eta$. Results in p–Pb collisions at $\sqrt{s_{NN}} = 8.16$ TeV are shown by filled in circle points. Results are compared to those from other centre-of-mass energies and other collision systems.

References

1. Aamodt K. *et al.* [ALICE Coll.] (2008) *JINST* **3** S08002. doi:10.1088/1748-0221/3/08/S08002
2. Adam J. *et al.* [ALICE Coll.] (2016) *Phys. Lett.* B **758** 389. doi:10.1016/j.physletb.2016.05.027
3. Vardan K. *et al.* [CMS Coll.] (2010) *JHEP* **1009** 091. doi:10.1007/JHEP09(2010)091
4. Vardan K. [CMS Coll.] *et al.* (2017) *Phys. Lett.* B **765** 193. doi:10.1016/j.physletb.2016.12.009
5. Adam, J. *et al.* [ALICE Coll.] (2017) *Nat. Phys.* **13** 535. doi:10.1038/nphys4111
6. Rafelski, J. and Müller, B. (1982) *Phys. Rev. Lett.* **48** 1066. doi:10.1103/PhysRevLett.48.1066
7. Andersen, E. *et al.* [WA97 Coll.] (1999) *Phys. Lett.* B **449** 401. doi:10.1016/S0370-2693(99)00140-9

8. Agakishiev, G. *et al.* [STAR Coll.] (2012) *Phys. Rev. Lett.* **108** 072301. doi:10.1103/PhysRevLett.108.072301
9. Abelev, B. *et al.* [ALICE Coll.] (2014) *Phys. Lett.* B **728** 216. 10.1016/j.physletb.2013.11.048
10. Acharya, S. *et al.* [ALICE Coll.] (2019) *Phys. Rev.* C **99** 024906. doi:10.1103/PhysRevC.99.024906
11. Cuautle, E., Paić, G. (2016) arXiv:1608.02101 [hep-ph]
12. Acharya, S. *et al.* [ALICE Coll.] (2019) *Eur. Phys. J.* C **79** 307. doi:10.1140/epjc/s10052-019-6801-9
13. Tsallis, C. (1988) *J. Stat. Phys.* **52** 479. doi:10.1007/BF01016429
14. Acharya, S. *et al.* [ALICE Coll.] (2019) arXiv:1908.01861 [nucl-ex]